Characterization of the Micro Injection Molding Process and Its Products

Jingsong Chu

Department of Chemical Engineering
McGill University, Montreal, Quebec, Canada

August 2009

A thesis submitted to the Faculty of Graduate Studies and Research in partial fulfillment of the requirement of the degree of Doctor of Philosophy

ABSTRACT

A micro-injection molding machine was used to obtain micro-moldings of high density polyethylene, polyoxymethylene, and polycarbonate, in order to characterize the process dynamics, and to investigate the effects of processing conditions on microstructure, mechanical properties, and thermal properties.

A data acquisition system was implemented to obtain traces of data regarding the evolution of process variables with time. Six characteristic process parameters (CPPs) and metering size were used to characterize both the cavity filling and packing stages. The method of design of experiments (DOE) was employed, in order to investigate the effects of machine variables on the CPPs. A simulation was conducted using Moldflow commercial injection molding software. The discrepancy between experimental and calculated injection pressure patterns was attributed to the utilization of the unrealistic rheological model and boundary conditions.

The samples were microtomed and examined using a polarized light microscope for investigation of morphology. Various microstructural features, such as morphological layer thickness and crystalline polymorphs, were observed and analyzed, in light of the thermo-mechanical history. These features were correlated with both macro and local mechanical properties.

A punch die was designed and fabricated to cut the micro molded samples precisely into tensile testing specimen. The tensile properties were measured accurately with a conventional INSTRON testing machine combined with specially designed sample holders to prevent slippage and to ensure sample alignment. Thermal characterization was performed using modulated differential scanning calorimetry. Local indentation moduli were measured with a Hysitron TriboIndenter. An effort was made to evaluate process-structure-property relations.

RESUMÉ

Une machine de micro-injection a été utilisée pour fabriquer des micro platines de polyéthylène de haute densité (PEHD), de polyoxyméthylène (POM), et de polycarbonate (PC), afin de caractériser la dynamique du processus de micro-injection, et d'étudier les effets des conditions d’injection sur la microstructure, les propriétés mécaniques et les propriétés thermiques des pièces formés.

Un système d'acquisition de données a été utilisé pour enregistre les données relative à l'évolution des variables du procédé avec le temps. Six paramètres caractéristiques du procédé (PCP) ainsi que la quantité d’injection, ont été utilisés pour caractériser à la fois le remplissage de la cavité et les étapes de compaction. La méthode de conception d'expériences a été employée afin d'examiner les effets des paramètres de la machine sur les PCPs. Une simulation a été réalisée en utilisant MOLDFLOW, un logiciel commercial pour simuler le processus d’injection. La différence entre le profil de pression d'injection observée experimentalement et celle obtenue par simulation a été attribuée à l'utilisation des modèles rhéologiques ainsi que des conditions aux limites irréalistes.

Pour l'étude de la morphologie, les échantillons ont été examinés à l'aide d'un microscope à lumière polarisée. Diverses caractéristiques microstructurales, tels que l'épaisseur des couches morphologiques et les polymorphes cristalline, ont été observés et analysés en function de l'histoire thermomécanique. Ces caractéristiques ont été corrélé avec les propriétés mécaniques au niveau local et macro échelle.

Un équipement à coupe sous pression a été conçu et fabriqué afin de couper les échantillons avec précision pour obtenir des spécimens pour les essais de traction. Les propriétés de traction ont été mesurées en utilisant, une machine standard de test, combiné avec des cardes de support de l'échantillon, spécialement conçu pour empêcher le glissement de l’échantillon et pour assurer l'alignement des échantillons. La caractérisation thermique a été réalisée à l'aide de la calorimétrie différentielle à balayage. Les modules locaux à l’indentation ont été mesurés avec une Hysitron TriboIndenter. Un effort a été fait afin d’évaluer les relations entre processus, structure et propriétés.

ACKNOWLEDGEMENT

In the first place, I would like to express my deepest gratitude to my research supervisor, Professor M. R. Kamal for his guidance, wisdom, understanding, and support throughout the course of the research. I would also thank Dr. Salim Derdouri, from the Industrial Materials Institute of the National Research Council of Canada (IMI/NRC), for providing the micro injection molding machine and materials and giving me advices during the research. I also would like to thank Professor Andy Hrymak, McMaster University, for offering machine use and materials during the early phase of the research and giving me advices as a member of my Ph.D study advisory committee. Professor Milan Maric is also greatly appreciated for introducing me to the fundamentals of polymer science and engineering and giving me advice as a member of my Ph.D study advisory committee. Furthermore, I would like to thank the following persons:

- Professor Pascal Hubert and Mr. Jonathan Laliberté for their help in the thermal property measurements;
- Professor Srikar Vengallatore, Ms. Janina Crocker, and Mr. Kaushik Das for their help in measuring the local mechanical properties;
- Professor John Dealy and Mr. Jen Shueng Tiang, for invaluable discussions on flow induced crystallization;
- Mr. Normand Nardini at IMI/NRC for his friendship and assistance in operating the micro injection molding machine;
- Mr. Alain Gagnon for his help in designing and fabricating the devices for accurate measurement of tensile properties;
- Mr. Walter Greenland, Mr. Charles Dolan, Mr. Csaba Szalacsi, Mr. David Simmonds, Mr. Roberto Tariello, Mr. Lou Cusmich, Mr. Frank Caporuscio, and Mr. Ranjan Roy, in the machine shop and departmental laboratories, for their various help and advice in this experimentally intensive project.

- Dr. Lijun Feng, Dr. Nitin Borse, Dr. L. Capt, Dr. Jorge Calderon, Mr. Vincent Mollet, Dr. Young-Mi Chung, Dr. Kevin Alam, and other colleagues, for their advices and assistances with various aspects of this project. Also, I would like to thank Dr. Calderon for translating the abstract.

Finally, I give my utmost appreciation to my family: my father, Wei, my morther, Guie, my brother, Guangyi, and especially my wife, Xihui, my daughter, Tianren, and my son, Tianxing, for their everlasting love, understanding and support throughout the course of my studies.

TABLE OF CONTENTS

LIST OF FIGURES

LIST OF TABLES

LIST OF EQUATIONS

1. INTRODUCTION

The micro injection molding process (μIM) involves the production of plastic parts with structural feature dimensions in the micron or sub-micro range. Micro-structured mold inserts are produced with the help of ultra precision processes. Although there is no clear way to define micro injection molding, applications of this process can be broadly categorized into three types of products or components [1, 2]:

1. The mass of the part is of the order of a few milligrams, and possibly has dimensions in the micrometer range;
2. The part dimensions are comparable to a conventional injection molded product, but it contains regions of detail or features with dimension(s) in the micrometer range;
3. The parts can have any dimensions, but they have tolerances on the micrometer scale.

The use of micromolding to produce very small plastics parts is growing, due to demands by the electronics, biomedical, and other industries for such parts and for the production of components for complex micro-electro-mechanical systems (MEMS). The polymer micro injection molding process is a key enabling technology for microsystems, because it has the potential to produce repetitively and consistently large numbers of micro components with complex shape and high surface quality at low cost [3]. Product examples like optical grating elements, micro pumps, micro-fluidic devices and micro gears, flat screens, biochips, and artificial organs have been manufactured successfully using micro injection molding of plastics [4-7]. Despite the fast growth of this manufacturing technology, little work has been reported regarding process characterization and the relevant process-microstructure development-product property relationships.

Many issues relating to flow and heat transfer during cavity filling in the micro injection molding process remain unclear. The plunger injection system adopted by many machine manufacturers, with separate screw melting, metering and injection units, introduces extra parameters, which make the process setup and optimization more difficult, in comparison with conventional injection molding. In the present study, a micro injection molding machine, instrumented with a suite of sensors, was used to obtain micro-moldings of polyoxymethylene (POM), high density polyethylene (HDPE), and polycarbonate (PC). A data acquisition system was developed for recording traces of data regarding the evolution of process variables with time. Cavity filling was followed using short-shot experiments and using traces of injection pressure, runner pressure, and plunger position, in the millisecond time scale. Six characteristic process parameters (CPPs) were defined to characterize both the cavity filling and packing stages for each process condition. This approach provides the opportunity to achieve viable process and product control and optimization, consistent with the actual operating characteristics of the machine. It also helps to achieve better understanding of the filling and packing stages of the process and to obtain more realistic and accurate inputs for modeling and computer simulation of the process. The method of design of experiments (DOE) was employed, in order to investigate the effects of machine variables on the CPPs. Metering size, optimized for each set of machine variables, in order to have a consistent switch-over position, was also used as a CPP.

With the growth and demand for micro injection molded thermoplastic parts, there is an increased need for determination and verification of material mechanical properties at the micro scale level for the design and dimensioning of micro sized parts, since the mechanical properties of macro samples are not valid for micro parts [4, 8, 9]. A precise punch die was designed and fabricated with the technology of micro-electro-discharge machining to cut the molded samples into dumbbell test specimens. A pair of sample holders were designed and machined to fit the pneumatic grips, to prevent slippage between the sample, sample holder, and grips, and to ensure that the long axis of the test specimen coincides with the direction of the pulling force. The mechanical properties of the specimen, including stress-strain curve, modulus and yield stress, were measured. A significant drop in modulus was observed in micro specimens for the materials studied.

The thermal properties of micro injection molded HDPE and POM were investigated, in order to help in evaluating the thermo-mechanical history experienced by the material during the micro injection molding process. The measurement of thermal properties was performed using a differential scanning calorimeter (DSC).

It is generally recognized that the final properties of injection moldings are strongly dependent on morphology, orientation, and stress [10-12]. The microstructural characteristics are especially important for micro injection molded products, because of the large ratio of skin layer thickness to the sample thickness, in comparison with conventional injection molding. However, the characterization of microstructure of microparts remains difficult because of the small dimensions involved. In the present study, the morphology of cross sections of micro moldings was characterized and the effect of process conditions on microstructure was analyzed statistically. Great care was taken to release the stresses causing the microtomed cross sections to curl, especially when sectioning polyoxymethylene moldings.

The commercial software Moldflow 6.0 was employed to simulate the µIM process, using machine variables and estimated filling control profile. In order to describe the flow and heat transfer accurately, the gate and runner systems were integrated with the product in the CAD model and meshed as tetrahedral elements. The crossed square of the four branch runners was selected as the sprue. Each node in this square was selected as the injection location and the simulated area of injection was the area surrounding the selected 285 injection locations.

At the end of the present study, the process–microstructure–property relationships were analyzed, on the basis of the experimental results for POM experiments.

2. BACKGROUND AND LITERATURE REVIEW

In this chapter, the literature background is divided into five sections. The first section provides a review of studies of the micro injection molding process. A summary of reports regarding to simulation of the micro injection molding process is given in the second section. The third section is devoted to crystallization and microstructural studies in conventional injection molding, since few reports are available with respect to microstructure development in micro-injection molding. The last two sections review studies regarding mechanical properties and shrinkage of micro moldings.

2.1 Micro-injection Molding Process Studies

The use of micro-molding to produce very small plastics parts is growing, due to demands by the electronics, biomedical, and other industries for such parts and for the production of components for complex micro-electro-mechanical systems (MEMS).

When the development of micro injection molding started in the late 1980s, no appropriate micro-machine technology was available. Therefore, only modified commercial units, hydraulically driven and with a clamping force of usually 25-50t, could be used for replicating micro parts with high aspect ratio [13]. For example, an Arburg Allrounder 221M 350-75 conventional injection molding machine, with a single cavity, cold runner mold was employed in Su's research [14], in which it was found that mold temperature is the key factor that decisively determines the quality of injection-molded micro parts (200ºC). Also, Yuan modified a tabletop injection molding machine in his research [15]: a thermal control unit was developed to control the mold temperature (125 ºC), and a vacuum unit was developed to evacuate the micro-cavity before filling it with plastic melt.

With the conventional injection molding machines, polymer can be homogeneously plasticized thanks to both thermal and mechanical heating supplied by a rotating screw in a barrel [7]. However, the following limitations were also reported. Firstly, the production of micro parts using conventional injection molding machines led to large wastes because the weight of the part represents only a few percent of the whole molded mass. Secondly, the material degradation occurred during the different processing steps (plasticization, injection, holding). Thirdly, hydraulic control of the metering size was not accurate enough for the replication of such small parts; thus electrical machines would be preferred for such application. Finally, the clamp forces provided by the conventional injection molding machine were much higher than that required for the small surface of injected polymer; Thus, the size of the injection unit parts (screw, barrel, nozzle and hot block) and the clamp unit can be decreased to limit the amount of material as well as the energy consumption.

Two types of micro injection molding machines have been developed by different machine suppliers to minimize waste and to limit degradation of the polymer. The first type machines are actually scaling down of conventional injection molding machines and are usually all electrically controlled. The second type machines features a plunger injection system, which employs separate screw melting, metering, and injection units and introduces extra parameters. On the basis of the work of Bibber et al. [16] and Giboz et al [7], the different micro injection molding machines and their critical specifications are listed in Table 2-1 (Reproduced from Table 1 of [7]). The size of the micromolding machines allows the fabrication of microparts with volume varying from 0.082 to 8 cm^3. A typical machine of the second type, which is employed in the present study, and its plunger injection system, are displayed in Figure 2-1 (a) and (b).

Table 2-1: List of micromolding machine commercially available and their characteristics [7]

Manufac-turers	Model	Clamp force (KN)	Injection Capacity (cm^3)	Injection pressure (MPa)	Plasticization (screw or plunger)	Injection speed (mm s^{-1})
Lawton	Sesame nanomolder	13.6	0.082	350	10 mm plunger	1200
APM	SM-5EJ	50	1	245	14 mm screw	800
Battenfeld	Microsystem 50	50	1.1	250	14 mm screw	760
Nissei	AU3	30	3.1	--	14 mm screw	--
Babyplast	Babyplast 6/10	62.5	4	265	10 mm plunger	--
Sodick	TR05EH	49	4.5	197	14 mm screw	300
Rondol	High Force 5	50	4.5	160	20 mm screw	--
Boy	12/AM 129-11	129	4.5	245	12 mm screw	--
Toshiba	EC5-01 A	50	6	200	14 mm screw	150
Fanuc	Roboshot S2000i 15B	150 KN	9	250	14 mm screw	525
Sumimoto	SE7M	69	6.2	196	14 mm screw	300
Milacron	Si-B17A	147	6.2	245	14 mm screw	--
MCP	12/90 HSE	90	7	172	16 mm screw	100

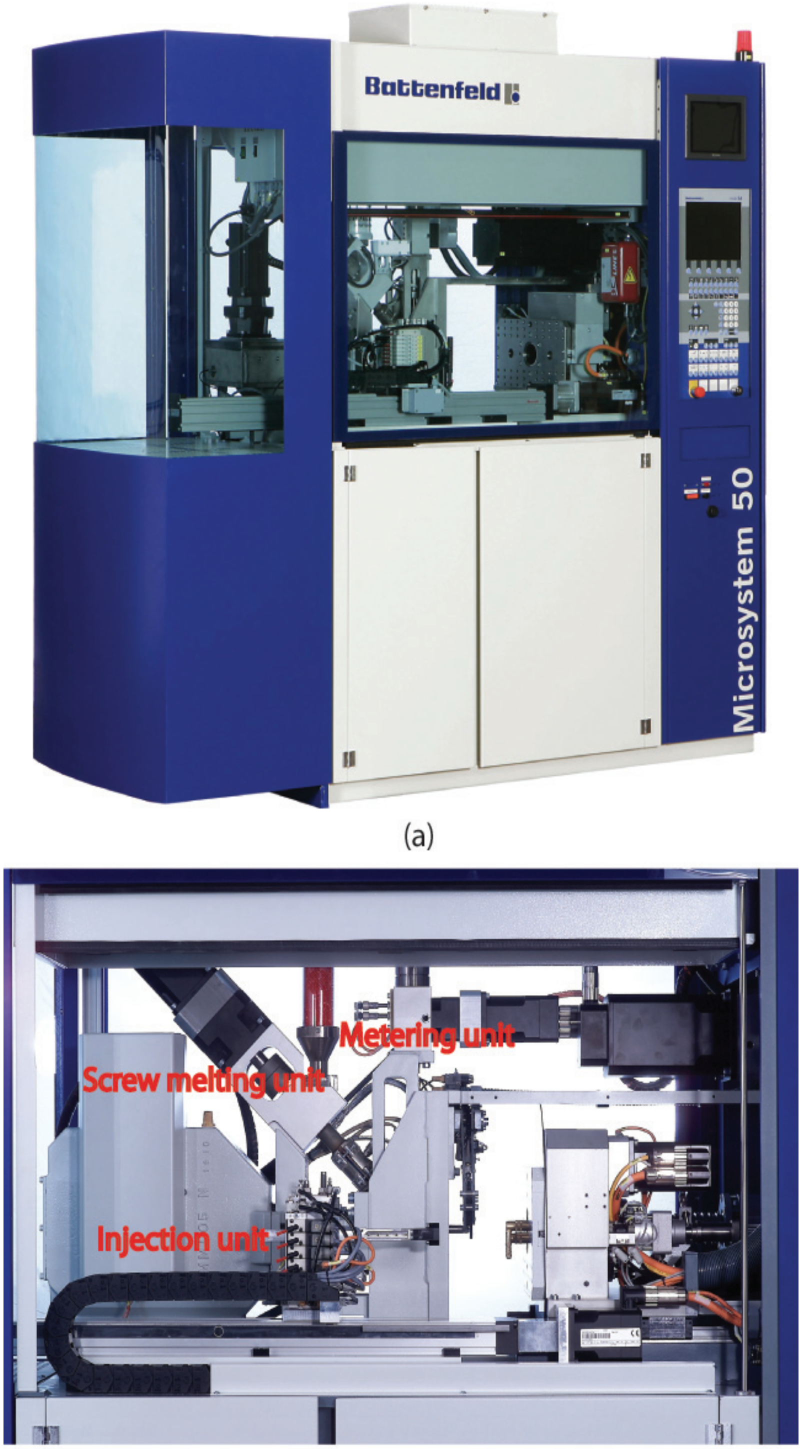

(a)

(b)

Figure 2-1 (a): Micro injection molding machine: Microsystem 50; (b): Plunger injection system (courtesy of Battenfeld Kunststoffmaschinen GmbH))

The main reasons for choosing this system configuration are to control metering accuracy and homogeneity of the very small quantities of melt in the micro injection molding process and to limit material degradation. The screw, typically 14 mm in diameter, to allow the use of regular polymer granules, provides heating based on both thermal and mechanical energy. It produces efficient and homogeneous plasticization. The melted material is then introduced into a 5 mm diameter metering barrel to a preset volume. The accuracy of this volume is critical for consistent processing, in view of both flow and heat transfer considerations. The metered melt is then delivered into the injection unit, where a 5 mm diameter plunger pushes the material into the cavity. The injection plunger, combined with the electrically-driven cam mechanism, provides high injection speed, high injection pressure, and low switch-over volume, which are necessary to avoid premature freezing and achieve accurate feature replication. However, it is difficult to study the different process variables, because of the very short filling time and the limited space available for installation of sensors. Also, the extra parameters associated with control of plunger movement and melt storage make the process setup and optimization more difficult, in comparison with the conventional injection molding (CIM) process [7, 13, 17].

Micro injection molded products include those made from both crystalline and amorphous materials. The products seen in the literature include micro-lenses, disposable needles, polymer micro-fluidic chips, biochip cartridges and analyzers and micro-gears. Some products have been developed and manufactured by micro injection molding successfully, for example, the polymer microfluidics chip (outer dimensions: 25x76x1.1mm) [18] and disposable needles [19]. However, some products are still under consideration or in the stage of prototype development. This includes micro-lenses [20, 21] and the disposable biochip cartridge [22]. Kristen Carlson and Matthew Chidley et al. [20] employed the injection-molded plastic miniature objective lens in the in vivo fiber-optic confocal reflectance microscope (FOCM). A schematic of FOCM is shown in Figure 2-2. The purpose of the research was to provide a fiber-optic confocal reflectance microscope with a cost-effective injection-molded plastic miniature objective lens for in vivo imaging of human tissue for detecting cancer in near real time. Annually, over 6 million people die from cancer and over 10 million new cancer cases are detected. The incidence and mortality of many cancers (e.g., cervical cancer) have been reduced through the use of screening programs to detect treatable precancerous lesions. However, many developing countries do not have adequate resources to implement currently available screening programs. This research has reduced the cost of miniature objective from $8000 to $350, and in a short term with a goal of $50 with reasonable production run estimate. This is not far from the goal of $10 disposable optical probes.

The micro gears as displayed in Figure 2-3 [2] is another micro injection molded sample used widely in the watch industry, in micro pumps, in micro motors, and in micro delivery systems. These plastic micro injection molded gears have been widely applied to replace those expensive micro-machined metal gears in drug delivery system, aerospace, automotive parts and many other micro electro-mechanical devices.

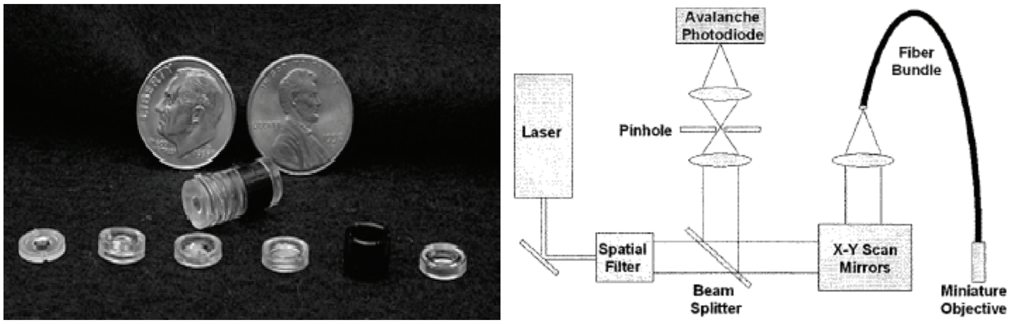

Fig. 3. Injection-molded plastic objective lens assembled and disassembled with U.S. coins.

Fig. 1. Schematic of fiber-optic confocal reflectance microscope (FOCM).

(a) (b)

Figure 2-2: (a): An assembled objective lens and a set of individual lenses; (b) The application of Micro-lenses in FOCM [20]

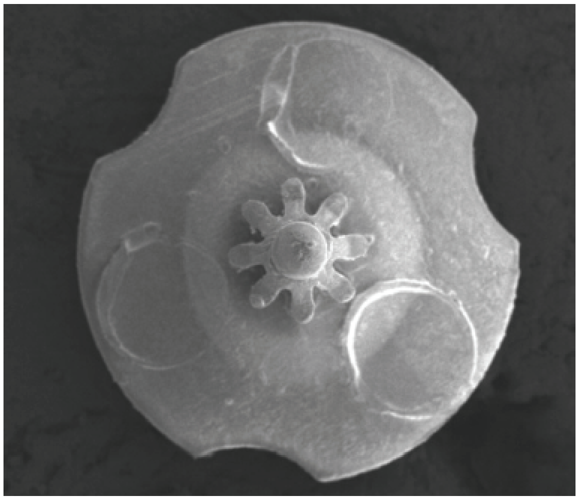

Figure 2-3: SEM image of a 0.008g microgear wheel [BIP Polyacetal copolymer]. The whole component and fine details such as the ejector pin markings can clearly be seen [2]

Due to the size restriction as defined above, the micro injection molding process is far from a scaling down of the conventional injection molding and poses new challenges in the following aspects in comparison to conventional injection molding [16, 23, 24]:

1. Design and fabrication of tool and mold insert;
2. Process monitoring and measurement for very short filling time;
3. Understanding of the material properties at extreme high shear rate and thermal gradient;
4. Characterization of structure and property of final products due to lack of handling facility and property inspection techniques;
5. Theoretical modeling and numerical simulation;
6. The possibility of raw material variation.

The micro injection molding process, based on the plunger injection system, has received considerable interest. However, most of reported research [3, 6, 25-27] has been devoted to empirical studies of the effects of machine variables on the quality of the molded product. Thus, conclusions made in these studies depend on the selected machine variables and the quality parameters of the different end products.

Zhao et al. [3] investigated the effects of machine variables on the micro molding process and part quality by molding a series of micro gears using the design of experiments (DOE) method. Battenfeld Microsystem 50 was used in the study and the micro parts studied were a series of micro gears as displayed in Figure 2-4. The polymer material used was a polyoxymethylene (POM), trade named Lupital F20-03. The plastics parts were well formed including the tooth structures that are in the dimensional ranges of a few tens of microns. Figure 2-4 (a) displays a spur gear of diameter 1 mm with 8 gear teeth and shaft structure and the 1 mm gear is shown Figure 2-4 (b) clearly. The molded 1 mm gear is displayed in Figure 2-4 (c). The following five factors were considered: mold temperature, melt temperature, injection speed, metering size, and hold pressure time. They found that holding pressure time and metering size and their interaction were the machine variables that had the most significant effects on part quality. However, the results do not provide insight into the flow and thermal behaviour of the melt during the process, because neither the holding pressure time nor the metering size could be related directly to variables in the governing equations. In addition, the metering size could be eliminated from the machine variables by setting it at an optimum level.

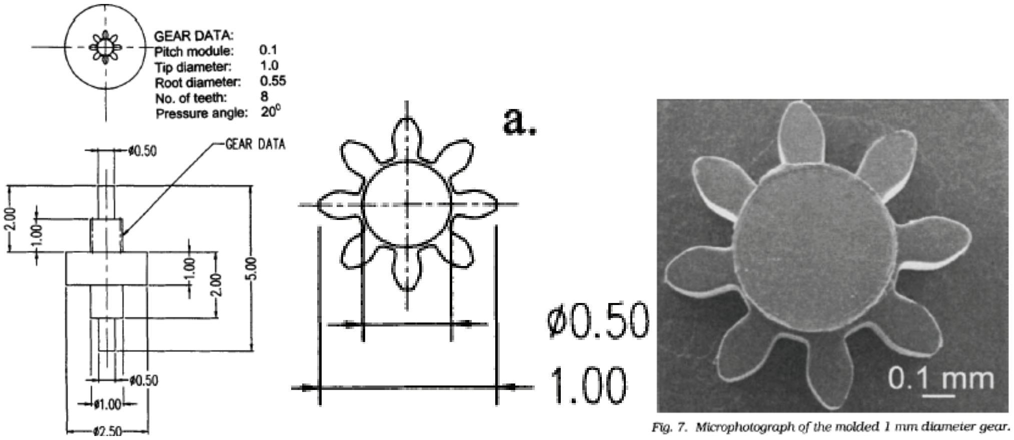

a b c

Figure 2-4: (a) Design of a 1mm gear with shaft; (b) Spur gear with 1mm tip diameter; (c) Microphotograph of the molded 1mm micro gear made with polyoxymethylene [3].

Pirskanen et al. [25] conducted a full factorial design for a specially designed mold insert. The design comprised 32 test runs and the five factors selected were: injection speed, metering size, vacuum, holding pressure and diameter of the plunger. The Battenfeld Microsystem 50 and the Battenfeld 'Master mold' with changeable inserts were used in the study. The commercial polycarbonate was selected for the study. The shapes of the test-pieces were a rectangular plate with 15 x 5 mm cross-section and 0.4 mm thickness and a round disc with 5 mm diameter and 0.4 mm thickness. The sub-micro features on the nickel insert were fabricated by lithography and was fixed on top of the core by welding. The best sub-micrometer features at the surface were obtained parallel to the melt flow direction. Figure 2-5 shows the difference in filling between the directions of flow and that of perpendicular to flow. The height of the feature in the direction perpendicular to the melt flow is 30% less than the height parallel to the melt flow. It was also found that the diameter of the plunger, shot size and injection speed had the greatest effects on replication of the sub-micrometer features. Yet, it is still difficult to understand the fundamental physics that contributed to these effects.

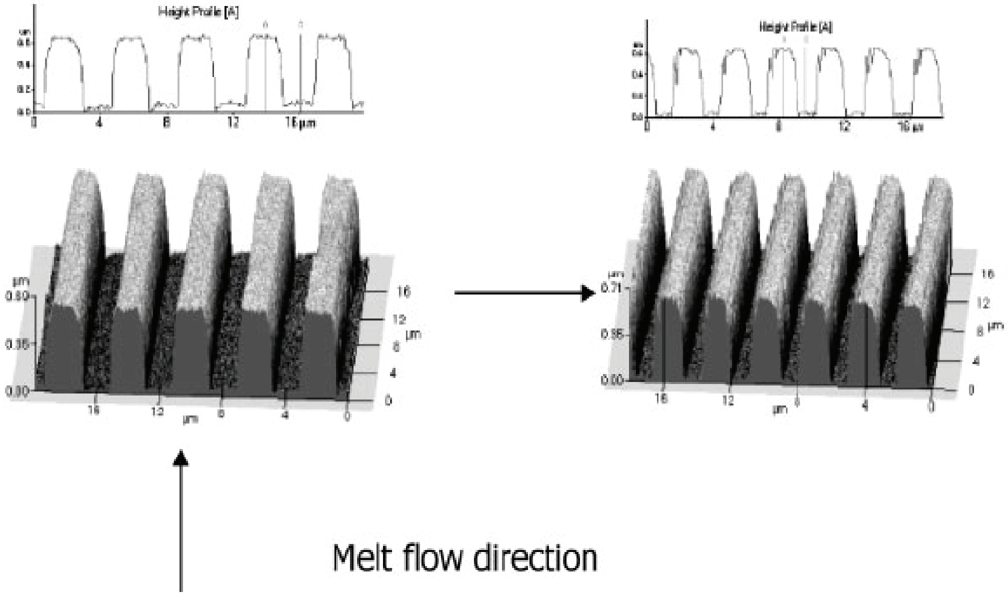

Figure 2-5: Shapes of feature affected by feature direction [25]

At a later time, Chu et al. [26] studied the microstructural characteristics of micro injection molded thermoplastics. A Battenfeld Microsystem 50 was used to obtain micro-moldings of high density polyethylene. The processing variables were estimated, based on experimental data and on simulation results. The morphology representing skin-core structure and flow pattern was evaluated with a polarized light microscope. The three-dimensional shrinkage distribution was measured with Nikon Measurescope and compared with simulation results. The local mechanical properties (modulus and hardness) were measured with a nanoindenter. The details regarding to experimental setup and experimental and modeling results are presented in later chapters.

Whiteside et al. [2, 28-34] have studied the micro injection molding process extensively for a variety of materials using different mold geometry on the Battenfeld Microsystem 50. The materials selected include BIP Polyacetal copolymer (grade POMC 109), a BP HDPE (grade Rigidex 5050) and an HDPE-based Hapex material. The Hapex is a biomedical bone analogue material consisting of sintered hydroxyapatite powder in a HDPE matrix. The mold inserts used in their studies include:

1. A stepped plaque cavity 7.4 x 3 mm containing steps of thickness 1, 0.5, and 0.25 mm, manufactured using a conventional EDM process followed by polish process; the photographs of short shots of the stepped plaque are displayed in Figure 2-6 [33].
2. Three rectangular plaque with geometries at 25 x 2·5 x 0·25 mm, 25x 2·5 x 0.5 mm, and 20 x 2·0 x 1·0 mm, manufactured using a Kern micromilling machine with cutter diameter 0.2mm rotating at 75, 000 rev min^{-1}; the photograph of short shots of the 1.0 mm plaque is displayed in Figure 2-7 [33].
3. A top hat shaped cavity containing sections of diameter 1.0 and 0.5 mm, 1.0 mm high, formed using a micro EDM technique; the geometry and dimension of the 'top hat' component are displayed in Figure 2-8 [34].

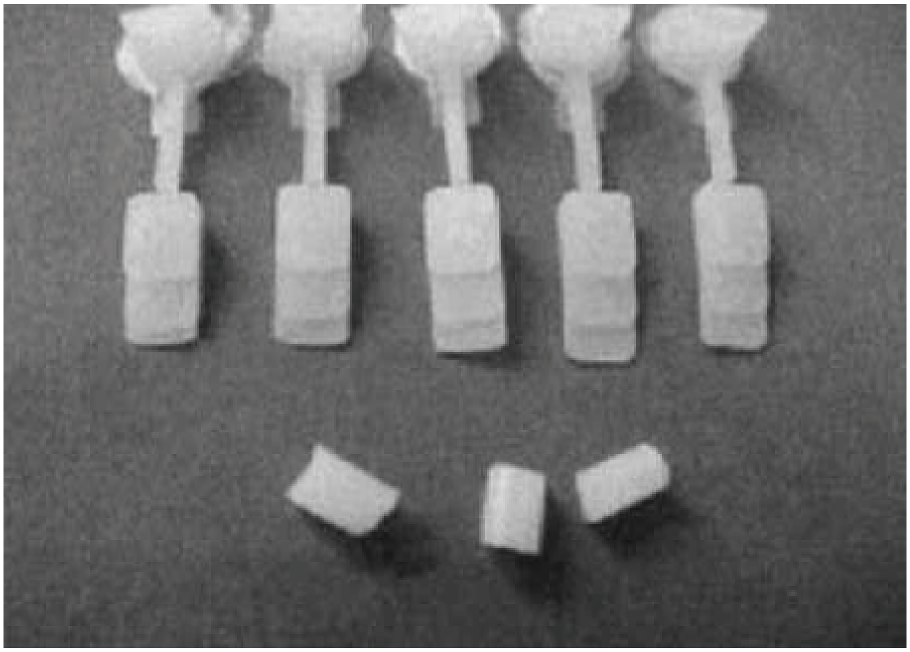

Figure 2-6: Photographs of short shots of stepped plaques moldings [33].

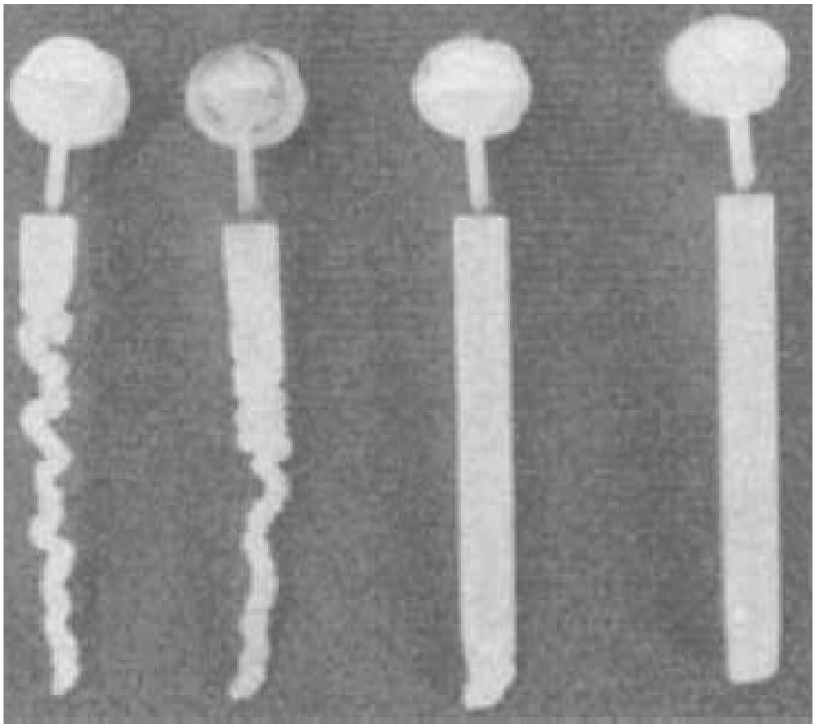

Figure 2-7: Photographs of short shots of the 1.0 mm plaque molding [33].

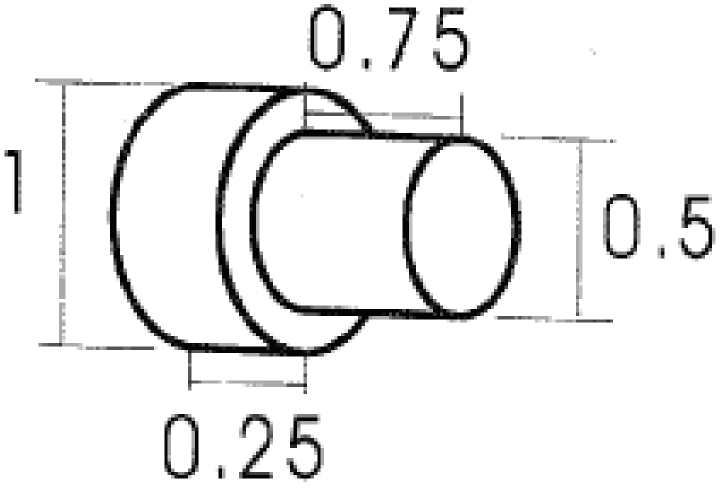

Figure 2-8: Schematic of 'top hat' component (dimension in mm) [34].

At early stage of their research [2, 28, 32-34], the efforts made by the authors has covered a wide range of related areas attempting to study the impact of a range of process variables upon the dimensional, morphological, and mechanical properties of the final product.

The apparent shear and extensional viscosity behaviours of a polyacetal at high wall shear rates were measured using inline capillary rheometer on the Battenfeld Microsystem 50 micromolding machine and a larger servo-electric injection molding machine [33]. It was found that the polymer behaved predictably at shear rates in excess of 10^6 s^{-1}, as shown in Figure 2-9. An atomic force microscope was applied for measuring the surface finishes of the moldings for both geometry 1 and geometry 2, as shown in Figure 2-6 and Figure 2-7. It was found that the surface features with length scales of order of a few micrometers were well replicated on the molded product and the quality of the surface finish is dependent on the melt pressure during molding [33].

The nanoindenting technology was used for measuring the material modulus [2]. Figure 2-10 displays the local moduli through the thickness of the stepped plaque HDPE molding, which indicated the presence of a skin-shell-core structure within the product as shown in Figure 2-11.

The micromolding process for the part with geometry of a top hat, as shown in Figure 2-8, was monitored with a specifically designed data acquisition system. A typical production cycle is presented in Figure 2-12 [28]. It was reported that the cavity pressure measurements offer the most sensitive indicators of process variation and the process repeatability decreased with decreasing cavity size [28].

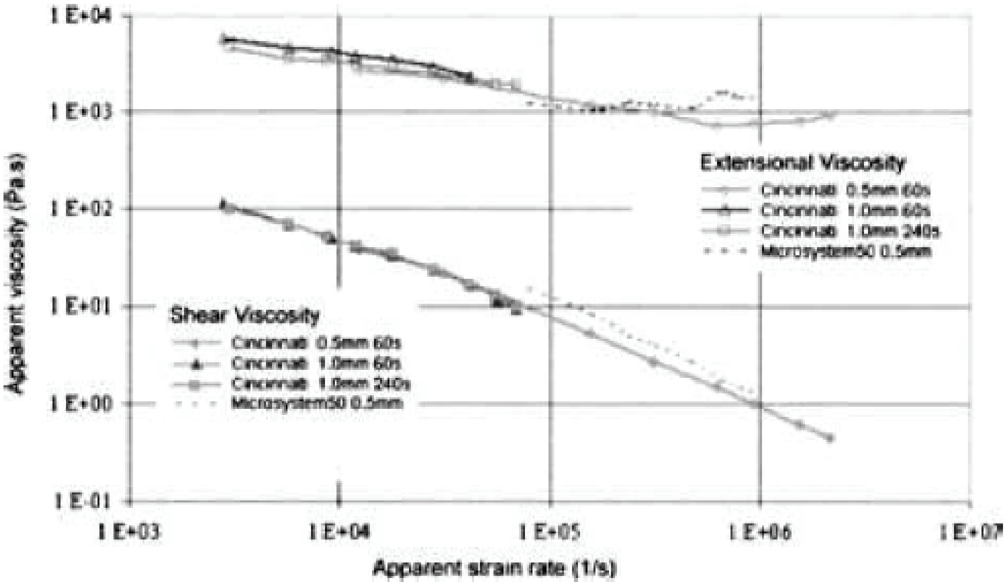

Figure 2-9: High shear viscosity data produced from high shear rheometry tests performed on Microsystem 50 and Cincinnati-Milacron 25 t IM machine [33].

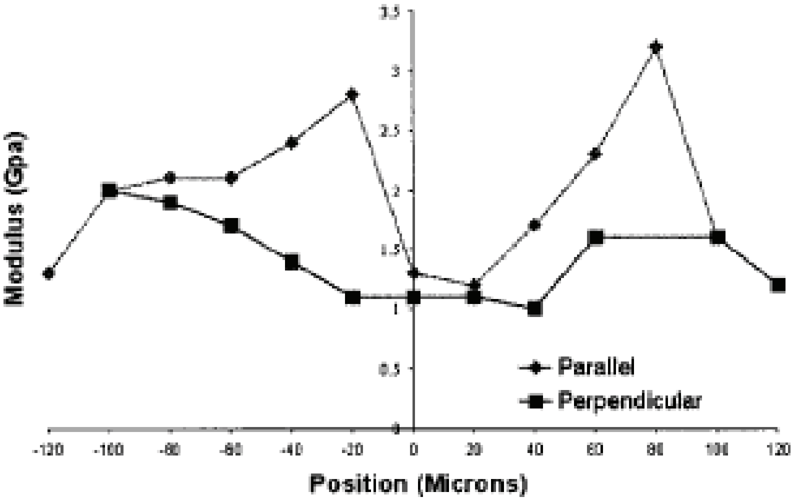

Figure 2-10: Nano-indenter moduli values through thickness of stepped plague HDPE moldings [2].

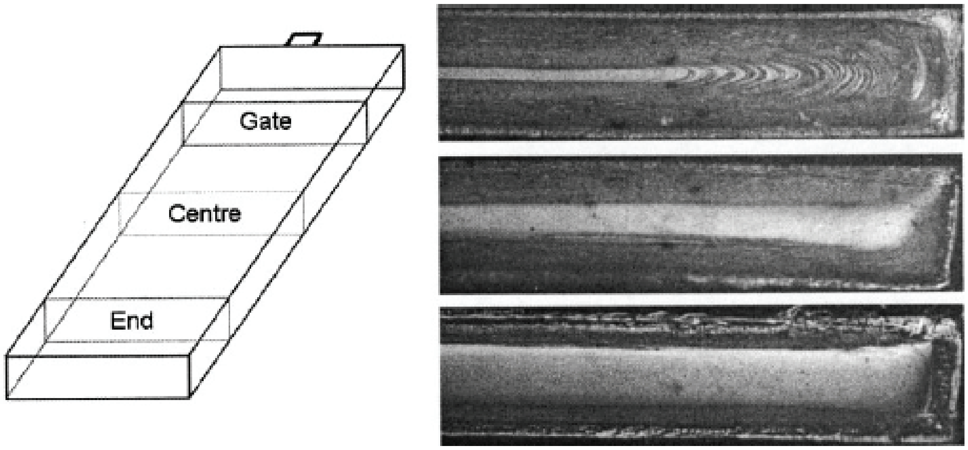

Figure 2-11: Etched sections of 0.25 mm HDPE plaque [2].

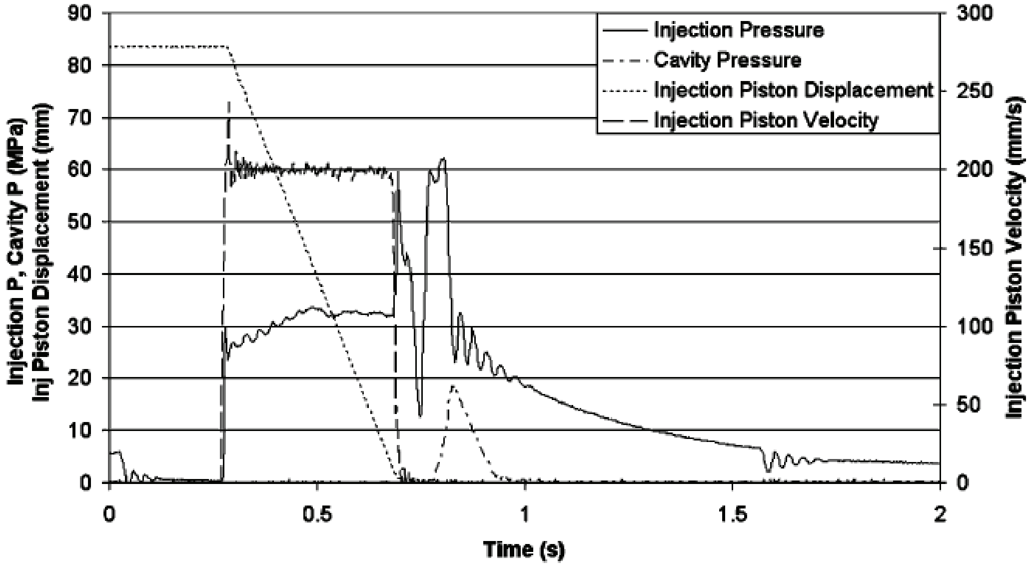

Figure 2-12: process data measured from single cycle of Battenfeld Microsystem 50 [28].

In a recent work presented by Whiteside et al., the flow behaviour was studied by both visualizing the polymer flow through a transparent cavity and employing the sol-gel film ultrasonic sensors for further understanding of the micromolding process [29]. Both flow visualization and ultrasonic measurements were useful in detecting the flow front position and could potentially measure shrinkage development. The flow visualization also showed its capability to observe the stress induced birefringence as shown in Figure 2-13. However, the cavity filling and packing stages were not described clearly and quantitatively. Thus, the relationship between process conditions and polymer melt behaviour during the micromolding process remains unexplored.

In the studies of the polymer degradation [31, 35], the piezoelectric film ultrasonic transducers were integrated onto the extrusion barrel and mold insert in order to measure the ultrasonic velocities in the polymer at the mold insert. It was reported that an apparent velocity increase (9.5%) was observed for the degraded parts at the mold insert [31].

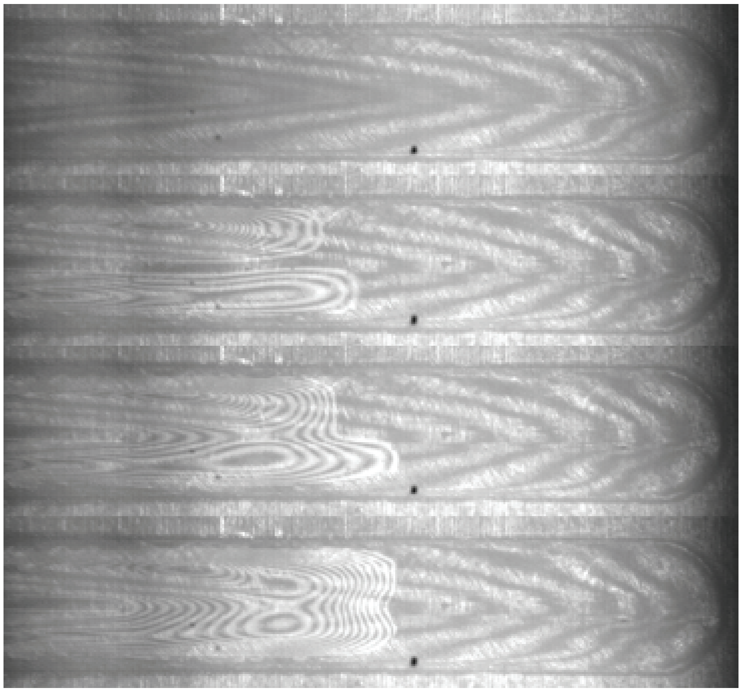

Figure 2-13: Birefringence observation by flow visualization [29].

Griffiths et al. [27] investigated the effects of tool surface quality in micro injection molding. In this research, the factors affecting the flow behaviour, including melt temperature, mold temperature, injection speed, are discussed. Three polymer materials, PP, ABS, and PC, were selected to perform molding tests using cavities with the same geometry but different surface finish. The design of the part is basically a series of runner sections through to a rectangular cavity as shown in Figure 2-14. The cavity is located at the end of runner system, with dimension of 10 mm x 2.5 mm x 0.5 mm. The surface roughness of the produced tools was Ra 0.07, 0.8 and 1.5 µm, respectively. The flow length results obtained from all 27 trials are presented in Table 2-2. The experiments showed that the flow length of PP was less susceptible to variations of process conditions. In the case of PC and ABS, the flow length was much more sensitive to changes of the process parameters and tool surface quality. However, any explicit relationship between the flow length and tool surface roughness was not observed.

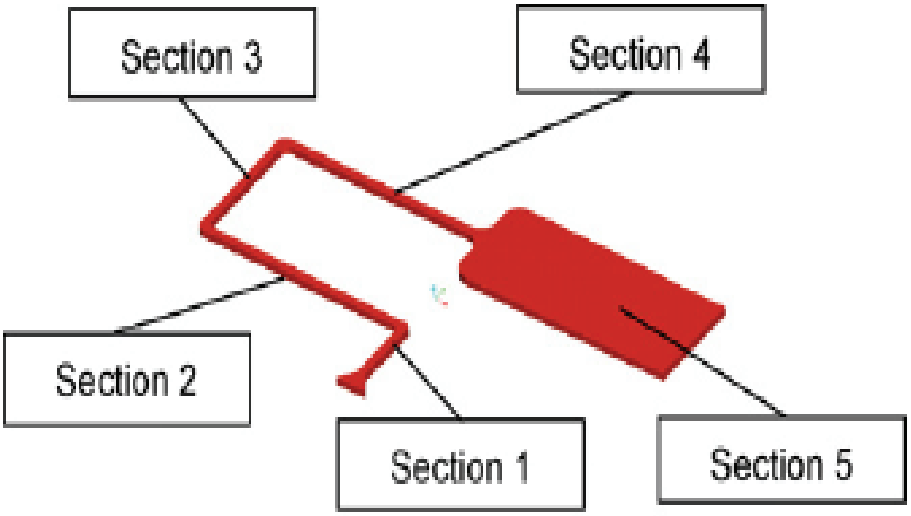

Figure 2-14: Design of test part and runner system [27].

Table 2-2: Flow length results [27]

Trials	Levels				Mean value of the flow length		
	R_a	T_b	T_m	V_i	PP	ABS	PC
1	1	1	1	1	47.2	42.6	22.8
2	1	1	1	1	52.0	42.4	39.0
3	1	1	1	1	54.7	45.0	39.3
4	2	2	2	2	48.9	39.8	17.2
5	2	2	2	2	52.8	32.5	22.3
6	2	2	2	2	54.6	29.3	26.2
7	3	3	3	3	49.7	32.8	21.7
8	3	3	3	3	52.7	36.4	25.6
9	3	3	3	3	54.1	33.1	22.7

2.2 Modeling and Simulation of the Micro-injection Molding Process

To avoid the risks of costly re-engineering and to decrease development time, the manufacturing steps including filling stage, packing stage, and cooling stage, and the properties of micro injection molded products, such as shrinkage, have been simulated using both commercial software developed for conventional injection molding [3, 14, 36-42] and in-house software [43, 44], with some consideration for micromolding process characteristics.

In Su's research [14], C-MOLD simulation software, which employs numerical solvers based on a hybrid finite element/finite difference method to solve the pressure, velocity and temperature fields of the Generalized Hele-Shaw (GHS) model, which was proposed by Hieber and Shen [45]. The assumptions of the GHS model are

1. The thickness of the cavity is much smaller than the other dimensions.
2. The velocity component in thickness direction is neglected, and pressure is also a function of x and y only.

3. The flow regions are considered to be fully developed Hele-Shaw flows, in which inertia and gravitational forces are much smaller than viscous forces and then are neglected.
4. The flow kinematics is shear-dominated and the shear viscosity depends on both temperature and shear rate.

The GHS model cannot predict the exact flow field near the advancing flow front or at the edges of the mold, because of its approximations. It was reported that the mold temperature is the key factor that decisively determines the quality of injection molded microstructures.

Kemmann and Weber [42] proposed that use of visco-elastic constitutive equations and incorporation of surface tension effects were required to adequately model the micro molding process in a three-dimensional simulation package.

Shen [36, 37] realized that the Hele-Shaw model neglects the inertia and the gap-wise velocity component for polymer melt flow in thin cavities. So the three-dimensional flow regions, i.e. flow around corners, or thickness-change regions, or the fountain flow effect at melt fronts cannot be represented in the Hele-Shaw model. Only a 3D numerical simulation can simulate the real situation. The Navier-Stokes momentum equation is expressed in Equation 2-1 as following:

$$\rho\left(\frac{\partial u}{\partial t}+u\frac{\partial u}{\partial x}+v\frac{\partial u}{\partial y}+w\frac{\partial u}{\partial z}\right)=-\frac{\partial p}{\partial x}+\eta\left(\frac{\partial^2 u}{\partial x^2}+\frac{\partial^2 u}{\partial y^2}+\frac{\partial^2 u}{\partial z^2}\right)+\rho g_x$$

$$\rho\left(\frac{\partial v}{\partial t}+u\frac{\partial v}{\partial x}+v\frac{\partial v}{\partial y}+w\frac{\partial v}{\partial z}\right)=-\frac{\partial p}{\partial y}+\eta\left(\frac{\partial^2 v}{\partial x^2}+\frac{\partial^2 v}{\partial y^2}+\frac{\partial^2 v}{\partial z^2}\right)+\rho g_y$$

$$\rho\left(\frac{\partial w}{\partial t}+u\frac{\partial w}{\partial x}+v\frac{\partial w}{\partial y}+w\frac{\partial w}{\partial z}\right)=-\frac{\partial p}{\partial z}+\eta\left(\frac{\partial^2 w}{\partial x^2}+\frac{\partial^2 w}{\partial y^2}+\frac{\partial^2 w}{\partial z^2}\right)+\rho g_z$$

Equation 2-1

It was reported that the mold temperature of micro injection molding process should be higher than the glass transition temperature of plastic material in order to fill the micro cavity. Otherwise, a short shot is obtained according to the micro injection molding simulation.

Validation of flow simulation for micro-molded parts was carried out using Moldflow MPI by Mehta [38]. The .igs files were converted to 3D surface and 3D meshes, for the part alone and for the part with its runners. The former had triangular elements, whereas the latter had tetrahedral elements. These models were used for three filling analyses: Hele-Shaw, Stokes, and Navier-Stokes. The Hele-Shaw analysis assumed planar flow and normal conductive cooling of the polymer melt, while the latter two allowed for three-dimensional flow and heat transfer. Viscous force was dominant with the Stokes equation, but inertial effects were added for the Navier-Stokes analyses. It has been reported that three-dimensional simulations produced fill patterns that were comparable with short shots from molding trials. The fill pattern was also significantly affected by the meshing of the models in the gate region and selection of the material. Similar results were also reported by Ilinca et al. [44].

Yao [43] indicated that, for extremely small dimensions of micro-parts, existing simulation packages are no longer sufficient to describe all the effects in micro-molding. He evaluated the consequences of micro-scale phenomena, particularly size-dependent viscosity, wall slip and surface tension, on the filling process of polymeric materials into micro channels. The standard injection molding simulation scheme of two and a half dimensions was modified to include the above-mentioned microscale effects. The Hele-Shaw model was used with micro-viscosity to account for the influence of intermolecular forces. The micro scale viscosity was modeled using the theory of Eringen and Okada [43]:

$$\eta(\gamma, T, p) = \phi(z)\eta_b(\gamma, T, p) = \left(1 + \xi \frac{g^2}{z^2}\right)\eta_b(\gamma, T, p)$$

Equation 2-2

Where η_b is macroscopic viscosity, ξ is a non-dimensional constant, g is the gyration radius of fluid molecules, and z is an external characteristic length.

The modified power-law slip model by Rosenbaum and Hatzikiriakos [46] was used in Yao's simulation study:

$$u_s = \frac{a}{1 + (\sigma_c / \sigma_w)^k} \sigma_w^i$$

Equation 2-3

where u_s is slip velocity, σ_w is wall shear stress, σ_c is the critical wall stress for slip, *i* is a power-law index, and *a* is a scalar coefficient. Because of the factor $1/\left[1 + (\sigma_c / \sigma_w)^k\right]$ with large power k, the slip velocity decreases sharply to be close to zero for stresses less than σ_c, and becomes about equal to one for shear stresses slightly greater than σ_c. It was also reported by the authors [43] that the wall slip has to take place in order to release the vast increase of the wall shear stress, when filling micro-to-submicro channels. The predicted pressure increase in filling micro-to-submicro channels was 20-30% higher than for standard filling. The calculations also showed that surface tension effect is not insignificant in micro molding.

None of the above investigations have showed significant agreement between simulation results and experimental process data, despite the progress made in understanding the flow and thermal behaviour of polymeric materials in the micro injection molding process.

2.3 Crystallization and Microstructure Development

The crystallization process that occurs during solidification produces a semi-crystalline product, with crystallinity, morphology, and crystalline structure that have profound influences on product properties. Crystallization kinetics and the morphology of the semi-crystalline product are strongly influenced by the cooling and deformation rates, system pressure and the presence of nucleating agents. This is especially important in the case of micro injection molding, which involves high injection pressure and high deformation rates and thermal gradients. Microstructure characterization has been a valuable tool for understanding the thermo-mechanical history experienced by the material and estimating the final properties, in the case of conventional injection molding [10, 11, 47-55]. Some microstructural studies reported for conventional injection molding will be reviewed in this section, since few reports are available with respect to microstructure development in micro injection molding.

2.3.1 Quiescent Crystallization

Most of the main features associated with crystallization of polymers from quiescent solutions and melts are well understood, and the resulting morphologies are well documented. Extensive literature reviews are available concerning the subject [56-60].

2.3.1.1 Crystal Structure

Keller [61] and Fischer [62] independently found that single polymer crystals could be formed from dilute solutions and that linear macromolecules crystallize into the form of thin platelets whose large upper and lower surfaces consist of an array of molecular folds. These folds are commonly referred to as “chain-folded crystals” or “chain-folded lamellae”. The latter term is usually reserved for folded structures in polymers crystallized from the melt. Figure 2-15 [60] shows schematically the general molecular structure and the hierarchical arrangement of polyethylene, a typical semi-crystalline material. The spherulitic structure, which is the largest domain with a specific order and has a characteristic size of 50 to 500 µm, is much larger than the wavelength of visible light, making semi-crystalline materials translucent and non-transparent.

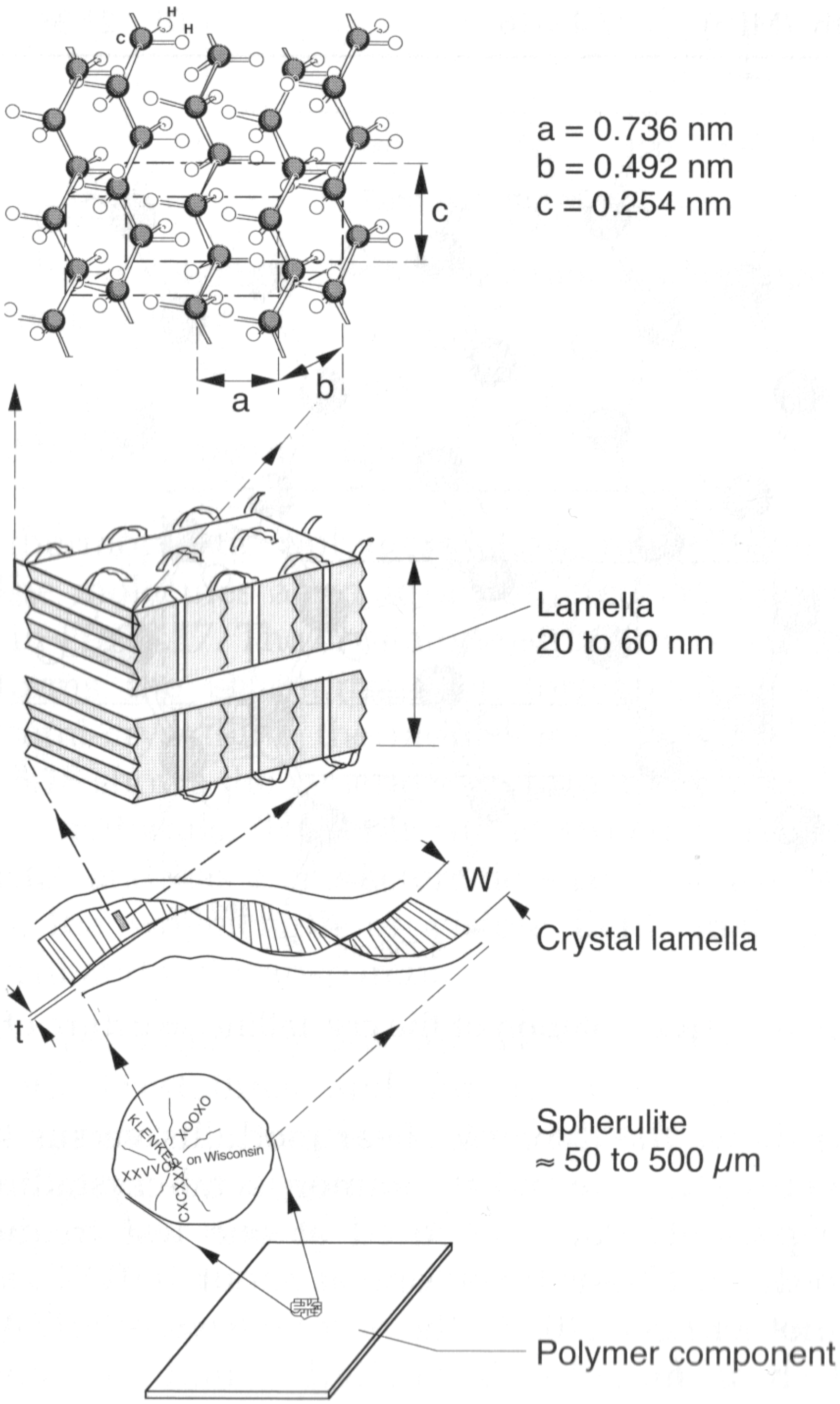

Figure 2-15: Schematic representation of the general molecular structure and arrangement of polyethylene [60].

The spherulite is composed of stacks of ribbon-like crystals, which are very long in comparison to their thickness. The chains are oriented approximately parallel to the thin dimension of the ribbon. The thickness of the crystal ribbon is of the order 100 Å. The inter-ribbon region is non-crystalline and may be composed of tie chains, dangling chain ends, totally unincorporated chains, and loose loops.

At the top of the schematic is the crystal structure of polyethylene, where the individual atoms form a true three-dimensional periodic array - a true crystal structure. In the crystalline state, polymer chains are aligned parallel to each other. In general, bonding along the chain is covalent, while bonding perpendicular to the chain is of van der Walls or hydrogen-bonding type and is much weaker.

The crystallization of polymers from the melt is not fundamentally different from crystallization from solution. In both cases, the polymer molecules are driven to uncoil from high entropy configurations [57]. The main difference between melt crystallization and crystallization from dilute solution is that in the former, the polymer molecules are in more intimate contact with each other in the coiled state.

In summary, the state of aggregation of polymer chains after quiescent crystallization is a two-phase composite of anisotropic, axially twisted crystal ribbons, separated from each other by soft, isotropic regions. The crystals exhibit all orientations over the volume of the workpiece, but are locally highly oriented.

2.3.1.2 Crystallization Kinetics

It is well known that the formation of spherulites from the melt is governed by two separate mechanisms: nucleation and subsequent growth. These, however, can take place at the same time, further spherulites being nucleated whilst the original ones are growing, so the final size of spherulites formed depends on the relative rates of the two processes for the particular crystallization conditions existing at the time [63].

The Avrami equation has been used successfully to describe the isothermal crystallization kinetics of polymers [64, 65]:

$$X(t) = 1 - \exp\left(-kt^{n}\right)$$

Equation 2-4

Where $X(t)$ is the relative crystallinity at time t with t=0 corresponding to the end of the induction period. The Avrami exponent, n, ranges from 1 to 4 and depends on the type of nucleation, growth geometry (rod, disk, sphere), and growth control mechanism. For example, the Avrami exponent for spherulitic growth from sporadic nuclei is around 4, disclike growth 3, and rodlike growth 2 [60]. If the growth is activated from instantaneous nuclei, the Avrami exponent is lowered by 1.0 for all cases. The crystallization rate, k, depends on the product of the rates of two processes: nucleation and crystal growth.

The crystallization temperature plays an important role in the crystallization rate [66]. Nucleation rates are high at low crystallization temperature, where chains are characterized by low energy levels. The greater the degree of supercooling in the melt, the smaller will be the critical nucleus size. Therefore, the nucleation rate increases rapidly with decreasing temperature below the melting temperature. At much larger degrees of supercooling, the nucleation rate decreases again owing to the increasing loss of mobility suffered by the polymer chains as the glass transition temperature is approached. On the other hand, high crystallization temperatures favour rapid crystal growth rates. Since the chains must be pulled in from the melt to the crystallizing surface, high temperatures decrease melt viscosity, thus increasing chain mobility and the rate of crystal growth. The crystallization rate becomes nucleation controlled at high temperatures and growth controlled at low temperatures.

The induction time t_i, denoting the time period at which the spherulitic nuclei appear in the polarizing microscope field of view, is strongly temperature dependent

$$t_i \propto \Delta T^{-\varepsilon}$$

Equation 2-5

Where ΔT is the degree of supercooling and the values of the parameter ε range between 2.5 and 9.0.

On the lamellar scale, it has been reported that increasing the temperature in isothermal crystallization increases the lamellar thickness, and the perfection of the crystals in the ribbon lamellae will increase as well [66].

Pressure is also a variable that affects all aspects of the crystallization process and the properties of the resulting structures. As an illustration of the pressure effect on the Avrami parameters, Hatakeyama et al. [67] reported that the Avrami exponent *n* decreases with a large increase of pressure. Generally, this observation is explained in terms of the pressure dependence of melting point, which can be described by the Clausius-Clapeyron equation as following:

$$(T_m)_P = (T_m)_{P_{atm}} \exp\left[\frac{(\hat{V}_a - \hat{V}_c)(P-1)}{\Delta H_f}\right]$$

Equation 2-6

Where $\hat{V}_a$ and $\hat{V}_c$ are the amorphous and crystalline specific volumes, P is the hydrostatic pressure, and ΔH_f is the atmospheric heat of fusion of the polymer. The equation tells us that there is an appreciable melting point elevation with pressure. It means that a pressurized melt at a given crystallization temperature is under a higher degree of supercooling. On the lamellar scale, lamellar thickening and even complete extended chain crystallization has been reported [68].

Matsuoka and Maxwell studied the effects of pressure during processing and observed large compressibility at higher pressure, as displayed in Figure 2-16 [69]. This result is due to the phenomenon of pressure induced crystallization, which is a consequence of the melting point elevation. This result was also correlated with the pressure-temperature history of a polymer melt in an injection mold cavity. Initially the material in the cavity is hot and at a high pressure, but as the "skin" cools and the mold gate freezes or the valve is closed, the hydrostatic pressure in the core decreases. The polymer melt would move toward the origin in a nonisothermal fashion, as shown in Figure 2-16. The part surface is cooled first, with pressure induced crystallization occurring simultaneously with the effects of conductive cooling. A spectrum of structures and morphologies would be obtained. Near the surface, structures with a high T_m and lamellar thickening are obtained due to high pressure induced crystallization, whereas near the center, structures are developed at almost atmospheric pressure.

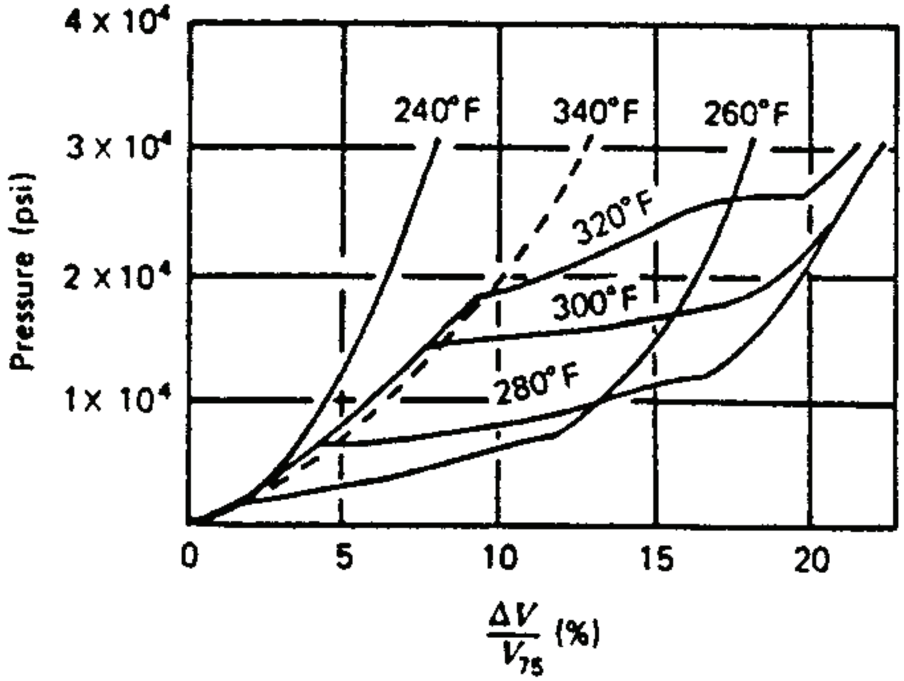

Figure 2-16: Bulk compressibility of HDPE at various pressures showing the phenomenon of pressure induced crystallization [69].

For nonisothermal quiescent crystallization, the differential form of the Nakamura model [70, 71] is commonly used:

$$\frac{D\theta}{Dt} = nK(T)(1-\theta)[-\ln(1-\theta)]^{\frac{n-1}{n}}$$

Equation 2-7

Where θ is the relative degree of crystallization, K is the rate constant, n is the Avrami index, T is temperature, t is time, and (*D/Dt)* is the material derivative.

2.3.2 Flow Induced Crystallization

2.3.2.1 Crystal Structure

Stress-induced crystallization yields the “shish-kebab” structure proposed by Pennings and Keil [72] for polyethylene crystallized from stirred solutions. When crystallization takes place under conditions of flow, a row nucleated or ‘shish kebab’ structure, which is different from the simple folded lamella, can be formed. Figure 2-17 [72] displays a schematic of a shish kebab structure formed by stirring dilute solutions of polymers during crystallization, where the shish is the elongated crystals in the row structure and the kebabs are the overgrown epitaxial plates. These structures can be termed flow induced single crystal morphologies [73].

Typically, the melt [74] or solution [72] is subjected to a highly elongational flow field at a temperature close to the melting or dissolution temperature. A non-spherulitic, crystalline microstructure forms from elongated crystals aligned in the flow direction and contains partially extended chains. At high flow rates, these micro-fibres, some 20 nm across, dominate the structure. At lower flow rates, the backbones are overgrown by folded chain platelets. This epitaxial growth on the surface of the extended chain produces folded chain lamella oriented perpendicular to the strain or flow direction [75]. The spatial density of the fibrillar threads increases with the degree of deformation, as depicted in Figure 2-18 [76]. Figure 2-18 (a) depicts the situation for a modest applied strain: sparsely arrayed fibrils with overgrowths long enough to exhibit significant twisting. Figure 2-18 (b) depicts the situation for a higher applied strain: the fibrillar array is denser, and the overgrowths twist very little before impingement.

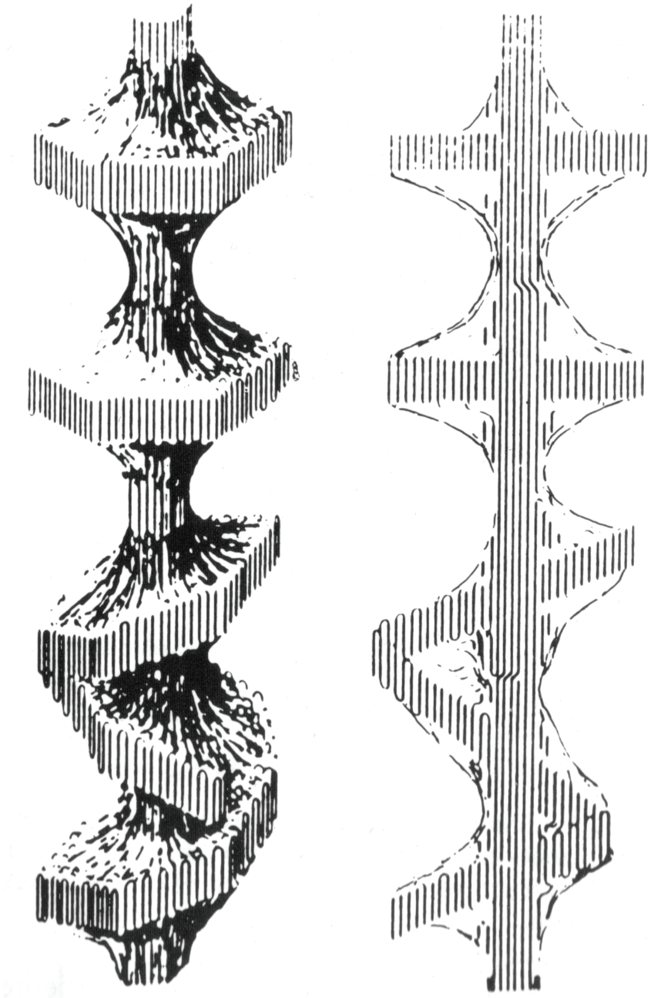

Figure 2-17: Schematic of shish kebab structure [72].

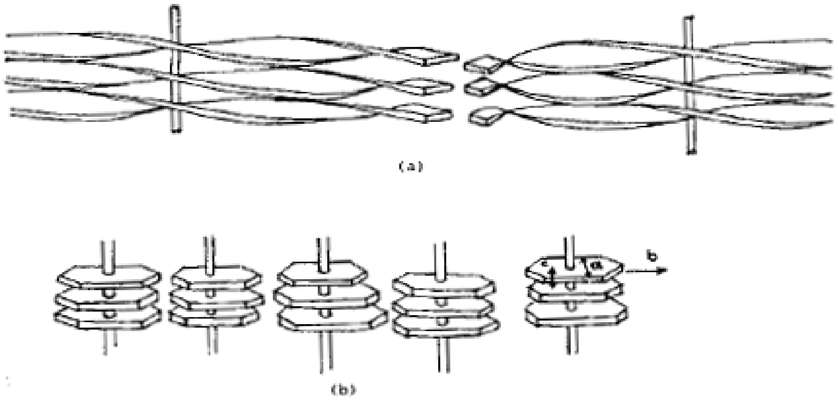

Figure 2-18: Model of the fibril-and-overgrowth crystallization of polymer under strain: (a) Under a modest applied strain; (b) under higher applied strain [76].

2.3.2.2 Flow Pattern and Orientation Development

In order to understand the micro-scale flow behaviour of polymer melts, it is necessary to review the studies on flow behaviour of conventional injection molding, which is relatively well established.

Flow visualization studies were reported for both experimental mold filling and for the results of mathematical simulation of the process [77-84]. The filling of an end-gated rectangular mold at moderate flow rates, whose width is much greater than its thickness, exhibits an orderly forward flow, as shown in Figure 2-19 [73]. During the early stages of filling, the flow is radial and the melt front circular, where a biaxial orientation would be expected [73, 81]. As the melt front advances away from the gate, the velocity component V_x should be much greater than V_z, because along the center line, only V_x should be observed. The front shape is either flat for isothermal filling or curved for filling into cold molds [79].

The detailed velocity and temperature profiles throughout the mold flow region, including the position and shape of the advancing front, can be better illustrated with mold filling simulation. The three regions indicated in Figure 2-19 (b) [73] will be discussed, based on the results of computer simulation by various workers.

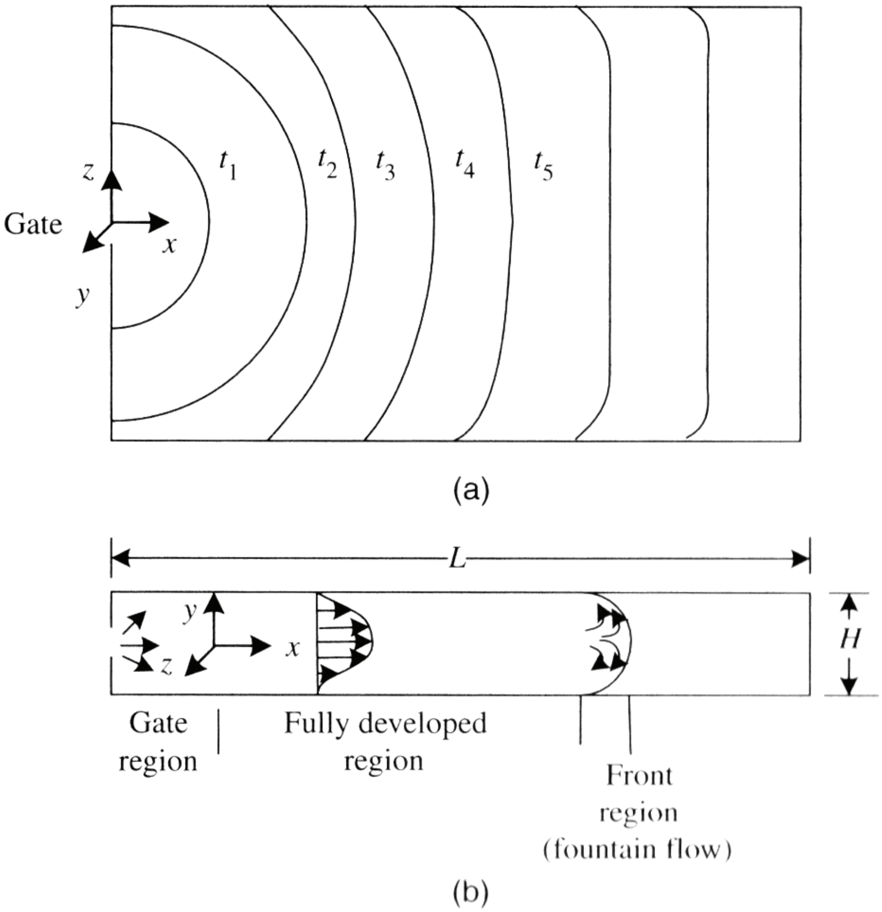

(a)

(b)

Figure 2-19: Schematic representation of the flow pattern a) Width direction flow fronts at various times. b) Velocity profiles in transverse direction in the gate region, in the fully developed region, and schematic representation of the fountain effect in the front region [73].

The fully developed region

The fully developed region features laminar shear flow. Most of the melt exhibits an almost fully developed flow in a narrow-gap configuration between cold walls during the filling process. This almost one-dimensional flow determines filling time, part core orientation, and the occurrence of short shots.

Wu et al. [85] simulated the filling of a center gated disk, where a frozen surface layer (frozen ‘skin’) can be formed during the filling process, which forces the fluid to flow through a channel of reduced cross section as shown in Figure 2-20 [73, 85]. The shape of the frozen skin profile has a characteristic maximum. Near the entrance, the skin is kept to a minimum due to the fresh hot melt, and near the front, the melt near the walls is still hot because it originates from the center region. The thickness of the frozen skin will decrease with increasing pressure, melt and mold temperature, and mold thickness [85]. The shape of the frozen skin creates both an axial stretching flow (extensional flow) and a z-component velocity [86].

The simulation results also indicate the importance of the ratio of the rate of heat generated by viscous dissipation to that lost by heat transfer to the cold walls. Isothermal flow could be assumed to estimate the filling time, when the ratio is close to unity. The flow front is found to advance at an ever decreasing rate, while the filling pressure builds up at an ever-increasing rate if the front is to advance at a constant filling rate.

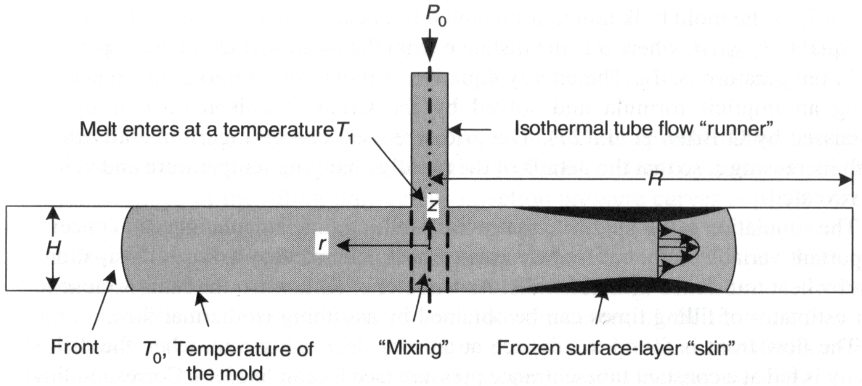

Figure 2-20: Cross-sectional view of a center-fed, disk-shaped mold cavity. Indicated schematically are the frozen-skin layers that can form during filling, as well as the "nipple "-shaped velocity profile [73, 85].

The Front Region

The advancing flow front features fountain flow, by which the fluid elements decelerate as they approach the slower moving front and spill over outwards toward the mold walls. The fountain flow effect is caused by the no-slip condition on the mold walls, which forces material from the center of the part to flow outward to the mold surfaces, as shown in Figure 2-19 [73, 87]. The fountain flow region extends approximately one gap length upstream. Fluid elements behind this region will be unaffected by fountain flow and move parallel to the centerline.

Tadmor [88] analyzed the front region in an attempt to model the experimentally observed molecular orientation distribution in the molded articles. He proposed that both the orientation in the close neighbourhood of the wall and the transverse orientation originate from the fountain flow in the advancing front region, whereas the source of the orientation in much of the bulk of the material results by-and-large from the shear flow upstream from the front. This is illustrated with velocity field in the advancing front region, using a coordinate system moving at the average velocity as shown in Figure 2-21 [89]. The molecular orientation is induced by the deformation of the polymer melt during processing. The flexible molecular chains are stretched. However, they cannot relax fast enough before the part cools and solidifies, because of the chain entanglements. At lower processing temperatures, this phenomenon is multiplied, leading to even a higher degree of molecular orientation.

The flow pattern in the central portion of the advancing front between two parallel plates is schematically shown in Figure 2-22 [90] for isothermal flow. Two symmetrically located fluid elements decelerate in the direction of flow and accelerate in the perpendicular direction, thus being stretched in the direction perpendicular to flow, moving toward the walls. After the fluid element has completed half a turn, it will be mainly affected by shear flow and pulled forward again since the fluid front has moved forward. Eventually, the fluid elements will be deformed into in a “V-shape” and deposited against the mold wall, as demonstrated in both experimental and simulation work [80, 89-91]. In summary, the evolution of fluid element shapes behind an advancing flow front is the result of integration of the fountain flow and the subsequent shear flow. Fluid elements near the centerline reach the flow front and finally the walls, getting distorted and stretched along the way. The movement of the outer layer is eventually stopped as it cools and solidifies.

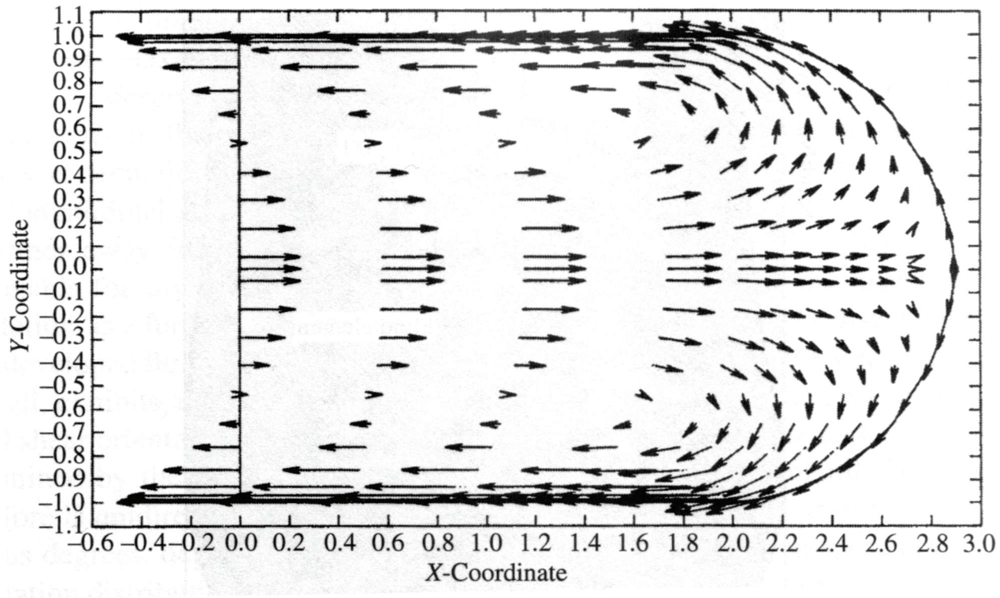

Figure 2-21: Numerical simulation of the velocity field behind an advancing liquid front, moving at constant speed inside a 2D channel [90].

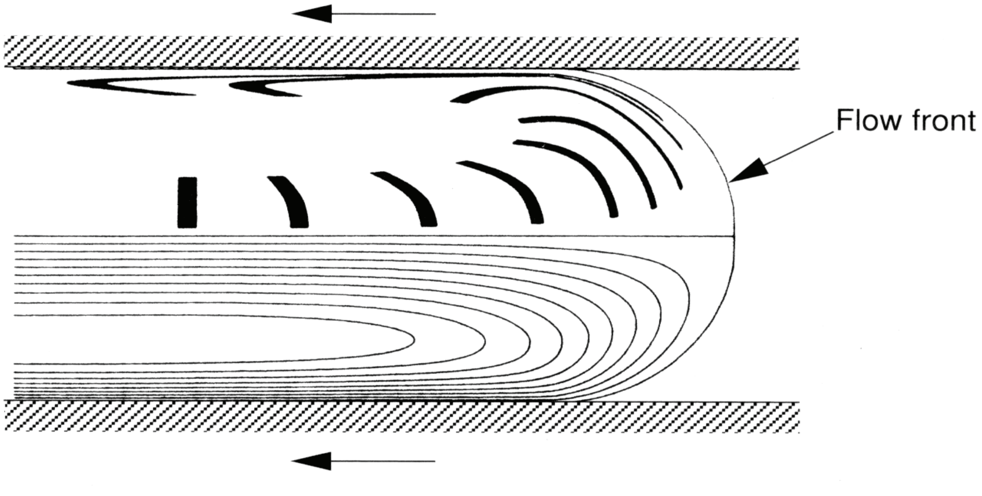

Figure 2-22: Deformation history of a fluid element and streamlines for frame of reference that moves with the flow front [90].

As a result of fountain flow, an oriented polymer layer originating from the central core of the advancing front experiences elongation before being deposited on the cold wall of the mold, where it solidifies upon contact with the cold wall, and retains its elongational orientation. Molecular relaxation occurs further away from the surface into the skin layer, reducing this orientation. The final orientation distribution in the skin layer will depend on the cooling rate and the spectrum of the relaxation times. The fountain flow mechanism suggests that in narrow-gap flow, skin-layer orientation is unidirectional in the direction of the advancing front.

Further away from the surface, the fully developed shear flow behind the front is responsible for any molecular orientation that may be present in the final product. Shear orientation, is a function of shear rate, which varies over the gap. The initial shear orientation relaxes to various degrees, depending on the cooling rate and the relaxation spectrum. Thus, the overall orientation distribution can be approximated by superimposing the elongational and shear orientations.

In addition to the flow induced orientation as discussed above, the thermally induced orientation refers to the orientation caused by cooling of the molded part after the completion of the filling process. So, the final anisotropy of the molded part is a composite effect, due to both flow and thermally induced orientation. However, the flow induced orientation is an order of magnitude higher than thermally induced orientation from the experimental investigations with birefringence measurements on molded and quenched strips [92].

Gate region

Biaxial orientation would be expected in this region, which is the same as in the case of flow into a circular cavity with gate at the center. The melt memory of the flow experience in this region soon decays or evolves, because of the effects of high temperature and flow rate.

2.3.2.3 Crystallization Kinetics

Most of the scientific studies on the modeling of the flow-induced crystallization are mainly concerned with experimental elucidation and qualitative understanding [93].

Hsiung and Cakmak [94] performed a simulation of injection molding of slow-crystallizing polymer, in which the crystallization kinetics was described by the Nakamura equation [95] in differential form, taking the effect of shear stresses on crystallization into account by making the Avrami exponents stress–dependent. The Avrami exponent represents greater dimensionality in the crystal growth process. An arbitrary simple linear relationship between Avrami Exponent n_c and shear stress τ was applied in the study, with n_c equal 3.0 at quiescent state ($\tau=0$) and as shear stress increase, n_c decrease to approach 1.0 [94].

Isayev and Guo [93] proposed a unified crystallization model, which is based on the description of the molecular deformation introduced by flow. During the induction period of crystallization, different shapes of nuclei are formed as the precursors for crystal growth, depending upon the molecular orientation prior to the start of crystallization. Such orientation is a function of shear rate and the temperature field, thus resulting in different crystallite types or polymorphs. A brief description of the unified crystallization model is given below.

A polymer melt at rest is generally thought of as consisting of coiled molecules that assume the “most random” configuration, which maximizes their entropy. The application of shear stresses to the melt results in two characteristic responses from polymer molecules, namely, the orientation and recoiling of polymer chains. These responses are associated with the macroscopic phenomena of polymer flow and configurational elasticity. Therefore, during non-isothermal flow, it is assumed that there are two characteristic competing structural processes: one is the growth of molecular orientation due to shear flow, and the other is the recoiling of molecules due to the elasticity of chains. The dynamic balance between the two structural processes dictates the probability by which nuclei having deformed shapes (such as thread-like) are produced, when the polymer melt undergoes the supercooled state and overcomes the energy barrier of crystallization.

Melt crystallization can be divided into two stages, nucleation (or induction) and crystal growth. According to the experimental observations [96], melt viscosity experiences an abrupt increase at the start of crystallization under flow. Because of this increase, melt flow slows down and ultimately solidifies. It is natural to suggest that flow-induced molecular orientation only affects the induction period of crystallization. Consequently, it is considered that the presence of shearing in a crystallizing medium greatly accelerates the overall crystallization process by shortening the induction time of crystallization. The stronger the deformation intensity is, the earlier the crystallization takes place.

After the start of crystallization, it is commonly assumed that crystallization follows the same temperature dependence as the “pure” quiescent crystallization. However, the crystal growth speeds may not be isotropic in the crystallizing melt, due to the original nuclei shapes introduced by flow. The Nakamura model given by Equation 2-7 can be used for the evaluation of crystallinity during flow-induced crystallization.

2.3.3 Typical Morphology of Conventional Injection Molding Parts

The skin-core morphology of micro injection moldings has been reported by Whiteside [3], Ito [4], and Chu [5] for HDPE, PP, and POM micro-injection moldings, respectively. However, the scientific studies on microstructure development at the extreme shear rates and thermal gradients, and relationships between morphology and processing conditions have not been reported. The characterization of micro parts remains difficult because of their extremely small dimensions. Here, we summarize literature relating to morphology development in conventional injection moldings for two similar semi-crystalline materials.

2.3.3.1 Polyethylene

An extensive study was carried out by Tan and Kamal [51] to characterize the morphology and orientation in injection molded high density polyethylene. The various morphological structures which were developed in the molding are shown in Figure 2-23. The longitudinal cross sections at various positions with increasing distance from the gate are shown from left to right in the top row, while the transverse cross sections of these positions are shown in the bottom row. The following four distinct morphological zones were reported for these cross sections.

Type I is a nonspherulitic structure which does not exhibit the Maltese cross pattern. When viewed in the longitudinal cross section at a magnification of 400X, this zone exhibits tiny slots of vertical bright lines arranged in rows and running parallel to the surface of the molding. The rows are separated by continuous dark banks. They form at the surface/or close to the surface of the molding in the zone commonly referred to as the skin of the molding. They may be interpreted as stacks of lamellae with chain axes nucleated in the flow direction and growing in the depth direction.

Type II contains very fine asymmetric spherulites of almost uniform size. These are spherulites that are formed under large thermal gradients and the nucleation rate is very fast, thus limiting the size of the spherulites.

Type III contains asymmetric oblate spherulites with axis of symmetry in the depth direction (i.e., in the direction of thermal gradient). These spherulites have a higher growth potential.

Type IV contains randomly nucleated spherulites that grow in all directions until impingement halts growth.

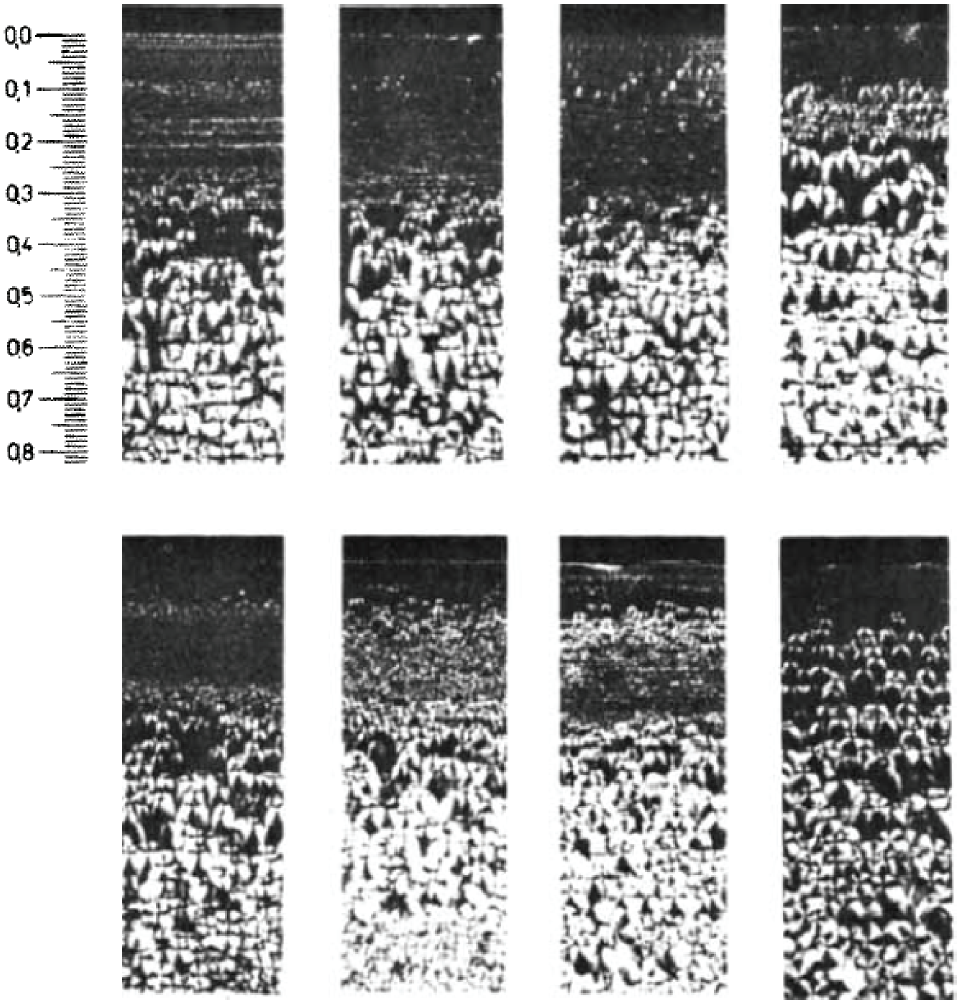

Figure 2-23: Morphology of injection molded polyethylene. Top row: longitudinal cross sections; Bottom row: transverse cross sections. The smallest division of the scale is 10 microns [51].

The authors [51] indicated that the sequences of formation of these zones from the surface to the central core are not the same throughout the molding. For the region near the gate, the sequence is as follows: types I, II, III, and IV, while the sequence for positions remote from the gate is different: types II, I, III, and IV. It was also reported that type II structure appeared occasionally within the matrix of type I structure and the thickness of each zone varies from position to position.

The estimated thickness of the solidified layer associated with the various stages of the molding process at the positions investigated are plotted in a cross-sectional view along the longitudinal direction as shown in Figure 2-24 [51]. The zones I and II may be formed during the filling stage and the other two tend to be formed during the packing and pressure holding stages of the molding cycle.

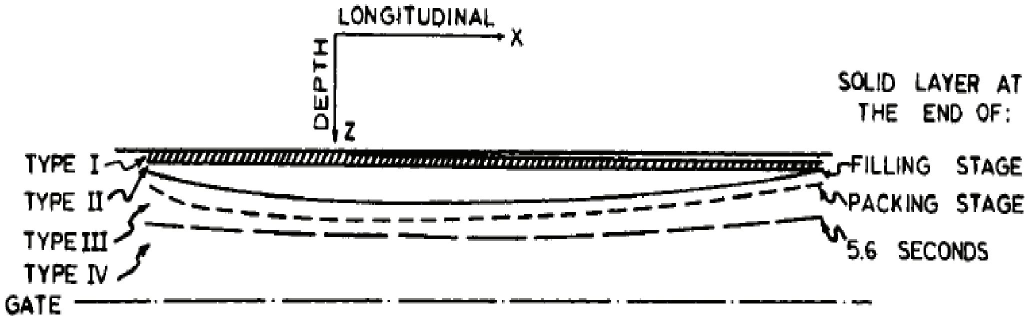

Figure 2-24. Thickness of the solid layer at various stages of the injection molding process. Solid line for the filling stage; short broken line for the packing stage; long broken line for the pressure-holding stage. Shaded area is the region of nonspherulitic type I structure [51].

Heckmann and Johnsen [97] studied the orientation distribution with depth. They found the highest degree of orientation at about 200 μm under the surface. They also observed a strong maximum in modulus and in melting temperature at the same depth. It was suggested that nucleation of fibrillar entities occurs in the most highly deformed melt, located a bit inward from the wall. The surface layer is a very fine microstructure that underwent nucleation under slip conditions, large undercooling and low deformation.

An extended polymer chain has a higher melting point than that of the bulk material so that, at a give temperature below the melting temperature, an extended chain will have a larger supercooling. Thus, there is a greater driving force towards crystallization. Moreover, the extended chain is closer to the final crystallized form of the polymer than a random coil, so an enhanced rate of crystallization might be expected. Figure 2-25 [63] shows the type of structure produced by this effect and known as row nucleated structure, where a string of spherulites have their origin in the same region of sheared material.

Figure 2-25: Section of polypropylene; crossed polars. Bar = 100 μm [63].

2.3.3.2 Polyoxymethylene

Clark [54-56] studied the morphology and its development for injection-molded tensile test bars of polyoxymethylene (POM: Delrin 500 NC-10 acetal resin) and proposed a three region model, as illustrated in Figure 2-26. At the surface is a well-defined skin layer, in which lamellae are oriented perpendicularly to both the surface and to the injection direction. In the next layer, termed “transcrystalline,” a distinct change in morphology is found. The lamellae remain perpendicular to the surface of the bar but lose their preferred orientation with respect to the injection direction. Farther away from the surface, a second, diffuse boundary is found, which results from the development of a spherulitic core having no preferred orientation of the lamellae.

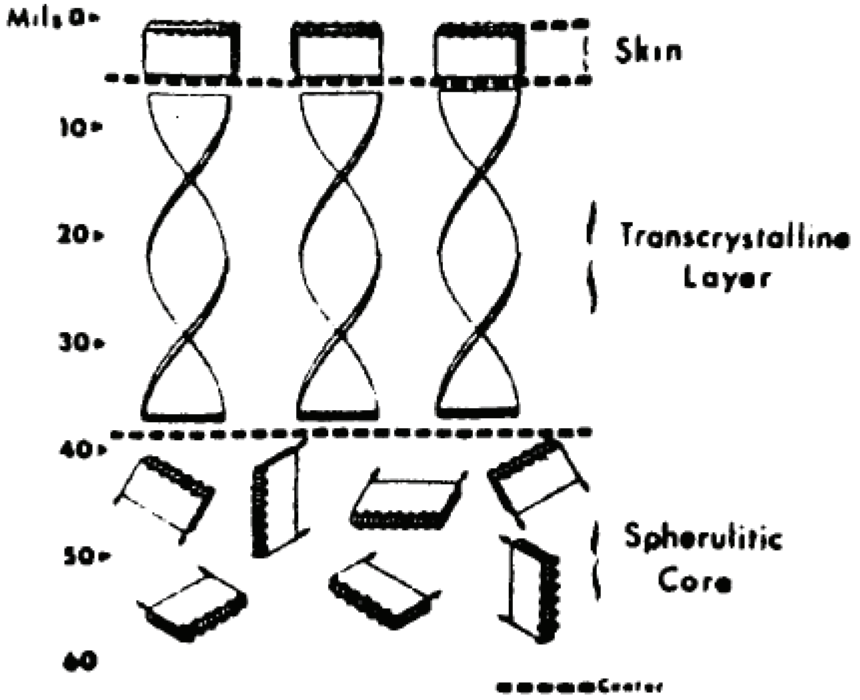

Figure 2-26: Schematic representation of the microstructure through the depth of an injection-molded polyoxymethylene bar [98]. The injection direction is from left to right, in the plane of the paper

The origin of these three types of morphology can be explained on the basis of crystallization mechanisms. Initially, a hot melt is forced under pressure into the mold, where the walls are kept at a temperature below the freezing point of the polymer. Crystallization begins at the mold walls and proceeds into the interior. This portion of the melt crystallizes under shear stress, which creates fibril nuclei from which the lamellae grow without twisting. After nucleation at the mold wall, further crystallization is influenced by the existing temperature gradients. Rapid flow of heat into the relatively cold mold wall sets up a high temperature differential directed into the hot melt. This causes the lamellae to grow with the characteristic fast growth axis parallel to this temperature gradient. The overgrowth of folded chain lamellae will be planar, and the net molecular orientation will consist of chains parallel to the flow direction. During mold filling, a velocity gradient will exist.

The oriented surface layer represents that portion of the melt crystallized during fill time. The depth of the oriented skin layer decreases along the length of the bar from gate to vent. Near the vent end, only the transcrystalline and spherulitic core regions are found. The morphology is analogous to that found in compression molding between cold platens (without shear). With melt velocity decreasing toward a low value at the vent end, no mechanism exists for molecular extension and creation of fibril nuclei. Nucleation is initiated at random sites and, in the absence of melt stress, crystallization proceeds in the form of twisted lamellae. At the gate end, the velocity of the flowing melt is high and, with a portion of the melt crystallizing on the cold wall, a large number of fibril nuclei are formed, and the orientation of molecules in the melt is high. Also, the pressure is the highest near the gate. Therefore, the freezing point would be expected to be highest at the gate end, lower at the center of the bar, and lowest at the vent end. At a constant mold wall temperature and constant thermal transfer through the melt, the crystallization rate should decrease along the length from gate to vent. This is observed as a variation of thickness in the oriented skin.

When the mold is filled, the stress decays rapidly to levels determined by shrinkage from crystallization and corresponding packing of the mold with additional melt. This results in a discontinuity in structure as the highly oriented skin morphology changes to the less highly oriented transcrystalline layer. Below this discontinuity, there is insufficient stress for creation of fibril nuclei. On the other hand, the temperature of the melt is too high for spontaneous nucleation and subsequent development of spherulites. The growth of this inner-oriented layer of twisted lamellae is, in effect, a continuation of growth of the skin. Because of the low stress level, the lamellae twist, as illustrated in Figure 2-26. The influence of a strong temperature differential between the mold wall and melt will cause the growth direction to be perpendicular to the wall.

As crystallization proceeds into the interior, the temperature of the melt decreases to a level at which new nuclei can form spontaneously. Nuclei are formed at random. The skin and transcrystalline layer insulate the molten core and prevent strong temperature gradients from developing.

Hemsley [63] proposed a spherulitic phenomenon of ‘comet’ spherulite, as shown in Figure 2-27, which was regarded to occur particularly with acetal. This is a product of the interplay between nucleation rate and growth rate, as influenced by the temperature. The outside was cooled more quickly than the interior, so the rate of nucleation falls off sharply with increasing temperature from the outside towards inside. This leads to more growth occurring on the high temperature side of the nucleus.

Figure 2-27: Section of acetal; crossed polars. Bar = 100 μm [63].

2.3.3.3 Models of Microstructure Development

In the literatures for conventional injection molding, the microstructure development models are introduced on the basis of experimental observation.

Clark [99] proposed that the orientation of lamellae of readily crystallisable polymers in injection molded samples can be interpreted in terms of the nature of the nuclei and the level of stress in the melt during crystallization. Three stages in crystallization can be defined: 1) initial creation of fibril nuclei and subsequent overgrowth of planar, folded-chain lamellae, 2) creation of additional fibril nuclei and overgrowth of twisted, folded-chain lamellae, and 3) development of non-specific nuclei and growth of spherulites. This mechanism and the three corresponding stages of processing were verified with the published data on the morphology of injection moldings of polypropylene and polyoxymethylene.

Katti [76] observed a good deal of similarity from the spectrum of morphologies reported for different polymers and proposed a common processing-microstructure model. The model is based on the following sequential operations:

- Development of flow patterns in the injected, molten polymer;
- Crystallization of fibrillar crystalline cores in regions of high melt strain and rapid cooling - i.e., near the cold walls;
- Lateral overgrowth on the fibrillar cores, resulting initially in row structures;
- Development of a transcrystalline layer in regions adjacent to the strain-induced row structures. The transcrystalline layer will continue to propagate until the undercooling of the adjacent melt becomes large enough for the nucleation of spherulites;
- Nucleation and growth of spherulites in the core region of relatively low melt strain and slow cooling.

2.3.4 Crystallinity Studies in Micro Injection Molding

Differential scanning calorimetry (DSC) is a technique for determining the quantity of heat that is either absorbed or released by a substance undergoing a physical or a chemical change. The properties of plastics are critically affected by their crystallinity. More crystalline molded parts are more rigid and stronger, but they are more brittle [100].

Similar to conventional injection molding, the polymeric material in micro injection molding process experiences simultaneous thermo-mechanical influences that are introduced by the interactions among the material, the geometry of melt delivery system and cavity, and molding conditions. In a DSC measurement, information about thermal and mechanical history is revealed during the first heating curve.

Haberstroh and Brandt [4] used DSC to measure the crystallinity of a series of micro moldings obtained under different process conditions for the semi-crystalline material in the study: POM, PP, PA, PBT, and PPS. It was found that the production conditions had only little influence on the degree of crystallinity. The crystallinity varied within the scattering range, but showed a tendency towards lower degrees of crystallinity with faster cooling.

Ito and Yagisawa et al. [101] studied crystallinity distribution along the flow length at different mold temperature for the molded product of polypropylene with cavity thickness at 0.3 mm. The melt temperature and the injection speed were set at 220 ºC and 110 mm/s, respectively, and the mold temperature was chosen at 40 ºC, 70 ºC, and 100 ºC. The crystallinity was found to vary in a narrow range near 40% along the flow direction, but the crystallinity in the vicinity of the gate showed a slightly higher value. Lower mold temperature led to lower crystallinity.

2.4 Mechanical Properties of Micro-injection Moldings

With the growth in demand for micro injection molded thermoplastic parts, there is an increased need for determination and verification of material mechanical properties at the micro scale for the design and dimensioning of micro sized parts, since the mechanical properties of macro samples are not valid for micro structures [4, 8, 9].

Two experimental techniques were employed to determine the mechanical properties at the micro scale: nanoindenting and tensile tests. The nanoindenting test was used to evaluate mechanical properties and surface mechanical behaviour of specimens with complex geometry [2, 5, 26]. In the adapted conventional tensile test or micro tensile test, the dimensions of dumbbell test specimens were determined either arbitrarily [9, 102] or by scaling down from the dimensions of specimens used in the standard test methods, such as DIN EN ISO 527 [4]. The test specimens were prepared by the micro injection molding process in both cases.

Haberstroh and Brandt [4, 8] used a micro tensile testing machine to systematically investigate the mechanical behaviour of various cross section areas ranging from 40 mm^2 to 1 mm^2 as displayed in Figure 2-28. The test specimen of geometry I was injection molded with an Allrounder 320S supplied by Arburg, LoBburg; while the three other sample geometries are produced with a FX-25 supplied by Ferromatik-Milacron Maschinenbau GmbH, Malterdingen. Nine different materials were considered in the research, including four amorphous and five semi-crystalline thermoplastics. The amorphous materials are ABS, PS, PC, and PMMA; and the semi-crystalline materials are PP, POM, PA, PBT, and PPS. The large test specimens (Geometries I and II) were measured with a conventional tensile testing machine by company Zwick, ULM; while the two small bar geometries III and IV are tested on a special micro tensile testing machine. Figure 2-29 and Figure 2-30 show the exemplary stress/strain-curves of Geometry III measured for both amorphous and semi-crystalline thermoplastics respectively. It was found that there is no typical run of the curve for the one or the other material class. Instead, the materials can be classified into brittle and ductile materials in the micro range. In the research, they also made conclusions that the geometry-dependent property changes not specific for the material classes of amorphous or semi-crystalline thermoplastics and that the mechanical properties determined at macro geometries can not be applied for micro parts. In terms of Young's modulus, the measured values were scattered too widely to be discussed. Furthermore, the minimum cross section area of 1mm^2 with lateral dimensions of 1mm were not sufficiently small, compared with the feature size in some micro parts such as micro gears.

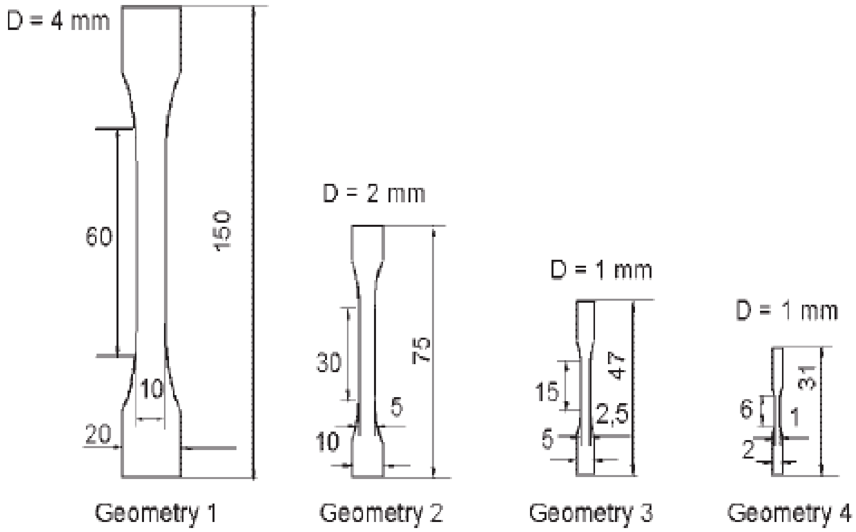

Figure 2-28: Geometries of the used test specimen [4].

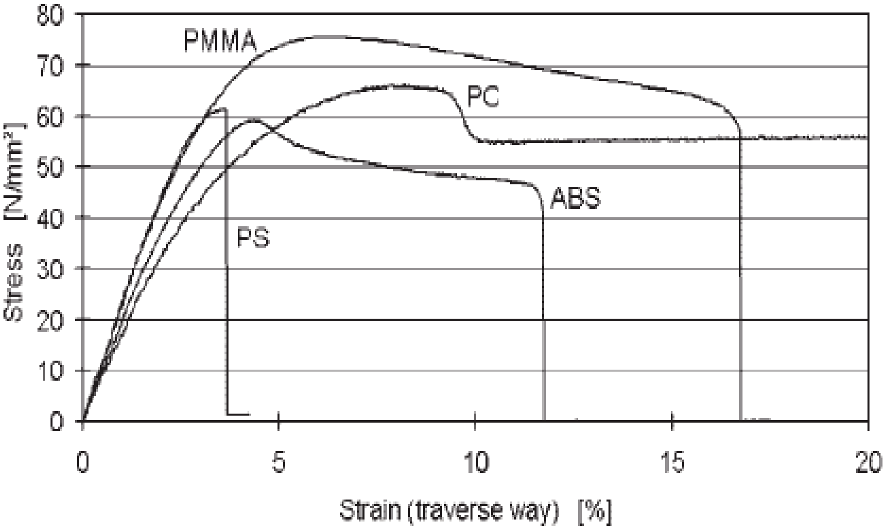

Figure 2-29: Exemplary stress/strain curves (amorphous thermoplastics, Geometry III) [4].

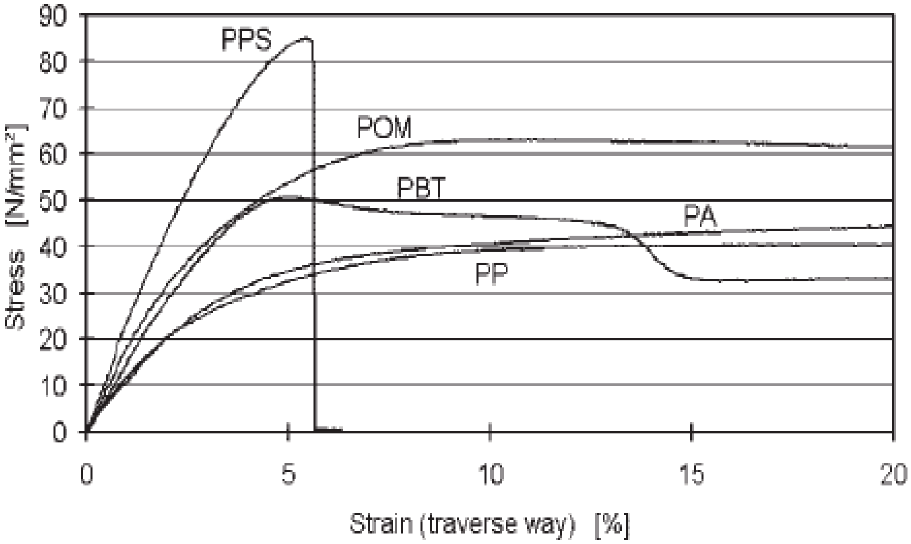

Figure 2-30: Exemplary stress/strain-curves (semi-crystalline thermoplastics, Geometry III) [4].

Tom, Layser and Coulter [9] conducted an experimental study for the purpose of understanding and formulating new underlying mechanical property concepts on the micro scale, by evaluating micro tensile test specimens of constant gate widths and varying thicknesses. Four injection mold brass inserts were used to produce micro scale tensile specimens of varying gate depths. Micro tensile test specimens were 3275 μm long with a gage width of 200 μm and varying thickness of 400, 200, 100, and 50 μm. The thermoplastic polymer materials selected were polyoxymethylene and Cyclic-olefin Copolymer. It was reported that the material yield strength and modulus increased with decreasing part size, especially at the micro scale level. At the smallest cross section tested, 0.02 mm^2, the modulus of both polyoxymethylene and cyclic-olefin copolymer were comparable to their macro-scale levels, at 2830 MPa and 3200 MPa, respectively. However, the variation of the micro-scale mechanical properties with process conditions was not studied.

McCullough [103] proposed a treatment of the moduli of semicrystalline polymers based on the rule of mixtures. Because the crystals are separated from each other along the mean chain direction by rubbery amorphous zones, the measurable tensile modulus E of the material, under constant stress σ acting on both regions, can be approximated by:

$$\frac{1}{E} = \frac{V_c}{E_c} + \frac{(1 - V_c)}{E_a}$$

Equation 2-8

Where E_a is the isotropic amorphous phase modulus, E_c is the anisotropic crystal modulus, and V_c is the volume fraction crystallinity. The value of E_c used depends on the mean orientation of the crystalline units. The order of magnitude value of the measurable modulus E is usually dominated by E_a, but is tempered within that order of magnitude by the local value of E_c.

It is well known that the Young's modulus increases with orientation along the tensile axis. Kanz et al [12] and Clark [99] have demonstrated that the tensile yield strength measured along the axis increased with the combined area fraction of shear and skin layers.

2.5 Shrinkage

The dimensional stability of a molded part refers to the extent to which it retains its dimensions and shape, from the instant of ejection out of the mold to the end of its lifespan. The dimensional instability comprises three phenomena: 1) shrinkage, a geometric reduction in the size of the part; 2) warpage, a distortion of the shape, resulting from non-uniform shrinkage; 3) residual stresses, frozen-in internal stresses, which may lead to deformation and other problems. Shrinkage, residual stresses, and warpage are interrelated in a complex manner. However, only the shrinkage of the plastic material, the most significant challenge in designing and manufacturing micro parts, will be studied in the present project.

Shrinkage is defined as a change in the dimensions of the plastic product relative to reference dimensions, usually the dimensions of the mold cavity [104]. The typical shrinkage equation in one dimension is:

$$Shrinkage = \frac{(d_m - d)}{d_m} \times 100\%$$

Equation 2-9

Where d_m is the reference dimension and d is the measured dimension of the molding.

Shrinkage in injection-molded pieces is both anisotropic and inhomogeneous [105-107]. Shrinkage development normally takes place during the following three stages [108-110]: 1) in-mold shrinkage occurs during the packing and pre-ejection cooling stages, while the part is still in the mold; 2) as-molded shrinkage occurs just after ejection as the part cools and equilibrates to ambient conditions; 3) post-molding shrinkage is the long-term shrinkage that occurs because of time effects during storage, such as physical aging and recrystallization. Shrinkage is manifested by volumetric and linear dimensional changes, for both amorphous and semi-crystalline polymers. Volumetric shrinkage is determined by thermodynamic pressure-volume-temperature (PVT) relationships or the equation of state and is generally isotropic. Linear shrinkage is due to shear and normal stresses acting on the injected polymer.

2.5.1 Volumetric Shrinkage

Volumetric shrinkage is mainly caused by the changes in specific volume, as the resin is first melted and pressurized, then cooled and depressurized. During these processing steps, the specific volume may vary by up to 35% [110]. The specific volume of the polymer at any point is governed by the PVT thermodynamic relationships.

2.5.2 Linear shrinkage

Linear shrinkage is determined primarily by the shear and extensional stresses acting on the polymer during the molding cycle. During the filling and packing stages, molecular orientation is developed by stretching and aligning the coiled and entangled structures of the polymer molecules [111]. The aligned structure is frozen into surface layers due to the fast cooling of the melt next to the cold mold wall. The interior material will then be insulated due to the low thermal conductivity of the frozen polymer skin. Thus, the temperature remains high in this region, allowing longer time for stretched molecules to return to their favoured coiled and compact state. The relaxation of orientation is associated with a reduction in dimensions, as linear shrinkage. As temperature decreases toward room temperature, the relaxation time increases dramatically.

Harrell et al. [112] studied the effects of injection molding conditions and the time and temperature of exposure to heating after molding on the shrinkage of injection molded polyvinyl chloride (PVC). The outer layers of the test plates were cold milled and then subjected to the same heating as the original plates. The milled plates exhibited 15-30% less shrinkage than the original plates. Thus, the conclusion was made that shrinkage after heating was due primarily to the outer layers.

2.5.3 Relationship between volumetric shrinkage and linear shrinkage

Volumetric shrinkage is the driving force for linear shrinkage. The relationship between the volumetric shrinkage and linear shrinkage of the component is affected by mold restraint, crystallinity and orientation. If the plastic were free to shrink in all directions isotropically, the linear shrinkage S_l would be approximately one third of the volumetric shrinkage S_v, as shown in Equation 2-10:

$$S_l = 1 - (1 - S_v)^{1/3}$$

Equation 2-10

Volumetric shrinkage for a given pressure, temperature and level of crystallinity will always be the same. The relationship between volumetric and linear shrinkage depends on stress relaxation and orientation.

In practice, the shrinkage in the plane of the molding will have values much less than one third the volumetric shrinkage value, because the material is constrained in its own plane while within the cavity. The cooling rate has a significant effect on the degree of relaxation. Raising mold temperature will reduce linear shrinkage relative to the volumetric shrinkage by allowing the material to relax. Materials that relax slowly will be highly stressed in the cavity and so exhibit high linear shrinkage.

Molecular orientation in the molding depends on the combined effect of shearing and freezing. In most cases oriented material will tend to relax, resulting in a higher shrinkage in the direction of flow than across the flow. This analysis is in good agreement with experimental results, that show that the longitudinal shrinkage of polypropylene plaques increases strongly with A_{si}, the area fraction of highly oriented material [12, 105, 106].

3. OBJECTIVES

The micro injection molding process has evolved as a technology for the mass production of minute, intricate, polymer and composite components for medical and MEMS applications. However, there is little scientific understanding of the details of process dynamics, the flow and thermal behaviour of the material, the microstructure development, the properties of molded products, and the process – structure – property relationships. This research aims to bridge the knowledge gaps and to improve the understanding of physical phenomena occurring in the micro injection molding process and eventually to contribute to both technology and product development. The specific objectives are outlined below,

- To characterize the cavity filling and packing stages of the micro injection molding process using defined characteristic process parameters (CPPs), and to conduct a statistical investigation of the effects of machine variables on the CPPs;
- To characterize the morphology and thermal properties of micro injection molded polyoxymethylene and polyethylene, and to analyze the effect of process on morphology and crystallinity;
- To characterize the mechanical properties and shrinkage of micro moldings, and to conduct a statistical investigation of the process – properties relationship;
- To employ the commercial MOLDFLOW© software for simulation of the micro injection molding process, using the experimental parameters and estimated CPPs as inputs, and to explain the discrepancy between experimental process data and simulation results.

4. EXPERIMENTAL: MATERIALS, EQUIPMENT & METHODOLOGY

All aspects related to the experimental work in the present study are presented in this Chapter.

4.1 General Aspects

4.1.1 Materials

The following materials were selected for the present study: Escorene high density polyethylene (HD-6719, MI=19, Density 0.952, Melting point 131^{o}C, supplied by Exxon Mobil Chemical), polyoxymethylene (POM) homopolymer (Delrin 900P; MFR: 11g/min, supplied by Dupont), NOVA high density polyethylene (HDPE) (Sclair 2714; MI: 51g/10min, supplied by NOVA Chemical), and polycarbonate (PC) (CALIBRE 1080 DVD; MFR: 80 g/10min, supplied by Dow Chemical).

POM has been widely used in micro injection molding studies, because of its processing characteristics, such as low viscosity, fast molding, and good processing stability for deposit-free molding. POM is also noted for its high mechanical strength and rigidity, excellent dimensional stability, natural lubricity, fatigue endurance, high resistance to repeated impacts, toughness at low temperature, and excellent resistance to moisture, gasoline and many other neutral chemicals. POM Delrin 900P was dried at 80 ºC (176 ºF) for 2 hours before use.

The main features of the NOVA HDPE include its wide processing window, excellent processability for applications requiring good stiffness and toughness, and good cold temperature impact properties. The extensive knowledge available regarding the process-structure-properties relationships for the material helps in understanding the thermo-mechanical history experienced by the material. HDPE Sclair 2714 was dried at 65 ºC (149 ºF) for 2 hours before use.

The Escorene HDPE was used in the early stages of this project. It is a narrow molecular weight ethylene-hexene copolymer, designed for a wide range of injection molding applications, combining easy processability with good toughness.

PC is an amorphous material with excellent and very consistent flow properties, very low level of impurities, and state-of-the-art demolding performance. The resulting compact disk (CD) properties include low birefringence over the whole play-length, low disk-staining and excellent pit reproducibility. The PC CALIBRE 1080 DVD was dried at 120 ºC for 4 hrs before processing.

The variation of viscosity with temperature and shear rate and the P-V-T properties of the selected materials are introduced in Appendix A.

4.1.2 Machine and Instrumentation

The plunger injection system, with separate screw melting, metering and injection units, has been adopted widely by machine manufacturers such as Battenfeld, Ferromatic Milacron, Boy, and Sodick, in order to achieve the metering accuracy and homogeneity required for the very small quantities of melt used in the micro molding process. The Battenfeld Microsystem 50 has been used by various researchers for µIM research [3, 6, 13, 25, 32, 113]. The machine features highly repeatable process control, accurate dosing of material, high injection speed and back pressure, clean room environment and a handling system capable of picking, inspecting and placing micro components [7, 114]. The machine maximum clamping force, injection speed, and injection volume are 50 KN, 760 mm/s, and 1100 mm^3, respectively. As shown in Figure 4-1, a 14 mm diameter extrusion screw, allowing sufficient channel depth to properly handle the standard size of plastics pellets, mounted at an angle of 45 degree to the injection axis, feeds into the metering unit for accurately preparing a dose of material against the pre-set volume. The pellets are heated by a combination of thermal and mechanical energy, producing efficient and homogeneous plasticization. The metering plunger delivers the shot volume to the injection barrel, after the set volume has been achieved. The injection plunger pushes the melt into the mold, and a holding pressure may be applied by a slight forward movement of the injection plunger. Backflow, which occurs in conventional injection molding machines during the movement of the screw ram, is minimized by careful design of the injection plunger. The injection plunger can move up to the split plane, which guarantees short flow paths with the lowest loss of pressure and an extremely precise injection process.

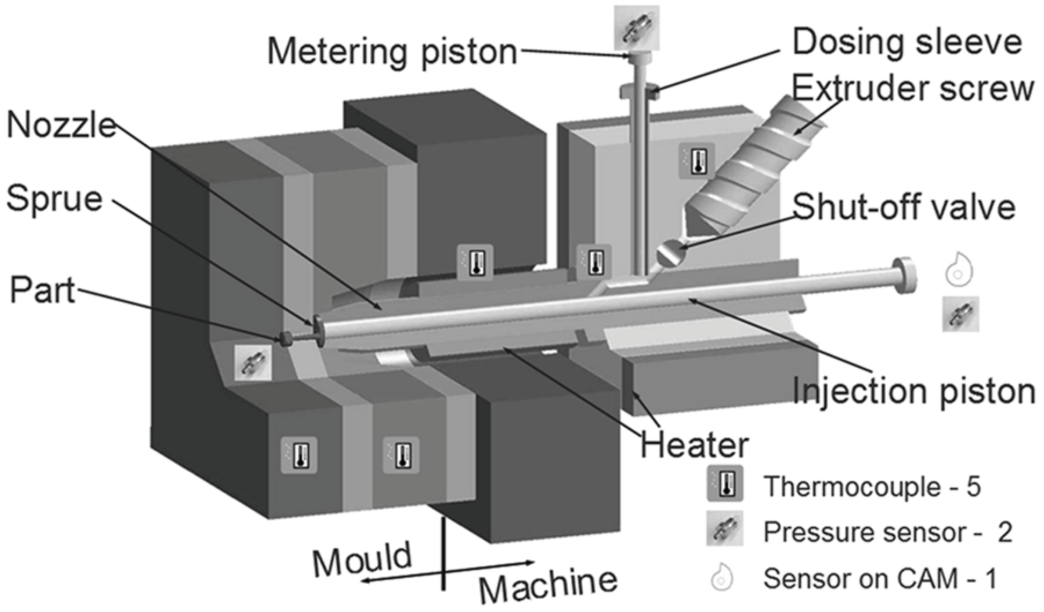

Figure 4-1: Sensor installation positions on the Injection unit of the Battenfeld Microsystem 50

The diameters of small injection plungers range from 4.89, 4.94, to 4.96 mm. According to Pirskanen and Immonen et al. [25], the diameter of the injection plunger has an effect on the replication quality. However, a consistent diameter of 4.89 mm was used for all experiments in the present study.

The cam mechanism, which drives the injection plunger during filling and packing of the mold insert, has not received sufficient attention in the literature, despite its importance in calculating the metering size and creating a viable process. The eccentric plate cam installed on the Battenfeld machine is used to translate circular movement to a smooth reciprocating (back and forth) motion of the plunger. A displacement diagram, which relates angular position of the cam to the linear displacement of the plunger, is displayed in Figure 4-2. Two regions in the cam profile, the injection ascent and the holding ascent, define the two linear relationships between cam rotation angle and the plunger displacement, corresponding to the filling and holding stages of the process. The melt volume for this mechanical switch-over, during which the plunger decelerates from injection velocity to packing velocity, amounts to only 2 mm^3. The packing stage is achieved within the relatively smooth section of the cam profile, under the control of the packing velocity profile.

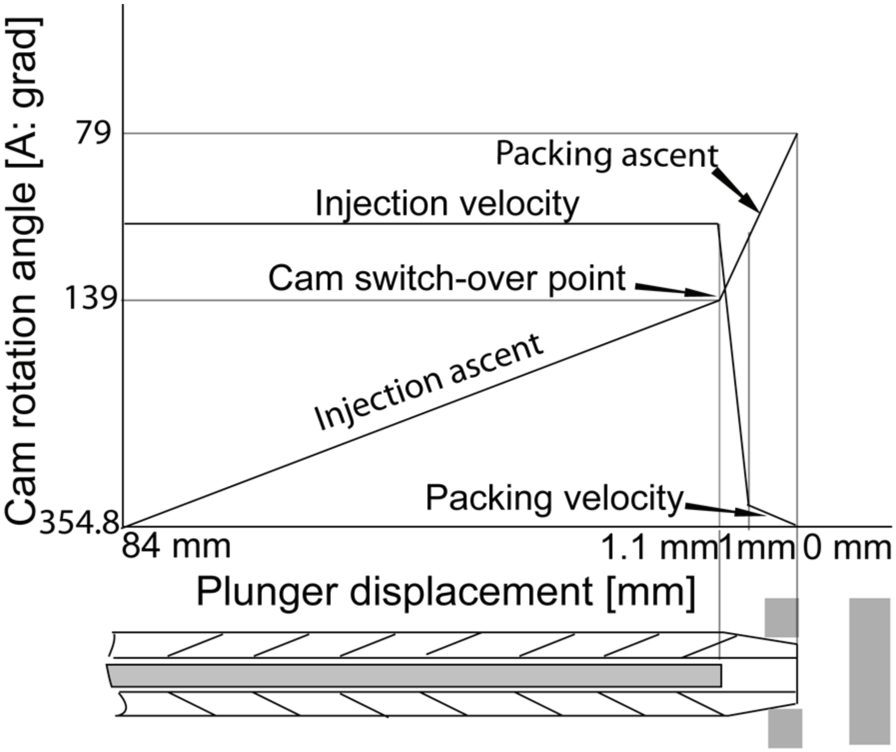

Figure 4-2: Plunger displacement vs. Cam rotation angle

A data acquisition system was designed for process monitoring and data recording. Figure 4-1 displays the suite of sensors installed on the machine. The thermocouples installed on the melt heater and in the mold plate were HASCO Z1295 type 1 and type 3, respectively. Three thermocouples that were installed on heaters were distributed on the extruder, distributor and nozzle, respectively, for controlling the melt temperature. In the present study, the temperature setting at the injection nozzle is regarded as the melt temperature and the melt temperature is assumed to be uniform. The thermocouples in the mold were installed at a distance from the melt/insert interface, and the mold temperature was found to be constant at the set-points. The injection pressure sensor and pressure sensor in the runner system were KISTLER 9204B and KISTLER 6183, respectively. The voltage signals representing the cam rotation angle were converted into plunger displacement according to two equations, corresponding to injection ascent and holding ascent as shown in Figure 4-2 [115]. The dynamic process data of injection pressure, runner pressure, and plunger position at different processing conditions were recorded and studied. In view of the restrictions of available space, no sensors were placed inside the cavity in this study. National Instruments DAQ card PCI – 6052E and LabVIEW 7.0 software were used as the hardware and software, respectively. The CPU of the computer was 2.53GHz and memory was 1GB. The true data sampling rate was found to be restricted by the execution time of the LabVIEW program. A minimum 5 ms of sampling rate was achieved, even when the sampling rate was set as 1ms on the control panel of the program.

4.1.3 Mold Insert and Part Geometry

The Battenfeld “Master Mold” concept and a square plate insert of simple geometry were used in the study as illustrated in Figure 4-3 (a). Figure 4-3 (b) displays a three dimensional view of the final molding of part II, modeled with CAD software. The final molding consisted of two parts at each end and a runner system, including a remaining sprue, a gap ring, two blind runners, and two real branch runners connected with two gates. Figure 4-3 (c) displays a side view of the whole molding.

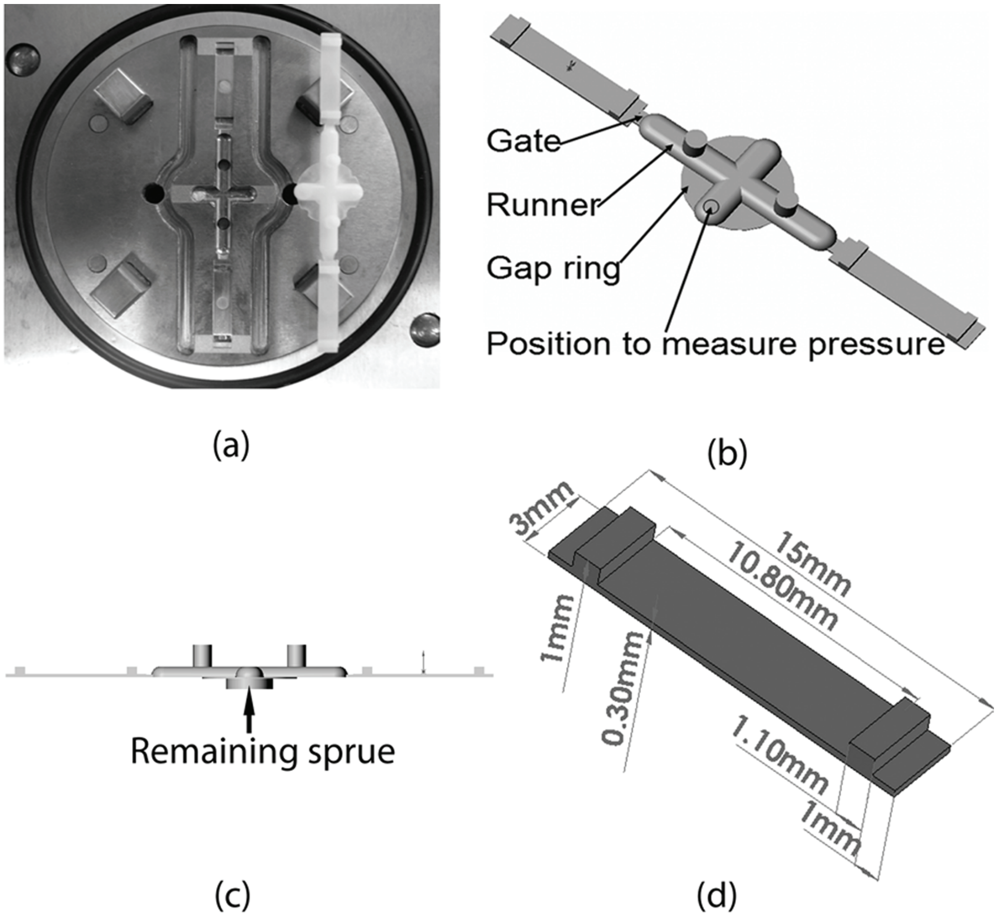

Figure 4-3: (a) Mold insert and a final molding (b) 3D view of the whole molding; (c) Side view of the whole molding; (d) 3D dimensions of a molded part

Two different parts can be produced with the same mold insert by switching a plug in the middle of the cavity, as shown in Figure 4-4. Part I has a hole in the middle and with three ribs passing through the hole as displayed in Figure 4-4 (a) and (b). The radius of the rib is 150 µm. Part II exhibits uniform thickness without hole in the middle of the cavity, as illustrated in Figure 4-4 (c).

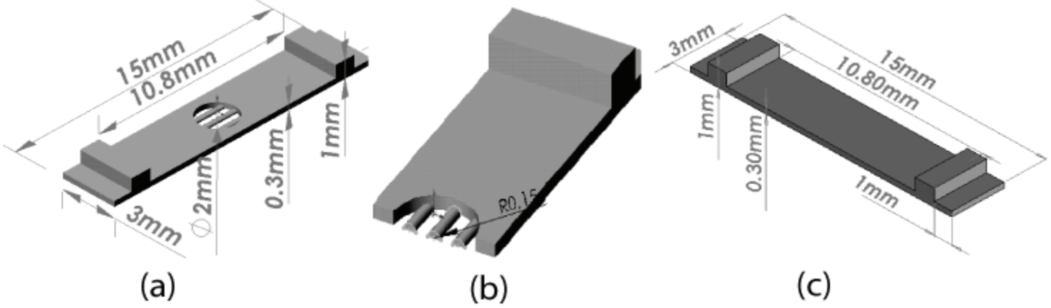

Figure 4-4: a) Three dimensional view of the part with hole; (b) Cross section of the hole; (c) Three dimensional view of the part without hole.

The thickness of the remaining sprue after molding depends on the plunger stroke during the packing stage, ranging from 0.1 mm, the minimum allowed to protect the mold insert, to 0.7 mm, when both injection speed and packing velocity are set to low levels. The volume of the whole molding with 0.99 mm thickness of the remaining sprue and 0.11 mm thickness of the gap ring is 148 mm^3, according to the modeling software. Figure 4-3 (d) displays detailed dimensions of a molded part, which has a volume and surface area of around 18 mm^3 and 112 mm^2, respectively. Thus, the ratio of surface area to volume and the ratio of part weight to the whole shot weight (including runner system) are around 6 and 24%, respectively.

4.1.4 Process Characterization

Short-shot trials were performed for polyoxymethylene to study the filling patterns for various process conditions, including both high and low levels of mold temperature, melt temperature, and injection speed. Filling patterns similar to those shown in Figure 4-5 were observed. The features of the filling pattern can be summarized as follows. The runner system is filled initially. Flow hesitation occurs at the 110 μm thickness gap between the nozzle end surface and the movable mold plate. During the early stage of the cavity filling, the flow is radial and the melt front is circular, where a biaxial orientation would be expected. As the melt front advances away from the gate, the front shape becomes almost flat in the middle and curved at the edge. This pattern is similar to that reported for polymer flow in the conventional injection molding process [79, 81]. Melt flow tends to be well balanced, in both the runner system and the two cavities. Filling of the gap ring proceeds at the same time with cavity filling.

Figure 4-6 (a) displays trace curves of injection pressure, runner pressure and plunger position, recorded for a single molding cycle for Case 1 of POM experiments, in which the injection speed, packing velocity, and mold temperature were set at 150 mm/s, 1 mm/s, and 70 ºC, respectively. The injection plunger traveled with almost constant speed at around 150 mm/s, equal to the set injection speed. The lower injection pressure before melt entrance into the cavity represents the injection pressure required for pushing the melt to reach the set injection speed. The injection pressure and runner pressure reached their highest values almost simultaneously. Then, the runner pressure decreased monotonically with variable slopes, while the injection pressure reached its second peak during the packing stage. In order to reveal the patterns of cavity filling and packing in detail, the time scale was expanded to exhibit changes at the millisecond scale, as shown in Figure 4-6 (b). The rapid rise in both injection pressure and runner pressure probably reflects arrival of the melt at the blind runner and entry of the melt into the cavity, respectively. This explains the small time difference between the first peaks of injection pressure and the peak of the runner pressure.

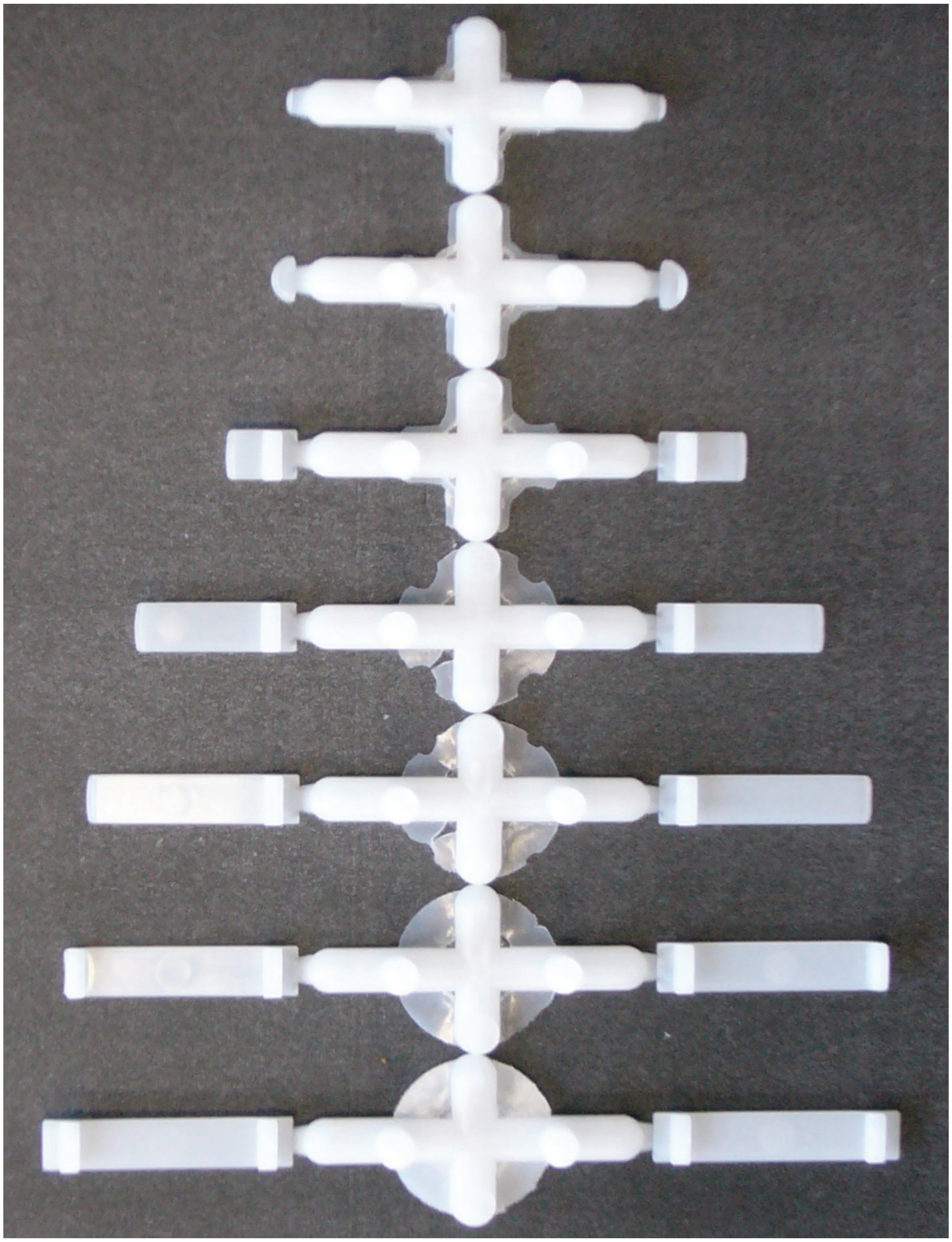

Figure 4-5: Filling pattern Image of short-shot trials

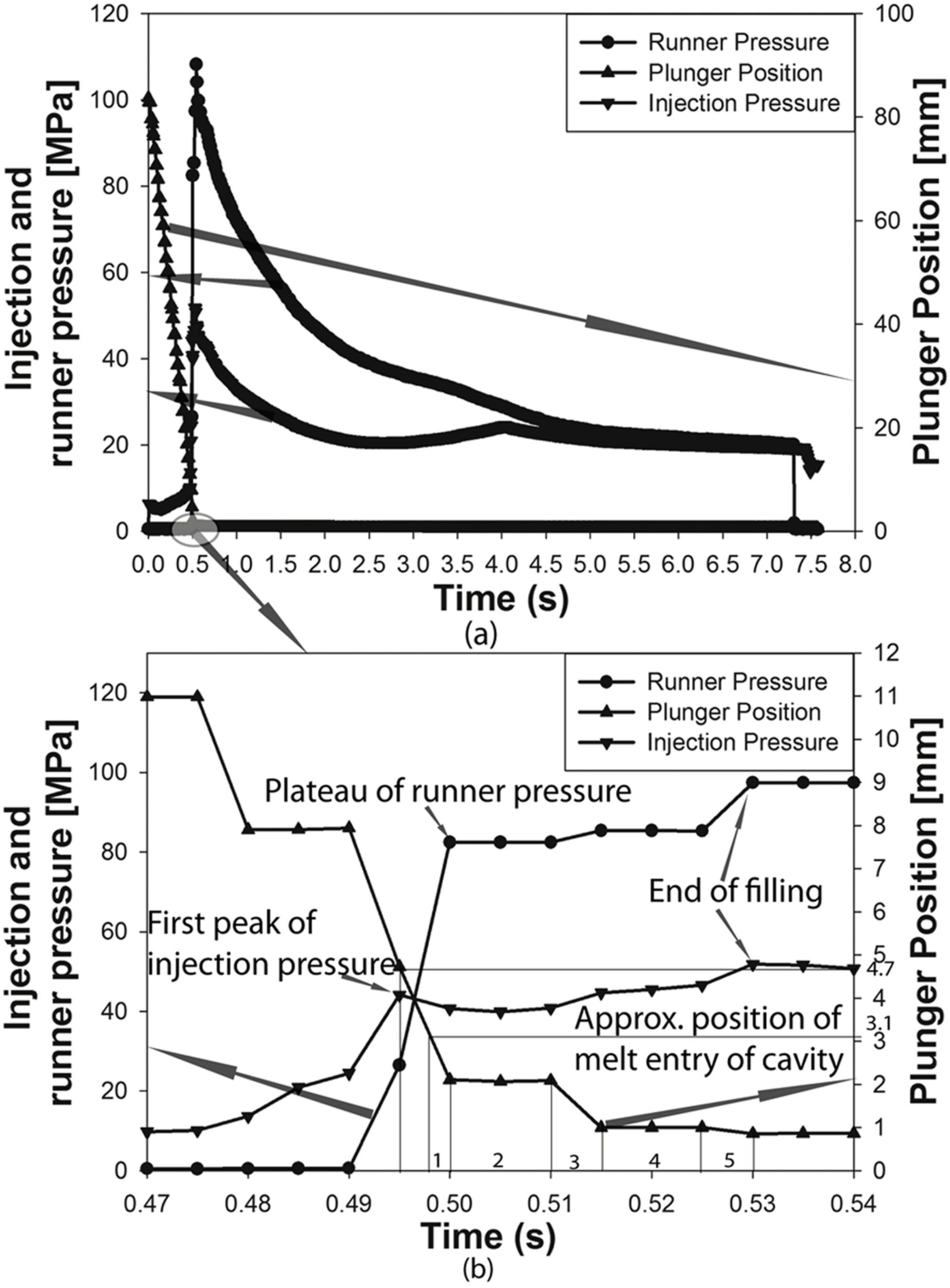

Figure 4-6: (a) Process data of one molding cycle (POM case 1); (b) Process data of cavity filling including five sub-stages (1. First filling; 2. First static; 3. Second filling; 4. Second static; 5. Third filling)

It would be reasonable to correlate the plunger displacement and velocity with cavity filling progress and flow rate. The sudden change in the slope of the injection pressure and the jump in injection pressure at around 8 mm plunger position, as shown in Figure 4-6 (b), indicate that the melt starts to enter the runner system when the plunger position reaches slightly more than 8 mm. However, after the melt enters the mold cavity, filling progress cannot be calculated simply based on the melt volume left in the barrel. This is manifested by the observation that the metering size required to fill the cavity is 176 mm^3, which is 19% higher than the combined volumes of the mold insert and the 0.99 mm thickness of the remaining sprue, which is around 148 mm^3. Obviously, this is due to the variation of specific volume with pressure and temperature.

It was found that a stable switch-over position of plunger could only be obtained at around 0.8 mm, which is slightly after the mechanical switch-over position according to cam structure, which is 1.0 mm. A stable switch-over position is an important indicator that the machine is under control. So, the whole mold insert could be regarded as filled when the plunger has moved from 9 mm to 0.8 mm in the barrel.

Now, it is necessary to establish the plunger position when the melt starts to fill the two cavities. As shown in Figure 4-3, there are totally four runners, two “flow runners” lead to two cavities and two “blind runners” have closed ends. Each flow runner is around twice as long as the blind runner. As shown in Figure 4-6 (b), the runner pressure sensor started to register pressure of 26.5 MPa at 0.495s, when the plunger position was at 4.7 mm, indicating that the cavity filling did not start yet, in view of the volume left in the barrel and the low pressure in the runner system. The injection pressure reached its first peak, due to the sudden decrease in flow cross section, as the two blind runners were completely filled with melt. The next runner pressure and plunger position data acquired 5 ms later, at 0.500s, were 82.5 MPa and 2.1 mm, respectively. The jumps in both the runner pressure and the plunger position indicate that the cavity filling started when the plunger was between 2.1 mm and 4.7 mm, during which the melt passed through the narrowest cross section at the gate. However, the exact position remains unclear, due to the limitation of data sampling rate. Further efforts were made to estimate the plunger position at the start of cavity filling, from the last filled volume of the two cavities and the gap ring. This volume was calculated at around 45 mm^3 using a 3D modeling software. Considering the effect of pressure in the barrel and runner system during cavity filling, the error of the estimation of the volume should be within 19% of the above values. Thus, it was assumed that the volume in the melt injection barrel in front of the switch-over position (0.8mm) was equal to the melt volume required to fill the two cavities and the gap ring, i.e., 45 mm^3. Accordingly, it was estimated that the plunger position to start cavity filling was at 3.1 mm.

The plunger movement from 3.1 mm to 0.8 mm in 0.035s was divided into five sub-stages which consisted of three filling sub-stages and two static stages, as shown in Figure 4-6 (b). The pattern of plunger movement indicates that the velocity and flow rate during filling of the two cavities and the rest of the mold insert is not constant, since the two cavities are filled in a changing velocity profile rather than at a constant flow rate, as shown in Figure 5-3.

The cavity pressure was not measured in the present study, due to the restricted space available for such measurement. However, Whiteside [32] and Kuek [116] found that, for similar gate dimensions at lower mold temperature, the cavity pressure increased for approximately 100 ms before starting to decrease due to gate freezing, as shown in Figure 4-7. In the present study, the characteristic process parameters for the packing stage are defined at 0.2s, when packing is still in effect.

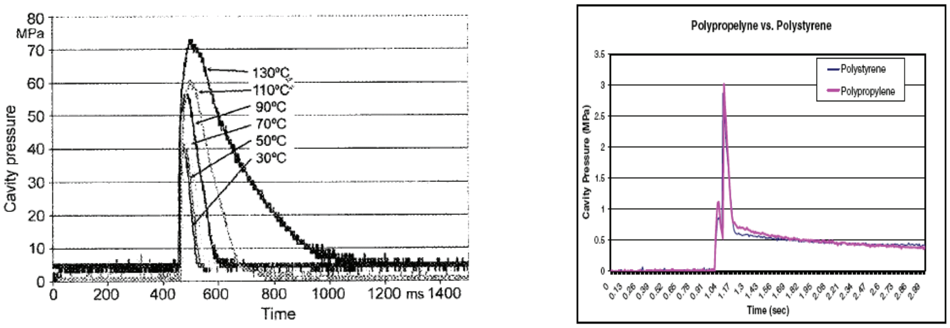

Fig. 9. Experiment 2 – cavity temperature variation: cavity pressure curves for each set cavity temperature, 30 to 130 °C

Figure 4: Cavity pressure curve of two different materials: polypropylene and polystyrene

a) b)

Figure 4-7: a) Cavity pressure curves of POM process at different mold temperatures [32]; b) Cavity pressure curves of two different materials: polypropylene and polystyrene [116].

Based on the above experimental facts, the main features of the micro injection molding process can be described as follows:

- Before melt enters the mold cavity, the plunger travels at the set injection speed.
- The switch-over position of the injection plunger occurs when the cavity filling is completed and the packing stage starts.
- The plunger position at the start of cavity filling was estimated at 3.1 mm.
- The plunger movement during the cavity filling stage consists of a series of filling and quasi-static sub-stages. The number of filling sub-stages was quite stable for a specific material and process conditions, while the number of quasi-static sub-stages varied randomly in a narrow range.
- The plunger speed varies with the progression of cavity filling.
- The cavity pressure rise may be maintained for only 100 ms, due to the fast freezing of the gate.

4.1.5 Design of Experiments

The design of experiment (DOE) method was employed in order to investigate the effects of machine variables on the characteristic process parameters (CPPs). The machine variables selected were injection speed (V_i), packing velocity (V_p), mold temperature (T_m), and barrel temperature (T_b), which are the key molding settings for the μIM process [7]. HDPE exhibited good processability over a wide range of mold and barrel temperatures. Thus a two-level four-factor half fractional design with 8 experiments was selected. Three additional cases were included for verifying statistical analysis results and also for evaluating the mechanical behaviour of HDPE at very high injection speeds. The barrel temperature was not considered for POM to avoid fast thermal degradation. Therefore, a two-level three-factor full factorial design was chosen. PC exhibited an even narrower processing window. Therefore, a two-level two-factor full factorial design was employed. Table 4-1 displays the DOE experimental matrix for the three materials. The statistical analysis was carried out, using the Design-Expert 6.0 analysis software. The injection speed high limit was tried only in additional runs for HDPE and POM, due to leakage through the back of the plunger. Every process condition was repeated twice in order to confirm the repeatability of process conditions. The repeatability of the process was found to be good. The experiments were conducted in a randomized sequence.

The characteristic process parameters (CPPs) of the filling and packing stages were defined to describe the material and flow behaviour during these stages. The CPPs for the cavity filling stage include peak injection pressure, average injection pressure, and average plunger velocity, all during filling. For the packing stage, plunger stroke at 0.2s packing, total plunger stroke during packing, and average injection pressure during 0.2s packing were the CPPs extracted from the process data recorded for plunger position and injection pressure. The metering size, a process parameter in other studies [3, 25], is normally optimized for each set of machine variables, in order to have a uniform switch-over position for each process condition. In the present study, it was also used as a CPP.

Table 4-1: Experimental matrix

DOE	Cases	V_i	V_p	T_m ºC	T_b ºC
		A	B	C	D
POM	Case 1	150	1	70	205
	Case 2	150	6	70	205
	Case 3	380	6	70	205
	Case 4	380	1	70	205
	Case 5	380	1	100	205
	Case 6	380	6	100	205
	Case 7	150	6	100	205
	Case 8	150	1	100	205
	case 9	265	3.5	85	205
	case10	650	6	100	205
HDPE	Case 1	380	6	70	230
	Case 2	150	1	70	230
	Case 3	380	1	35	230
	Case 4	150	6	35	230
	Case 5	380	6	35	190
	Case 6	150	1	35	190
	Case 7	380	1	70	190
	Case 8	150	6	70	190
	Case 9	265	3.5	52	210
	Case10	650	6	35	230
	Case11	650	6	70	190
PC	Case 1	700	N/A	75	N/A
	Case 2	350	N/A	75	N/A
	Case 3	700	N/A	110	N/A
	Case 4	350	N/A	110	N/A

In the present study, the holding pressure option is selected as "Start Inj. Press. – Specific", which means that the process is switched over to the packing stage when runner pressure reaches a specified pressure. The metering size is obtained by trial-and-error starting from 148.1 mm^3, which is the total volume of the molding, including the remaining sprue and gap ring, as shown in Figure 4-3. At this dosage, the final moldings are found to be short shots and the switch-over to the packing stage could not occur. The metering size is then increased at an increment of 3 mm^3 to obtain full parts first and then to have a switch-over position at around 1.1 mm, which is the switch-over position of the cam mechanism. The stable switch-over positions were only found at around 0.8 mm. This was probably due to the inertial of the plunger. Fine tuning of metering size may be required to stabilize the switch-over position. The accuracy of metering size is very important to obtain high repeatability and reproducibility of the molding process.

The volume average plunger velocity is defined on the basis of the plunger velocity vs. shot volume percentage profile as the sum of products of velocities of each filling sub-stage and their corresponding percentage of the shot volume, over the total melt volume of the two cavities and gap ring as shown in Equation 4-1. The calculation is started from last filling sub-stage, whose shot volume was calculated from the difference between switch-over position and start position of the last filling sub-stage.

$$\begin{aligned}&\text{Average plunger velocity in filling} = V_3 \times P_3 + V_2 \times P_2 + V_1 \times P_1\\&P_1 = 1 - P_2 - P_3\end{aligned}$$

Equation 4-1

Where V_1, P_1, V_2, P_2, V_3, and P_3 are the velocities and shot volume percentage of the series of filling sub-stages. The velocities in each filling sub-stage were assumed to be constant. The static sub-stages were excluded from the calculation of average plunger velocity during filling. Minor modifications may be needed in order to adapt Equation 4-1 to the cases with more or less filling sub-stages. At least two filling sub-stages were found for all process conditions in the present study. The main limitation related to the estimation of plunger velocity arose from the estimation of the velocity of the first filling sub-stage, which is only a part of the sampling period as shown Figure 4-6 (b).

Process data for five molding cycles were recorded after the machine reached steady state, which usually took about 5 to 10 minutes for each process condition. The process stabilization was identified by monitoring the switch-over position, peak runner pressure and peak injection pressure on the machine screen. An unstable process condition is often caused by unexpected accumulation of leaked material behind the plunger at high injection speed. Regular checking and clean-up were needed, when the injection speed was set to a high level.

4.2 Thermal Properties

4.2.1 Differential Scanning Calorimeter (DSC)

Differential scanning calorimetry (DSC) is a commonly used thermal analysis technique. Heat flux to the sample is monitored against time or temperature, while a certain temperature program is imposed under controlled atmosphere, for instance, nitrogen. The fundamental theory and application of DSC to polymer characterization have been reviewed in detail [100]. For a first order transition process (melting-crystallization) of semi-crystalline polymers, DSC can be used to measure accurately the heat of melting and crystallization and to determine the experimental melting and crystallization temperature.

In this research, thermal analysis was performed with a TA Q100 Differential Scanning Calorimeter. The temperature and the heat flow were calibrated with Sapphire in crimped pans-Inv Lid (T_{onset}=157.89 ºC, K_{cell}=1.0582). The contribution to the DSC curves by the empty aluminium specimen pan was subtracted from each measurement. All measurements were performed under nitrogen.

4.2.2 Specimen Preparation

Figure 4-8 displays the sampling positions (a) for comparing the crystallinity of samples obtained under the different process conditions and (b) for crystallinity distribution along the molding flow length. The specimens were prepared by using a sharp scalpel with a ruler under a magnification lamp.

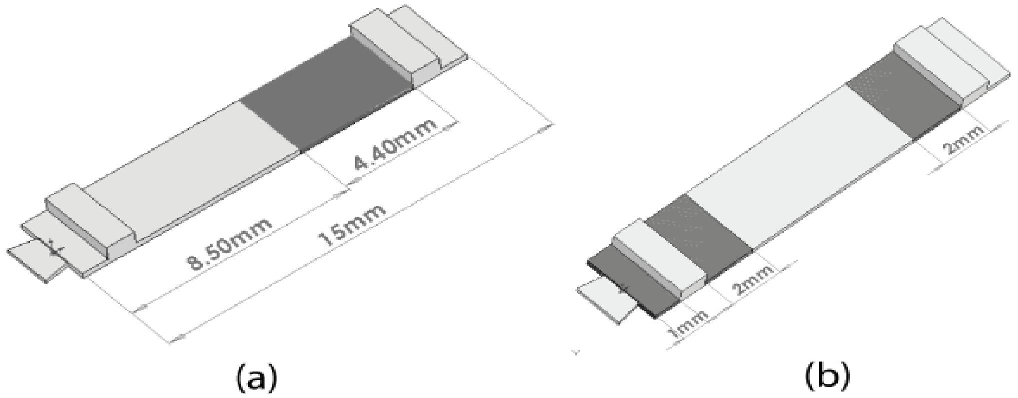

Figure 4-8: a) Sampling position for crystallinity comparison among designed process conditions; b) Sampling position for crystallinity distribution.

Figure 4-9 shows a typical 1st heating curve of a molded HDPE part. The heat of fusion was calculated by linear integration of the peak area and the crystallinity is determined by dividing the heat of fusion, ΔH_m, by the literature value for 100% crystalline material, ΔH_m^0. For simplicity, the heat of fusion is used to represent the crystallinity in the present study.

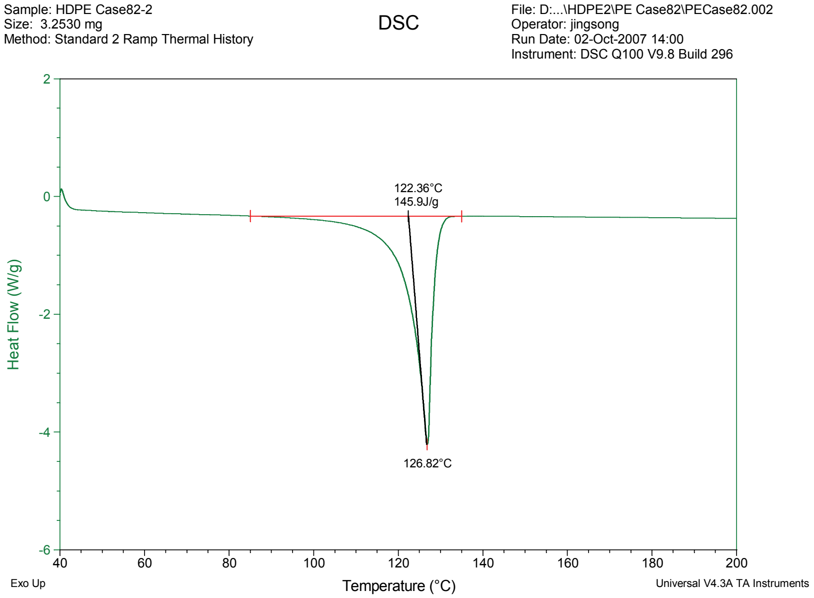

Figure 4-9: Typical 1st heating curve of micro injection molded HDPE

4.3 Morphology Studies

The HDPE micro moldings were first cut into small pieces using a scalpel and then sectioned using a Leica Reichert Ultracut microtome. The POM micro moldings were first cut into the shape of tensile bar using a specially designed cutting die for easy accurate positioning, and the tensile bars were then sectioned using a Leica Reichert Ultracut microtome. Both longitudinal (XZ) and transverse (YZ) cross sections were obtained for the different positions, as illustrated in Figure 4-10 for HDPE (Escorene 6719), and in Figure 4-11 for POM (Delrin 900P) and HDPE (Sclair 2704). The thin sections, 10 microns for POM and 20 microns for the two HDPE materials, were immersed in microscope immersion oil (Resolve Low Fluorescence, low viscosity at 150 cs, Stephens Scientific), and observed between crossed polarizers using an Olympus BX50 System Microscope. The photomicrographs in this study were taken at magnifications of 40X, 100X, and 200X, consecutively, using the polarized light microscope. The thicknesses of morphologic zones were measured directly from the photomicrographs.

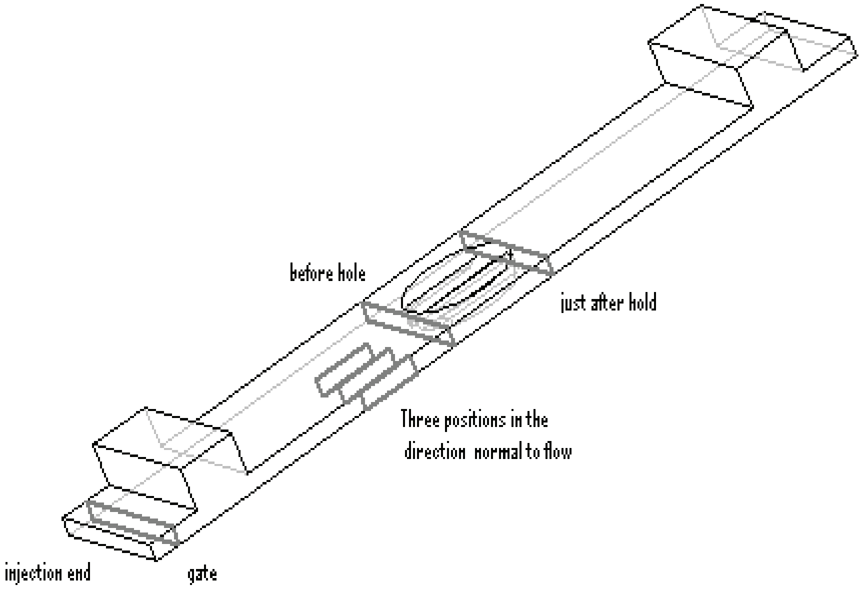

Figure 4-10: Skin-core structure measuring positions in both the flow direction and the normal direction for HDPE (Escorene 6719)

For POM (Delrin 900P) and HDPE (Sclair 2704), the microstructural features were evaluated at positions from A to H, with different distances from gate, as displayed in Figure 4-11. The positions are represented in the figure with transverse cross sections, yet both longitudinal and transverse microstructural characteristics are evaluated.

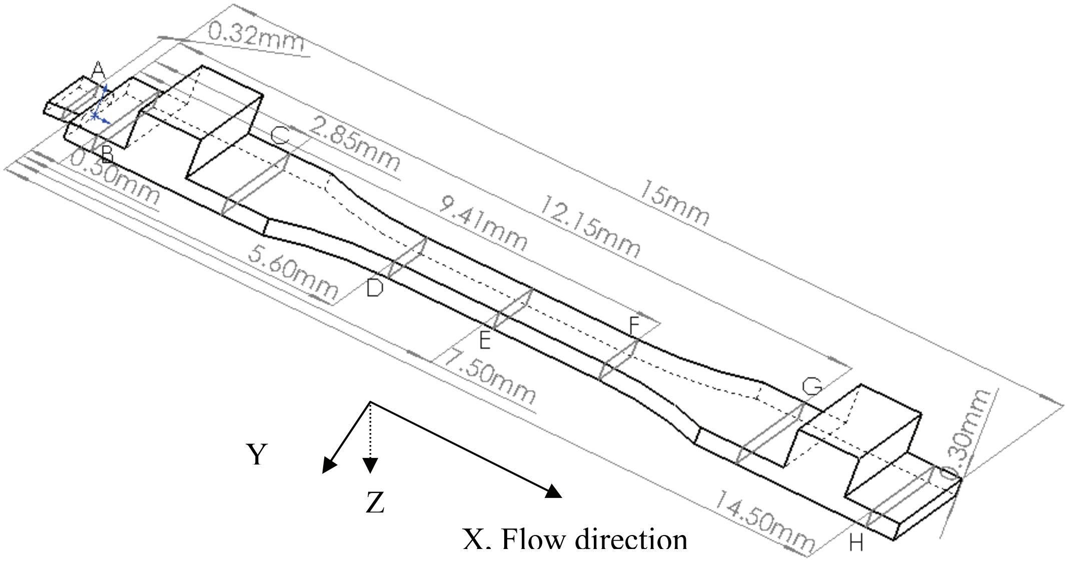

Figure 4-11: Designated positions for microstructural studies in the moldings for POM (Delrin 900P) and HDPE (Sclair 2704)

4.4 Mechanical Properties

4.4.1 Specimen Preparation

The test specimens were prepared by die cutting micro injection molded plates. The dimensions of the specimen were determined by scaling down the Type V of ASTM 638-03. Figure 4-12 displays the geometry of a typical tensile test specimen. The comparison of critical dimensions and tolerances between the specimen for the present study and the Type V is shown in Table 4-2. The gauge length and the width of the narrow section are half of those of Type V, while the radius of fillet is only a quarter of that of Type V. A punch die was designed and fabricated by micro-electro-discharge machining (MEDM), as shown in Figure 4-13. The dimensions and tolerances of a tensile test specimen by die cutting are displayed in Figure 4-14 (Unit: mm). The width of the narrow section was taken as the distance between the cutting edges of the die in the narrow section. The specimen-to-specimen variations in both width and thickness dimensions of the narrow section were measured to be less than 1% of the designed dimensions. The strain was calculated by dividing the grips separating displacement by the parallel gauge length, 3.81mm.

The test specimens were conditioned at 23 ± 2 ºC and 50 ± 5% relative humidity for not less than 40h prior to test. The tests were conducted at the same conditions as those for conditioning.

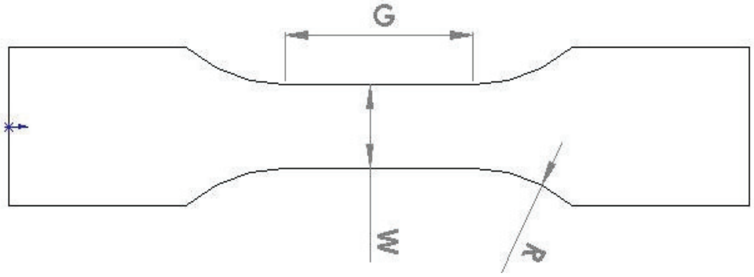

Figure 4-12: Geometry of a typical test specimen

Table 4-2: Comparison of critical dimensions and tolerances between the test specimen and Type V of ASTM 638-03

Dimensions and Tolerances	Type V (mm)	Specimen (mm)
W-Width of narrow section	3.18 ± 0.03	1.59 ± 0.015
G-Gage length	7.62 ± 0.02	3.81 ± 0.01
R-Radius of fillet	12.7 ± 0.08	3.18 ± 0.02
Thickness	≥ 1	0.3

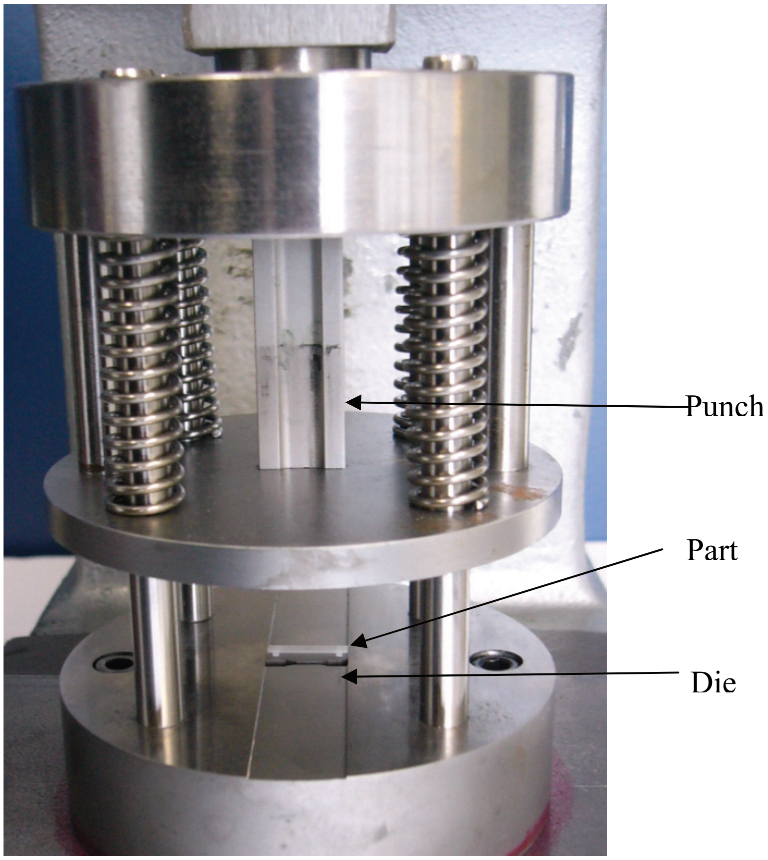

a)

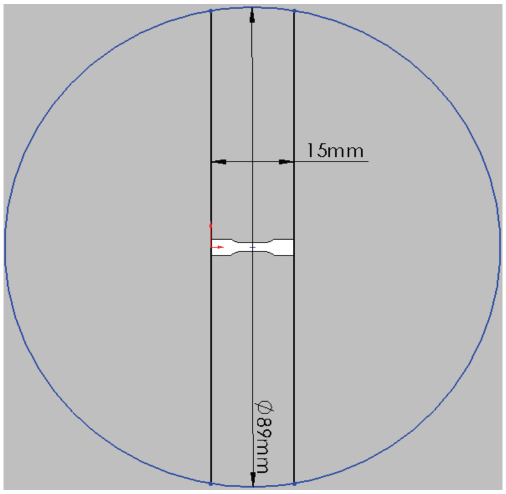

b)

Figure 4-13: a) Punch and die installed on a press; b) Top view of the die

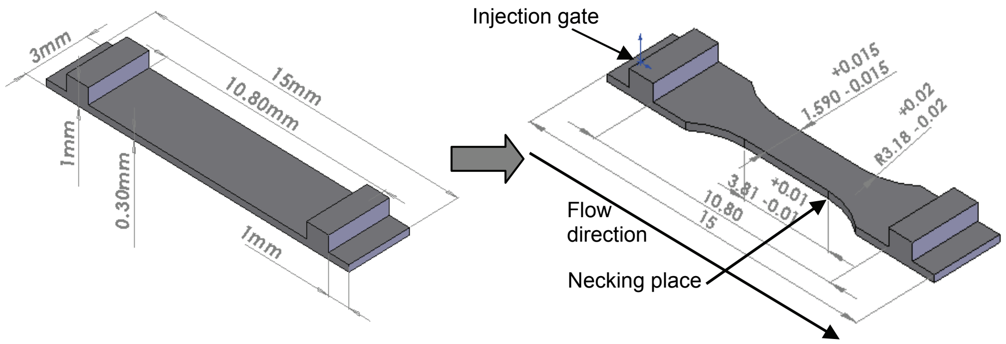

a) b)

Figure 4-14: a) Micro injection molded plate; b) Tensile test specimen by die cutting (Unit: mm)

4.4.2 Design and Fabrication of the Specimen Holder

The pneumatic side action grips installed on the Instron testing machine were self-aligning grips, which moved freely into alignment, as soon as any load was applied, so that the long axis of the test specimen coincided with the direction of the applied pull force through the center line of the grip assembly. Thus, the bending effect due to misalignment of the two grips was minimized. However, the grips were not designed to clamp small samples, as those in this study. This created problems in mounting and aligning the specimens and in the slippage between the grip and specimens.

These problems were solved by the design of a pair of specimen holders as displayed in Figure 4-15. Each holder consisted of two parts: a fixed part fitting the pneumatic grip and a movable part for easy mounting and de-mounting of specimen. The two parts were connected by two screws. The specimen holder offered the following advantages compared to conventional grips: (i) easy and accurate positioning of samples with great repeatability, (ii) elimination of slippage between specimen and specimen holder, between the two parts of the specimen holder, and between the grip and specimen holder, (iii) accurate alignment between the long axis of the test specimen and the applied pull force. A shim of 250 µm, with the shape of the movable part of the sample holder but having the space for specimen, was made and fitted between the two parts of the specimen holder, in order to tighten the specimen evenly and firmly to the degree necessary to prevent slippage between specimen and the sample holder, but not to the point where the specimen would be crushed. This design also ensures all specimens are tightened to the same extent, so that least scattering of data can be obtained.

Figure 4-16 displays the whole experimental setup after mounting the specimen. The distance between grips is around 6.8 mm, depending on the shrinkage of the part in the length direction. Because the strain was calculated by dividing the grips separating distance by the parallel gauge length, 3.81mm, the calculated strain should be greater than the real strain.

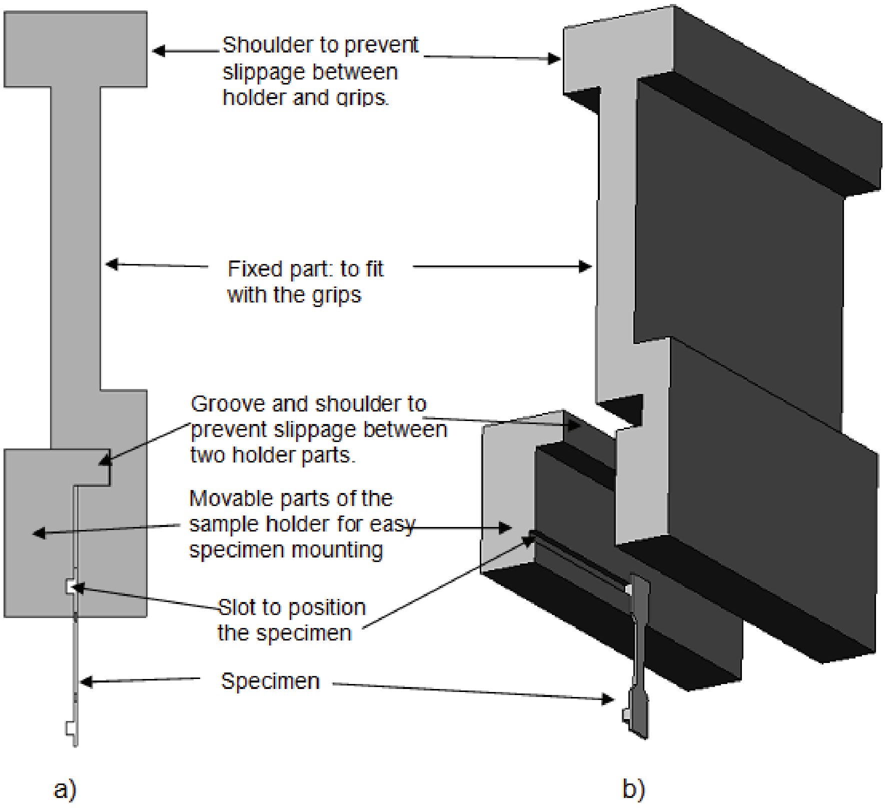

Figure 4-15: Design of the specimen holder

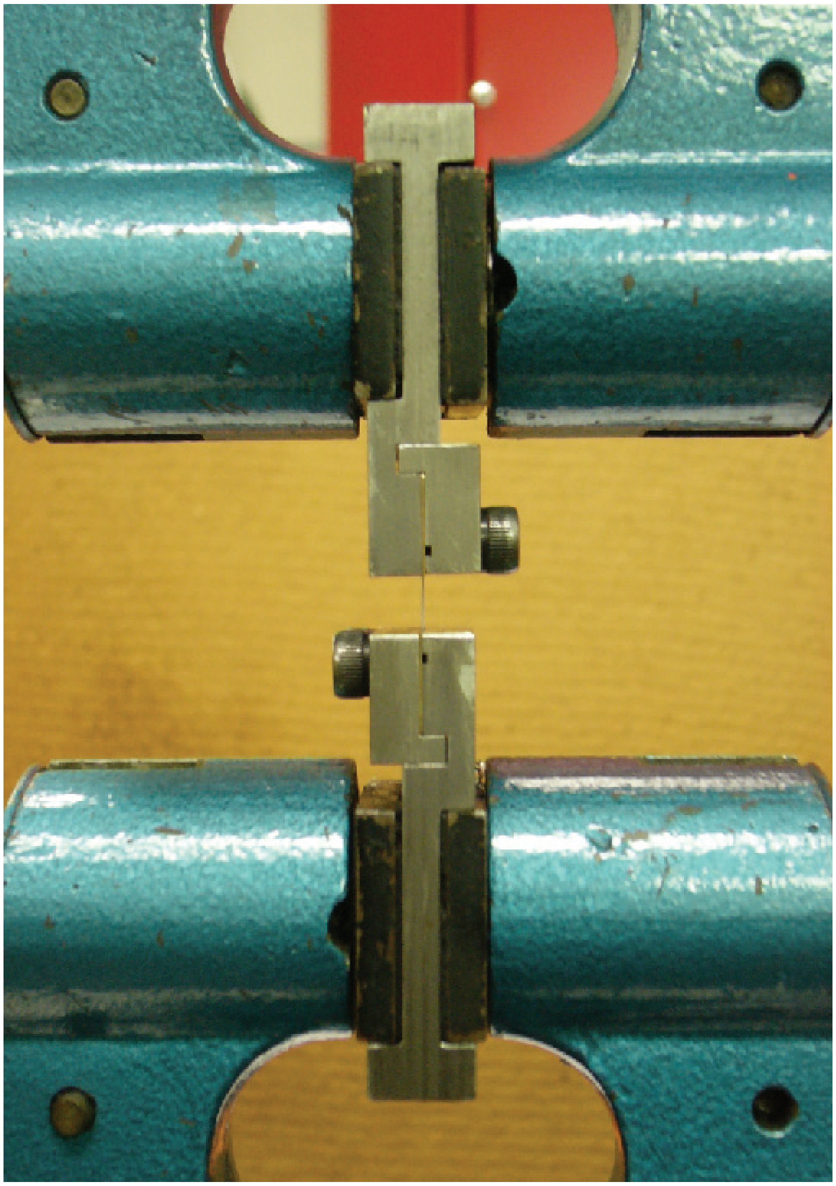

Figure 4-16: Experimental setup after mounting the specimen

4.4.3 Tensile Testing Machine

The tensile properties of the samples were measured as per ASTM D638–03 test methods [117], using the Instron Universal Machine, Model 1123. The possible test speeds ranged from 0.001 to 1000 mm/min and the speed accuracy was ± 0.05% over the range selected. A speed of 1 mm/min was selected for comparing effects of process conditions, while 0.5 and 2 mm/min were selected for comparing the effect of strain rate. The extension measurement resolution was ± 0.001 mm and the accuracy of the load weighing system was ± 0.002% of load cell capacity (10 kgf) or ± 0.5% of reading, whichever is greater. The low pass filter of the signals was turned on, in order to obtain better resolution of the low level signal in the load channel that drives the recorder. All the tests were done at a temperature of 23 ± 2ºC and 50 - 60% humidity. An Instron load cell, model A217-12 (S.N.: 0165), having full scale ranges of 10, 20, 50, 100, 200, 500 kgf, was used in the 0 -10 kgf range in conjunction with the Instron tester.

4.4.4 Mounting Procedure

Correct mounting of specimens is critical for accurate comparison among test results. The following procedures were followed closely during tensile measurements.

1. The samples were cut to obtain the designated specimen using the precision punch die, with the gate position on the sample always at left side. Then, the cut specimens were conditioned according to ASTM D618 – 05, at least 40h in the laboratory environment.
2. The two sample holders were installed onto the pneumatic grips and aligned in both the horizontal and vertical directions by contacting the two end surfaces. Then compressed air was applied to maintain the alignment.
3. The specimen was mounted onto the movable part of the upper holder by inserting the rib at the gate side into the marked position and assembling the movable part with the fixed part using two screws;

4. The movable crosshead was carefully tuned up and down to a position where the other rib of the specimen could be mounted onto the fixed part of the lower holder without applying any load to the specimen;
5. Again, the movable part was assembled with the fixed part of the lower holder using two screws.

4.4.5 Calculations

In the majority of applications of polymers, stiffness, strength and toughness are of significant practical interest. Stiffness represents resistance to deformation, while strength and toughness relate to failure. Strength is the ultimate stress which a material can withstand before it fails, whether by fracture or by excessive deformation, while toughness represents the work required to fracture a material.

The tensile strength of the samples was calculated by dividing the maximum load in Newtons by the original cross-section area of the specimen in square meters. In the present study, the yield strength is reported in Mega-Pascal (MPa) for all three materials. The specimen yield was determined by detecting the first point at which the slope of the test curve is zero since the materials under test consistently exhibited a zero slope yield. The Young's modulus was obtained from the slope of a "least squares fit" straight line, drawn through the steepest linear region of the testing curve. The steepest linear region is searched from the start of the testing curve to the yield point. The break strength and toughness are not discussed here, because these data were more scattering than the modulus and yield stress.

To obtain statistically dependable data, 5 specimens were tested for the samples from each process condition. The specimens that broke at some flaw were discarded and retests were conducted.

The standard deviation of the results for different specimens was estimated as follows:

$$s = \sqrt{\left(\sum X^2 - n\overline{X}^2\right)/(n-1)}$$

Where:

S = estimated standard deviation;

X = value of single observation;

N = number of observations, and

$\overline{X}$ = arithmetic mean of the set of observations.

4.5 Nanoindentation

The nanoindentation technique has been used widely to evaluate the mechanical behaviour of polymers and their nanocomposites [118-127]. It can provide the near-surface mechanical properties of materials, such as modulus and hardness, by applying a localized deformation on the surface of the material by a hard indenter [128-131]. In micro injection molding studies, the nanoindentation technique was used to verify skin-core morphology across the thickness of the molding [2, 26] and for measurement of surface properties of micro injection moldings with complex geometry [5].

4.5.1 Principle of Nanoindentation

The working principle of nanoindentation is similar to that of the well-established hardness test for material characterization [128, 130, 132-134]. An indenter, such as a Berkovich diamond tip, is forced into a specimen, and the size of the residual indent in the material is measured after the indenter is fully unloaded. The maximum applied load and size of the residual indent are then used to estimate the hardness of the specimen. Nanoindentation is different from the standard hardness test in two aspects. Firstly, the magnitudes of the applied loads and resulting displacements are significantly smaller. Loads on the order of micronewtons and displacements ranging from a few nanometers to one micrometer are typical for nanoindentation. Therefore, small volumes of materials can be sampled and measured. The second difference is that the displacement of the indenter is monitored continuously during the loading and unloading cycles in nanoindentation. Therefore, nanoindentation is also referred to as depth-sensing indentation.

The basic loading and unloading phase of nanoindentation are illustrated in Figure 4-17 . The output from such a nanoindentation test is a graph relating the applied load and the corresponding indenter displacement during the loading and unloading phases. The load-displacement graphs are then analyzed to estimate the mechanical properties.

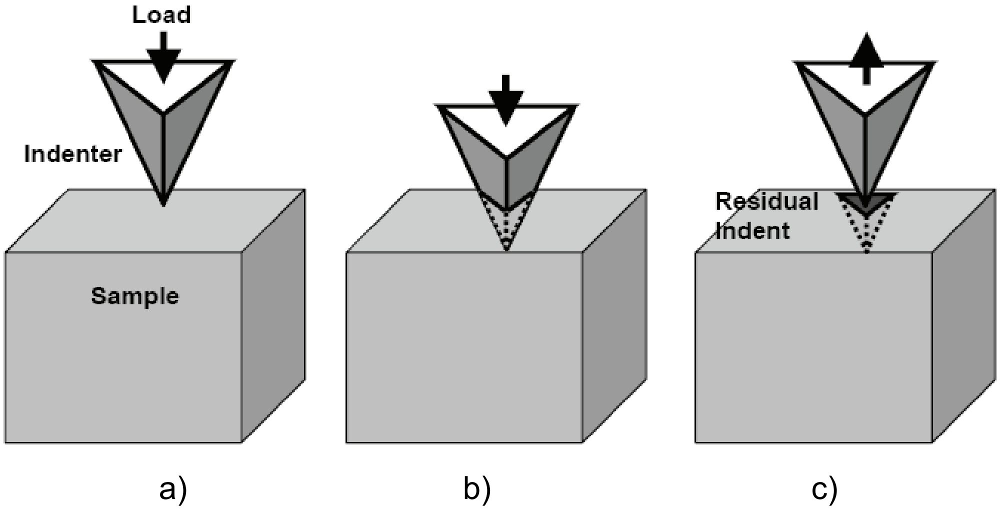

a) b) c)

Figure 4-17: A schematic illustration of the process of indenting a material. From left to right: a) a load is applied to the indenter; b) the indenter penetrates the test specimen; c) the load is removed by withdrawing the indenter out of the material. A residual indent remains in the specimen [132].

4.5.2 Nanoindenter

The commercially available Hysitron TriboIndenter [135], which permits depth-sensing nanoindentation and imaging of a specimen surface, was used in the present study for evaluating the distribution of mechanical behaviour across the thickness of the specimen.

Figure 4-18 (a) [135] displays the instrument showing both the external acoustic enclosure chamber and the electronics control panels. The chamber acts to prevent acoustic or thermal noise. Figure 4-18 (b) displays the translation stage inside the insulation chamber. The nanoindenter tip is mounted on a TriboScanner, which is capable of lateral scanning. The fine vertical motion is under control of piezoelectric and capacitive actuators. The main components of the TriboIndenter system are shown schematically in Figure 4-19 [135].

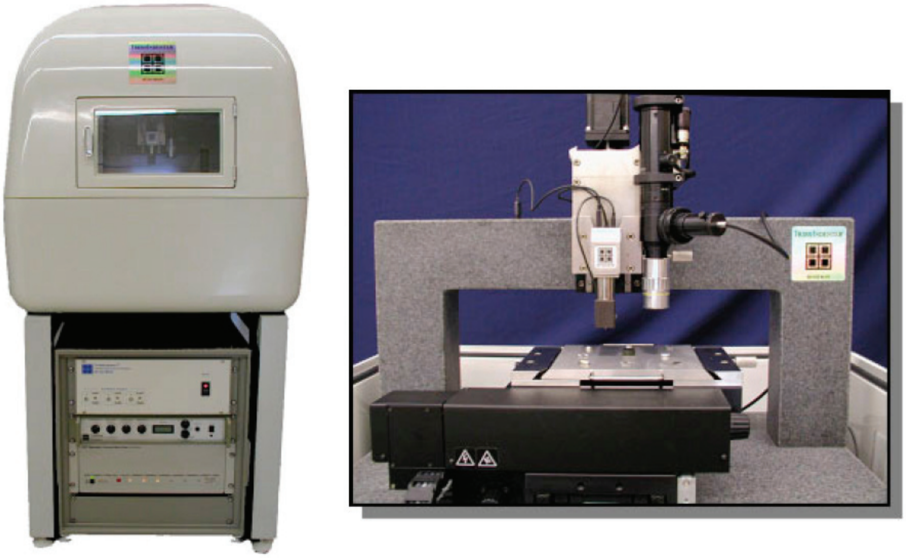

(a) (b)

Figure 4-18: The Hysitron TriboIndenter: a) The Hysitron TriboIndenter with the acoustic enclosure and control panels; b) The TriboIndenter inside the enclosure [135].

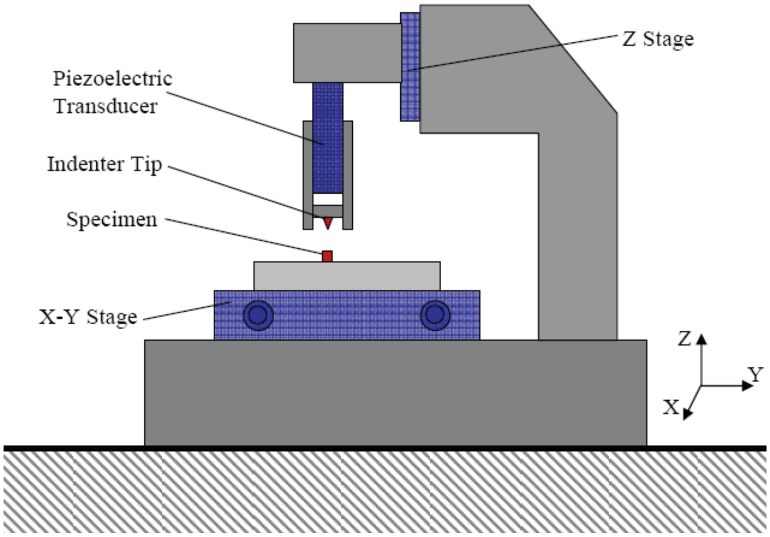

Figure 4-19: Schematic illustration of the TriboIndenter [135].

4.5.3 Design of Embedding Mold and Sample Preparation

The micro injection molded samples were initially embedded in a specially designed mold as displayed in Figure 4-20. With this mold it was possible to measure accurately the mechanical behaviour at any predefined position, in both transverse and longitudinal direction. The embedded samples were ground stepwise using ascending grit number of silicon carbide papers: 240-320-400-600-800 and then polished using polishing cloths and slurries of descending size of particles: diamond 6 μm, aluminium oxide 3 μm, 0.3 μm and 0.05 μm. The polished samples were washed with distilled water. The washed samples were then air dried at room temperature for nanoindentation test.

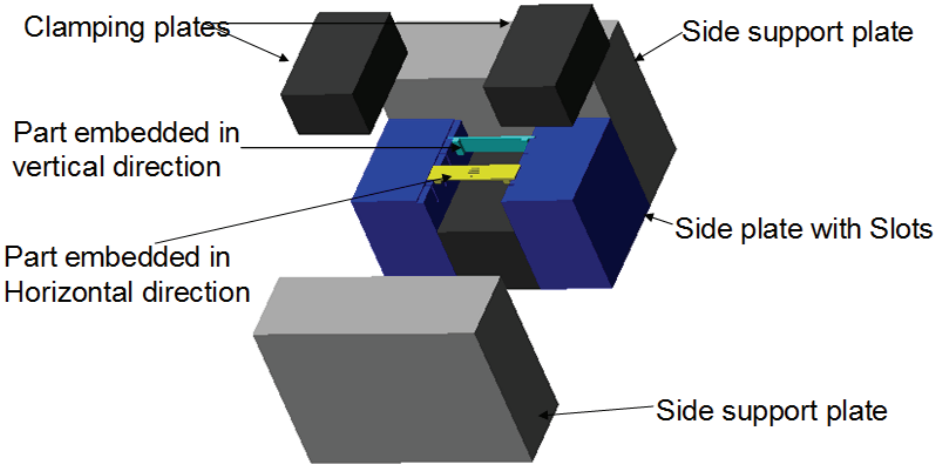

Figure 4-20: Illustration of the embedding mold and positioning of specimens

4.6 Shrinkage

4.6.1 POM

The longitudinal shrinkage between two ejection ribs in POM micro moldings were measured for each process condition, as displayed in Figure 4-21. This part of the plate, having a designed dimension of 10.80 mm, was constrained in its own plane by both the mold wall and two slots forming the two ribs. Five samples were selected for measuring the shrinkage for each process condition, and the average and standard deviation were calculated.

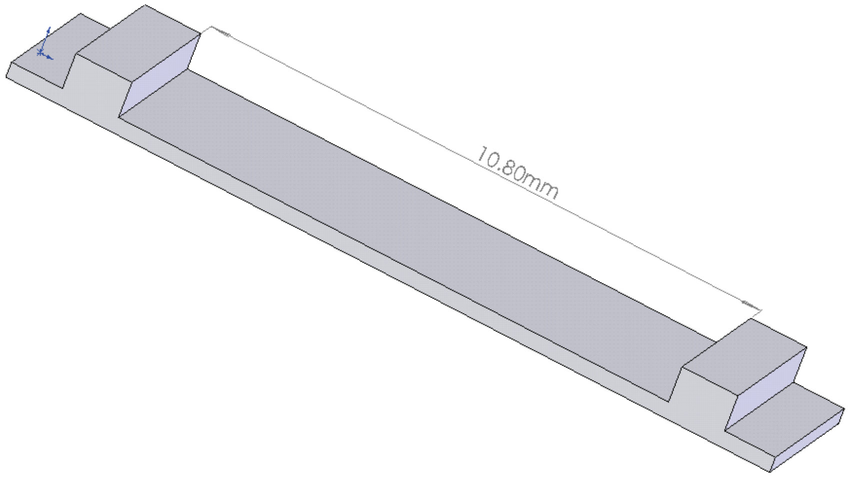

Figure 4-21: The longitudinal shrinkage measuring positions for POM samples

4.6.2 HDPE (Escorene HD-6719)

The three dimensional shrinkage of part I manufactured with Escorene HD-6719 was measured, as shown in Figure 4-22. The total shrinkage in the x direction was measured between the injection end and cavity end of the sample plate. Measurements of total shrinkage in the y direction were made at positions from A to G. The shrinkage in the z direction was measured at positions H, K, and I, where the measuring rod of the micrometer was placed (Mitutoyo Electronic Outside Micrometers, Mitutoyo Corporation). The shrinkage at each position in the Y and Z directions were measured for ten samples.

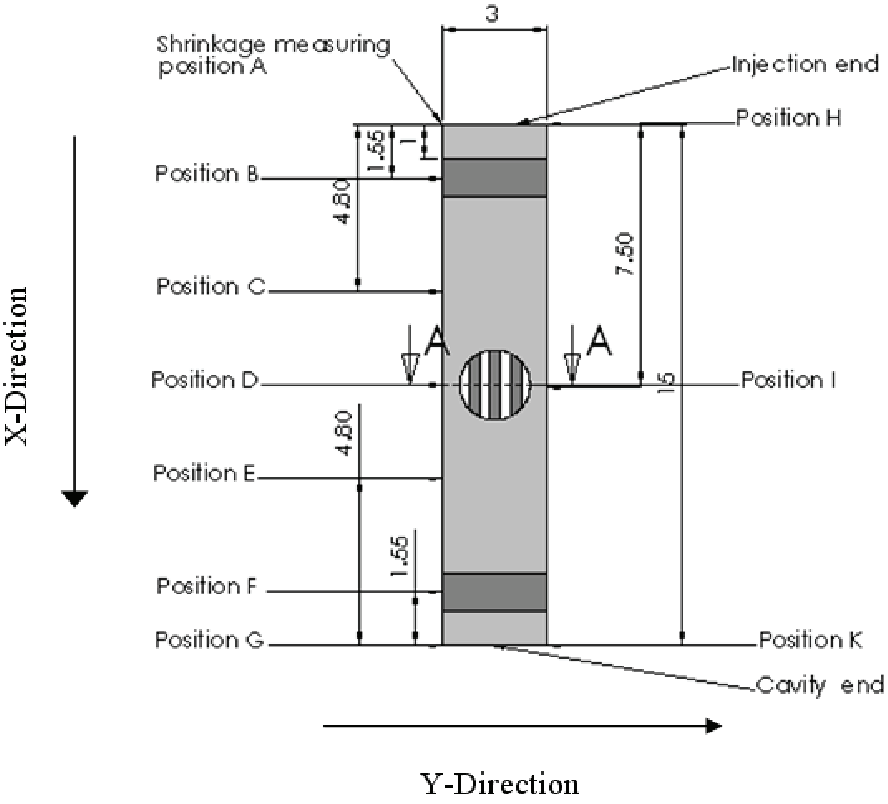

Figure 4-22: Top view of sample plate and its shrinkage measuring positions (Unit: mm)

5. MODELING AND SIMULATION

Commercial Moldflow 6.0 software (donated by Moldflow Pty, Australia) was employed for analyzing the flow and thermal behaviour of the melt during the micro injection molding process. Commercial 2-D and 3-D meshes were employed in conjunction with MOLDFLOW. MOLDFLOW fusion mesh modeling provides more outputs, but the 3-dimensional mesh possibly yields a more accurate description of the process.

5.1 Geometrical modeling and mesh generation

The first geometry shown previously in Figure 4-4 (a) was meshed in both 2D and 3D, as shown in Figure 5-1, and simulations are compared between Moldflow 2D fusion mesh and 3D analysis. For the second geometry without the hole, only 3D analysis was carried out. In order to describe the flow and thermal behaviour of the polymer melt more accurately, the gate and runner system were integrated with the part in the CAD model and meshed with tetrahedral elements, as shown in Figure 5-2. The modeling and simulation of the first geometry were performed for HDPE (Escorene 6719). For the second geometry, the modeling and simulation were only performed for POM, with the experimental data from case 1.

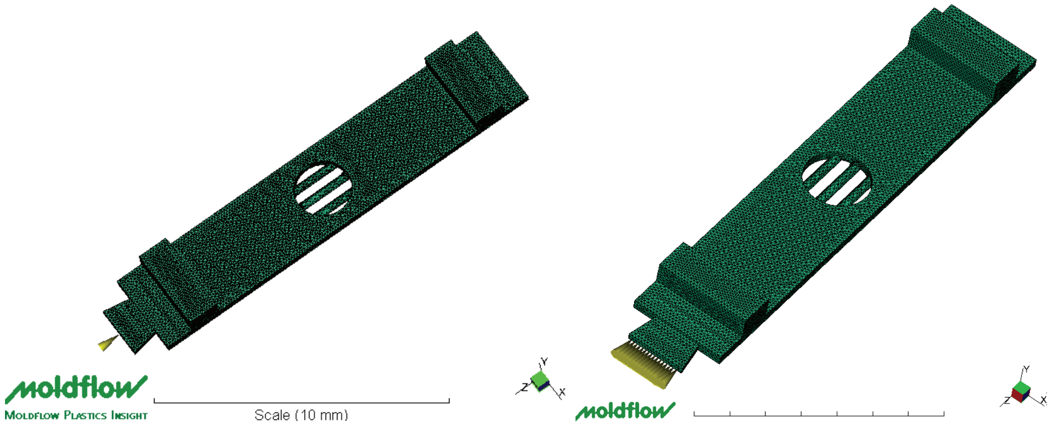

(a) (b)

Figure 5-1: Mesh of part I: (a) 2D fusion mesh; (b) 3D solid mesh

As shown in Figure 5-2, the crossed square of the four branch runners was selected as the sprue. Each node in this square was selected as an injection location, and the simulated area of injection was the area surrounding the selected 286 injection locations.

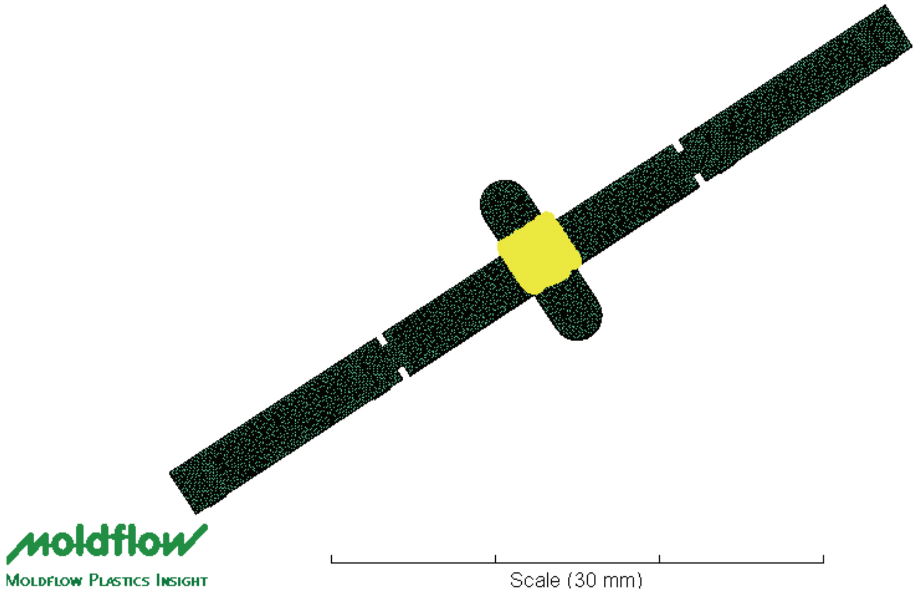

Figure 5-2: 3D solid mesh of integrated molding system (including runner system and gate)

5.2 Modeling and Simulation

The governing equation used in Moldflow and the assumptions applied for the material properties are introduced in Appendix B.

The material data for Escorene HD-6706.19, which is similar to HD-6719, were used in the 2D and 3D modeling studies for the first geometry, because these data were available in the Moldflow database. The material data for Delrin 900P NC010, verified by Moldflow, were selected for the 3D modeling of the second geometry.

The modeling of the first geometry for HDPE (Escorene 6719) covered both the filling and packing stages. The mold surface temperature, melt temperature, and flow rate were set at 50 ºC, 220 ºC, and 11.74 cm^3/s, respectively.

For the modeling and simulation for case 1 of POM (Delrin 900P), the coupled 3D solver was selected. With this solver, flow was modeled in 3D meshes, using Navier-Stokes equation. The process parameters in the software were set according to the machine variables and estimated process data as follows:

(a) Mold surface temperature: 70 ºC;
(b) Melt temperature: 205 ºC;
(c) Mold material: Tool steel P-20;
(d) Filling control: the estimated %Flow rate vs. %shot volume curve from the trace data of the injection plunger (solid line in Figure 5-3), was used as the filling profile in Moldflow for simulation; the nominal flow rate was 12.8 cm^3/s.

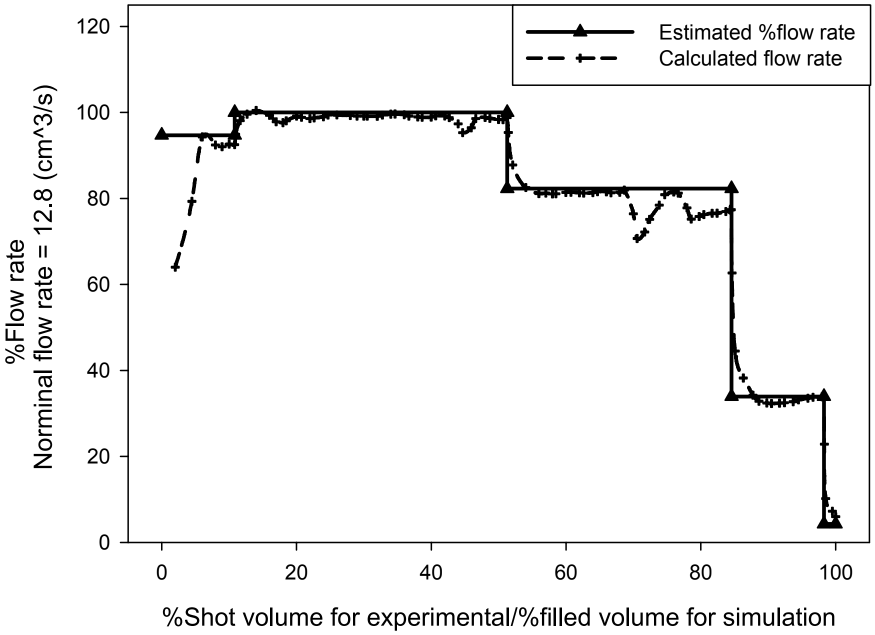

Figure 5-3: Estimated experimental cavity filling flow rate and simulated results

6. RESULTS AND DISCUSSION

6.1 Process Characterization

6.1.1 POM

Figure 6-1 shows typical injection pressure trace data for typical molding cycles for each of the selected process conditions for POM experiments. These curves exhibited different characteristics corresponding to machine settings. Higher peak injection pressure during the filling stage was observed for the process conditions at higher injection speed, i.e., cases 3, 4, 5 and 6. Higher injection pressure in the packing stage was observed, when higher packing velocity was employed, i.e., case 2, 3, 6, and 7.

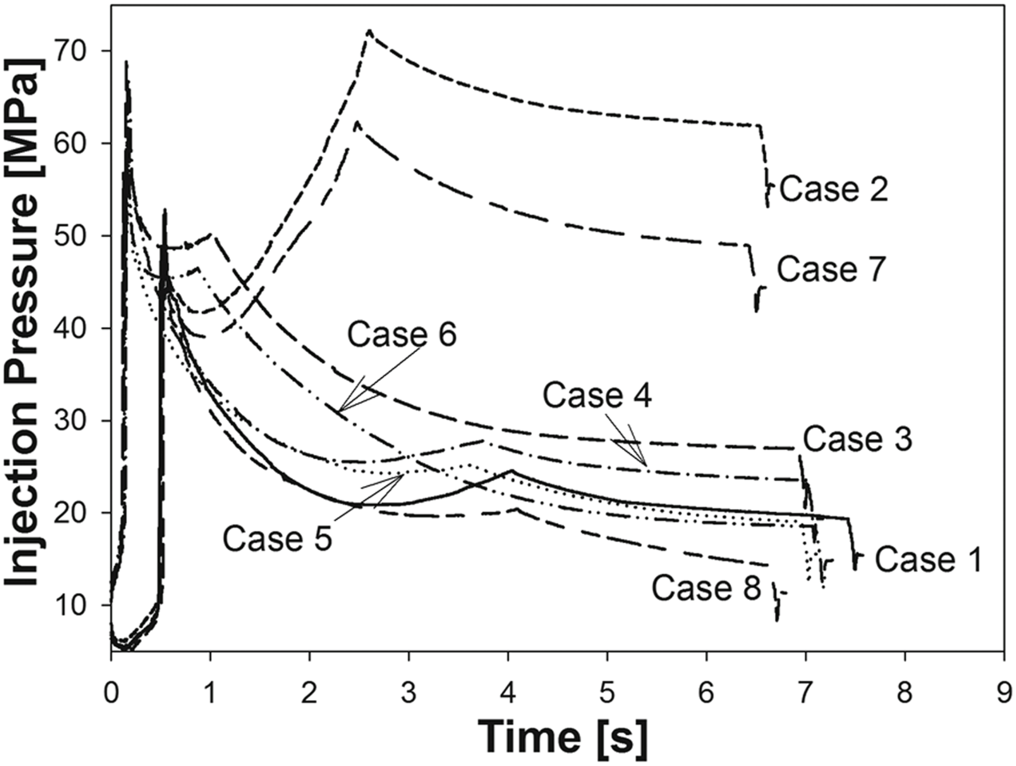

Figure 6-1: Injection pressure traces of the molding cycle at eight processing conditions; Material: POM.

Figure 6-2 displays the mean values and standard deviations of peak injection pressure, average injection pressure, average plunger velocity of the filling stage, and metering size for each process condition for the POM experiments. The estimated average plunger velocities during filling ranged from 374 mm/s to 697 mm/s, which were higher than the injection speed setting, due to the exclusion of the static sub-stages. The average plunger velocities were generally higher for high injection speed settings than for low injection speed settings. At the same injection speed setting, the average plunger velocities at high mold temperature were higher than those for low mold temperature. This is probably because of the low viscosity of the material at high mold temperature.

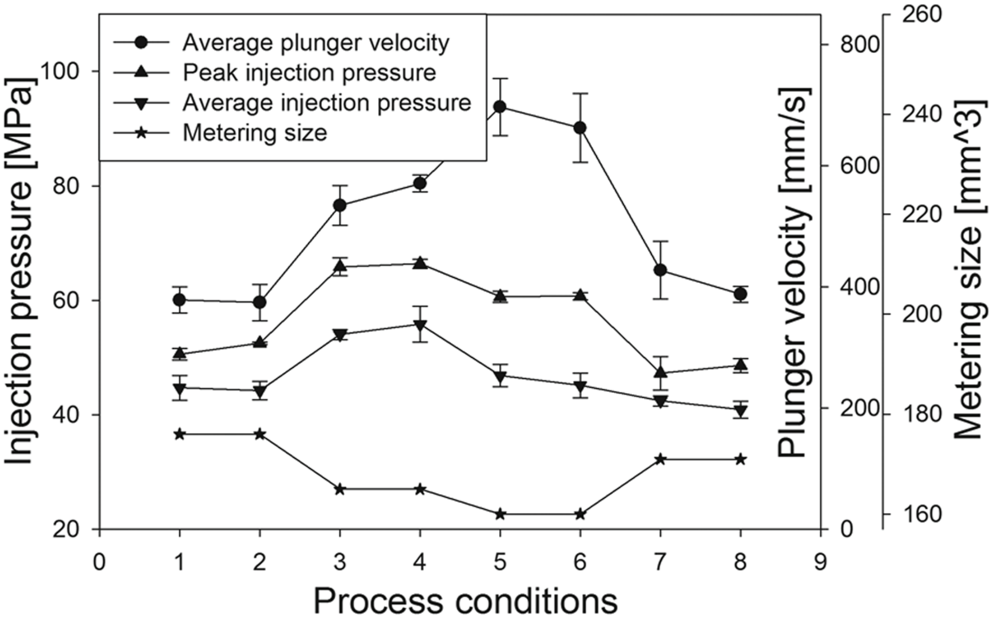

Figure 6-2: Characteristics process parameters of the filling stages for each process condition for POM experiments

The peak injection pressure and average injection pressure during filling followed approximately a similar pattern, in which the high values were associated with high injection speed and low mold temperature. The injection pressure was controlled to permit reaching the injection speed setting, so it was directly related to the flow resistance or the viscosity of the material.

The metering size decreased with increasing mold temperature and injection speed, and the highest metering size was required for the case with low injection speed and low mold temperature. This suggests that the metering size was mainly determined by the average material temperature, which is attributed to both shear rate and heat transfer between the mold surface and the melt. Higher metering size indicates that more material was injected into the cavity during the filling stage.

Figure 6-3 displays the standardized effects of the machine variables and their interactions on the CPPs of the filling stage. Injection speed was the major positive factor in affecting average plunger velocity, peak injection pressure, and average injection pressure, while it was the major negative factor in affecting metering size. An increase in injection speed resulted in an increase in all CPPs, except the metering size which decreased. The mold temperature was another factor that had a considerable effect on the CPPs. An increase in mold temperature resulted in an increase in average plunger velocity, but decreases in the other three parameters. Injection speed/mold temperature interaction had noticeable effects, which are similar to those of the mold temperature, but to a smaller extent. The other interactions of injection speed/packing velocity and packing velocity/mold temperature are not discussed because of process data variability.

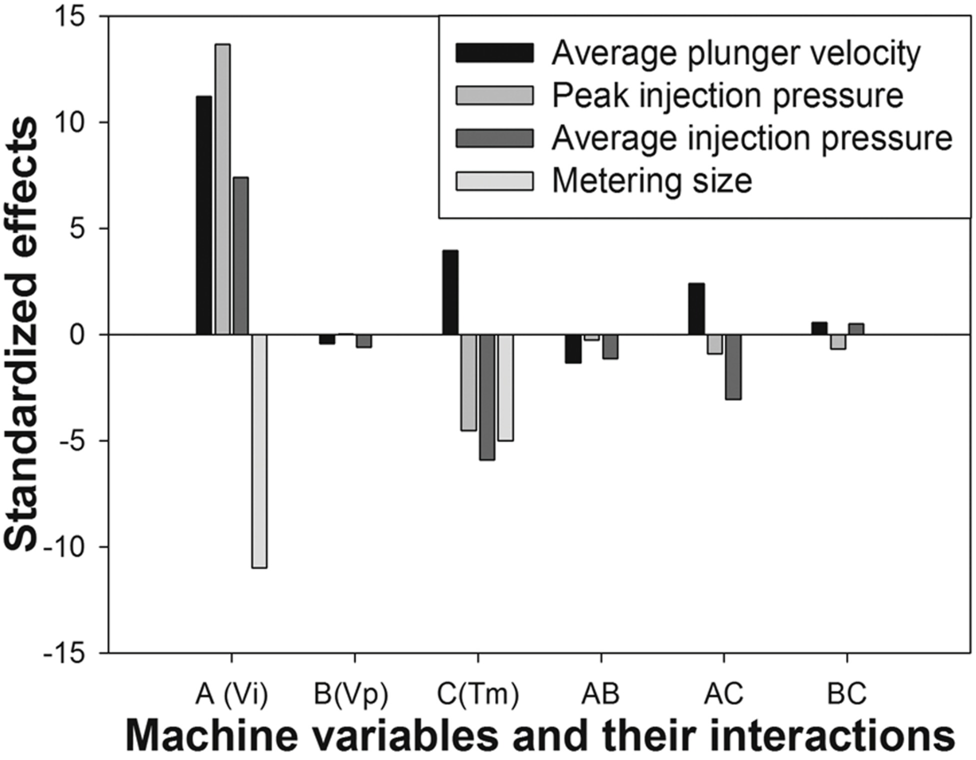

Figure 6-3: Standardized effects on the characteristic process parameters of the filling stage for POM experiments

Figure 6-4 displays the patterns of plunger stroke at 0.2s packing, total plunger stroke, and average injection pressure during 0.2s packing for each process condition for POM experiments. The plunger stroke at 0.2s of packing, representing the effective compensation for material shrinkage before gate freezing, was generally higher at high injection speed than at low injection speed. The total plunger stroke during packing, calculated from the difference between switch-over position and last position of the plunger, varied in a narrow range, for the process conditions of high injection speed or high packing velocity. The minimum total plunger stroke during packing was found at low injection speed and low packing velocity, i.e., case 1 and case 8. The average injection pressure during 0.2s of packing can be regarded as an extension of the injection pressure during filling, as both followed approximately a similar pattern.

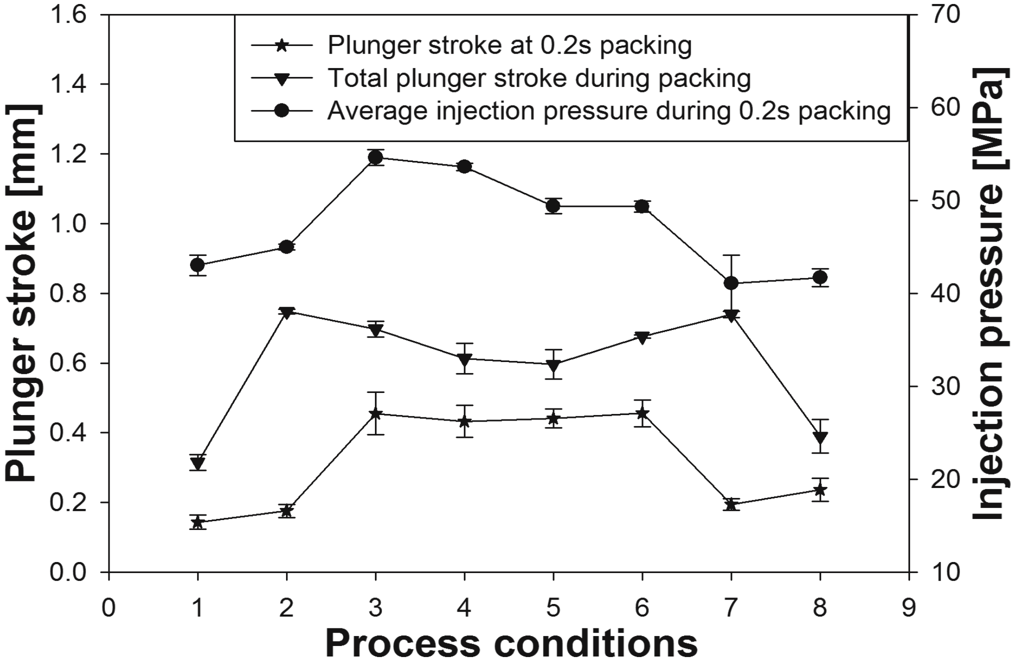

Figure 6-4: Characteristic process parameters of packing stage for each process condition of POM experiments

Figure 6-5 displays the standardized effects of the machine variables and their interactions on the CPPs of the packing stage. Injection speed was the major positive factor in affecting plunger stroke and average injection pressure at 0.2s packing, but it was a minor positive factor in affecting total plunger stroke during packing. The packing velocity was the major positive factor affecting the total plunger stroke during packing. The mold temperature had a considerable negative effect on the average injection pressure during 0.2s packing. This was probably due to the decrease of the material viscosity in the runner system and cavity with increasing mold temperature.

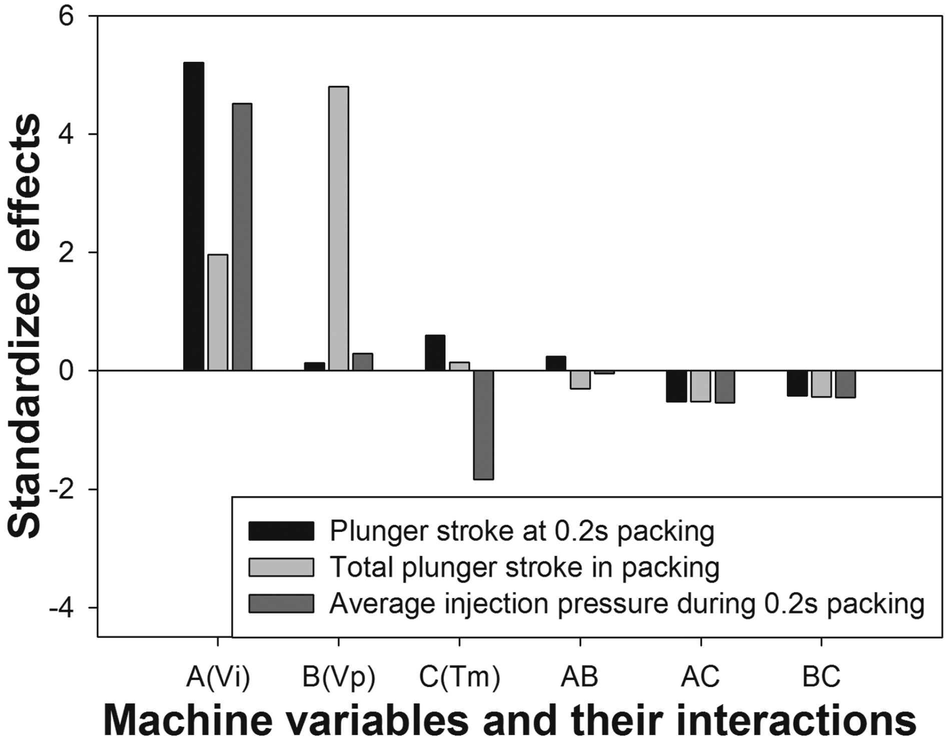

Figure 6-5: Standardized effects on the CPPs of packing stage for POM experiments

The coefficients of variation (COV) of the six CPPs defined for both the filling and packing stages are presented in Figure 6-6 to evaluate the process repeatability. Overall, the process conditions associated with higher injection speed exhibited better repeatability than those of low injection speed. The peak injection pressure during filling and average injection pressure during 0.2s packing had better repeatability than other CPPs. Plunger stroke at 0.2s packing had the highest COV at around 15%. This was probably due to the small absolute value of the plunger stroke at the 0.2s. The COVs for the other CPPs are comparable to the results for peak cavity pressure and cavity pressure curve integral reported by Whiteside, Martyn, and Coates [32] for a 23 mg product. The COVs of the average plunger velocity, ranging from 2.43% to 11.2 %, indicates the validity of both Equation 4-1 and the methodology used to describe the filling stage.

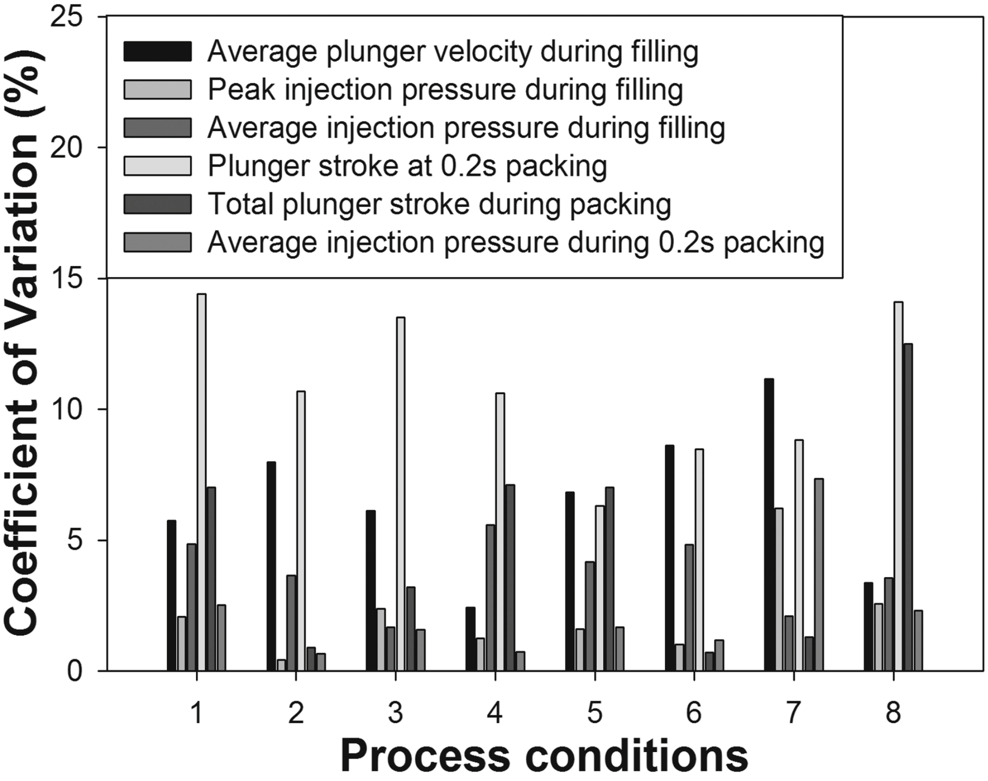

Figure 6-6: Coefficient of variation of the CPPs for POM experiments

6.1.2 HDPE (Sclair 2714)

Figure 6-7 displays average plunger velocity, peak injection pressure, and average injection pressure during the filling stages, and metering sizes for each process condition for HDPE experiments. The estimated average plunger velocities during filling ranged from 401 mm/s, at the low injection speed setting, to 965 mm/s, at the extremely high injection speed setting. Generally, at the same injection speed setting and comparable mold temperature setting, the injection pressure of HDPE was lower than for POM, but the average plunger velocity was higher than for POM. This was probably because the HDPE (Sclair 2704) has a much higher melt flow index. The average plunger velocity during filling and the peak injection pressure generally followed similar patterns, which are mainly determined by the injection speed setting. The only exception to this pattern was case

11, which had extreme high injection speed, high mold temperature but low melt temperature. At the same extreme high injection speed, the peak injection pressure and average injection pressure during the filling for case 11 were significantly lower than for case 10, which had low mold temperature and high melt temperature. It seems that the mold temperature at the extreme high injection speed changed the flow behaviour significantly. The patterns of peak injection pressure and average injection pressure during filling for HDPE were not similar to those for POM experiments. The lowest metering sizes were required for cases 1 and 3, which had high injection speed and high melt temperature. The highest metering sizes were required for case 6, which had the low settings of injection speed, mold and melt temperature.

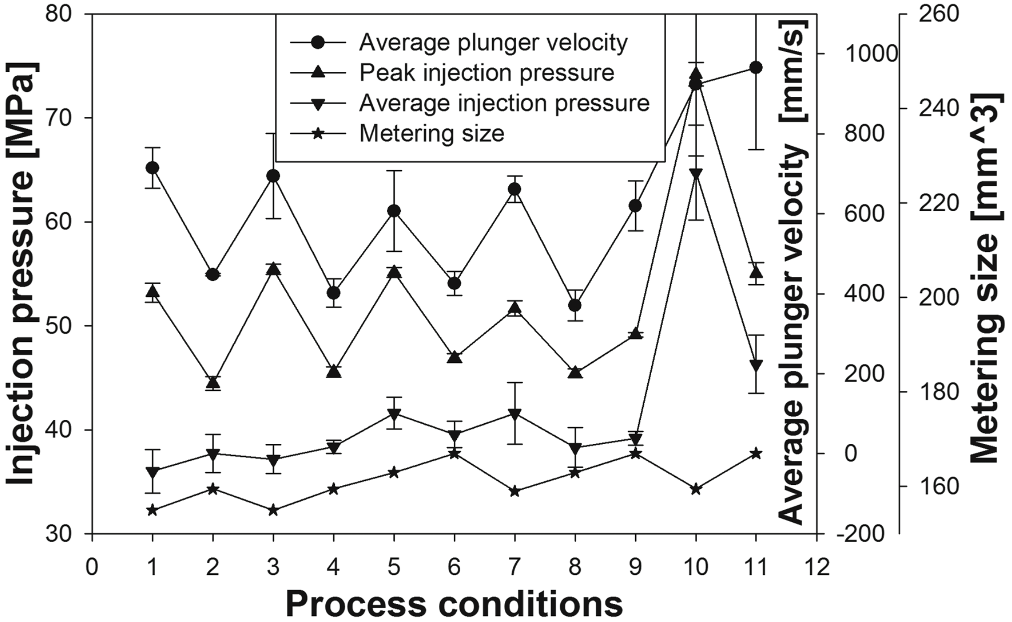

Figure 6-7: CPPs of the filling stage at each process condition for HDPE experiments

Figure 6-8 displays the standardized effects of the machine variables and their interactions on the CPPs for the filling stage of HDPE. Injection speed was the major positive factor in affecting peak injection pressure and average plunger velocity, and was also a minor negative factor in affecting metering size. Melt temperature was the major negative factor in affecting average injection pressure and metering size, and was also a minor positive factor in affecting average plunger velocity. Mold temperature had noticeable negative effects on peak injection pressure and metering size. Since the DOE design of HDPE was a resolution IV design, the interaction of two machine variables was always confounded with interaction of the other two machine variables. High resolution design is needed in order to make confident conclusions with regard to the interactions between two machine variables.

The above analysis results were confirmed with the additional experiments of cases 9 and 10, but large discrepancies appeared in case 11.

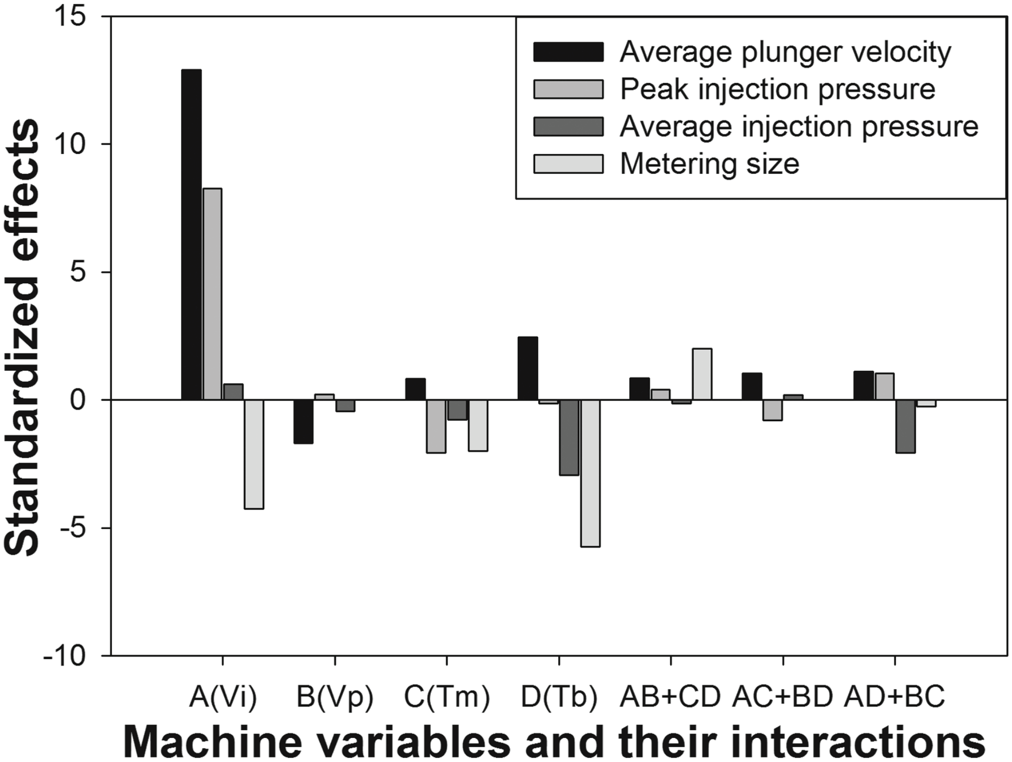

Figure 6-8: Standardized effects on the CPPs of filling stage for HDPE experiments

Figure 6-9 displays the CPPs for the packing stage for each process condition of HDPE experiments. The plunger stroke and average injection pressure at 0.2s packing approximately followed a similar pattern, which was mainly determined by the injection speed. The lowest total plunger strokes were found for case 2 and case 6, which had the low injection speed and low packing velocity. At the extreme high injection speeds of cases 10 and 11, the plunger reached the end of its stroke within 0.2s of the packing stage, so the plunger stroke at 0.2s packing were equal to total plunger stroke.

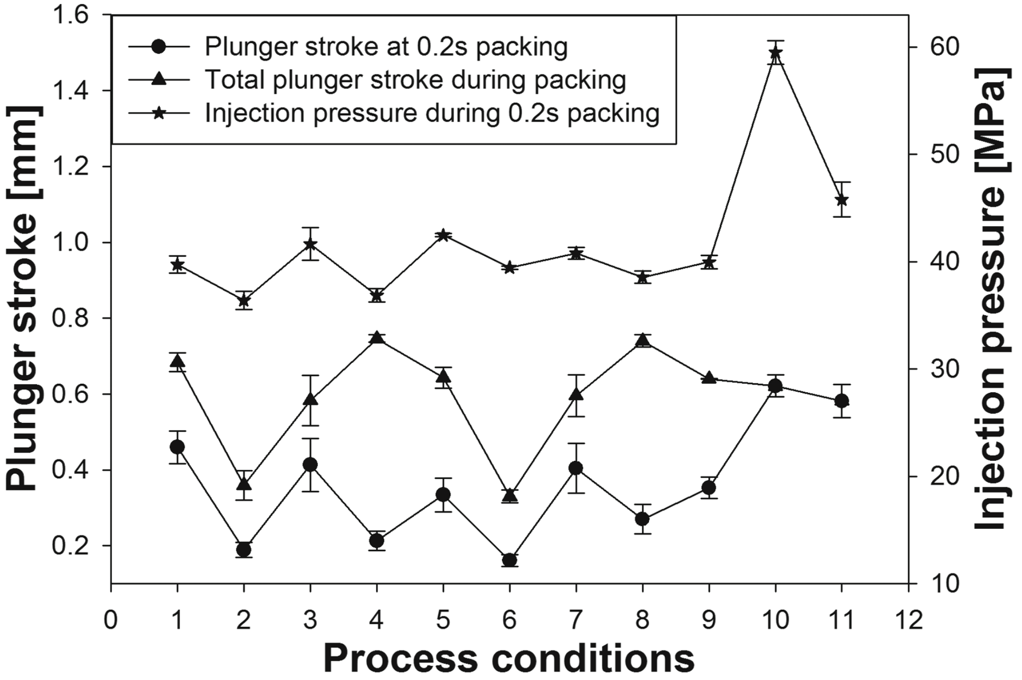

Figure 6-9: CPPs of the packing stage at each process condition for HDPE experiments

Figure 6-10 displays the standardized effects of machine variables and their interactions on the CPPs of the packing stage for HDPE experiments. Injection speed was the major factor in affecting plunger stroke and average injection pressure at 0.2s packing, and it was also a minor factor in affecting total plunger stroke. Packing velocity was the major factor in affecting the total plunger stroke. The mold and melt temperature had similar effects on the three selected CPPs, with significant negative effects on average injection pressure and minor positive effects on the plunger strokes at 0.2s packing. The interaction injection speed/packing velocity, which was confounded with the interaction mold temperature/melt temperature, had a significant negative effect on total plunger stroke. Since both the injection speed and the packing velocity had more significant effects than mold and melt temperatures, the injection speed/packing velocity interaction should also be more significant [3, 136]. It can therefore be concluded with a high confidence level that it is the injection speed/packing velocity interaction, which has the significant negative effect on total plunger stroke during packing.

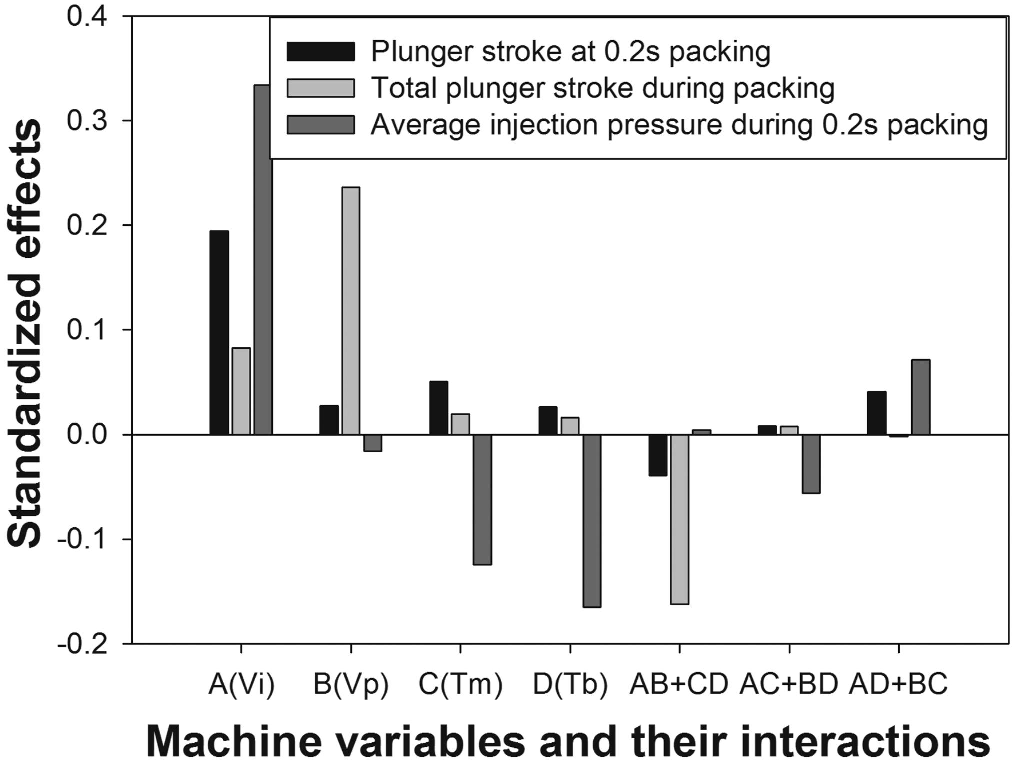

Figure 6-10: Standardized effects on CPPs of packing stage for HDPE experiments

The coefficients of variation of the six CPPs are presented in Figure 6-11 to evaluate the process repeatability for polyethylene experiments. In contrast with the POM experiments, the process conditions of low injection speed setting exhibited better repeatability than those of higher injection speed. In terms of CPP repeatability, the peak injection pressure during filling and average injection pressure during 0.2s packing had the better repeatability compared to other CPPs, as in the case of POM experiments. Again, the plunger stroke at 0.2s packing had the highest COV at around 20%.

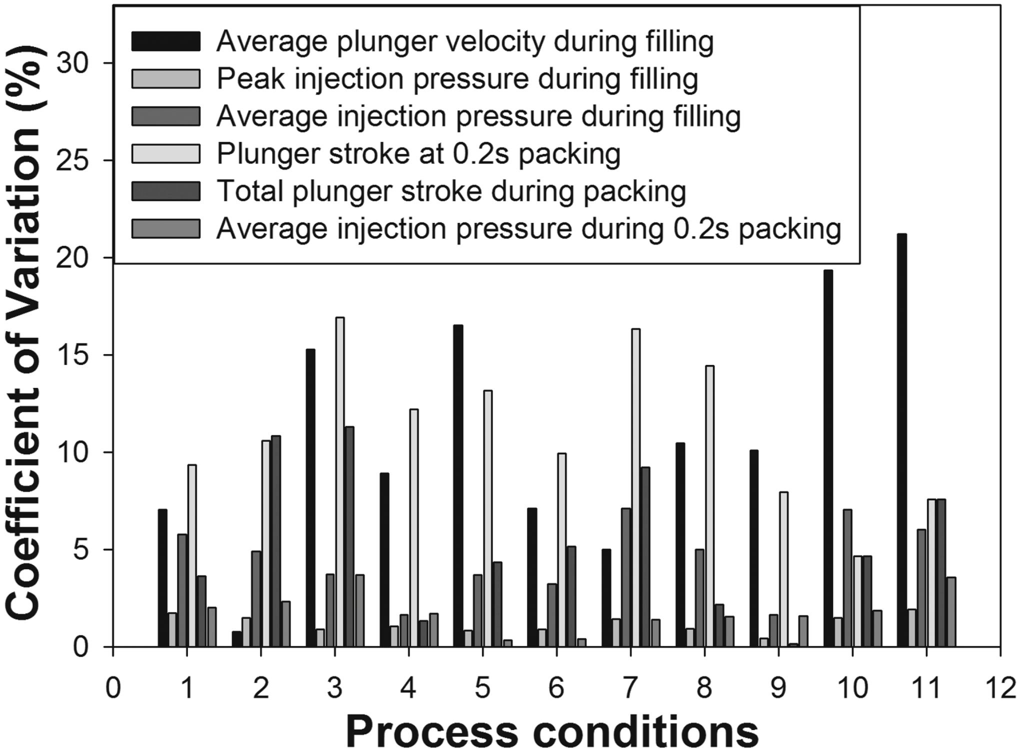

Figure 6-11: Coefficients of variation of the CPPs for each process condition of HDPE experiments

6.1.3 PC

When the injection speed was set at 700 mm/s in the PC experiments, the switch-over position could only stabilize at 0.5 mm or 0.6 mm rather than 0.8 mm as in the case of lower injection speed setting. This was probably caused by the high inertia of the plunger at the high injection speed. A higher metering size may be required for the later switch-over position.

Figure 6-12 displays average plunger velocity, peak injection pressure, and average injection pressure for the filling stages, and metering size for each process condition for PC experiments. The average plunger velocities were generally higher for high injection speed settings than for low injection speed settings. However, at the same injection speed setting, the average plunger velocities at high mold temperature tended to be lower than for low mold temperature. This was different from both POM and HDPE experiments, where the mold temperature was a positive factor in affecting the average plunger velocity. Both peak injection pressure and average injection pressure varied in a narrow range. The peak injection pressure tended to be higher at low mold temperature, while the average injection pressure tended to be higher at high mold temperature. The trend of peak injection pressure could be responsible for the variation of average plunger velocity with mold temperature. These variations are probably related to the machine control mechanism employed in the micro injection molding machine used in this study.

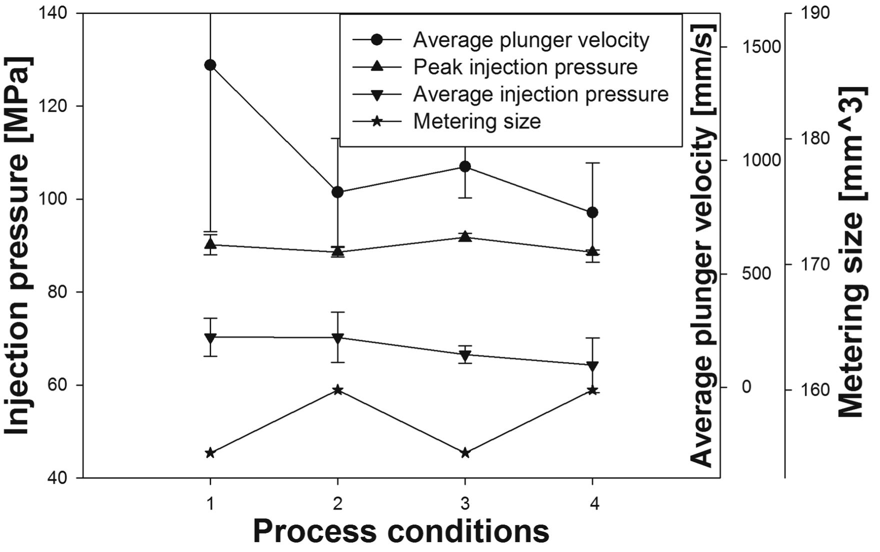

Figure 6-12: CPPs of packing stage for each process condition of PC experiments

Figure 6-13 displays the standardized effects of the machine variables and their interactions on the CPPs during the filling stage for PC. Injection speed was the most significant factor in affecting peak injection pressure, average plunger velocity and metering size. The mold temperature was the most significant negative factor in affecting average injection pressure during filling, and the minor negative factor in affecting average plunger velocity.

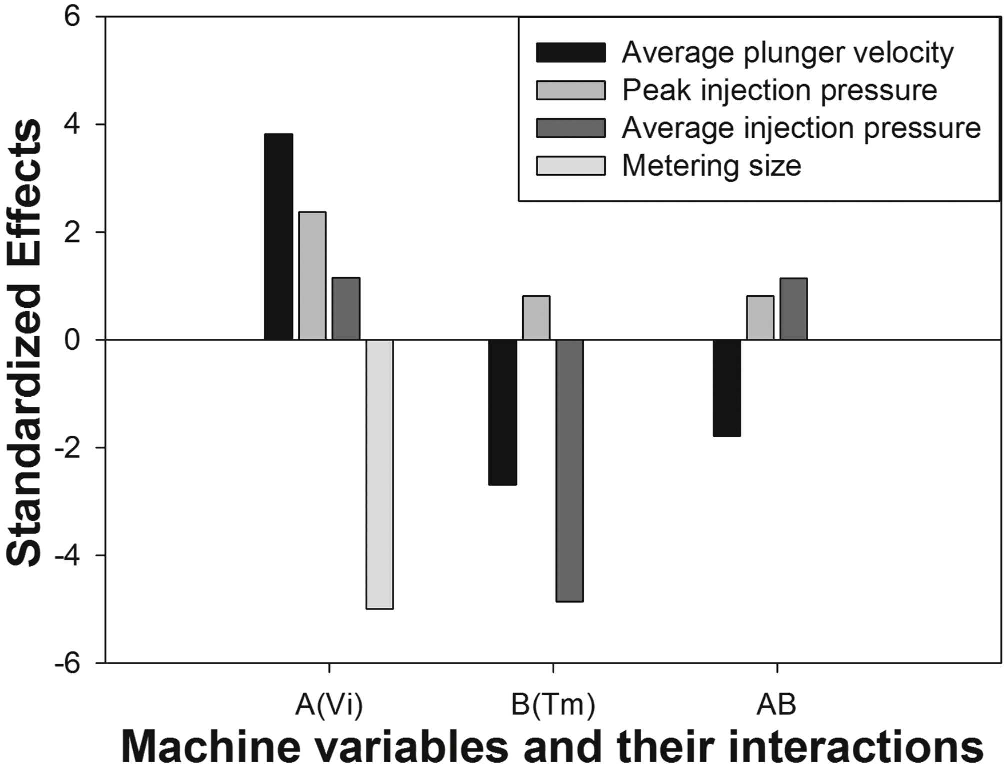

Figure 6-13: Standardized effects on the CPPs of filling stage of PC experiments

Figure 6-14 displays plunger stroke at 0.2s packing, total plunger stroke, and average injection pressure during 0.2s packing for each process condition for PC. The average injection pressure during 0.2s packing mainly depends on injection speed setting. According to Figure 6-15, injection speed was the dominant factor in affecting all three characteristic process parameters in the packing stage of PC experiments.

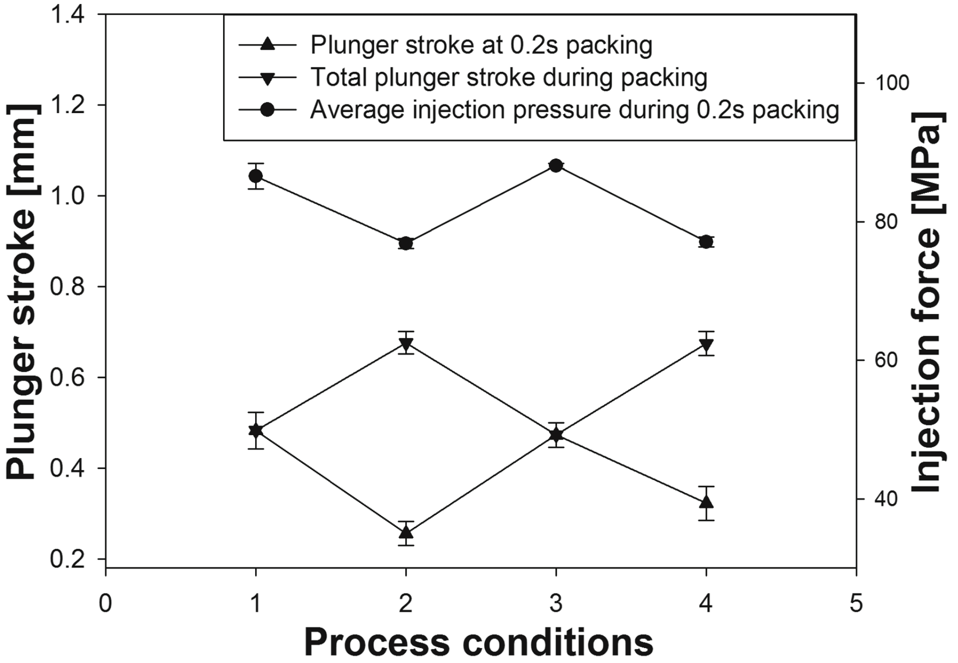

Figure 6-14: CPPs of the packing stage for each process condition for PC experiments

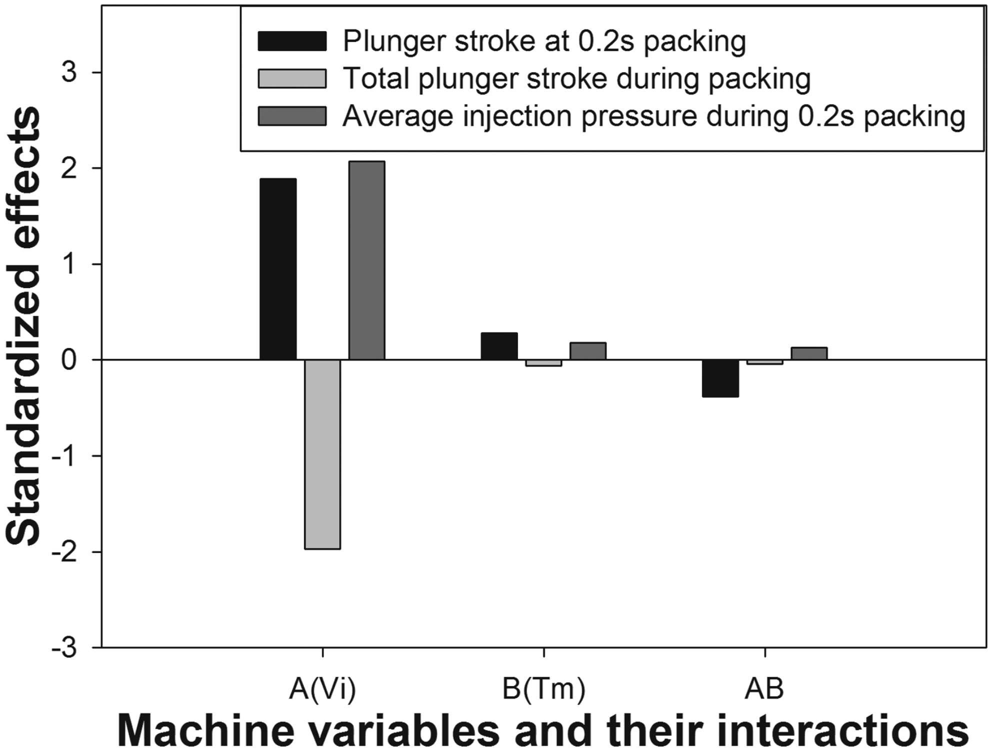

Figure 6-15: Standardized effects on the CPPs during the packing stage for PC experiments

The coefficients of variation of the six CPPs are presented in Figure 6-16 to evaluate the process repeatability. PC case 3, with high injection speed and high mold temperature was found to have the highest repeatability. In terms of CPPs, again the peak injection pressure and average injection pressure during 0.2s packing had the better repeatability over other CPPs. The average plunger velocity during filling was much noisier than other CPPs, probably due to the high injection speed setting.

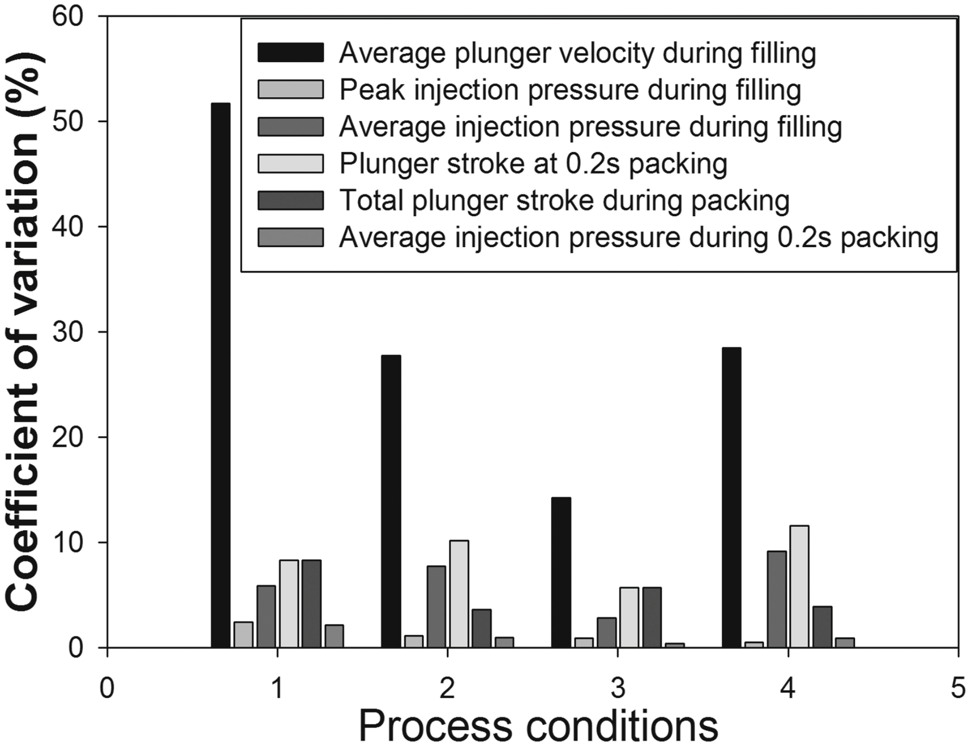

Figure 6-16: Coefficient of variation of the CPPs for each process condition for PC experiments

6.2 Simulation Results

6.2.1 POM (Delrin 900P)

6.2.1.1 Injection pressure

The simulation was conducted using the estimated experimental %flow rate vs. %shot volume curve as the filling control profile, as shown in Figure 5-3. Figure 6-17 shows a comparison between the calculated injection pressure and the recorded experimental injection pressure. The calculated injection pressure features two peaks during cavity filling, corresponding to changes of %flow rate in the simulation, as shown in Figure 6-17.

During the cavity filling stage, the calculated injection pressure varied in a range from around 10 MPa to around 100 MPa, while the experimental injection pressure varied in a much narrower range from around 43 MPa, to 51 MPa. The calculated highest injection pressure was around twice as high as the highest measured injection pressure during the cavity filling stage. The big discrepancy could be attributed to the hydrodynamic characteristics of microscale and nanoscale polymer flows, such as slippage at polymer-mold, liquid-solid, and polymer-polymer interfaces [27], which are not considered in the current commercial software developed for conventional injection molding.

The filling time in the simulation was shorter than the experimental filling time, because of both the smaller volume of the simplified geometry for high mesh quality and the higher interpolated value of flow rate at the position close to the end of filling profile, as shown in Figure 5-3.

In the following discussion, results will be considered mainly for the cavity filling stage, after the melt arrives at the gate.

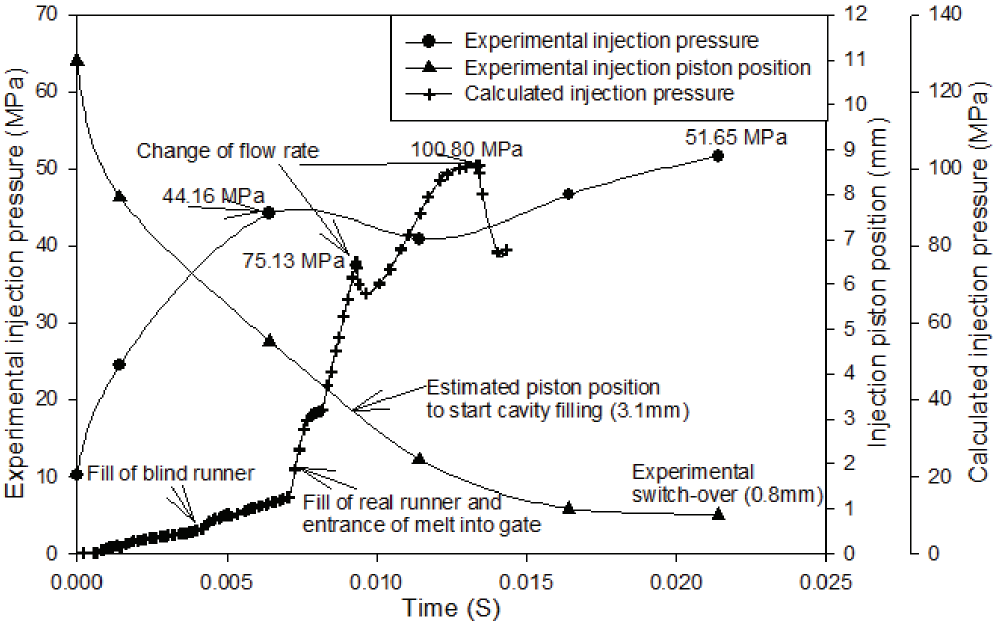

Figure 6-17: Calculated pressure at the injection location vs. measured injection pressure

6.2.1.2 Extension rate

Figure 6-18 displays the calculated extension rate distribution across the thickness in the middle of gate at 0.0090s filling time. The extension rate represents the amount of elongation the polymer undergoes as it passes through a change in thickness. In injection molding, the extension rate is more dependent on flow rate and geometry than the material property, which may influence the extension rate.

In the gate region, where the flow rate is high and the thickness change is large, the extension rate is strongest. When the extension rate is higher than 200 1/s, the effects of extension viscosity need to be considered [137]. The extension viscosity model used in Moldflow commercial software is given by Equation 6-1 and Equation 6-2.

$$\overline{\eta}(T,P,\dot{\gamma},\dot{\varepsilon})=f(\dot{\varepsilon})\eta_s(T,P,\dot{\gamma})$$

Equation 6-1

$$f(\dot{\varepsilon}) = 1 + \frac{A\dot{\varepsilon}}{B + \dot{\varepsilon}}$$

Equation 6-2

Where $\overline{\eta}$ is the unified viscosity, η_s is the shear viscosity, T is the temperature, P is the pressure, $\dot{\gamma}$ is the shear rate, $\dot{\varepsilon}$ is the extension rate, and A and B are data-fitted coefficients. The detail discussion regarding extension viscosity can be found in the literature [138-141], however, it will not be presented in this thesis.

In the present study, the extremely high extensional rate reached around 20,000 1/s. However, it was not considered at this stage of the study, since the calculated highest injection pressure was already much higher than the experimental highest injection pressure without considering the extensional viscosity.

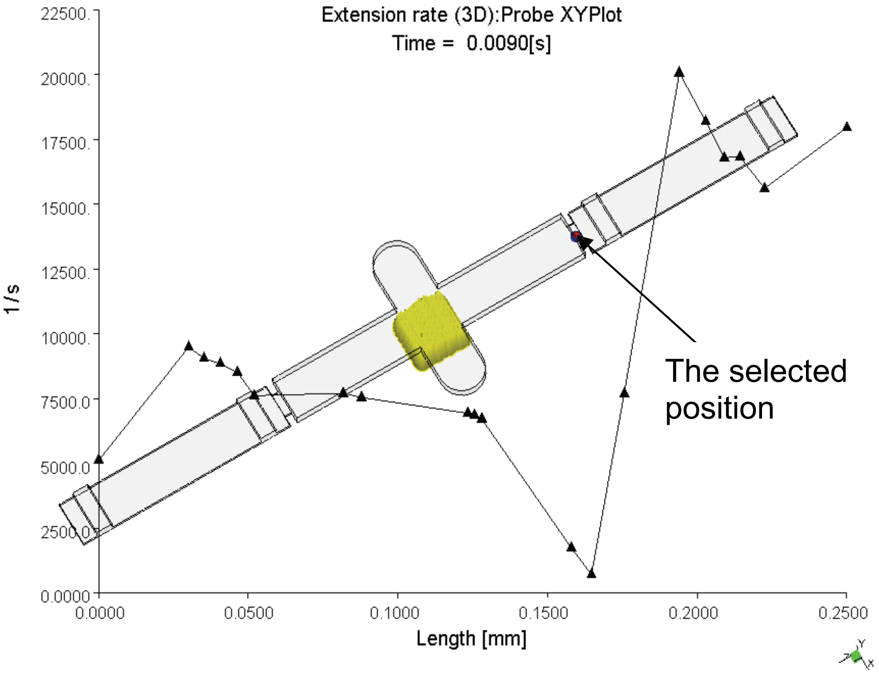

The selected position

Figure 6-18: Extension rate distribution across thickness in the middle of gate

6.2.1.3 Velocity

The velocity distribution was calculated at 0.0090s filling time. The flow front position at this filling time is shown in Figure 6-19. Figure 6-20 displays the y-z cutting plane view of 3D velocity distribution along the flow direction in the gate region at this time. The figure shows that the melt velocity is high in the narrow section of the gate and relatively low as the melt passes through the thicker sections of the mold.

When the polymer flows from a thick section to a narrow section, as shown in Figure 6-20, the melt experiences mixed shear and extensional deformation at the position with abrupt dimensional change. A unified viscosity model as a function of the extension rate and the shear rate may be required in this situation for future study.

The high and unidirectional velocity in the gate section may result in high deformation of polymer molecules, such as disentanglement, slippage of chains over each other, and molecular alignment in the direction of applied stress.

When the polymer flows from a narrow section to a thick section, the velocity is directed to a space with less flow resistance, thus reducing the molecular chain orientation.

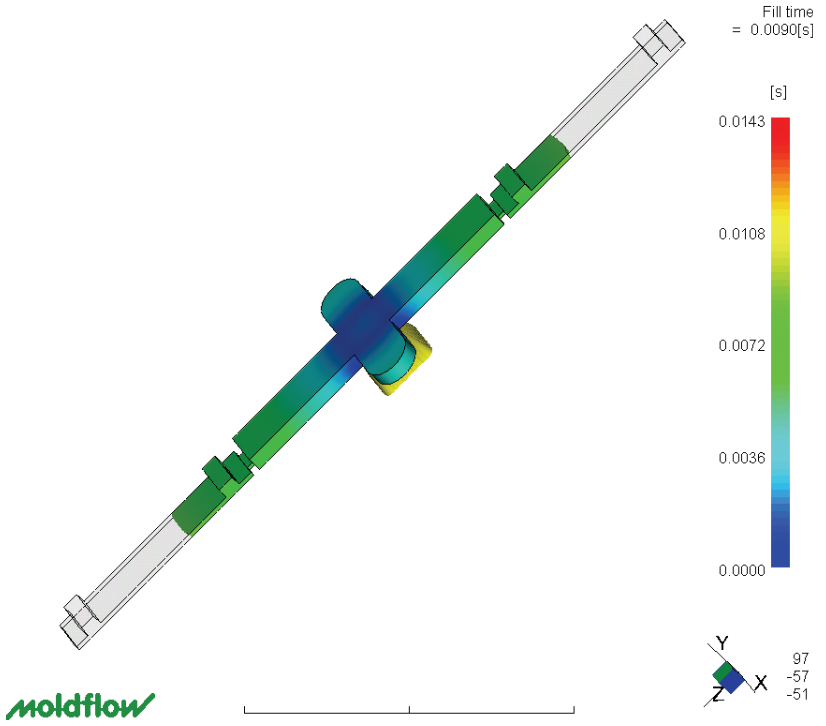

Figure 6-19: The flow front position at filling time of 0.0090s

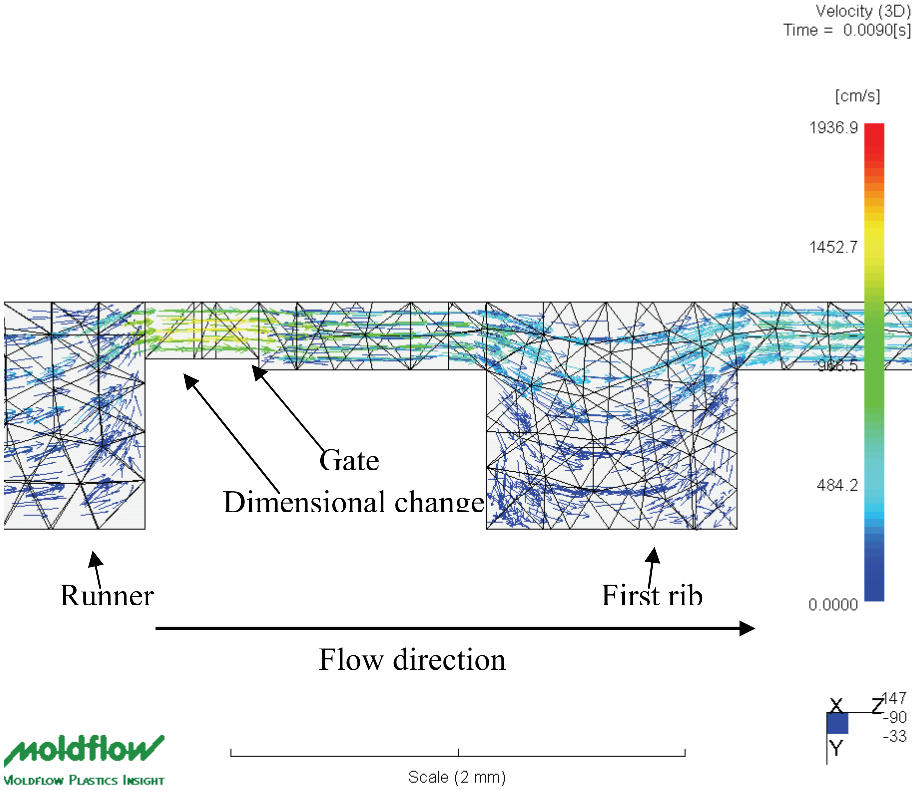

Figure 6-20: Y-z cutting plane view of 3D velocity

6.2.1.4 Shear rate

The shear rate is the velocity gradient in laminar flow of parallel adjacent layers of a fluid body under shear. If this happens too fast, the polymer chains break and the material degrade. Figure 6-21 displays a steady simple shear flow [142], in which a fluid is confined between two plates that are a small distance H, apart. The bottom plate is stationary and the top plate moves with a constant speed v_x in the x-direction due to application of a force F. The velocity gradient is called shear rate as shown in Equation 6-3.

$$\tau_{zx} = \mu \frac{dv_x}{dz} = \mu\dot{\gamma}$$

Equation 6-3

Where τ_{zx} is the shear stress, μ is the viscosity of the fluid.

The shear heating is caused by the deformation of the melt as it flows into the cavity. A widely accepted model for the calculation of the shear heating is shown in Equation 6-4 [143]:

$$\dot{w} = \eta\dot{\gamma}^2$$

Equation 6-4

Where $\dot{w}$ is the viscous heating, η is the viscosity function, $\dot{\gamma}$ is the shear rate.

In Moldflow, the maximum shear rate is generated at a given node up to the time the result was written. Figure 6-22 displays the y-z cutting plane view of the calculated maximum shear rate in the gate region along the flow direction. Shear rate is the rate of change of shear strain with time. The highest shear rates, as high as 377,300 1/s, appear at the melt/mold interface in the gate region, due to the fast movement of adjacent material elements over each other in this region. In the uniform thickness section of the part, the calculated shear rate was mainly determined by the filling control profile of the simulation. In this section, the shear rate is zero at the centerline because there is no relative material element movement due to flow symmetry.

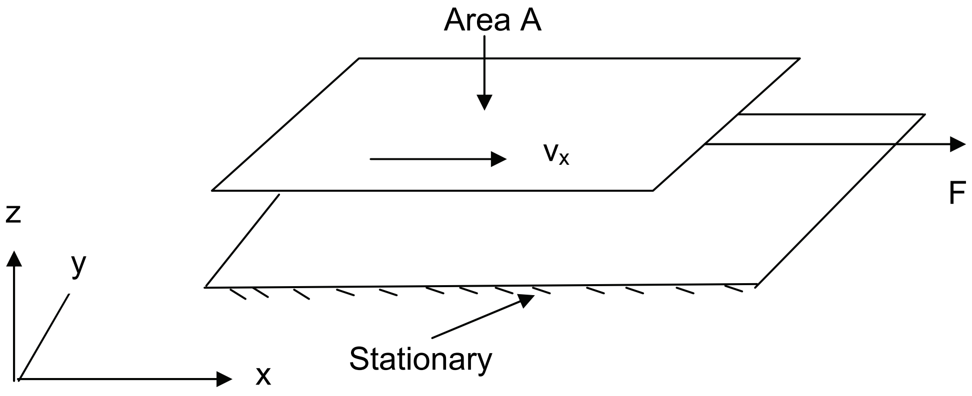

Figure 6-21: Steady simple shear flow

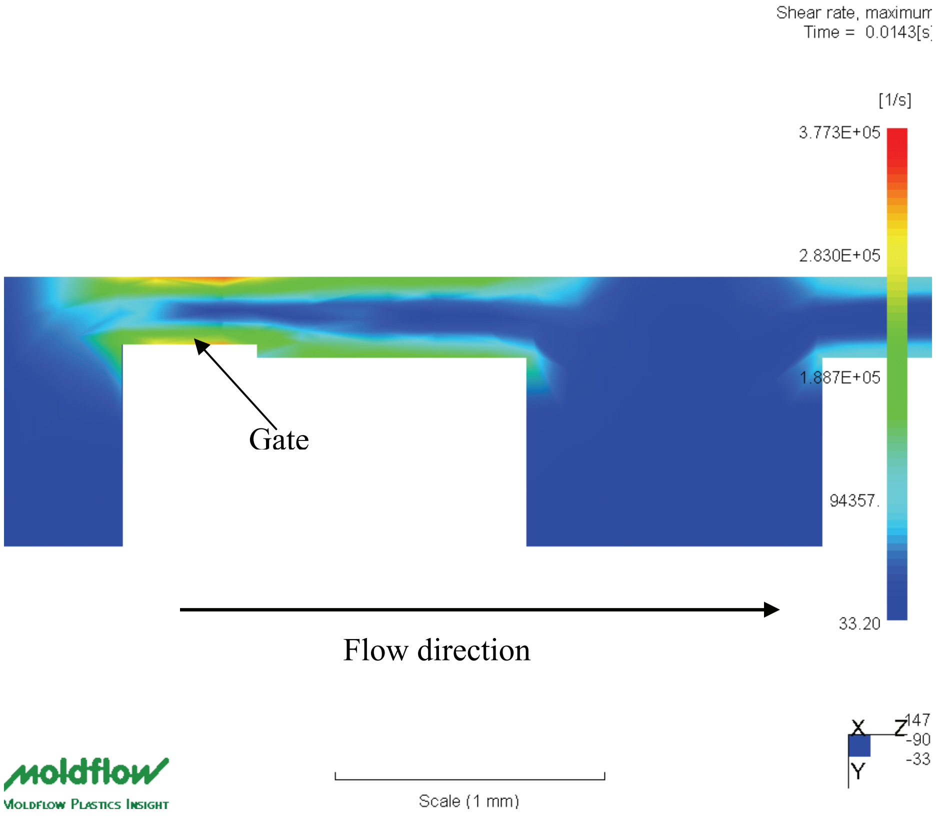

Figure 6-22: The calculated maximum shear rate in the gate region

6.2.1.5 Temperature

The Temperature (3D) results are generated from a 3D flow analysis and show the temperature of the polymer when the flow front reaches a specified node. Figure 6-23 and Figure 6-24 display the temperature distribution across the thickness at 5 positions selected along the flow direction at filling times of 0.009s and 0.0143s, respectively. At filling time of 0.0143s, the mold is filled completely. The curve for position 5 is not shown in Figure 6-23, because the flow front had not reached that position at filling time of 0.0090s.

At filling time of 0.0090s, the temperature did not show much variability with position along the flow length, due to the short flow length. When the mold is filled at 0.0143s, the bulk temperature was increased significantly from position 1, close to the end of runner, to position 5, close to the cavity end. The increase of the bulk temperature can affect the formation of skin layer since less material will be frozen during the filling stage at high bulk temperature. Theoretically the skin layer will become thinner and the molecules will become less oriented along flow direction. The increase of material temperature was probably due to shear heating considered in Moldflow. Also, the temperature at filling time of 0.0143s was significantly higher than the temperature at filling time of 0.0090s, especially for the positions between the gate and the cavity end. This was probably because the heat generated from viscous dissipation exceeded the heat loss from the melt to the mold wall, due to the high shear rates realized in micro injection molding process. With the increase of the bulk temperature with time, the material will have longer time to relax before solidification. As a result, the skin layer may become thinner and the molecules may become less oriented across the thickness at a position filled at later times.

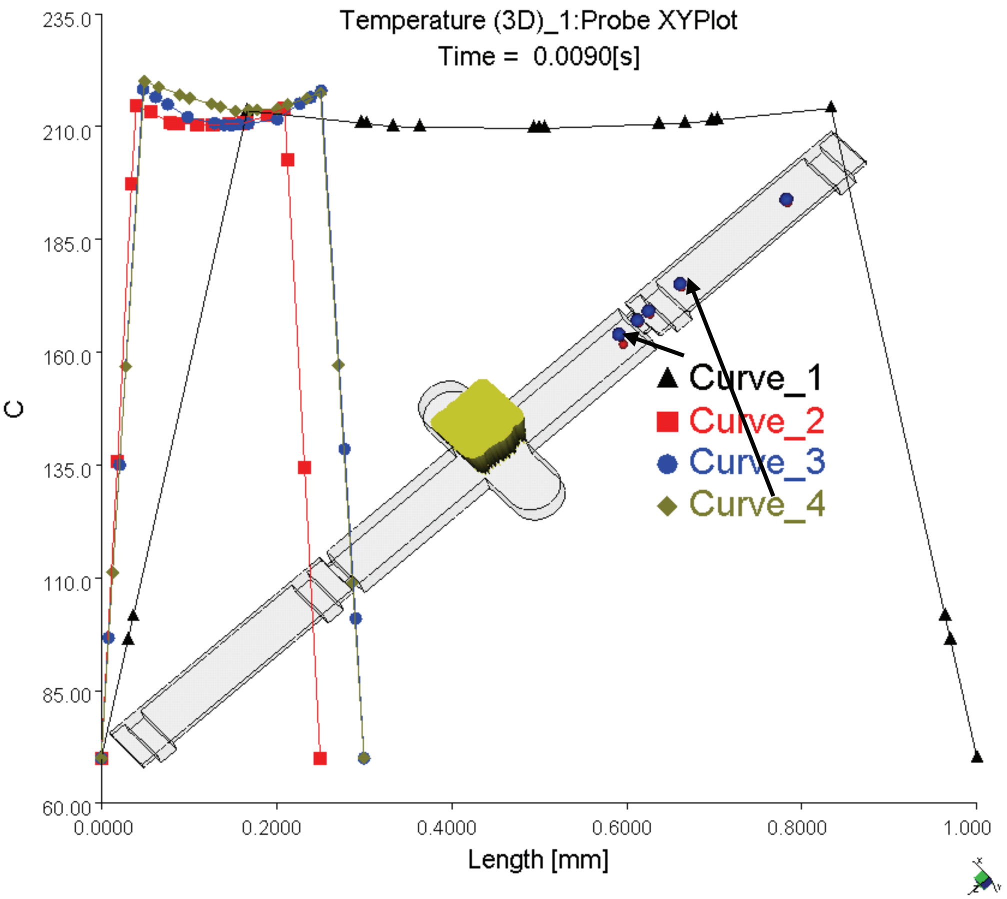

Figure 6-23: Temperature distribution along the flow direction at filling time of 0.0090s (Vertical axis unit: ºC).

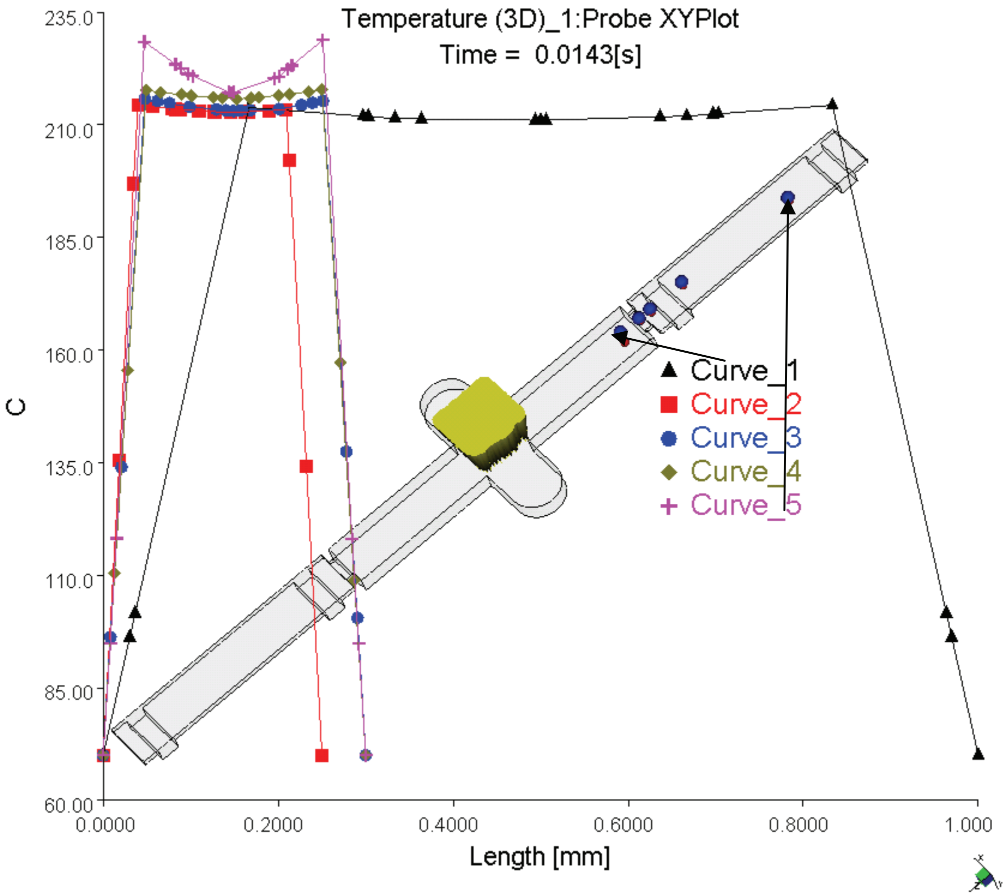

Figure 6-24: Temperature distribution along the flow direction at filling time 0.0143s (Vertical axis unit: ºC).

6.2.1.6 Viscosity

The shear viscosity of a material is a measure of its ability to flow under an applied shear stress. The viscosity of polymers is dependent on temperature, pressure, and shear rate. In general, as the temperature and shear rate increase, the viscosity will decrease, indicating a greater ability to flow under a given applied pressure gradient. The Cross-WLF viscosity available in the Moldflow commercial software model is selected for the present study is given by Equation 6-5 and Equation 6-6.

$$\eta = \frac{\eta_0}{1 + \left(\frac{\eta_0 \dot{\gamma}}{Tau^*} \right)^{(1-n)}}$$

Equation 6-5

$$\eta_0 = D1 \exp\left[\frac{-A1\left(T - T^*\right)}{A2 + \left(T - T^*\right)} \right]$$

Equation 6-6

Where η is the viscosity, $\dot{\gamma}$ is the shear rate, T is the temperature, T*=D2+D3*P, where P is pressure, A2=A2~+D3*P, and where n, Tau*, D1, D2, D3, A1, A2~, are data-fitted coefficients. Tau* is related to the relaxation time of the material, D2 is related to the glass transition temperature T_g.

Figure 6-25 and Figure 6-26 show the calculated viscosity distributions along the flow path at filling times of 0.0090s and 0.0143s, respectively. The highest viscosity appears at or near the center line at all positions, where the shear rate is zero. The lowest viscosity is at the melt/mold interface, where the shear rate reaches its maximum. The reduction of viscosity with shear rate is referred to as shear-thinning behaviour, which can be attributed to the deformation of polymer molecules, such as disentanglement, slippage of chains over each other, and molecular alignment in the direction of the applied stress. The resistance exhibited by the polymer to flow decreases with such deformation [144].

The viscosity at position 1 in the runner appeared to be higher than at any other position, probably due to the lower temperature and shear rate at that position. From position 2 in the middle of the gate to position 5 close to the end of flow, the viscosity increased with the decreasing shear rate, despite the increase of temperature along the flow direction, as shown in Figure 6-25 and Figure 6-26.

At all the shown positions, the viscosity at 0.0143s filling time was around twice as high as the viscosity at 0.0090s filling time. This is probably due to the drop of shear rate, which is controlled by the filling profile for simulation, as shown in Figure 5-3.

Since extensional viscosity and the possibility of slip was not considered in the present study, it is reasonable to consider that the big discrepancy in injection pressure between experimental data and calculated results might be related to the employed rheological model. Further experimental work is required in testing the material micro flow behaviour (i.e. Flow in micro channels at high injection speeds).

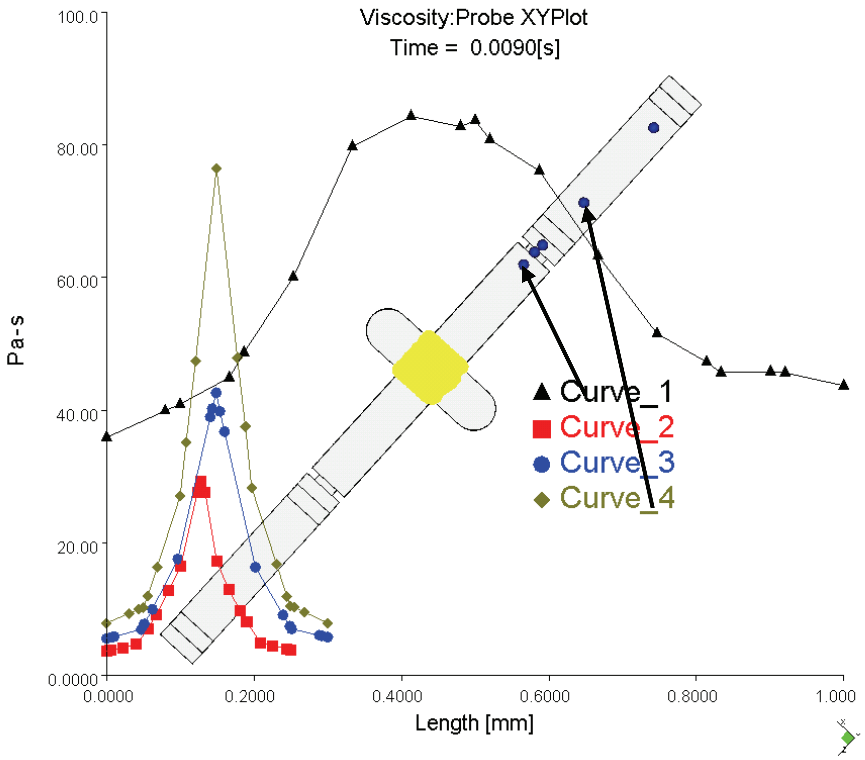

Figure 6-25: viscosity distribution along the flow direction at filling time of 0.0090s

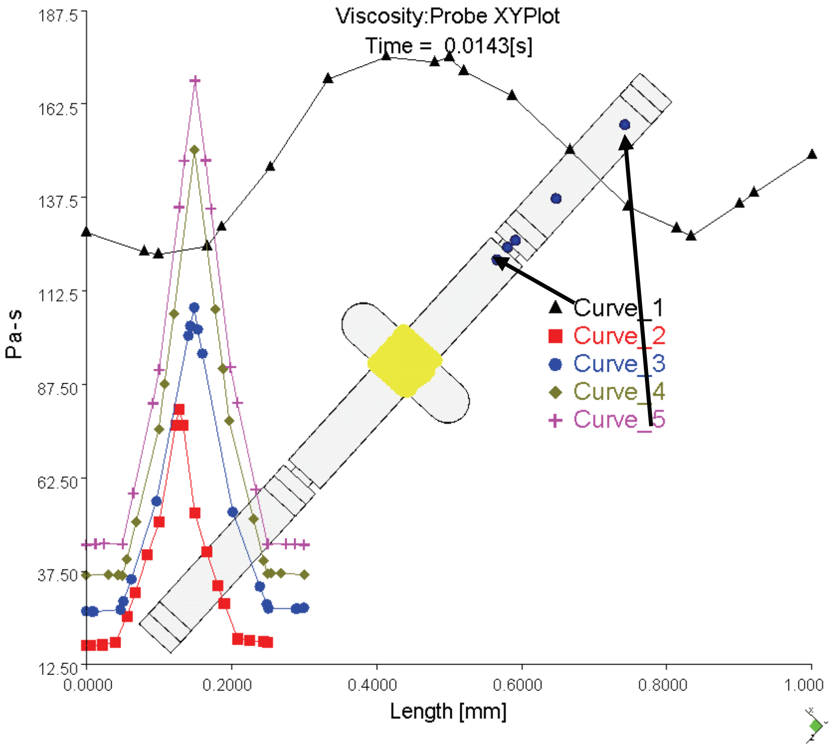

Figure 6-26: Viscosity distribution along the flow direction at filling time of 0.0143s

6.2.2 Escorene (HD-6719)

6.2.2.1 Flow pattern after hole

Figure 6-27 displays the calculated flow pattern just after the hole, using fusion mesh modeling. The pattern confirms the material flow behaviour reflected by the morphology, as shown in Figure 6-28 [26]. The melt flow fronts from two sides of hole met at a high angle and converged in front of the middle rib in the hole. The two flow fronts seem to have undergone some crystallization before meeting, thus possibly forming a weak weld line.

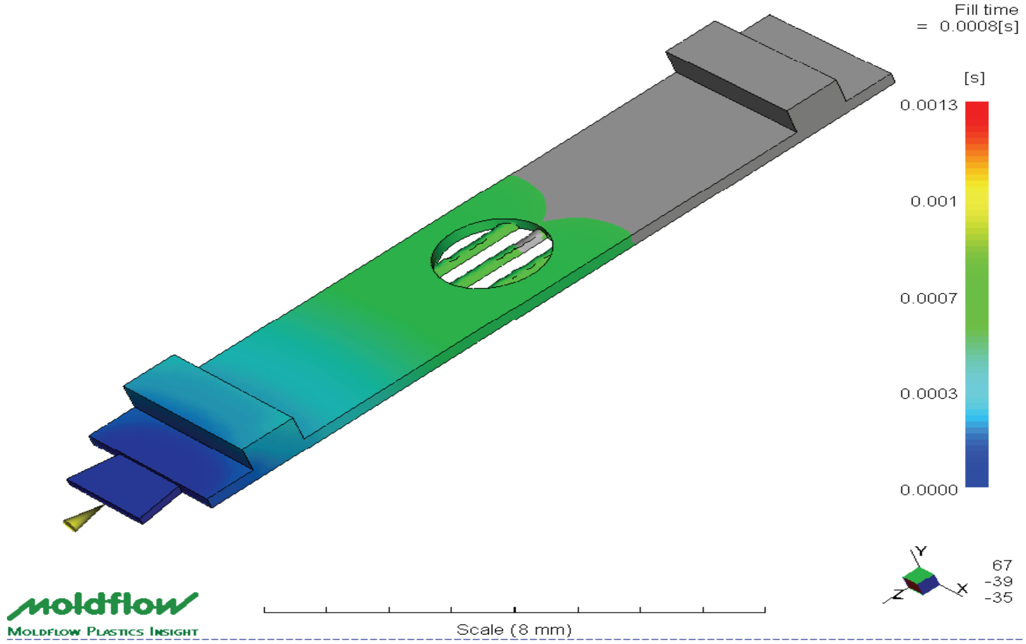

Figure 6-27: Flow pattern after the hole (result of fusion mesh)

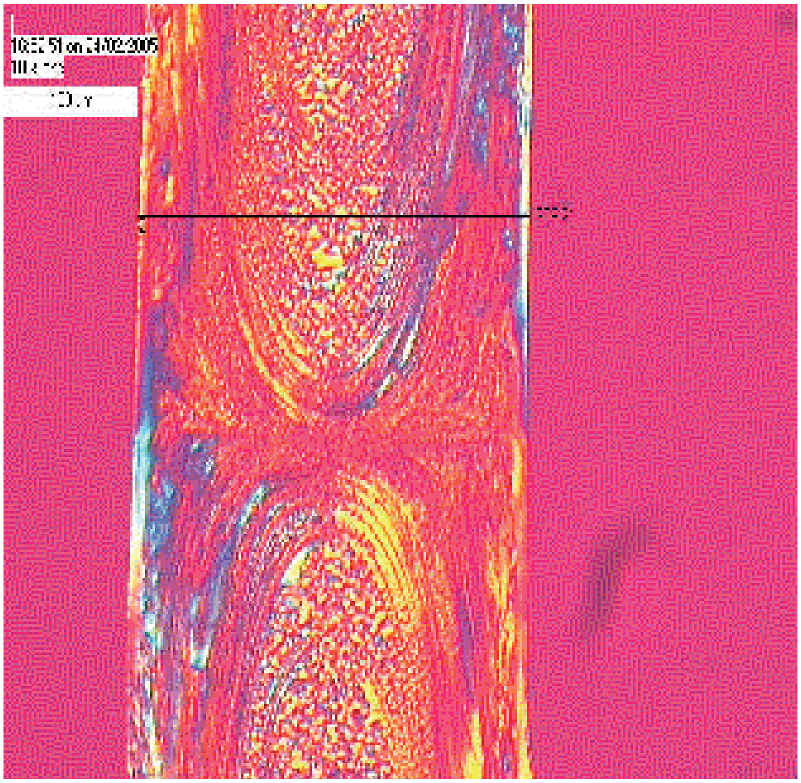

Figure 6-28: Morphology microphotograph after the hole (Escorene HD-6709). (Magnification: 40x)

6.2.2.2 Temperature and pressure distribution

The temperature profiles at different positions along the flow direction are shown as a function of time in Figure 6-29. At around 0.009s filling time, the temperature of the melt far from gate exceeded the temperature closer to gate. This may be attributed to viscous dissipation at high shear rates. Figure 6-30 dispalys the pressure profiles at different positions along the flow direction. A significant pressure drop was observed for the two positions across the hole.

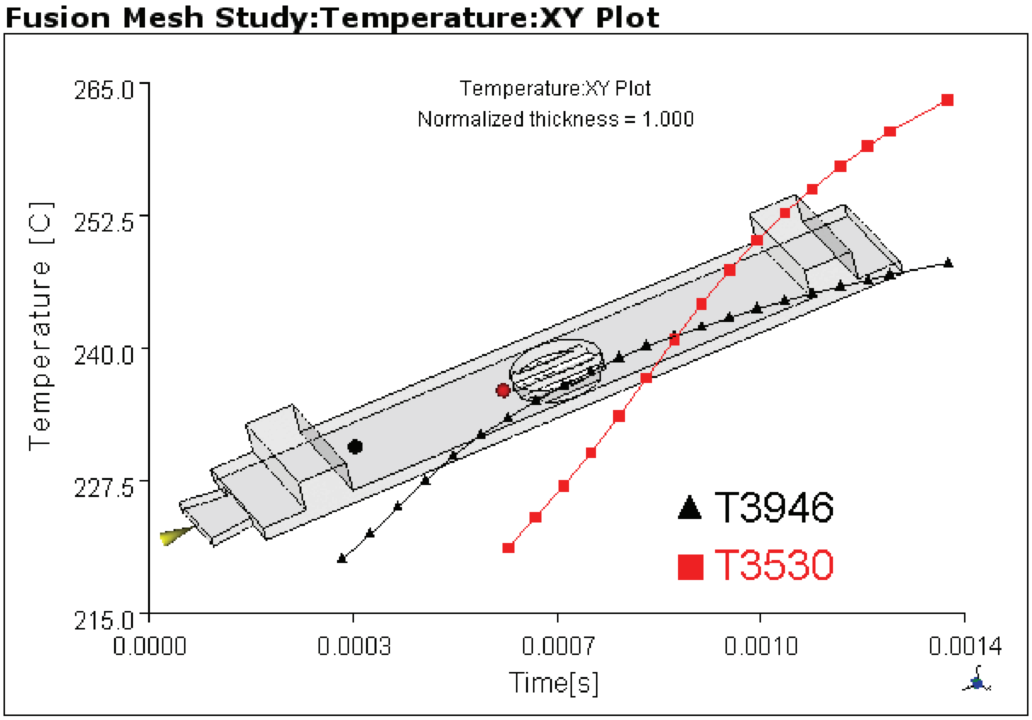

Figure 6-29: Temperature distribution along the flow direction (Result of fusion mesh)

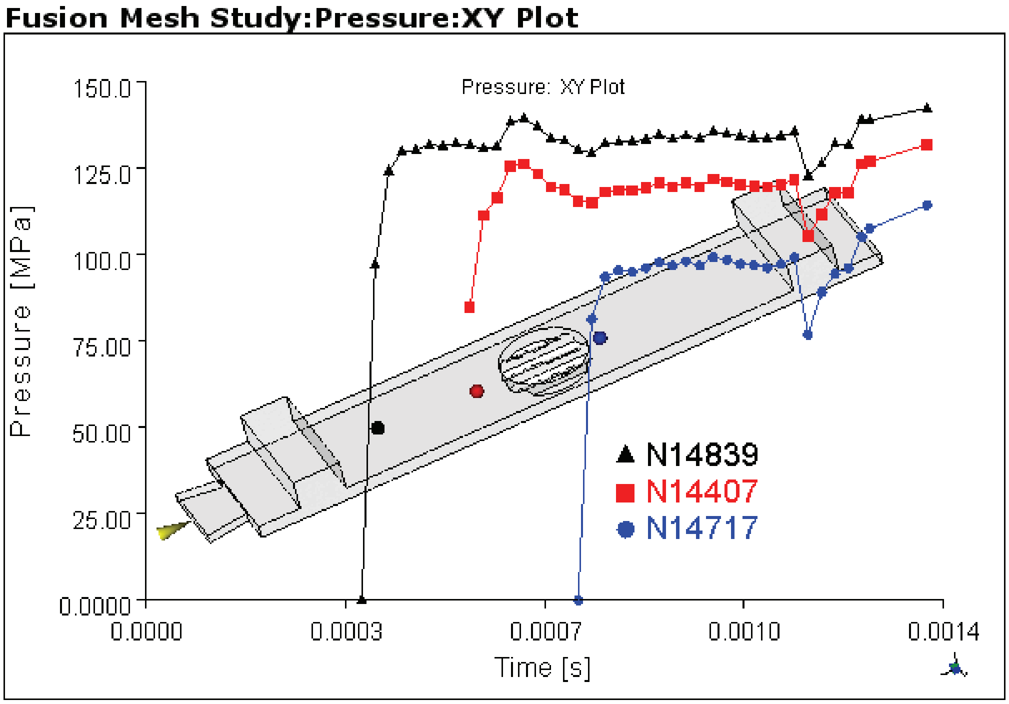

Figure 6-30: Pressure distribution along flow direction. (result of fusion mesh)

6.2.2.3 Maximum shear rate

Figure 6-31 shows that the maximum shear rate occurs at the mold wall in the gate region. The highest shear rate reached was 6.267E + 06 s^{-1}, which is much higher than the maximum shear rate reported in the Moldflow database, 6.5E + 04 s^{-1}. The actual experimental shear rate may be significantly lower, due to possible slippage, which may occur at interfaces of the polymer-mold wall, solid-liquid polymer, and polymer-polymer.

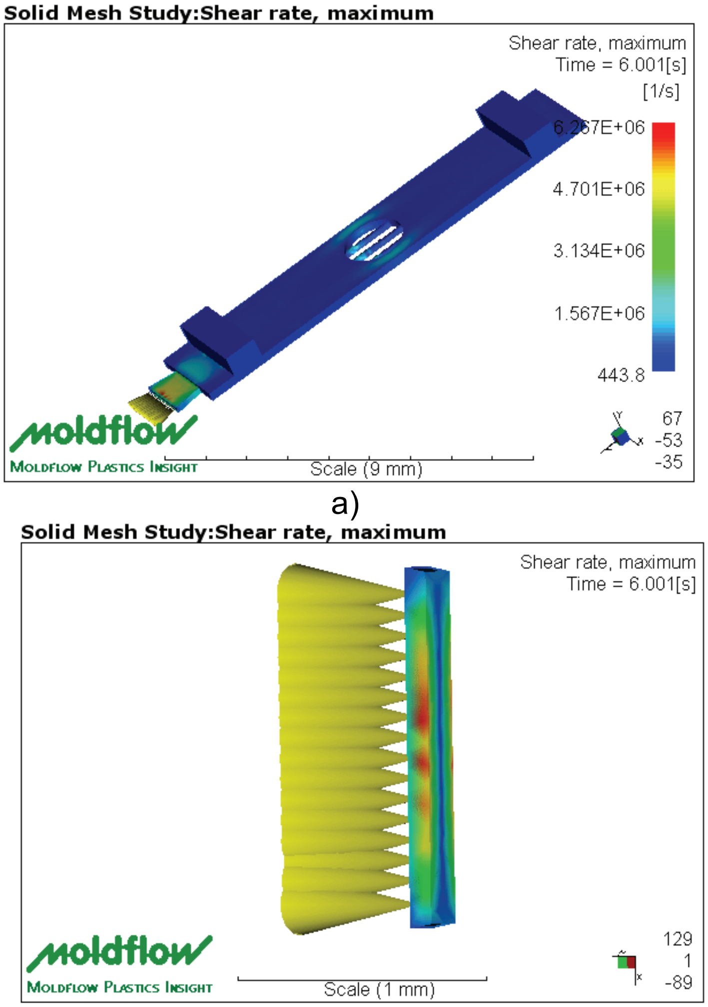

a)

b)

Figure 6-31: a) Maximum shear rate distribution in the whole part; b) Cutting plane view of maximum shear rate in the gate region. (Result of solid mesh)

6.2.2.4 Shrinkage

Figure 6-32 shows that the calculated volumetric shrinkage distribution is in reasonable agreement with measured linear shrinkage in the Y-direction along the flow direction, as shown in Figure 6-33, which was measured for the positions as shown in Figure 4-22. The measured average linear shrinkage in the transversal Y-direction is lower than one third of the volumetric shrinkage.

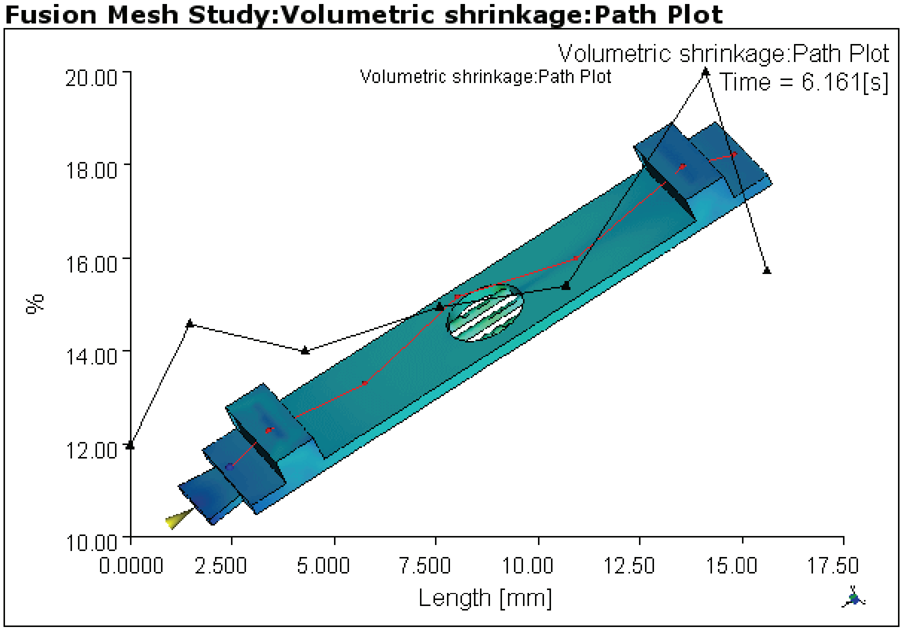

Figure 6-32: The calculated volumetric shrinkage distribution along flow direction (fusion mesh, the points connected with red line on the part are selected to display the results)

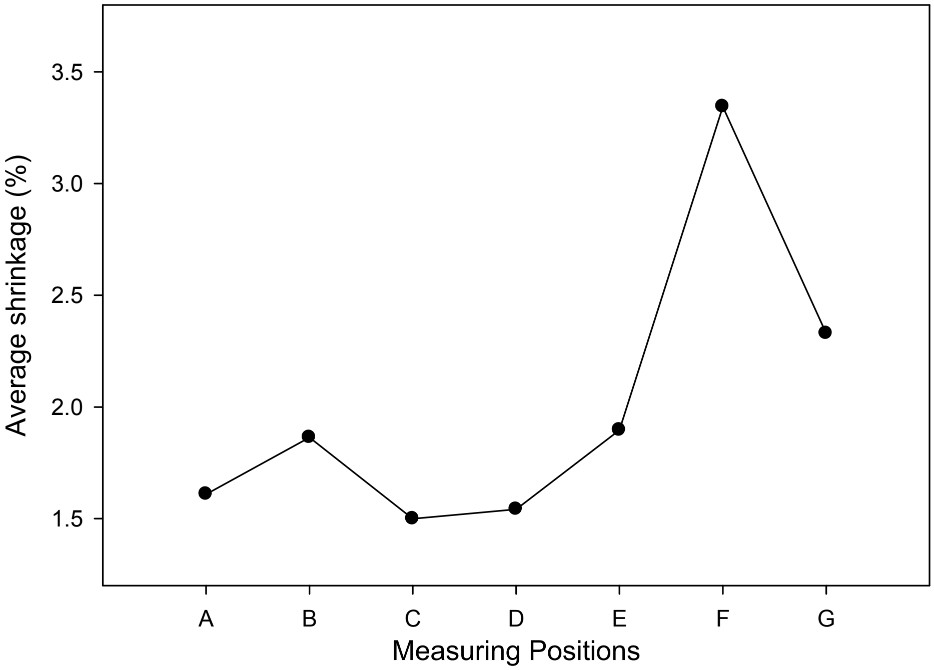

Figure 6-33: Shrinkage of Y-direction along flow at measuring positions

6.3 Thermal Properties

6.3.1 POM

The sampling position for the variation of thermal properties with process conditions is illustrated in Figure 4-8 (a). Figure 6-34 shows that the crystallinity of micro injection molded POM ranges from 151.7 J/g to 159.4 J/g, which are 12.4% to 16.7% lower than the heat of fusion of the resin measured at a cooling rate of 10 ºC/min (ca. 182 J/g). This reflects the fact that the cooling rate during the micro molding process was significantly higher than 10 ºC/min. Both onset temperature and peak temperature varied in very narrow ranges, and roughly followed a similar pattern. The highest onset and peak temperatures were found in case 5, which had the lowest heat of fusion. In case 5, both the injection speed and mold temperature were set to high levels. It seems that with growth of lamellae and crystallites, more amorphous material remains in the gaps among the crystalline parts of the larger spherulites. The data variation evident in Figure 6-35 may be partially due to DSC system characteristics and partially to process variation, such as temperature fluctuations in the system, material inconsistency, deviations in machine control system, and imperfectly balanced flow in the two cavities [29].

Figure 6-35 shows that both injection speed and mold temperature are major negative factors in affecting the heat of fusion. Increases in injection speed and mold temperature resulted in decrease in heat of fusion.

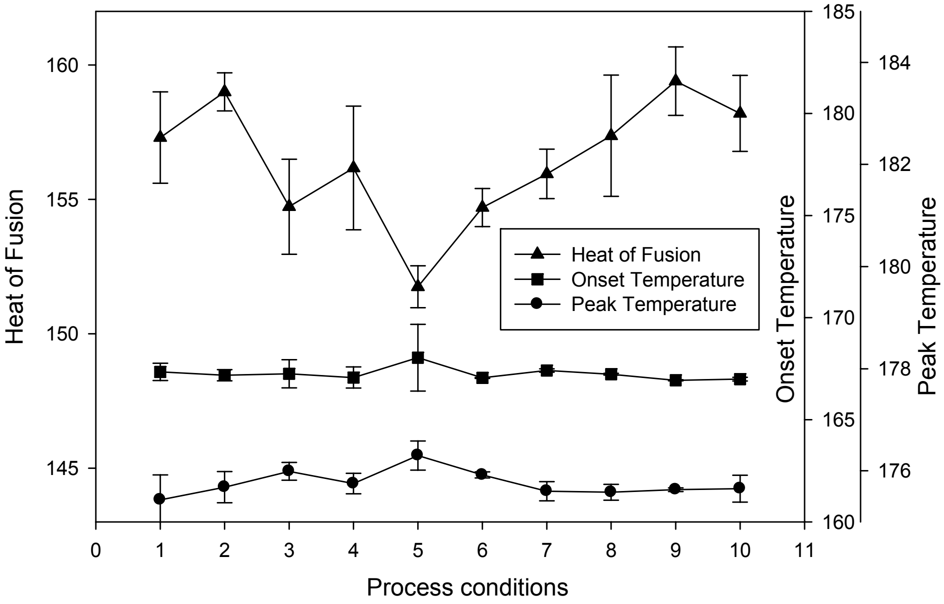

Figure 6-34: Thermal properties of micro injection molded POM specimens

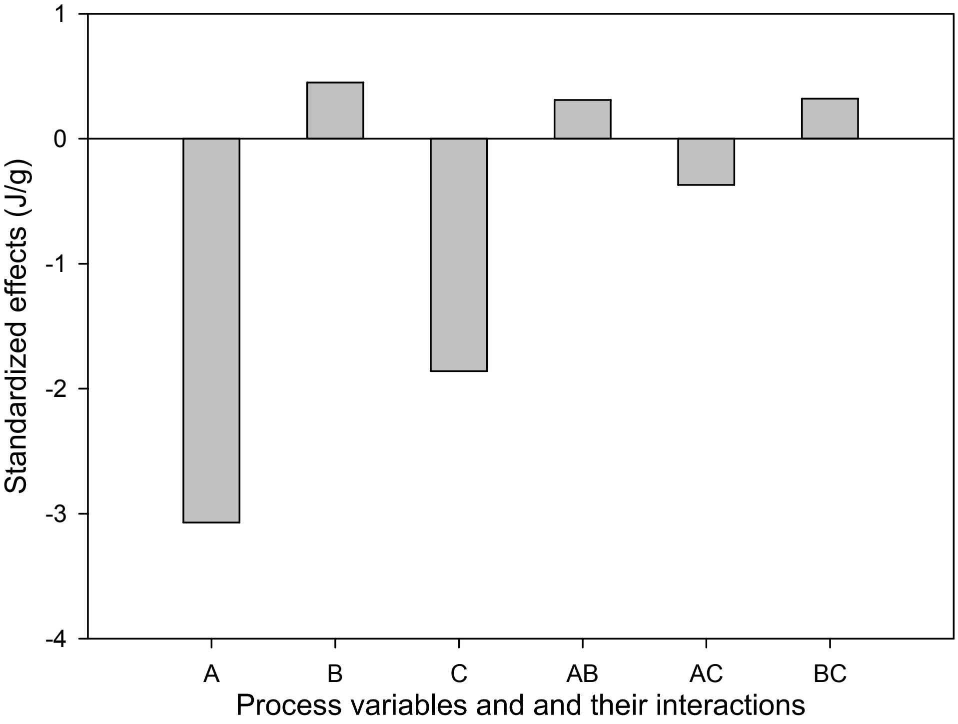

Figure 6-35: Standardized effects on heat of fusion of POM specimens

6.3.2 HDPE

Figure 6-36 shows that the heat of fusion of micro injection molded HDPE (Sclair 2704) ranges from 141.8 J/g to 150.85 J/g, which is 11% to 16.6% lower than the heat of fusion of the resin measured at a cooling rate of 10 ºC/min (ca. 170 J/g). This reflects the fact that the cooling rate during the micro molding process was significantly higher than 10 ºC/min.

The heat of fusion and onset temperature approximately followed a similar pattern with some minor deviations in case 4 and case 8 and a large discrepancy in case 11, which had the extreme high injection speed, high mold temperature, and low melt temperature. Case 11 had the highest heat of fusion (crystallinity) and lowest peak temperature.

The lower onset temperature tended to occur with lower mold temperature, where the melt was subject to greater supercooling. This was probably because the greater supercooling shortened the induction time and increased the nucleation rate, thus resulting in thinner lamellae and less perfect crystallites. The above analysis was not applicable to case 10, which had lower mold temperature but extreme high injection speed.

The melting peak temperature T_{pm} is the temperature at which most of the crystallites melt. The peak temperature tended to vary within the scattering range, and no conclusions could be made with high confidence.

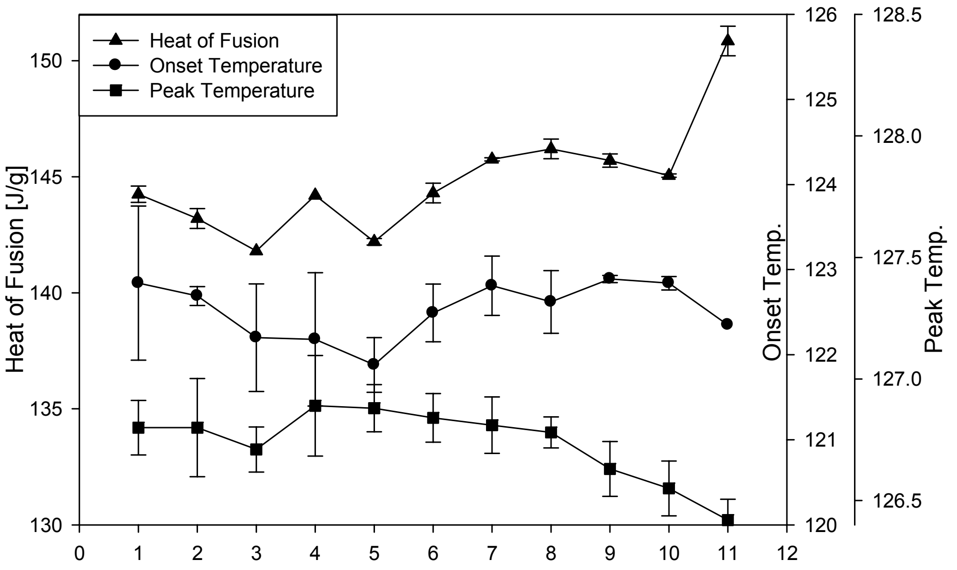

Figure 6-36: Thermal properties of micro injection molded HDPE Specimens

As displayed in Figure 6-37, the mold temperature is the major positive factor affecting the crystallinity, while the injection speed, melt temperature, injection speed/packing velocity interaction, and injection speed/mold temperature interaction had minor effects, either positive or negative, on the heat of fusion of micro injection molded HDPE specimens. The effect of mold temperature on crystallinity was probably because higher mold temperature extended the crystallization time. This conclusion agrees with the results in literature for both conventional injection molding [47, 49, 145] and micro injection molding [101].

Since the DOE design was a resolution IV design, the injection speed/packing velocity interaction was confounded with mold temperature/melt temperature interaction, and the injection speed/mold temperature interaction was confounded with packing velocity/melt temperature interaction. Since the packing velocity was the least significant individual factor in affecting the crystallinity, the interaction without packing velocity should tend to be more significant [3, 136]. A full factorial experimental design is needed in order to obtain more accurate and more confident conclusions for the effects of coupling factors.

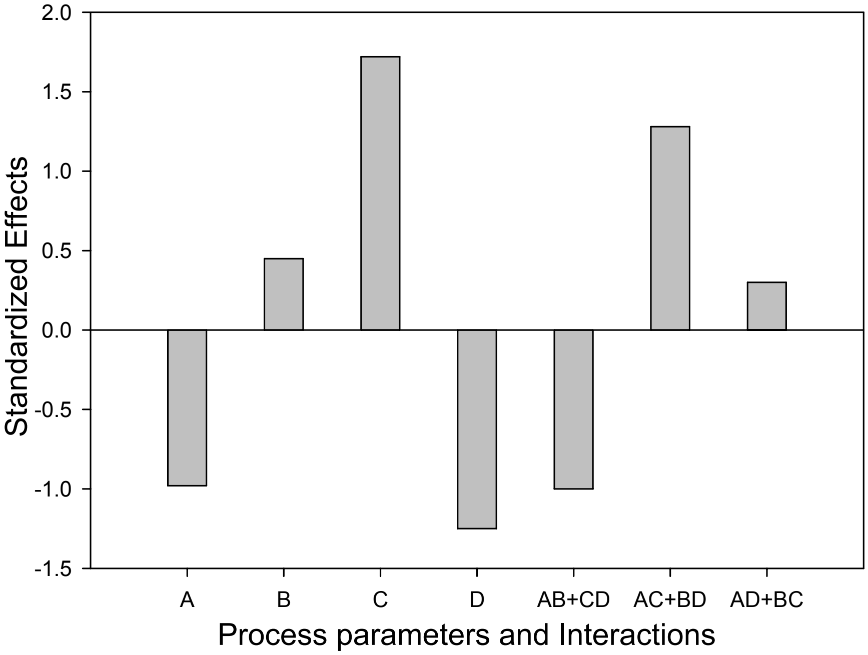

Figure 6-37: Standardized effects on heat of fusion of HDPE specimens

6.3.3 Distribution of Thermal Properties

The distribution of thermal properties along the flow direction was studied for micro injection molded POM. The sampling positions for thermal properties distribution are illustrated in Figure 6-38 (b). The DSC measurements of the specimens indicate that the sample in the vicinity of the gate showed a slightly higher heat of fusion than the sample far from the gate. Examination of the melting curves of the three specimens indicates that they exhibited significantly different features, as displayed in Figure 6-39.

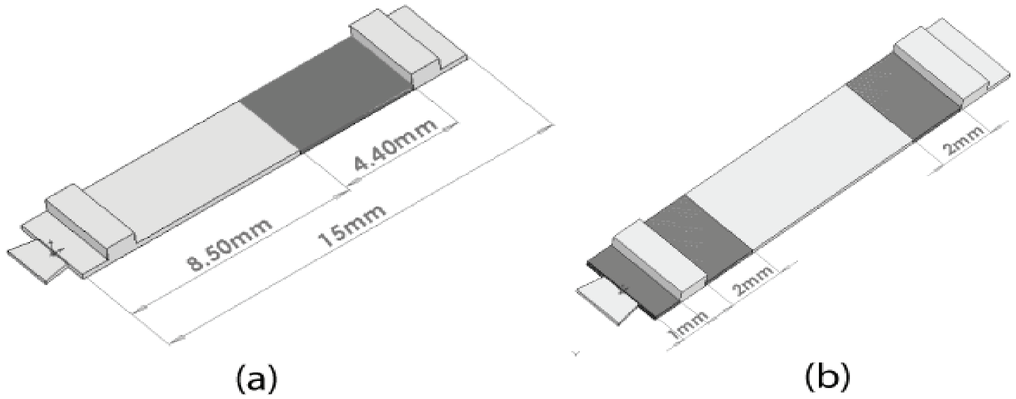

Figure 6-38: a) Sampling position for crystallinity comparison among designed process conditions; b) Sampling position for crystallinity distribution.

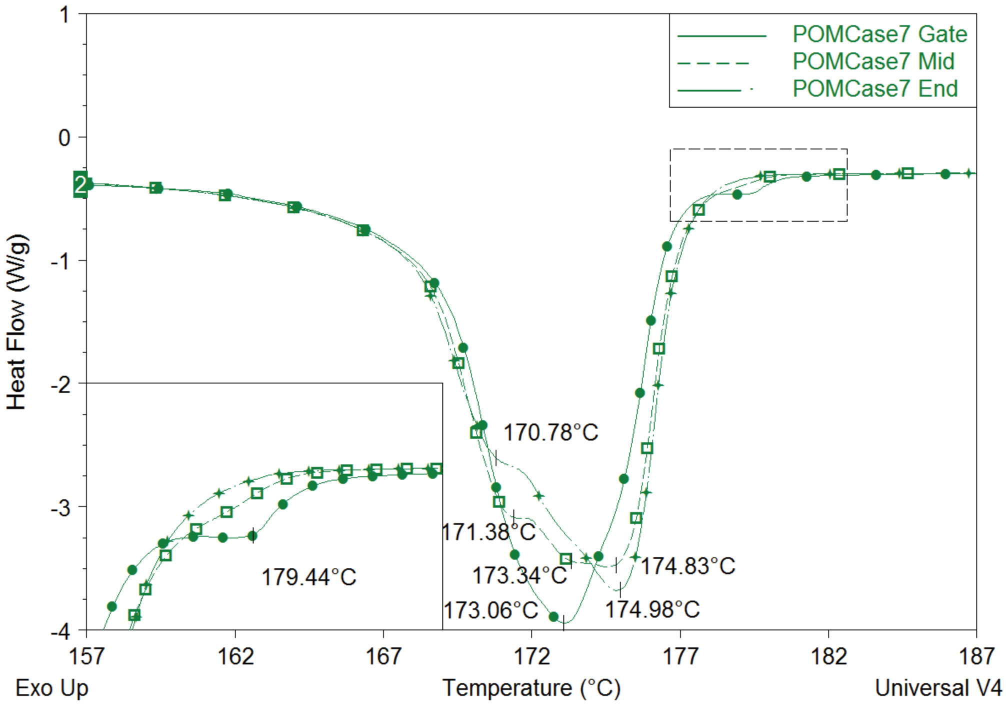

Figure 6-39: DSC melting curves at different positions

The specimen near the gate exhibited two melting peaks, at 173.06 ºC and 179.44 ºC. The high melting temperature peak may be associated with the fraction of polymer that is crystallized under the effects of orientation [51]. The specimen in middle position tends to have three melting peaks, including two shoulder peaks at 171.38 ºC and 173.34 ºC, and a primary peak at 174.83 ºC. The specimen in the end position exhibited two melting peaks, including a shoulder peak at 170.78 ºC, and a primary peak at 174.98 ºC.

It would be reasonable to relate these peaks to various crystal structures possibly existing in the specimen, for example, the shish-kebab in the skin layer, transcrystalline structure, and 3D spherulite [51, 98, 99, 146-150]. In Table 6-1, the peak temperatures measured using a DSC are related to their positions and to possible corresponding crystalline structures. The peaks at lower temperatures could be related to the melting of kebab in the shish-kebab structures, fine spherulites, and amorphous regions. On the other hand, peaks at higher temperature could represent the melting of the 3D spherulites and stretched chains of shishes, which tend to be thermodynamically more stable than the other structures. The material melting at 179.44 ºC was probably shishes or highly oriented molecules, as will be shown in the zoomed views at position A and position B in Figure 6-51 in the following section, since it appeared only in the gate region. The material melting at 174.83 ºC and 174.98 ºC was probably 3D spherulites, which was found in both middle and end specimens. The material melting at 173.06 ºC and 173.34 ºC was probably fine spherulites or kebabs which had lower melt temperature than 3D spherulites and appeared only in gate and middle specimens. The materials melting at 170.78 ºC and 171.38 ºC were probably the amorphous region in the skin layer since it was only found in the middle and end specimens.

Table 6-1: The Melting temperature and structure relations

Temperature	Structure	Specimen position
179.44 ºC	highly oriented molecules or shishes in the shish-kebabs	Gate specimen
174.83 ºC and 174.98	3D spherulites	Middle and end specimens
173.06 ºC and 173.34 ºC	Fine spherulites or Kebabs	Gate and middle specimens
170.78 ºC and 171.38 ºC	Fine spherulites	Middle and end specimens

The slope difference appears near the end of the rising flank of the melting peak as shown in the inset view of Figure 6-39. The gate specimen exhibits its second peak in this region. For the end specimen, the heat flow approaches the baseline asymptotically with increasing temperature, whereas for the middle specimen the heat flow approaches the baseline in an approximately linear way. This is probably due to the relative amount of the highly oriented molecules in the specimen, since the difference appears in the same temperature range as the second peak of gate specimen. This could be regarded as indirect evidence for the existence of shishes in the skin layer, which has been sought by previous researchers [99, 149]. The asymptotic pattern implies that there is probably no presence of highly oriented skin layer in the end of sample.

6.4 Morphology

This section presents the results of microstructure characterization for the micro injection molded POM and HDPE moldings.

6.4.1 POM

6.4.1.1 The skin-core structure and morphology

Figure 6-40 displays the skin-core morphology obtained with polarized light microscopy for a polyoxymethylene molding (Case 5, sample No. 14). The image was taken at position F for a transversal cross section as shown in Figure 4-11, at magnification of 40X. Comparison with the typical morphological characteristics reported by Clark [148] for conventional injection moldings suggests significant differences. The twisted lamellae structure occupied more than half of the cross section in conventional injection molded POM Delrin 500 NC-10. Figure 6-40 shows that, in this work, the above morphology was replaced by fine spherulites and oblates, for micro injection molded POM Delrin 900P.

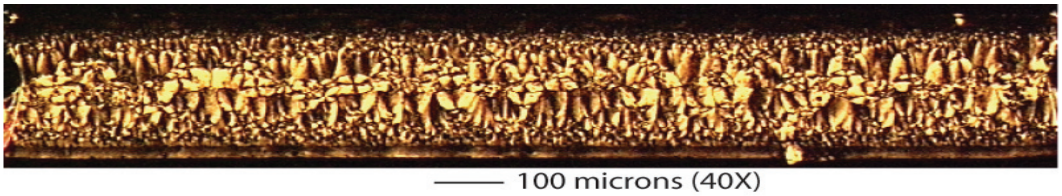

Figure 6-40: Microphotograph of a cross section at magnification of 40X

The details of the micro injection molding skin-core morphology are illustrated at higher magnification (100x) in Figure 6-41. The photomicrograph displays the morphology from the surface to approximately two thirds of the total thickness (212 µm from the top surface). The direction of view is along the X-axis of the plate, and the cold temperature surface of the plate appears at the top.

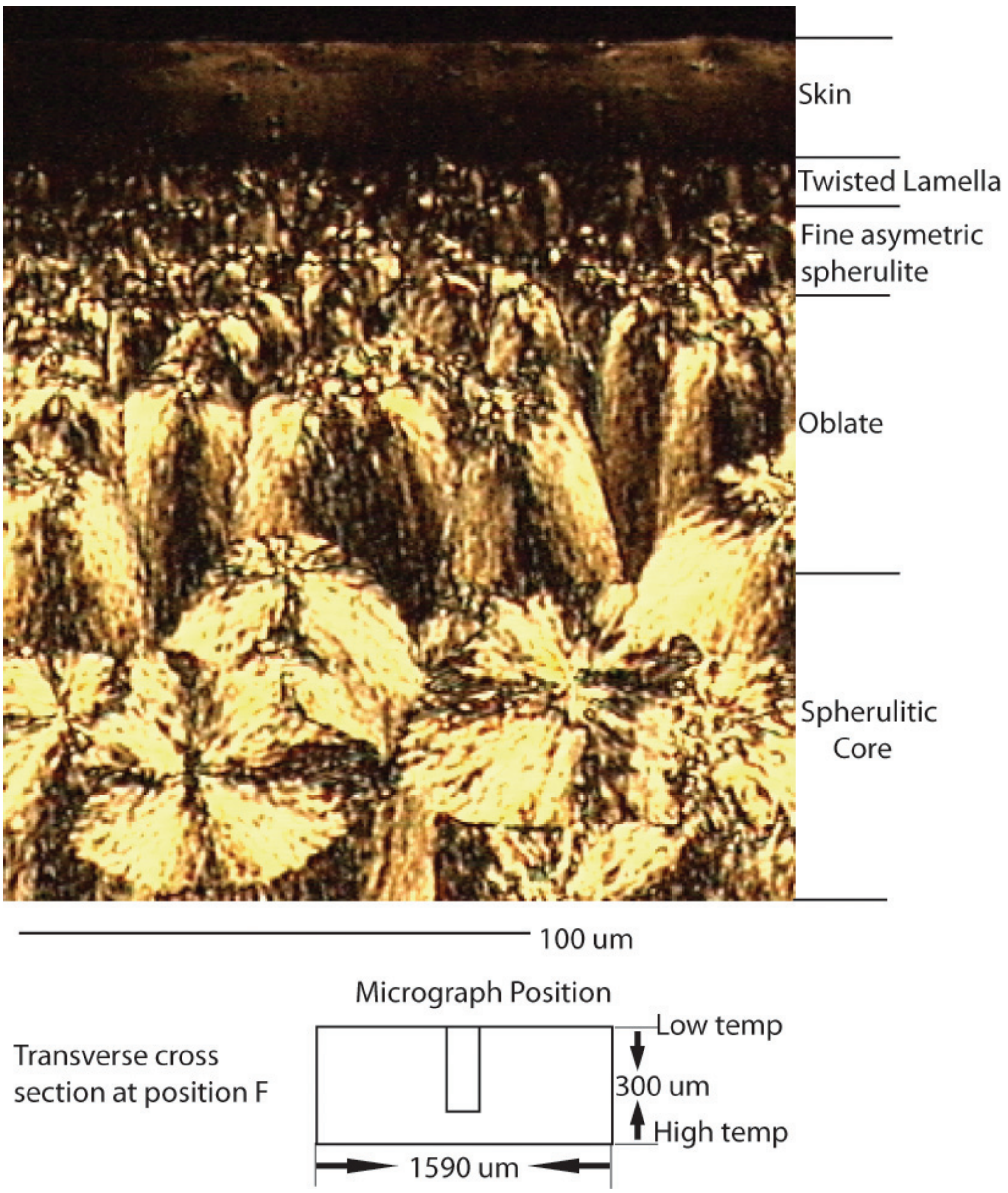

Figure 6-41: The five morphologic zones in a micro injection molded polyoxymethylene part viewed in transversal cross section. (Magnification: 200x)

In contrast with the three layer structure reported for conventional injection molded Delrin 500 NC-10 (Dupont acetal homopolymer) [98, 99, 148], the following five distinct polymorphs can be identified for the micro-molded Delrin 900P (Dupont acetal homopolymer) as shown in Figure 6-41.

1) a nonspherulitic skin layer, having a high degree of chain orientation parallel to the injection direction (Type I);
2) a twisted lamellae layer, which has a clear boundary with the skin (Type II);
3) a fine asymmetric spherulitic layer (Type III);
4) an oblate spherulitic layer with axis of symmetry in the depth direction, i.e., the direction of the thermal gradient (Type IV);
5) a random spherulitic core (Type V).

The formation of these zones from the surface to the central core followed the sequence from Type I to type V. However, the relative amounts of the five morphological layers varied with the processing conditions and with their positions along the flow direction. It was also observed that type III structure appeared occasionally within the matrix of type II structure. At the vent end of the flow, only type III, type IV, and type V appeared in the cross section morphology. The origin of the five-zone structure can be explained according to the crystallization mechanism reported for conventional injection molding of polyoxymethylene and high density polyethylene [51, 98, 148, 151, 152].

The non-spherulitic skin layer crystallizes during the mold filling stage. When the hot melt is forced under pressure into the cooled cavity of the mold, some entangled molecules will stick to the cold wall and crystallize while others will flow by. This condition provides a mechanism for extension of connecting groups of molecules and crystallization of a complex fibril [98]. At high melt stress, the overgrowth of folded-chain lamellae will be in a planar manner and the orientation of polymer chains in the lamellae will be parallel to the flow direction.

Similar to conventional injection molding of Delrin 500 NC-10, the skin layer of the micro injection molded Delrin 900 P appeared translucent under the white light optical microscope. This is probably because the untwisted lamellar morphology may have structures at a size comparable to the wavelength of visible light that does not scatter light. The twisted lamellae layer, fine asymmetric spherulitic layer, oblate and spherulitic zones looked opaque because of their larger morphological units. This similarity could confirm the mechanism of structure development of the skin layer in micro injection molding.

As in the case of conventional injection molding, the above morphological characteristics suggest the following mechanism of structure development of the skin and other layers during micro injection molding. Upon completion of mold filling, the shear and extensional stresses decrease suddenly to a level determined by the amount of additional melt packed into the mold to compensate for shrinkage from cooling and crystallization. A discontinuity arises in the microstructure, as the highly oriented skin morphology transits to the lower oriented layers. Below this discontinuity, stress is insufficient for creation of fibril nuclei. Two competing mechanisms could exist for crystallization below the skin [98]: (i) the continued growth of twisted lamellae from the skin layer and (ii) the creation of new (non-fibril) nuclei and the formation of spherulites.

Opposite to the case of conventional injection molding [98], the formation of fine spherulites dominates the process due to very high thermal gradients in the case of micro injection molding. The twisted lamella region, which forms a wide region between the skin and spherulitic core in conventional injection molding of POM, is very narrow or sometime absent in micro injection molding, as shown in Figure 6-41 and Figure 6-42. The fine spherulites are formed under large thermal gradients. Accordingly, the nucleation rate is very high, thus limiting the size of the spherulites [8]. The competing mechanisms often result in a mixture of twisted lamellae with fine asymmetric spherulites near the skin interior boundary. The spherulite size increases slightly toward the oblate layer.

Further towards the mid-thickness of the molding, the temperature of the melt is at such a high level that spontaneous nucleation cannot occur. This results in the second discontinuity in morphology, where the fine asymmetric spherulitic morphology changes to oblate of much larger size. The oblate layer is a product of the interplay between nucleation rate and growth rate, as influenced by the temperature distribution. The outside undergoes faster cooling than the interior, and the nucleation rate decreases sharply with increasing temperature, upon proceeding inwards from the outside [63]. This causes more growth to occur on the high temperature side of the nucleus.

A clearly defined spherulitic core only appeared in case 5 and case 6, as shown in Figure 6-42. Here, the oblates start to grow earlier from a position closer to the upper and lower surfaces of the part. Thus, both time and space are available for random nucleation and subsequent growth, since random nucleation in the core region occurs after the oblate due to the temperature gradient.

The spherulite size increases with increasing distance from the skin-shear zone boundary to the oblate layer, and then decreases to the spherulite core. The smaller size of the spherulites in the core region is probably because the growth is halted by impingements among the growing spherulites in the core region and with neighbouring oblates.

The skin layers are probably formed during the filling stage, which provides the orientation for structure development. The twisted lamella structure, fine asymmetric spherulites, oblates, and spherulitic core are probably developed in the subsequent packing and cooling stages under low melt stress. Their relative volumes are determined, at least in part, by the rate of heat transfer to the mold wall.

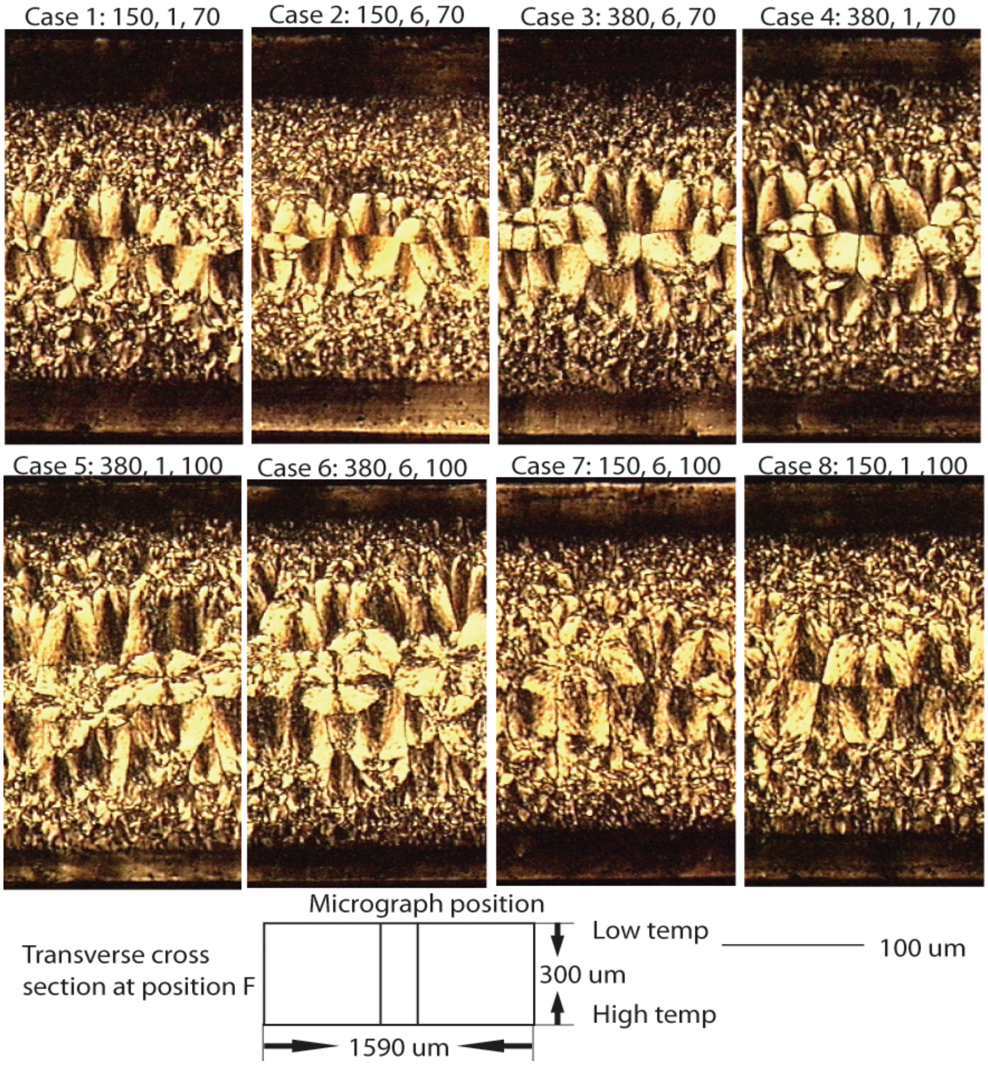

Figure 6-42: Morphology micrographs of micro injection molded polyethylene at position F for eight designed process conditions (Numbers above each micrograph denote the machine variables of injection speed (mm/s), packing velocity (mm/s), and mold temperature (ºC) respectively; Magnification: 100x)

It is worth noting that the morphology on the two sides of the spherulitic core is not symmetrical or identical, especially in the skin layer and its neighbouring region. The morphology on the fixed plate side has more apparent twisted lamellae, a slightly brighter and thinner skin layer, and bigger size of spherulites in the fine asymmetric spherulite layer, than the corresponding zones on the moving plate side, which has better temperature control. Careful examination of the experimental setup suggests that the non-symmetry in morphology is most likely due to the temperature imbalance between the moving plate and the fixed plate. The latter is assembled directly with the injection nozzle. Because the nozzle has a temperature close to melt temperature of the material, the average temperature of the fixed plate is actually higher than that of moving plate, which has better temperature control. Whiteside [2] reported a thermal gradient in the fixed plate, starting from the nozzle center towards the vent end of the cavity. With a higher mold wall temperature, longer time is needed to reach the freezing point, thus, less material crystallizes during the filling stage and more spherulitic material is formed. Subsequently, the large surface of the molding formed on the fixed plate side will be referred to as the high temperature surface, while that formed on the moving plate side will be referred to as the low temperature surface.

6.4.1.2 Morphology variation with process conditions

Figure 6-42 shows the morphologies across the whole thickness observed for eight designed processing conditions. The micrographs are taken in the middle of the transverse cross section at position F, using the polarized light microscope at magnification of 100X. The direction of view is along the X-axis of the plate, and the low temperature surface appears at the top. The narrowest spherulitic cores were found in case 1 and case 2, which involved the lowest injection speed and mold temperature. The packing velocity does not seem to be a noticeable factor in affecting the morphology. Increasing the injection speed from 150 mm/s in case 1 and case 2 to 380 mm/s in case 3 and 4, while keeping mold temperature constant, results in a significantly thicker oblate layer and narrower skin layer and more frequent appearance of random spherulites between oblates. Increasing the mold temperature from 70 ºC in case 1 and case 2 to 100 ºC in case 7 and case 8, while keeping injection speed constant, results in slightly increased thickness of the oblate and spherulitic zones and an increased average spherulite size as well. Also, it seems that the oblates are mixed with a number of small uniform spherulites. The effect of increasing both injection speed and mold temperature in case 5 and case 6 seems to yield the combined effects of increasing them individually. The oblate layer starts to grow from a position very close to the upper or lower surface and a clearly defined random spherulitic core appears between two oblate layers.

In order to evaluate the effect of processing conditions on morphology quantitatively and statistically, the cross section was divided into three morphological evaluation zones. The evaluation zone boundaries and the thicknesses of the three zones were roughly estimated from the photomicrographs of the transverse cross sections. The skin layer thickness, denoted as T_s, is a sum of the skin thicknesses of both surfaces. Because fine spherulites occasionally appear in the matrix of narrow twisted lamellar layer, the combined thickness of the two layers was measured and denoted as T_{ft}. The symmetric oblate layers and spherulitic core were measured together and denoted as T_{os}, since a clearly defined random spherulitic core does not always appear. In order to take into account thickness variation in the same specimen and among different specimens, three positions were selected from the microphotographs of the transversal cross section for each specimen and five specimens were selected for each processing condition.

The average values and standard deviations of measured thicknesses of the above defined three morphological evaluation zones are shown in Figure 6-43. The skin layer thickness T_s, fine spherulite and twisted lamella layers T_{ft}, and their sum, T_s+T_{ft}, follow a similar pattern, while the combined thickness of the oblate and spherulitic layers T_{os} follows the opposite pattern, as expected. The T_s ranged from around 45 µm in cases 5 and 6 to 85 µm in cases 1 and 2, which accounted for 15 to 28 percent of the total thickness. The T_{ft} ranged from 82 µm to 133 µm, which accounted for 27 to 44 percent of total thickness. The total percentage of the skin and fine spherulites and twisted lamella layers was up to 42 to 72 percent of the total thickness. Compared to conventional injection molding, the optimization of processing conditions in micro-injection molding could be more critical for tuning the microstructure needed to achieve the desired product properties, because of the larger fraction of the skin layer in micro injection molding.

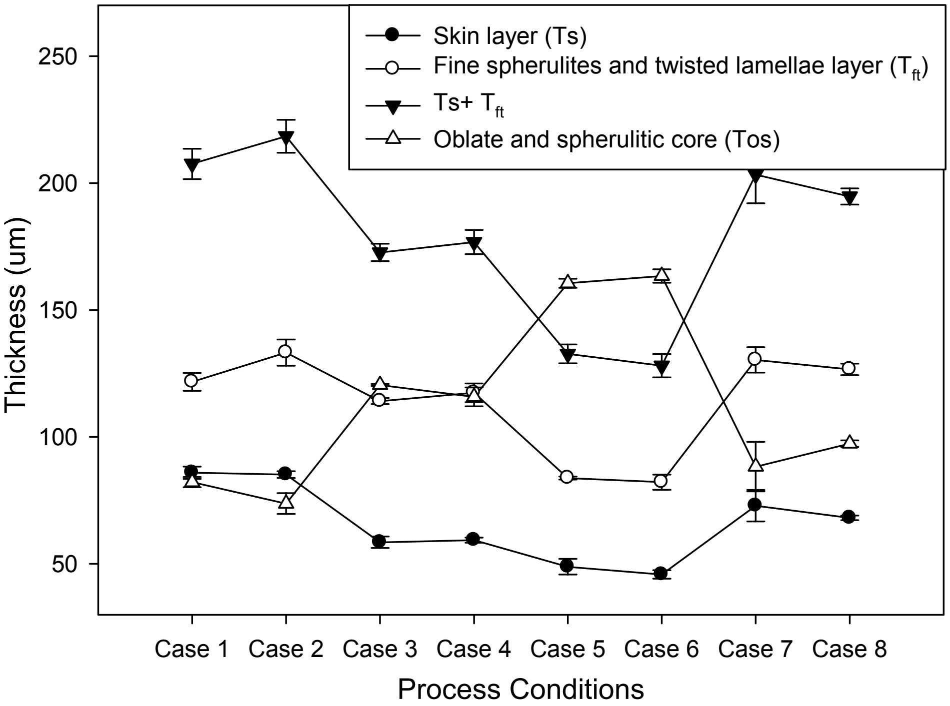

Figure 6-43: Variation of average thickness of three defined morphological evaluation zones with process conditions for polyoxymethylene

According to Figure 6-44, injection speed is the most significant factor that affects the thicknesses of the defined morphological evaluation zones. Increases in injection speed will result in a thinner skin layer, a thinner fine spherulite and twisted lamellae zone, and accordingly thicker oblate and spherulitic core. The mold temperature has a similar effect, but to a lower extent. The injection speed/mold temperature interaction may also have noticeable effect on the microstructure development, as shown in Figure 6-44. The above analysis implies that the relative amount of the skin layer is a function of flow and heat transfer during the filling and packing stages.

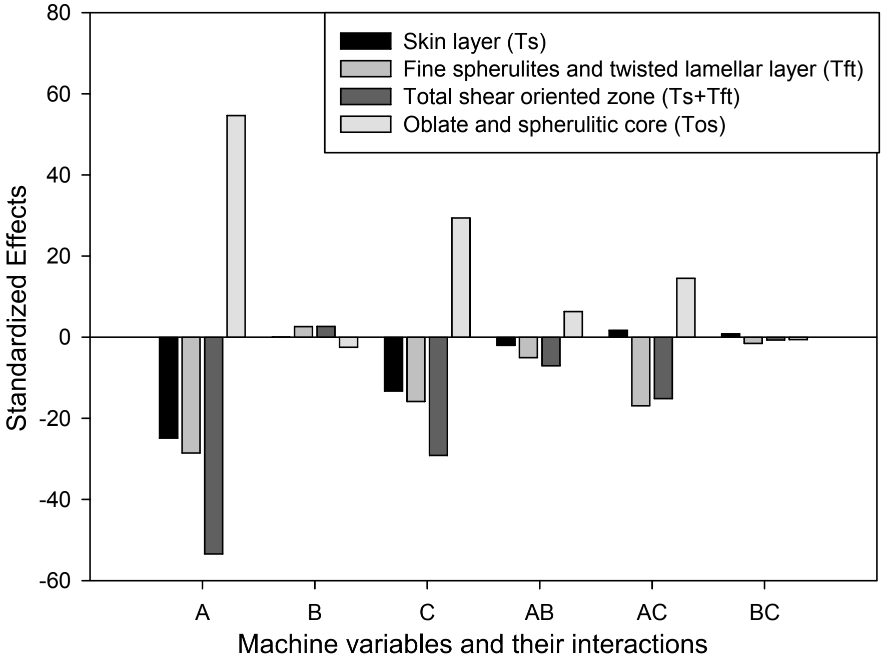

Figure 6-44: Standardized effects of process conditions on defined morphological evaluation zones

The effect of mold temperature here agrees well with findings for conventional injection molded polyoxymethylene [98], polyethylene (PE) [51], polyethylene/polypropylene (PE/PP) copolymer [153], and polybutylene terephthalate (PBTP) [154]. Lower mold-wall temperature and, thus, a higher temperature difference between the wall and the crystallization temperature produce a greater depth of oriented structures, because a thicker layer of melt reaches the crystallization temperature during the filling and packing stages.

Few reports could be found regarding the effect of injection speed on morphology for conventional injection molding, since injection pressure is the primary process control variable for conventional injection molding machines. The high injection speed setting in micro injection molding results in high melt temperature, due to shear heating at very high shear rate, and requires high injection and cavity pressures.

In conventional injection molding, the area fractions of the skin and shear zones for PE and PP homopolymer decrease linearly with melt temperature [12, 51, 107]. At higher melt temperature, less material is crystallized during the filling and packing stages, and more spherulitic material is present. The injection/cavity pressure will affect the microstructure, depending on the sensitivity of the freezing point to pressure. As the melt pressure increases by increasing the injection speed, the crystallization temperature of the polyacetal melt increases by about 2 ºC/1000 psi increase in pressure [148]. Therefore, the greater is the injection pressure, the greater is the temperature difference between the crystallization temperature and the constant mold-wall temperature and hence, the thicker is the surface layer of preferred orientation.

Since injection speed appears to be the most significant negative factor in affecting thickness of the skin layer and the most significant positive factor in affecting the oblate and spherulitic core layers, it is reasonable to suggest that shear heating plays a dominant role in the micro-injection molding process over high pressure during the filling and packing stages. The experimental observations are in good agreement with the simulation results regarding temperature distribution as shown in Figure 6-23 and Figure 6-24.

Figure 6-45 displays the morphology micrographs taken for a center point case and an extreme high injection speed case, in order to validate the above analysis. The variation of the morphological evaluation zones for the center point case seems to conform to the above analysis. However, the morphology appears to deviate from the above pattern for the extreme high injection speed case.

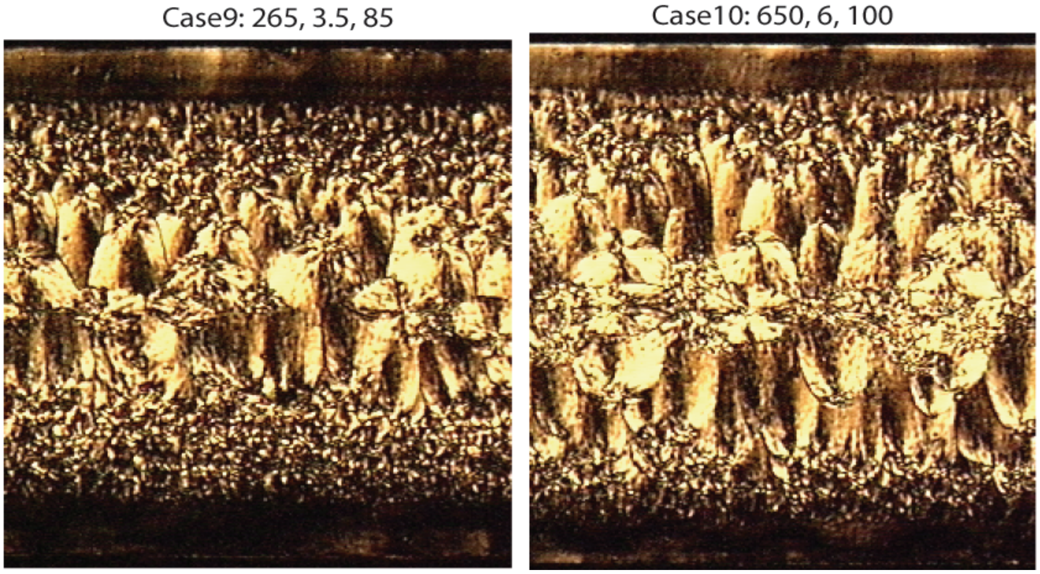

Figure 6-45: Morphology microphotographs of micro injection molded polyoxymethylene at position F for case 9 and case 10. (Numbers above each micrograph denote the machine variables of injection speed (mm/s), packing velocity (mm/s), and mold temperature (ºC) respectively; Magnification: 100x)

Figure 6-46 displays the variation of the thicknesses of the defined morphological evaluation zones with injection speed. Upon increasing the injection speed from 150 mm/s to 380 mm/s, the skin layer thickness and the thickness of the fine spherulites and twisted lamella zone decreased significantly with increasing injection speed. Upon increasing injection speed further from 380 mm/s to 650 mm/s, the skin layer thickness decreased slightly, while the thickness of fine spherulites and twisted lamellae remained almost constant. Accordingly, the thickness of the oblate and spherulitic core increased significantly with the increasing injection speed from 150 mm/s to 380 mm/s, and then increased slightly when injection speed increased from 380 mm/s to 650 mm/s. Since the statistical analysis does not seem to be applicable for injection speeds exceeding 380 mm/s, it is reasonable to speculate that the conventional viscosity model is not applicable in the micro scale cavity at high injection speed. It is possible that slippages occur at polymer-mold, melt-solidified polymer, and polymer-polymer interfaces.

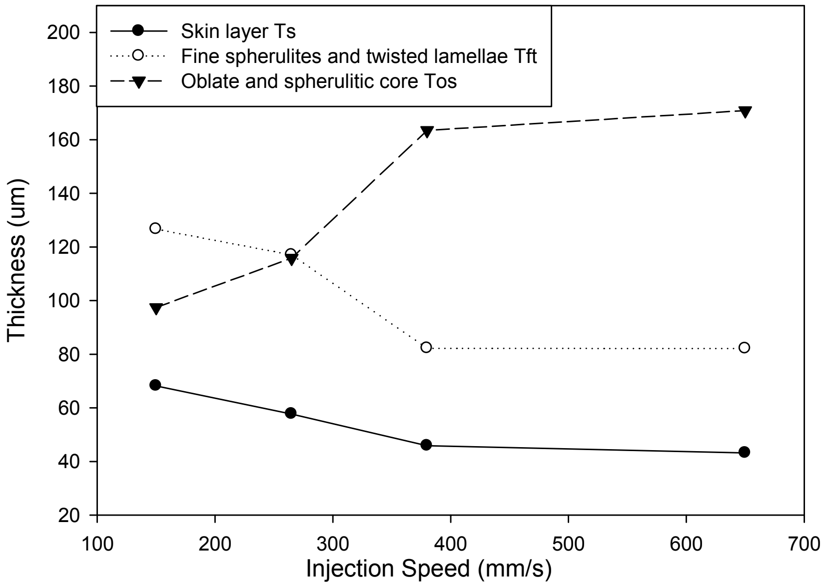

Figure 6-46: Morphology variation with injection speed

Figure 6-47 shows the variation of spherulite size with depth at positions D and F for both case 2 and case 5, where the injection speed and mold temperature were set to low levels in case 2 and high levels in case 5. In all four positions selected, the spherulite size increased from the interior of the skin layer toward the spherulitic core, due to variation of cooling rate. The variation of spherulite size is a combined effect of pressure, shear stress, and temperature distributions in the three-dimensional mold [51]. Firstly, the fast cooling near the skin layer gives rise to small spherulites, while slow cooling close to the spherulitic core gives large ones [63]. Secondly, the spherulites near the skin layer may be formed during the cavity filling and packing stages, when the nucleation rate is enhanced by higher pressure and shear stress. Moving towards the core region, the material crystallizes at a lower nucleation rate due to higher temperature, lower pressure, and lower shear stress, so the spherulites grow to a larger size until impingement.

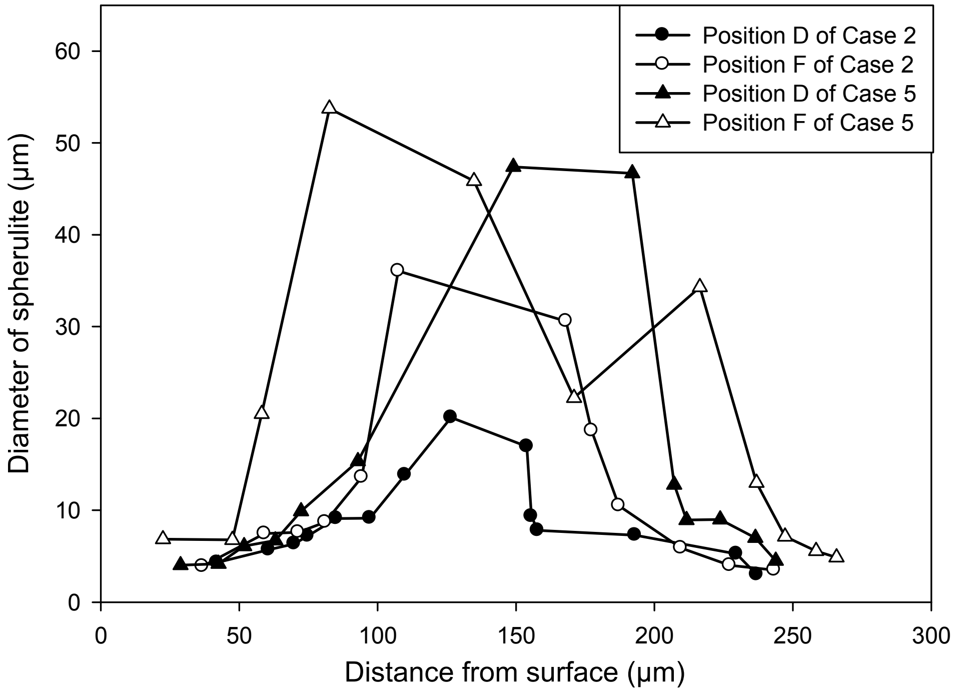

Figure 6-47: Spherulite distribution across thickness of Case 2 and Case 5

The average spherulite size in case 5 is significantly larger than that in case 2, and the spherulite size at the central core of position F is larger than that of position D in both cases. The larger size of spherulites in the core region at position F could be attributed to the high bulk temperature of the material, as a result of shear heating. The larger spherulite size in case 5 is mainly attributed to the higher average bulk temperature of the material, as a result of larger shear heating effect at the higher injection speed, and less heat loss to the mold wall in case of high mold temperature.

It has been suggested in the literature [155-159] for conventional injection molding that polymers crystallized with large spherulites are associated with higher crystallinity than smaller spherulites. However, the former tend to be more brittle due to a greater concentration of defects, including voids, at the edges of the large spherulites, which have more time to reach a higher degree of perfection. To avoid the negative effects of these defects, heterogeneous nucleants may be used in order to achieve smaller spherulitic structure in manufactured micro products.

6.4.1.3 Morphology evolution along flow

Figure 6-48 shows morphology evolution along the flow direction from position B to position D and to position F. The longitudinal cross sections (XZ plane), with increasing distance from the gate, are shown from left to right in the top row. The transverse cross sections (YZ plane) of these positions are shown in the bottom row. The following observations can be made regarding the evolution of morphological features

1) The skin layer morphology of the sample near gate presents the V-shape pattern at the wall, which will be discussed in detail in the next section;
2) The spherulitic core thickness becomes larger with increasing distance from gate;
3) At high mold temperature, the skin layer near the XZ cross section surface appears to be more distinct and uniform than the corresponding layer in the YZ cross section;
4) The skin layer thickness decreases with increasing distance from gate;
5) The cross section morphology is not symmetric along the center axis.

In order to fully appreciate the effect of flow behaviour and heat transfer in the micro injection molding process, the sample was cut firstly along YZ plane into 10 to 12 slices and then cut longitudinally along the center XZ plane into slices of 10 μm thickness. The morphology microphotographs were viewed in the longitudinal cross section (XZ plane) for each specimen at a magnification of 40x and the evolution of morphology was followed by placing the microphotographs sequentially according to their original position before cutting, as shown in Figure 6-49.

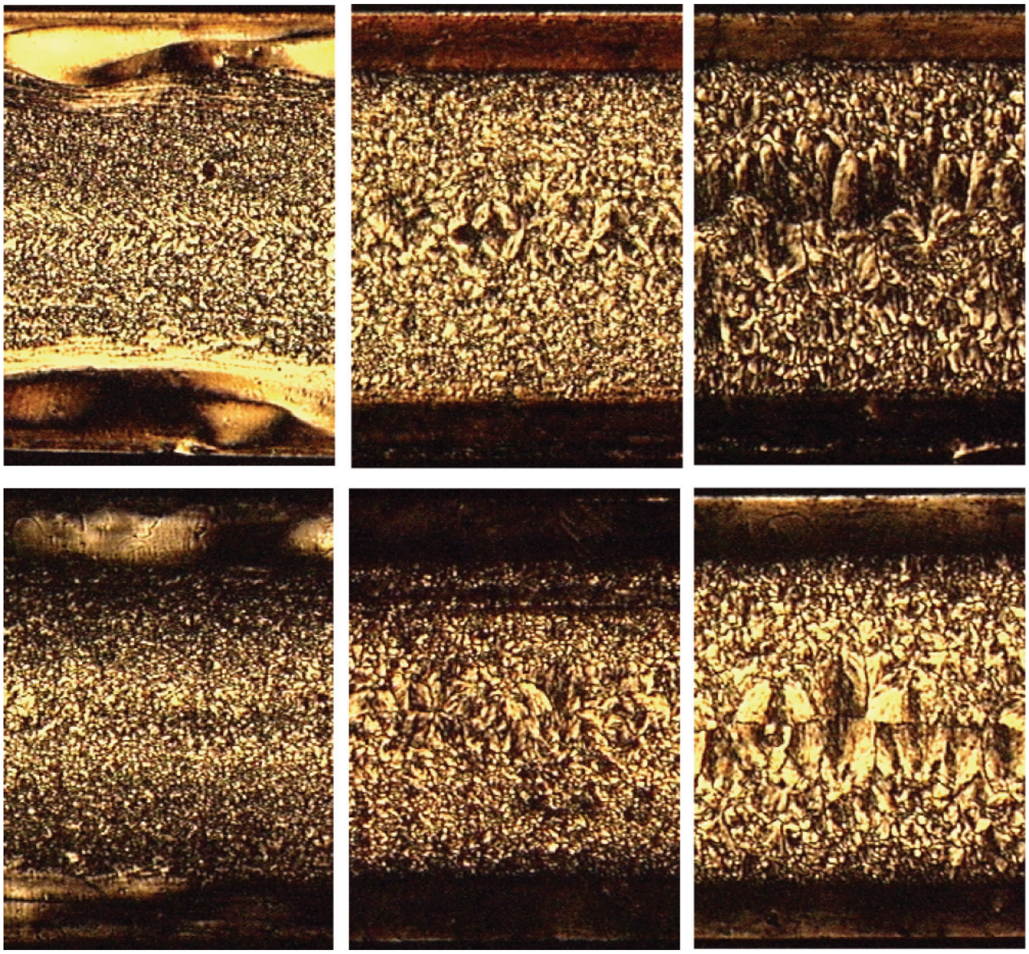

Figure 6-48: The evolution of morphology along the flow direction in case 7 for POM. Top row: longitudinal (XZ) cross section at positions B, D, and F (from left to right). Bottom row: YZ cross section at the above positions. (Magnification: 100x)

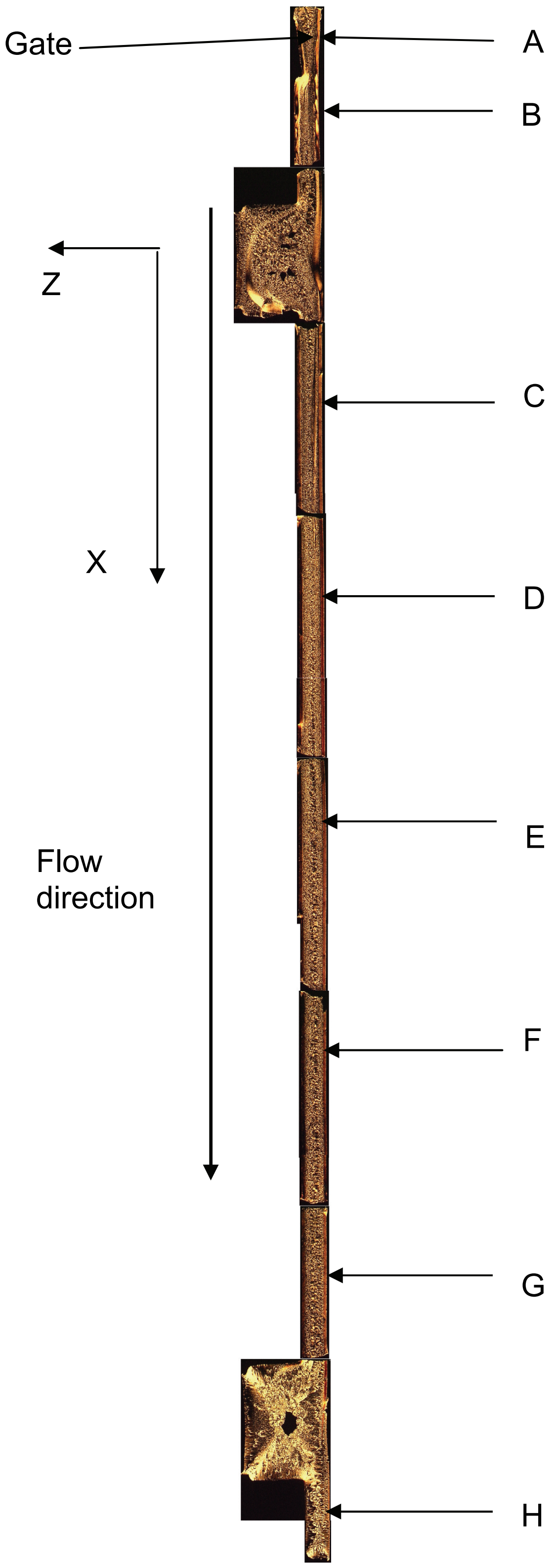
Gate
A
B
Z
C
X
D
E
Flow direction
F
G
H

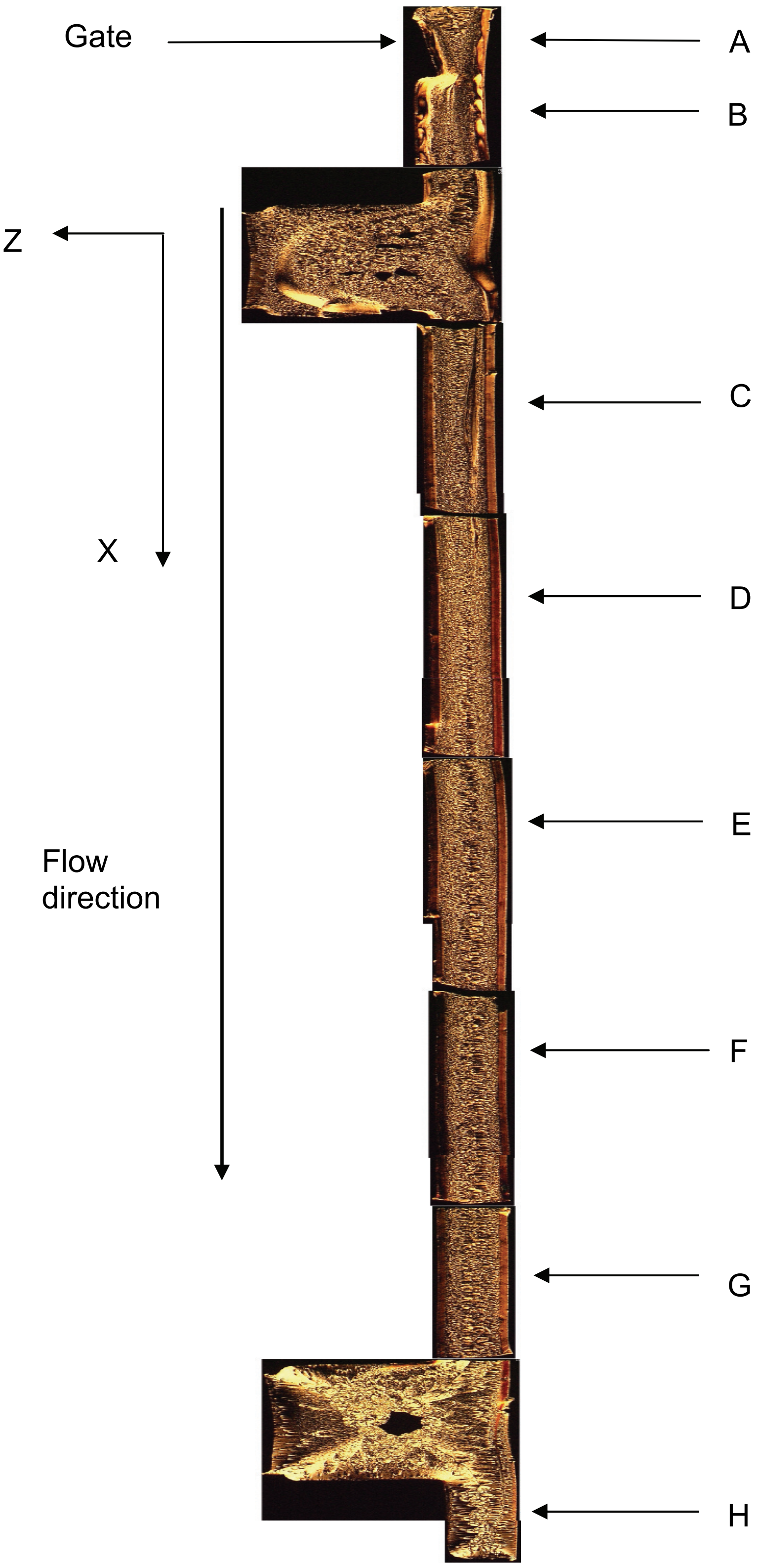

Figure 6-49: (a) Morphology of XZ cross sections of micro injection molded polyoxymethylene (case 7, at a magnification of 40x); (b) Morphology of XZ cross section with tripled scale of width in Z-direction

Figure 6-50 displays the evolution of the thickness of the morphological zones along the flow directions from position B to position H. The skin layer thickness T_s decreased along the length of the plate from 120 μm at position B near the gate to position H near the vent end, where no evidence of a skin layer was observed. Near the vent end, only fine spherulites, oblate, and spherulitic core were present. In the uniform thickness section, from Position C to position G, the thicknesses of the skin, T_s, and the fine spherulites and twisted lamellae, T_{ft} decreased almost linearly, except at position E, where there was a hole around 20 μm deep, reserved for the installation of a pressure sensor. This finding agrees with the skin layer variation reported for conventional injection molding [98] for a similar material, where the variation in skin layer thickness was attributed to variations in both velocity of the polymer melt during filling and pressure along the flow direction.

The melt velocity is high near the gate close to the mold surface. As a portion of the melt crystallizes near the wall, large numbers of fibrillar nuclei are formed, because of the high molecular orientation near the crystallizing surface, due to the high velocity of the melt. The melt velocity decreases, as the melt progresses from the gate to the melt front toward the vent end during the filling stage. Also, the crystallization temperature is expected to be high near the gate, because the pressure is highest in that region, and it decreases along the flow direction, reaching the lowest value at the vent end. These factors should contribute to a thinning of the skin layer, as the melt progresses from the gate to the vent. The variation of thickness in the oriented skin layer along the flow direction for the micro injection molded POM, shown in Figure 6-50, confirms the above analysis. No mechanism exists at the vent end of the plate for molecular extension and creation of fibril nuclei with the melt velocity decreasing toward a low value. Nucleation is initiated at random sites, and, in the absence of melt stress, crystallization proceeds to form oblates near the wall and random spherulites in the core.

The structure distribution along the flow length suggests that, during the mold design stage, it would be advisable to position the part of the molding requiring for high modulus and strength near the gate, where the skin layer thickness is high.

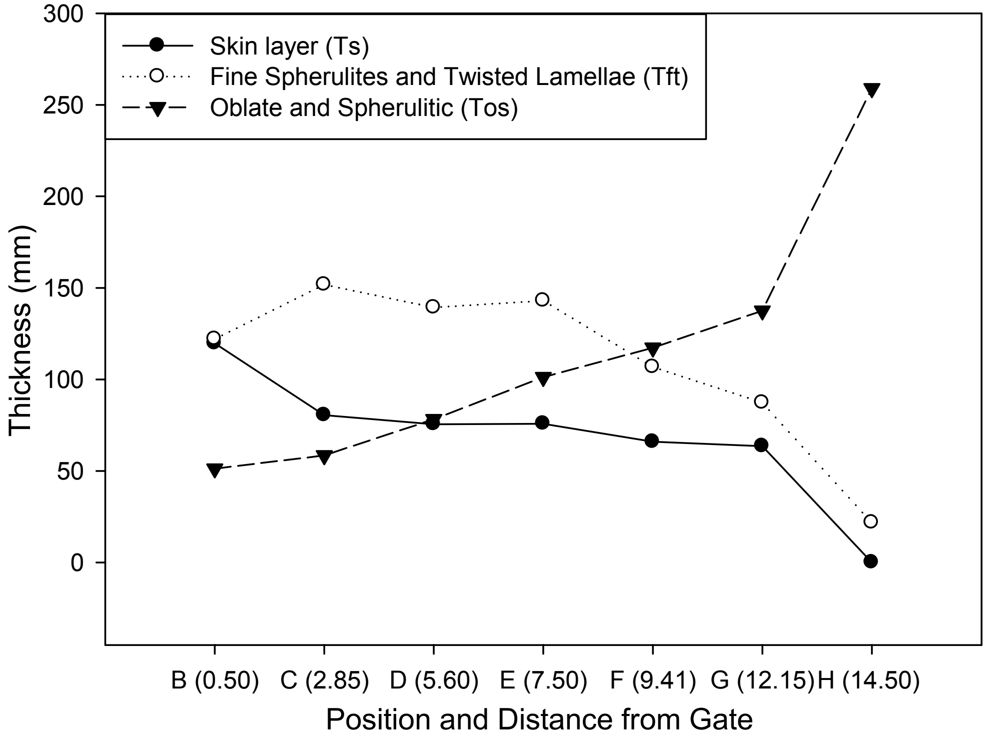

Figure 6-50: Morphology variation along flow direction of POM Case 7

6.4.1.4 Morphology in the gate region

Figure 6-51 displays the morphological characteristics in the gate region for POM Case 4. Three features can be observed. The first feature is the consecutive V-shape yellow pattern. The V-shape pattern may have been caused by remelt and flow of the interior part of the skin layer. The skin layer is a non-spherulitic layer, having a high degree of orientation of chain molecules parallel to the injection direction. When the hot melt is forced under pressure into the cooled cavity of the mold, some clusters of entangled molecules will stick to the cold wall and crystallize while others will flow by, thus providing a mechanism for extension of connecting groups of molecules and crystallization of a complex fibril [98]. Under conditions of high melt stress, the overgrowth of folded-chain lamellae will be planar and the net molecular orientation will be parallel to the flow direction.

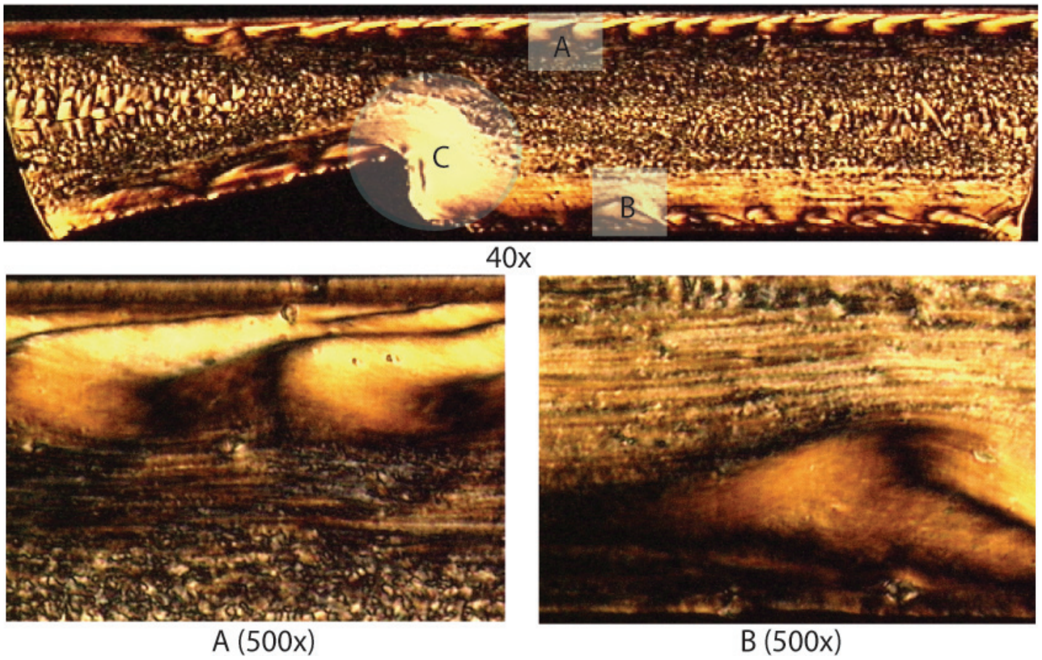

Figure 6-51: Morphology characteristics in the gate region of POM Case 4

Theoretically, the skin layer will continue to grow during cavity filling. However, the growth of the crystallized skin layer will slow down the removal of heat from the melt to the cold mold wall due to its low heat conductivity. Eventually the interior part of the skin layer may gain more heat from the material flowing by the crystallizing surface than the heat it loses to the mold wall, especially in areas such as the gate region, where viscous dissipation is large due to the high shear rate. As a result, the interior part of the frozen skin layer may be remelted and the remelted material will be dragged forward by the shear flow, forming the V-shape as observed in Figure 6-51. The consecutive V-shape pattern may be caused by the shaking movement of the injection plunger, and the formation of V-shapes may also contribute to the plunger shaking.

Another possible reason for the V-shape pattern could be slip-stick flow, which was reported at the polymer melt/mold wall interface for the conventional injection molding process [160-163]. However, this was not supported by the results of the examination of the morphology in the gate region of short shots as shown in Figure 6-52. The V-shape pattern did not appear in the morphology of the short shot, so it was most likely formed after the skin layer was developed during the filling stage. The ball-shape material in front of the flow front was probably formed by the spill of the melt from the center of the flow front while the flow stopped suddenly at end of the short shot.

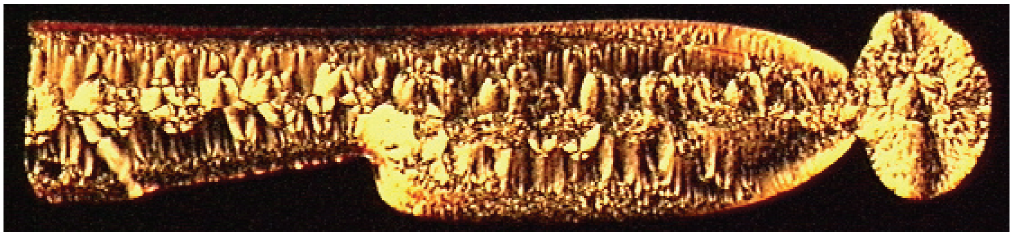

Figure 6-52: Morphology in the gate region of a short-shot molding (Magnification: 40x)

The second feature is the presence of highly oriented polymer chains next to the skin layer, as shown in the zoomed views at position A and position B as shown in Figure 6-51. The formation of the skin layer will forces the melt to flow in an even narrower channel and increases the shear stress. The extended polymer molecules freeze quickly because they are close to the skin layer. The highly oriented structure may be responsible for the high melting temperature observed in the DSC results, as shown in Figure 6-39 for the gate specimen.

The third feature is the high molecular orientation at the junction of the gate and the part indicated as position C in Figure 6-51. The polymer experiences a positive extension in the tapered gate, due to the gradual reduction in thickness along the flow direction. This is followed by a negative extension (i.e. expansion), when the melt enters the thicker part of the cavity. The material at position C should have lower molecular orientation than the region to its left, but the orientation could be frozen in quickly in the molding, before it relaxes completely due to the large ratio of mold surface area to material at this position.

The three microstructural features observed for the micro injection molding process reflect important effects of the special boundary conditions of microscale melt flow, which do not exist in or are probably not as important in the conventional injection molding process.

The above observations were supported by further evaluation of the morphological characteristics of the gate region under different process conditions, as shown in Figure 6-53. The V-shapes obtained under the process conditions of low injection speed, such as in case 2 and case 7, are sparser and larger, while those at high injection speed are denser and smaller. Also, the V-shapes obtained at high injection speed appear closer to the gate entrance than those obtained at low injection speed. These observations are probably because the frozen skin layer could be remelted and dragged more easily at high injection speed, due to the thinner skin layer, higher shear stress, and higher material temperature, when the injection speed is set at a high level.

The molecular orientation at position C appears to be stronger for process conditions at low mold temperature, such as in cases 2 and 4, than at high mold temperature, such as in cases 6 and 7. At lower mold temperature, the material freezes more quickly due to faster removal of heat from the polymer melt. As expected, the highest polymer molecular orientation at position B can be easily observed in case 4, which has the high injection speed and low mold temperature.

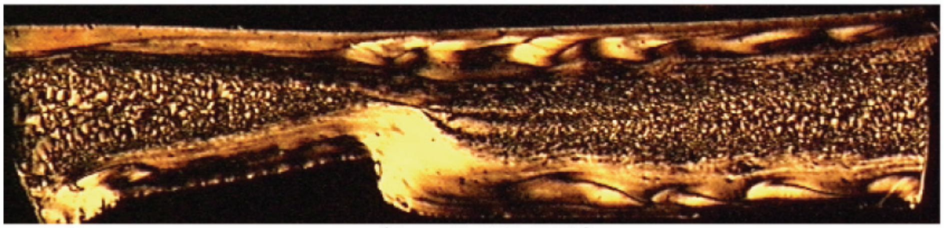

(Case 2: 150, 6, 70)

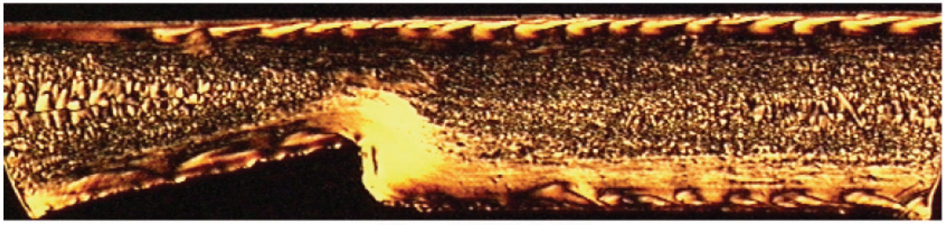

(Case 4: 380, 1, 70)

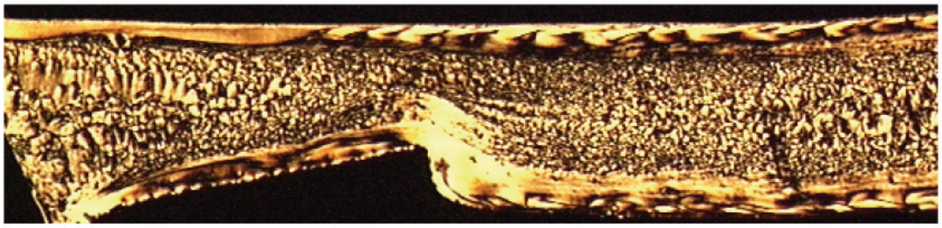

(Case 6: 380, 6, 100)

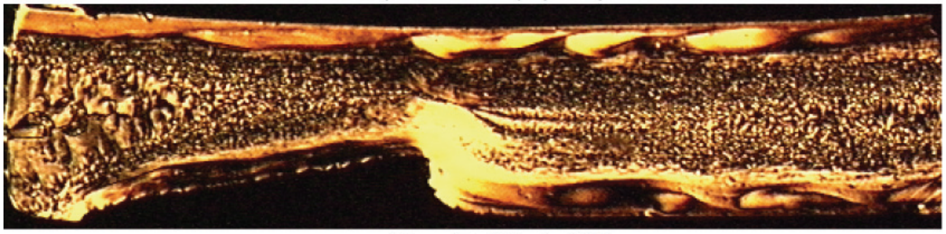

(Case 7: 150, 6, 100)

Figure 6-53: Morphology microphotographs of the gate region under different process conditions. (Magnification: 40x)

6.4.2 HDPE (Sclair 2714)

6.4.2.1 The skin-core structure

In order to observe the morphology of micro injection molded HDPE (Sclair 2714), the samples were firstly cut in the transverse direction (YZ plane) at position F and five samples were selected for each set of process conditions. Surprisingly, all tests showed evidences of jetting and flow irregularity, as will be shown later in this section. Relatively stable skin-core structure was only observed in case 4 and case 6, where injection speed and melt and mold temperatures were all set to low levels, as illustrated in Figure 6-54. Multiple morphological patterns were observed in the individual samples prepared under experimental conditions with higher parameter settings.

Figure 6-54 shows the morphology from the surface to a depth of 163 μm, around half way across the thickness of the sample. Three layers could be identified:

1. a non-spherulitic skin layer, having a high degree of chain orientation, parallel to the injection direction;
2. an intermediate layer, comprising a thin layer of twisted lamellae mixed with fine spherulites;
3. a random spherulitic core, having essentially no preferred orientation.

The boundary between the non-spherulitic skin and intermediate layers appears quite sharp, while the boundary between the intermediate layer and spherulitic core appears diffuse. Microscopic observation of the skin between crossed polarizers along the flow direction reveals no perceptible crystalline development, except a bright yellow serrated edge, which is most likely a cutting artefact according to Kantz et al. [12]. However, the bright line observed by Tan and Kamal [51] was regarded as a layer of fine spherulites for polyethylene.

In contrast to the morphology reported for POM in the last section, an obvious oblate layer is missing for micro injection molded HDPE (Sclair 2714). The factors considered for POM microstructure development may be applicable to explain the microstructure development for HDPE.

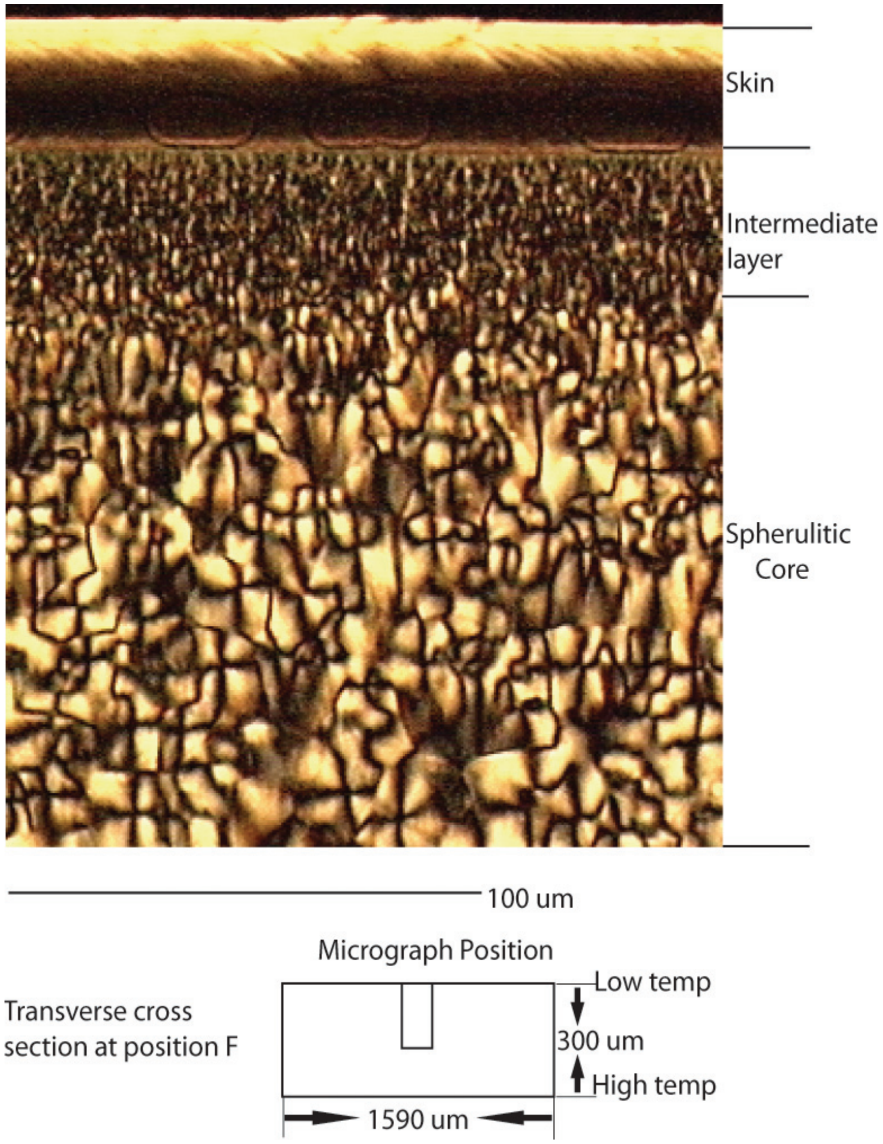

Figure 6-54: The skin-core morphology of micro injection molded polyethylene. (Magnification: 200x)

6.4.2.2 Morphology variation with process conditions

Although multiple morphological patterns were observed for individual sets of process conditions, the mechanical properties of each of these process conditions appeared to be quite stable, as shown in Figure 6-73. On the other hand, the mechanical properties were found to be sensitive to various process conditions. So, it is interesting to explore the morphology variation with process conditions. Figure 6-55 to Figure 6-65 display typical morphological patterns observed for each process condition. The most common feature of the morphology of micro injection molded HDPE (Sclair 2714) is the row nucleated structure, where a string of lamellae have their origin in the same region of sheared material. This structure was attributed to the extension of polymer chains by Hemsley [63]. An extended polymer chain has effectively a higher crystallization temperature than that of the bulk material, so that, at a given temperature below the crystallization temperature, an extended chain will have a larger supercooling, compared to the unextended material. Thus, there is a greater driving force towards crystallization. Moreover, the extended chain is closer to the final crystallized form of the polymer than is a random coil. So an enhanced rate of crystallization might be expected [63].

In the micro injection molding process, the extension of polymer chains is probably caused by the relative movement of the melt at interfaces between the first jet of material and subsequent filling flow afterwards, or simply by the shear flow. Jetting usually occurs when polymer melt is pushed at a high velocity through the gate, which has the smallest cross section, into a thicker plate, without forming contact with the mold wall [137, 141]. When jetting occurs, the material at the surface of the snake-like stream of polymer melt may have cooled and crystallized during jetting, then it would be remelted and stretched by the forward or backward filling flow. The polymer chains at the irregular interface could act as the origin of row nucleation.

Figure 6-64 displays the morphology of case 10, which has the largest elongation-to-break in all HDPE samples. It is clear that the sample of case 10 has a large fraction of the self row nucleated structure, especially in the left microphotograph, where the evidence of irregular flow can be identified clearly. The large strain of this case may be attributed to a cooperative deformation and slippage of lamellae between tie molecules in the row structure when strained [149]. Case 11 shows that a much more stable flow pattern than in case 10 may be obtained, when the melt temperature was set to a low level.

The flow problems encountered with the process imply that gate repositioning or a different shape of gate may be required for processing the HDPE (Sclair 2714) [141]. An optimized piston-speed profile could also be used so that melt-front velocity is initially slow when melt passes through the gate, then increases once regular filling flow is achieved [137].

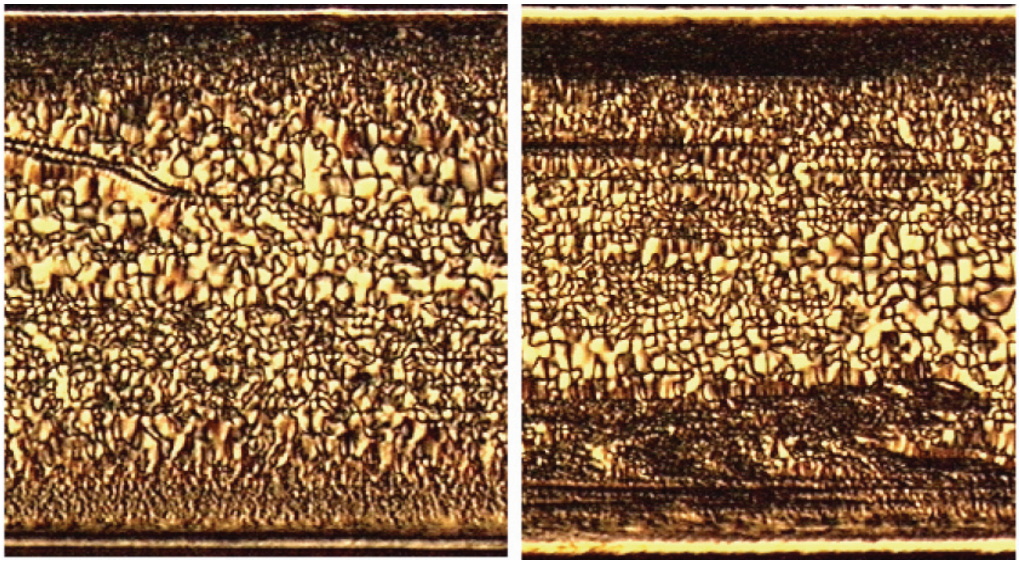

Figure 6-55: Transversal cross section at Position F of HDPE Case 1. (Magnification: 100x)

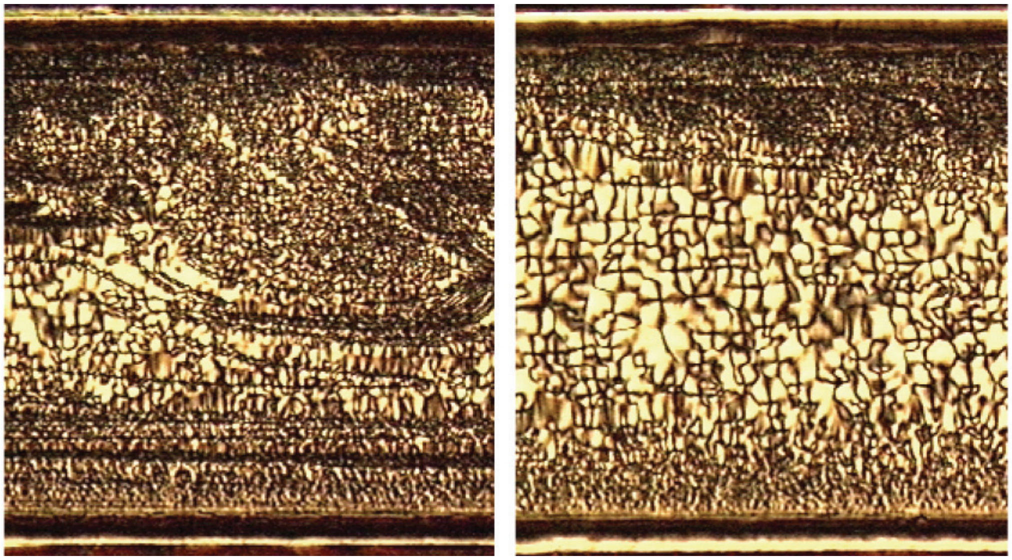

Figure 6-56: Transversal cross section at Position F of HDPE Case 2. (Magnification: 100x)

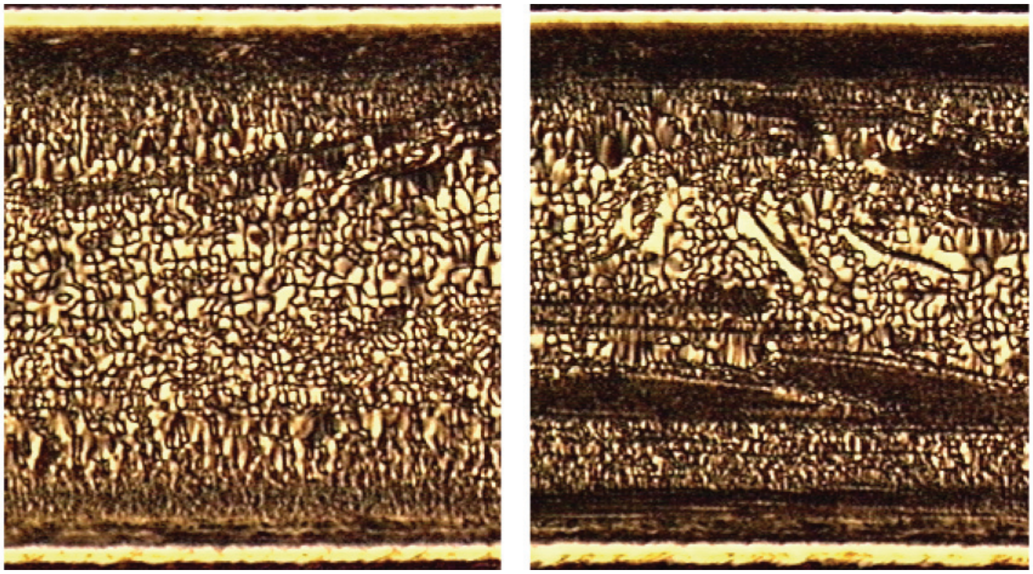

Figure 6-57: Transversal cross section at Position F of HDPE Case 3. (Magnification: 100x)

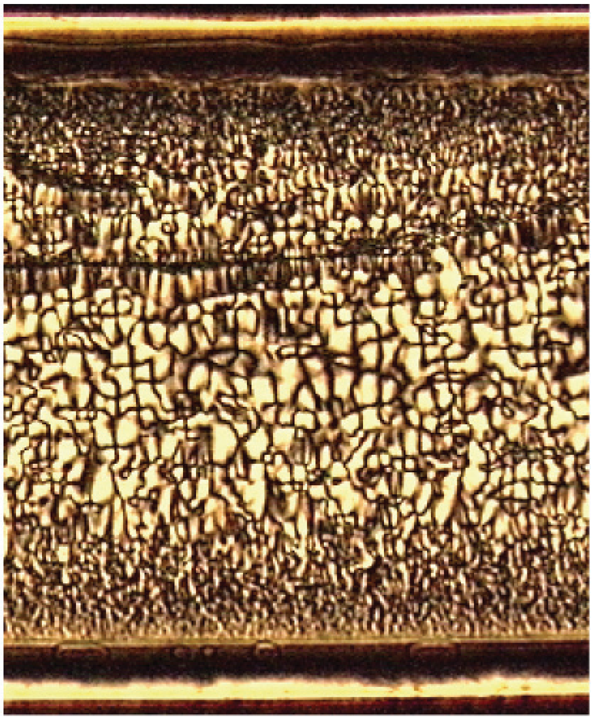

Figure 6-58: Transversal cross section at Position F of HDPE Case 4. (Magnification: 100x)

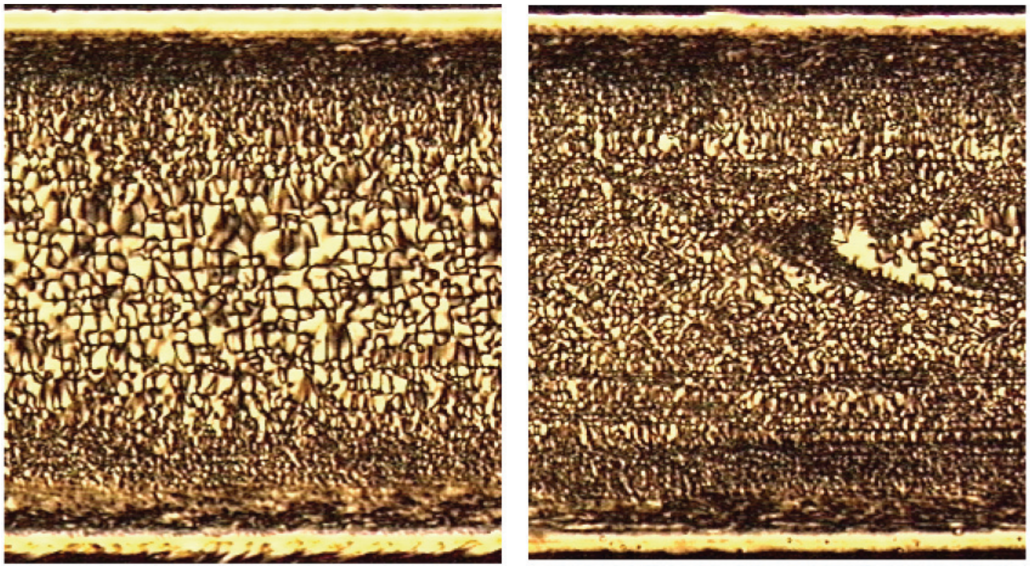

Figure 6-59: Transversal cross section at Position F of HDPE Case 5. (Magnification: 100x)

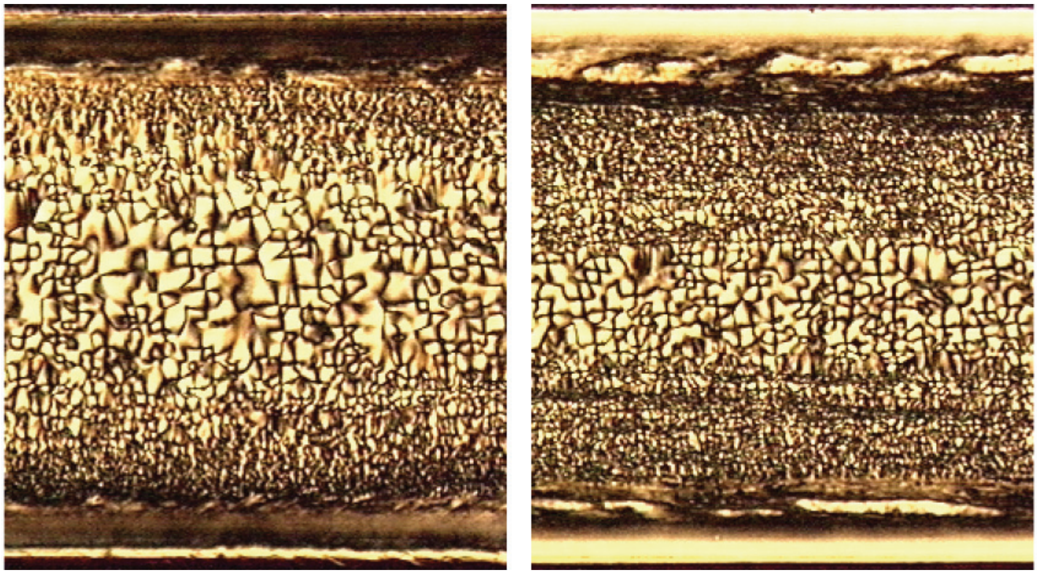

Figure 6-60: Transversal cross section at Position F of HDPE Case 6. (Magnification: 100x)

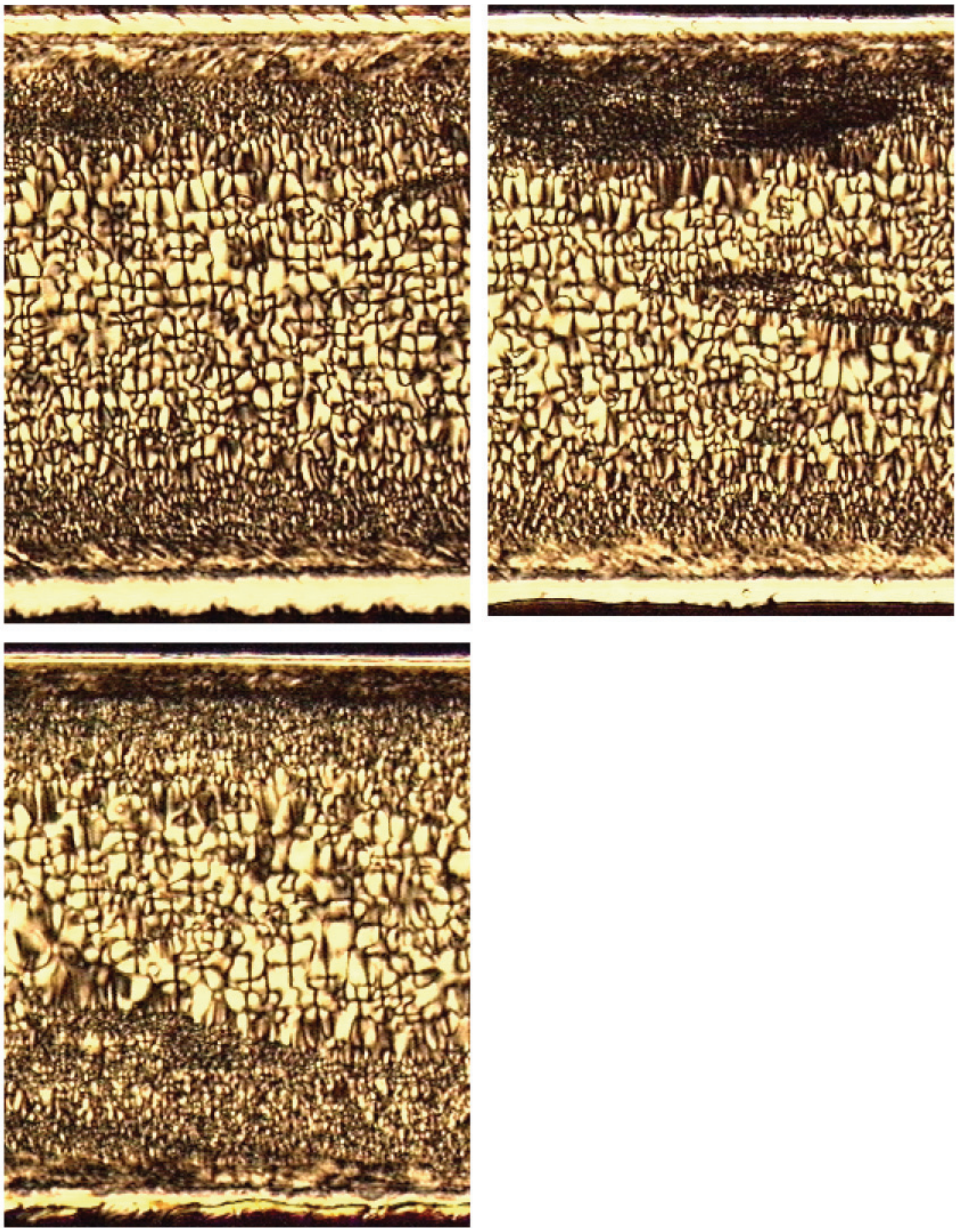

Figure 6-61: Transversal cross section at Position F of HDPE Case 7. (Magnification: 100x)

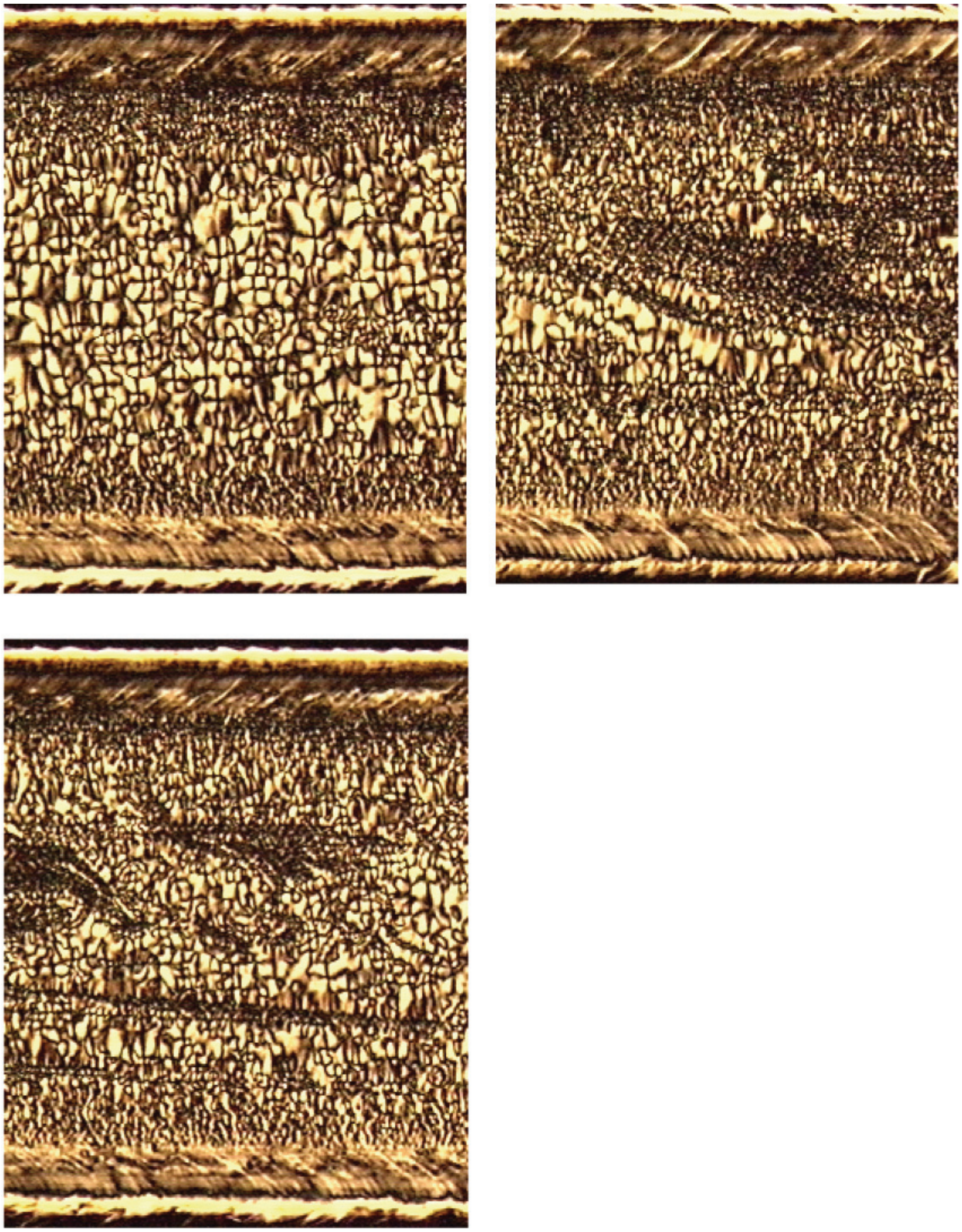

Figure 6-62: Transversal cross section at Position F of HDPE Case 8. (Magnification: 100x)

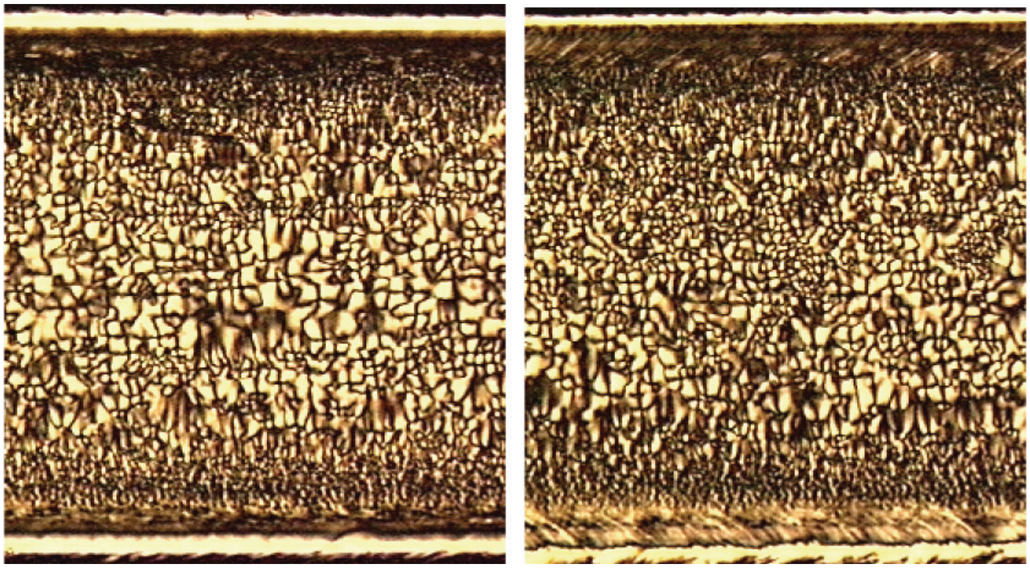

Figure 6-63: Transversal cross section at Position F of HDPE Case 9. (Magnification: 100x)

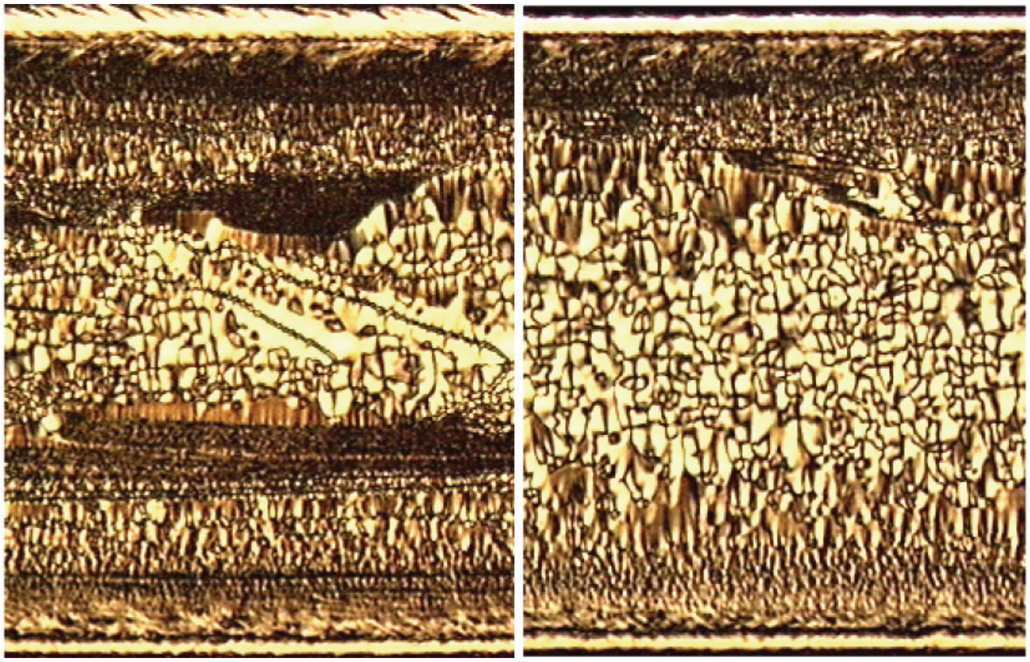

Figure 6-64: Transversal cross section at Position F of HDPE Case 10. (Magnification: 100x)

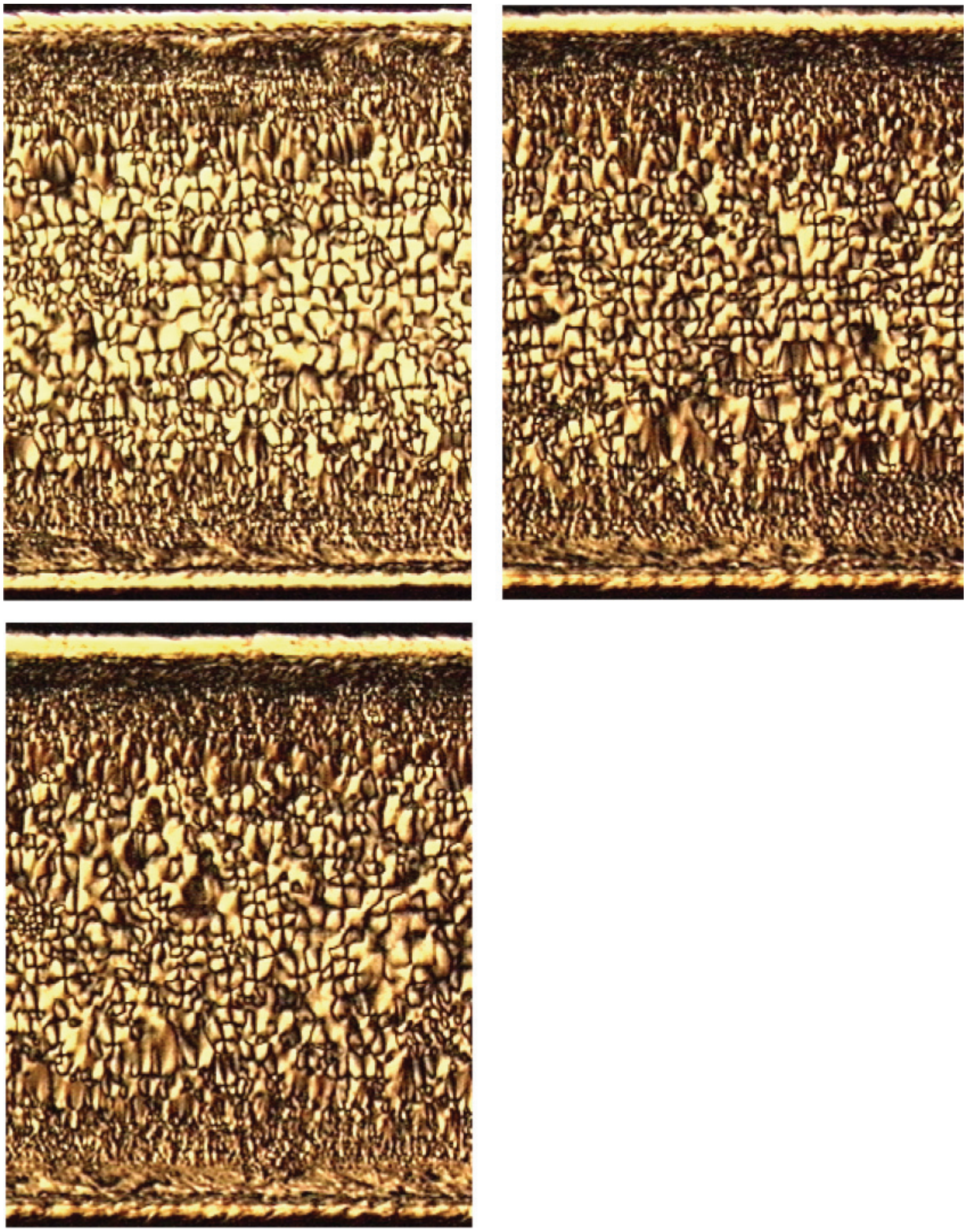

Figure 6-65: Transversal cross section at Position F of HDPE Case 11. (Magnification: 100x)

Due to the flow irregularity and its apparent impact on morphological irregularity in the experiments of HDPE (Sclair 2714), the skin layer thickness was selected as the only parameter to evaluate the effect of process conditions on microstructure development. Despite the complex flow behaviour, the skin layer thickness of micro injection molded HDPE Sclair 2714) exhibited significantly lower data dispersion than was observed with polyoxymethylene as shown in Figure 6-66. The largest skin layer thickness was found in case 6, in which injection speed, mold temperature, and melt temperature were set to low levels.

According to Figure 6-67, injection speed was the dominant negative factor affecting skin layer thickness. An increase in the injection speed resulted in a decrease in skin layer thickness.

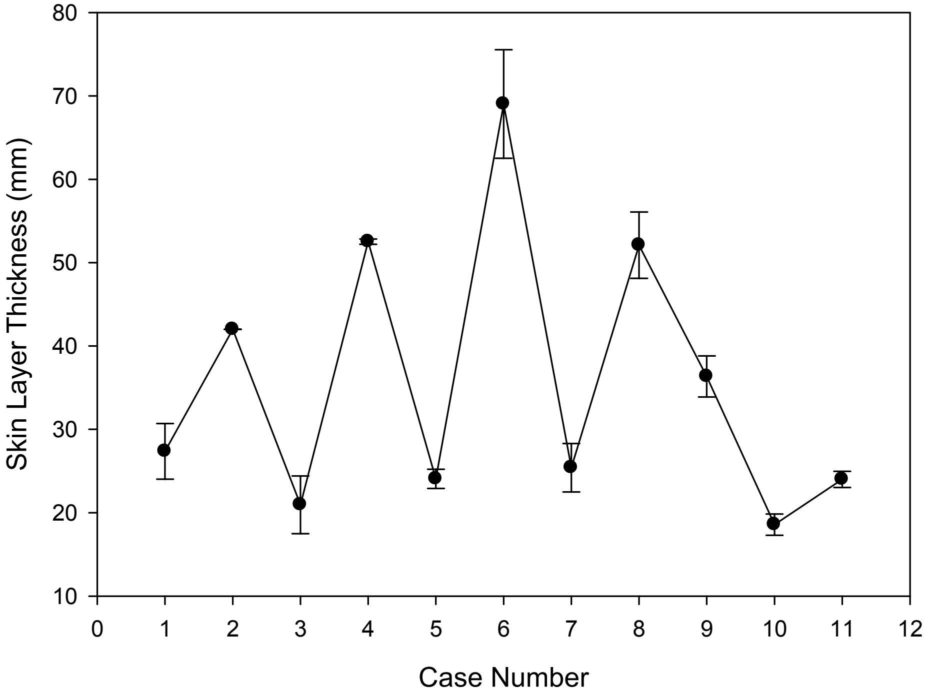

Figure 6-66: Skin layer thickness variation with process conditions

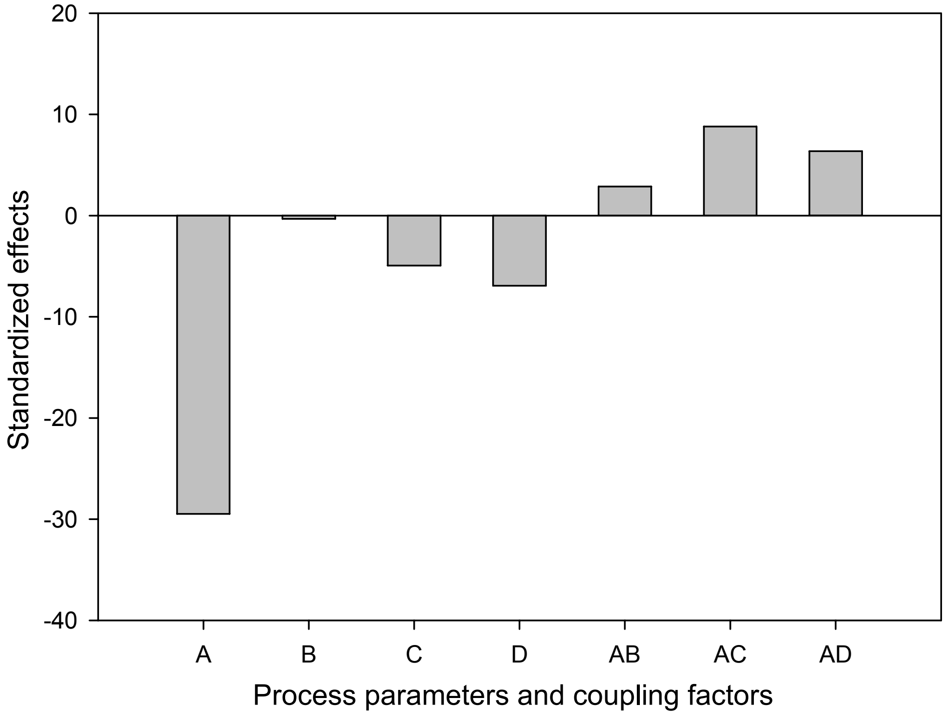

Figure 6-67: Standardized effects on skin layer thickness of HDPE (Sclair 2704)

6.4.2.3 Morphology evolution along flow

In order to understand more clearly flow behaviour and heat transfer in the micro injection molding of HDPE, a sample obtained for case 6 was cut firstly along the YZ plane into 10-12 pieces and then cut longitudinally along the center XZ plane into cross sections of 20 μm thickness. The morphology microphotographs were viewed in the longitudinal cross section (XZ plane) for each specimen at a magnification of 40x and the evolution of morphology was followed by placing the microphotographs together sequentially according to their original positions, as shown in Figure 6-68.

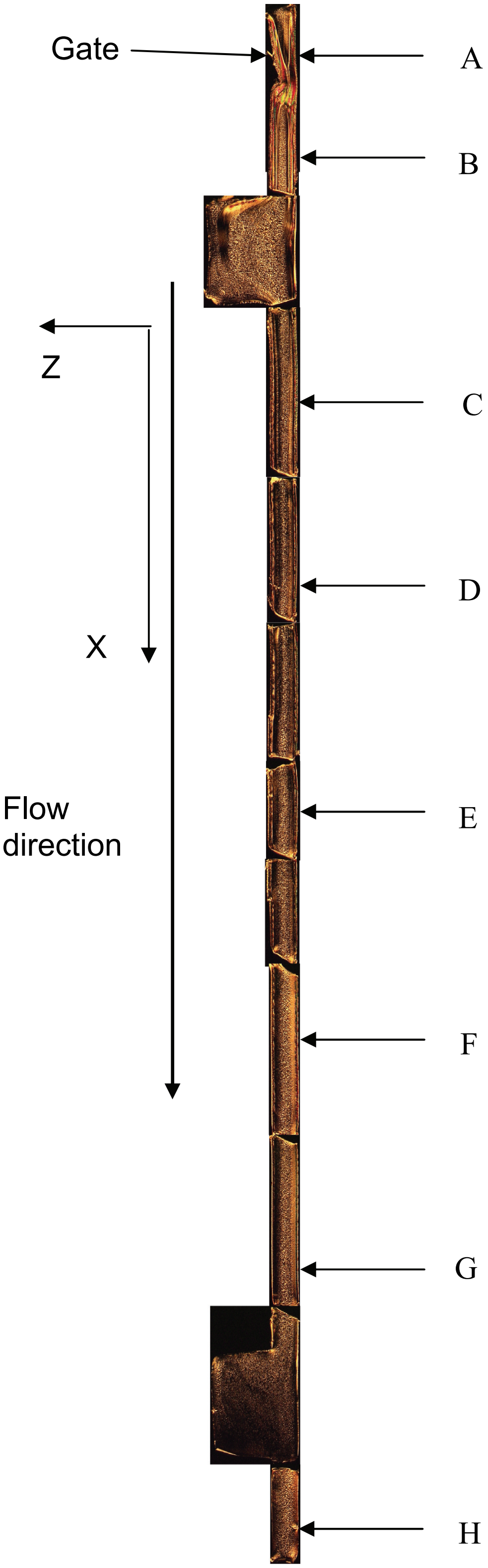
Gate
A
B
Z
C
D
X
Flow direction
E
F
G
H

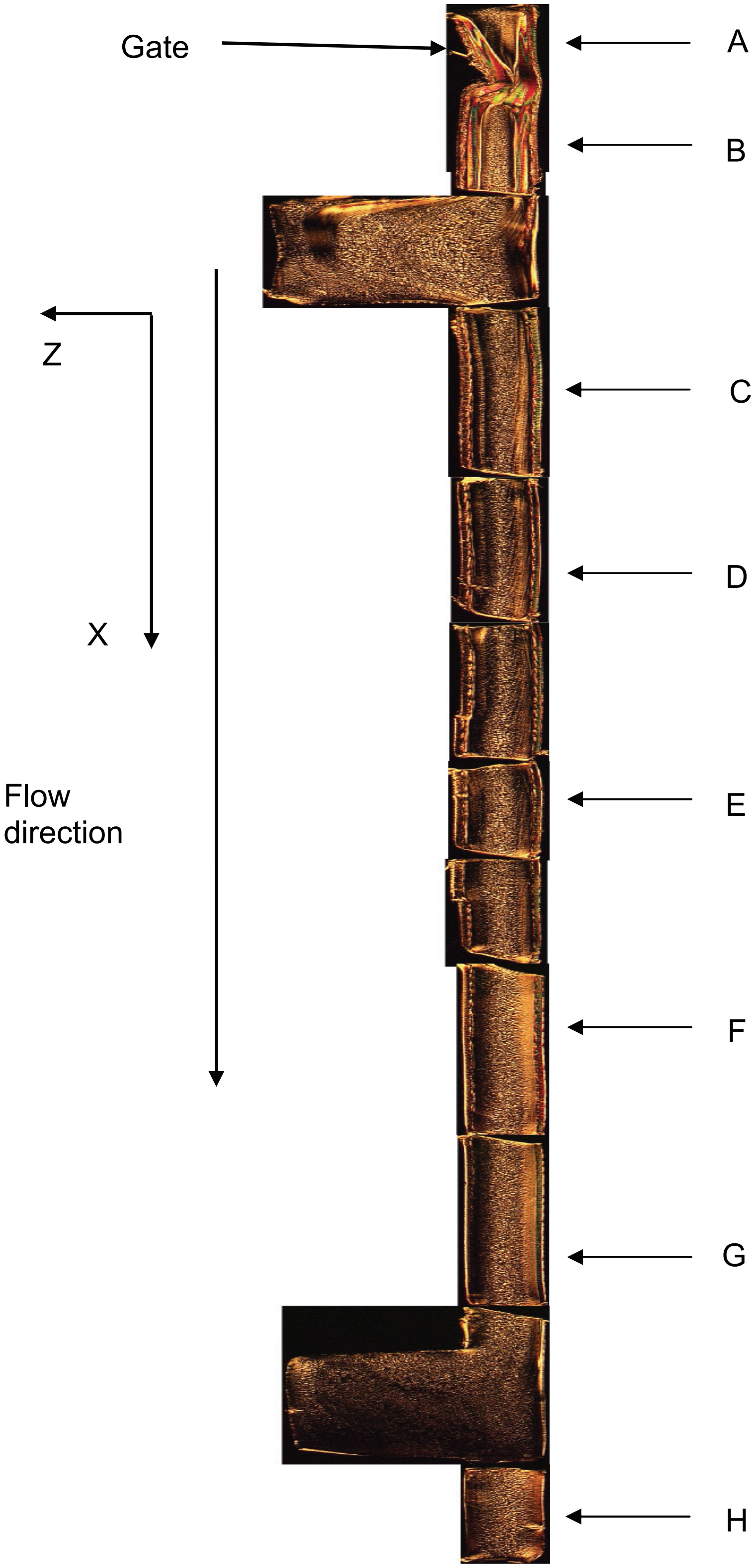

Figure 6-68: (a) Morphology of the XZ cross sections of micro injection molded HDPE (Case 6) along the whole flow length (Magnification: 40x); (b) Morphology with tripled scale of width in Z-direction

Figure 6-69 displays the evolution of the thickness of morphological layers along the flow direction from position C to position H. The skin layer thickness T_s decreased almost linearly along the length direction of the plate from 103 μm at position C near the gate to position H near the vent end, where no evidence of a skin layer was observed. It is interesting to note that the thickness of the spherulitic core decreased from position C to position D, and it increased again from position D until the end of flow, where the thickness of spherulitic core reached its maximum. The pattern of spherulitic core may reflect the effect of viscous dissipation. The heat loss to the cold mold wall and viscous dissipation could reach a balance at around position D, during the filling stage. After position D, viscous dissipation may exceed heat loss to the cold mold wall, thus resulting in increases in the thickness of the spherulitic core.

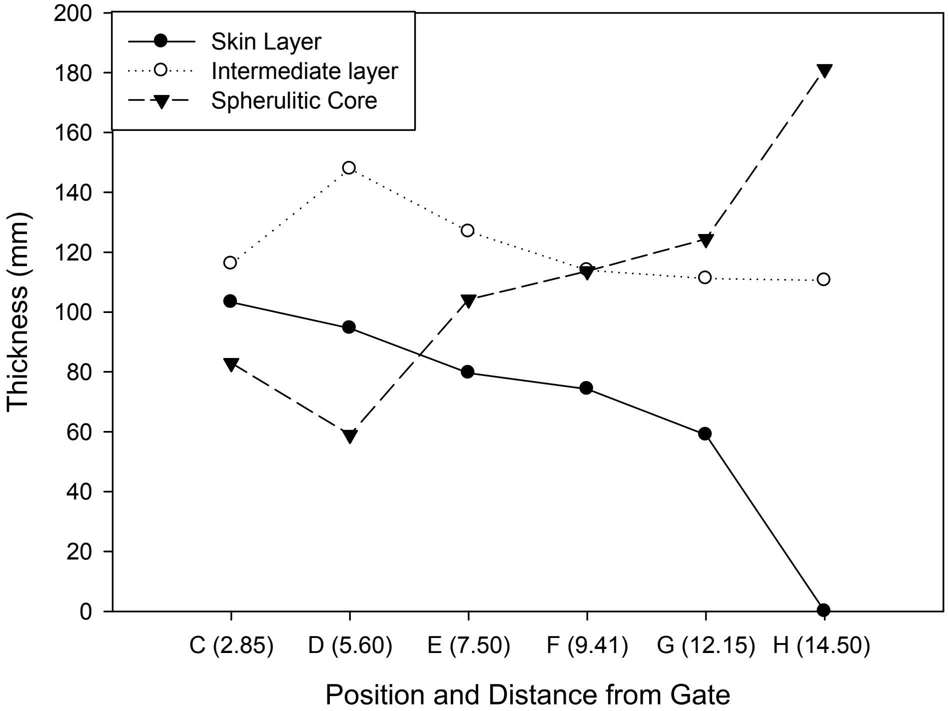

Figure 6-69: Morphology variation along the flow direction of HDPE (Sclair 2714)

6.5 Mechanical properties

6.5.1 Typical Stress Strain Curves

Figure 6-70 suggests that the HDPE, POM, and PC samples may be classified as soft and tough, rigid and strong, and rigid and tough, respectively, according to the common classification of the various types of mechanical behaviour [164].

The stress–strain curve of HDPE showed the characteristics of soft and tough, since it exhibited low modulus but high elongation and energy to break. These characteristics are in good agreement with those reported for larger cross sections [4, 60, 145, 165]. As shown in Figure 6-70, an initial linear elastic region was followed by a yield point, which in turn was followed by the formation of a neck, a form of shear yielding, in which the cross-section dropped suddenly (necking) and a decrease of nominal stress was observed [164]. The necking grew at the expense of material cross-section and proceeded until the rupture occurred at the end of the cold-drawing. Strain hardening, due to both strain-induced re-crystallization and molecular orientation [159, 166, 167], normally observed for some semi-crystalline materials leads to increases of modulus and tensile strength. Such strain hardening was not obvious for the HDPE specimens.

The stress–strain curve of POM displayed typical rigid and strong characteristics, with high modulus and tensile strength, medium elongation, and limited yield. Compared to the behaviour of HDPE and PC shown in Figure 6-70, the strain of POM samples was small and the necking process was not obvious. The stress-strain curves were in good agreement with the stress/strain curves reported by Haberstroh and Brandt [4] for a similar material with 2.5 mm^2 cross-section.

The stress–strain curve of PC displayed the rigid and tough characteristics, with high modulus, reasonable strength, and high elongation and energy to break. The amorphous PC polymer was probably toughened by the occurrence of low-temperature secondary transitions, such as the β-transition [167]. The theory suggests that the flexibility imparted to the chain by secondary chain motion contributes to the chain's ability to respond to stress. The PC stress-strain curve exhibited a yield point at about 10% strain, which was followed by necking, and an obvious strain hardening process. The strain hardening of amorphous materials generally results from molecular orientation, which increases the modulus and tensile strength. The stress-strain curves obtained for PC were again in good agreement with the behaviour reported by Haberstroh and Brandt for PC specimens with 2.5 mm^2 cross section [4, 8] and other results reported for conventional injection molded specimens [60, 165].

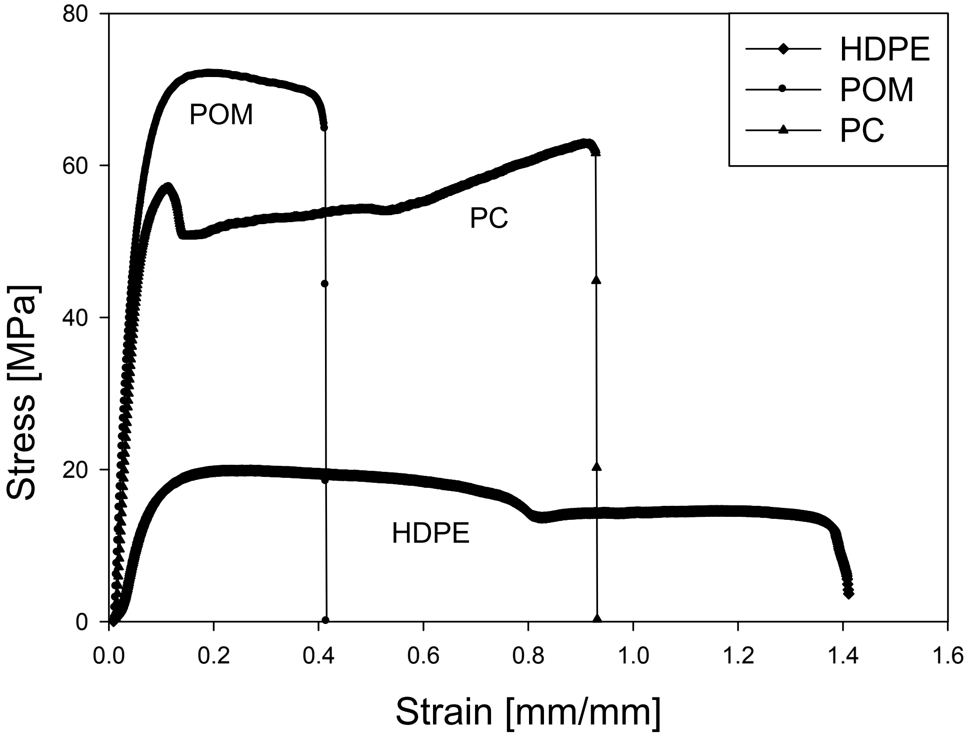

Figure 6-70: Typical stress vs. strain curves of micro injection moldings for three selected materials

A common feature observed for the three materials was that almost all specimens necked and failed near or exactly at the interface between the parallel length of the narrow section and the fillet close to the cavity end. The possibility of flaws due to the cutting die was ruled out by switching the specimen in the punch die. The consistency of the failure position may be attributed to both the decrease in mechanical strength along the flow length and the stress concentration at the interface [168]. The changes in mechanical properties along the flow direction may be attributed to the decreases in skin layer thickness for the two semi-crystalline materials, as shown in Figure 6-50 and Figure 6-69, respectively. The stress concentration at the interface might have been magnified, due to the small radius of the fillet, which is only a quarter of that specified for type V, while the gauge width and gauge length are half of those of type V. The lower mechanical strength, possibly due to both morphology and stress concentration might have acted as a notch, which caused failure at the above position [167]. In other words, the modulus and yield stress measured for each process condition are actually mechanical properties at a specific position on the specimen. The apparent deterioration in strength along the flow length suggests that the section of the product that demands higher mechanical strength should be positioned closer to the gate, during the design stage.

6.5.2 POM

As shown in Figure 6-71, the modulus and yield stress for POM follow a similar pattern. The modulus ranged from 1484 MPa to 1628 MPa, which indicates that the modulus of the micro part was 46% to 52% lower than the modulus of macro samples (ca. 3000 MPa) [169]. The modulus could be manipulated in a range up to approximately 10% by varying the processing parameters. The yield stress ranged in an even narrower range from 71 MPa to 72 MPa, which fell within the data range reported by the material supplier [87] and was also in good agreement with the data reported by Haberstroh and Brandt [4]. The tensile modulus measured in the present study is in good agreement with the data reported by Tom, Angelov, and Coulter [5] for a micro injection molded gear manufactured from a similar material from non-heated mold experiments. The modulus measurement was performed with a nanoindenter.

According to Figure 6-72, injection speed was the dominant negative factor in affecting both the modulus and yield stress. An increase in injection speed results in higher melt bulk temperature, due to higher viscous dissipation. In turn, the higher melt temperature results in thinner skin layer as shown in Figure 6-43, because less material solidifies during the filling stage. Also, the higher melt temperature leads to lower degree of molecular orientation, due to longer cooling and solidification times and faster molecular relaxation [89]. Thus, lower mechanical properties would be expected for high injection speed. In view of the variability of the measured modulus and yield stress, the minor factors and their interactions will not be discussed here.

The POM samples did not exhibit significant necking before breaking. The break of POM sample always occurred near or at the interface between the parallel length and the fillet. The dispersion of the data was probably caused by some types of flaws or defects in microstructure, including voids at the edges of large spherulites, whose size increased along the flow direction.

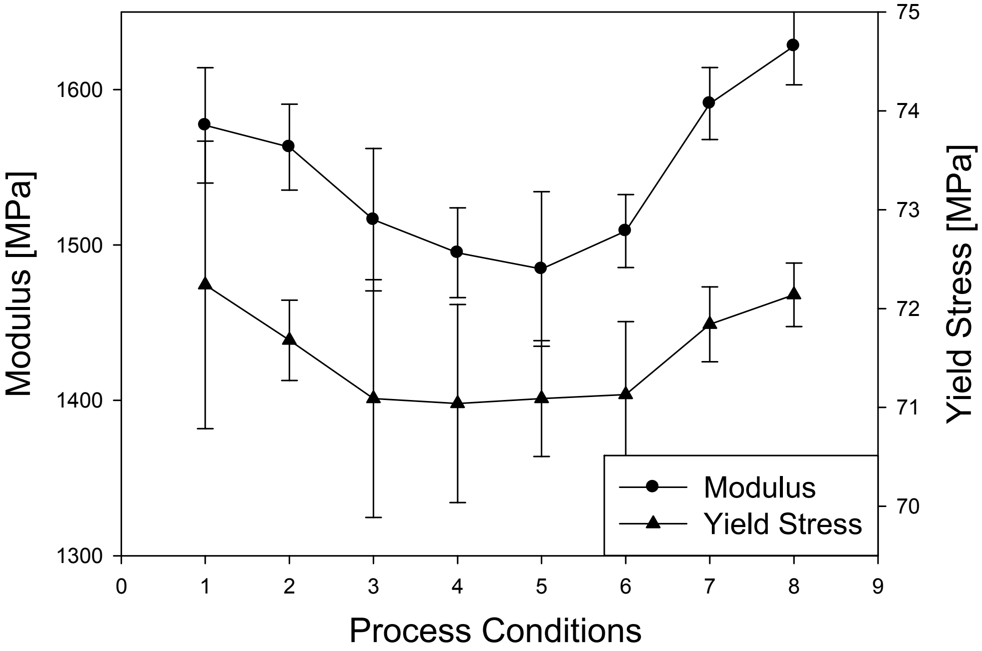

Figure 6-71: Modulus and yield stress of POM specimens

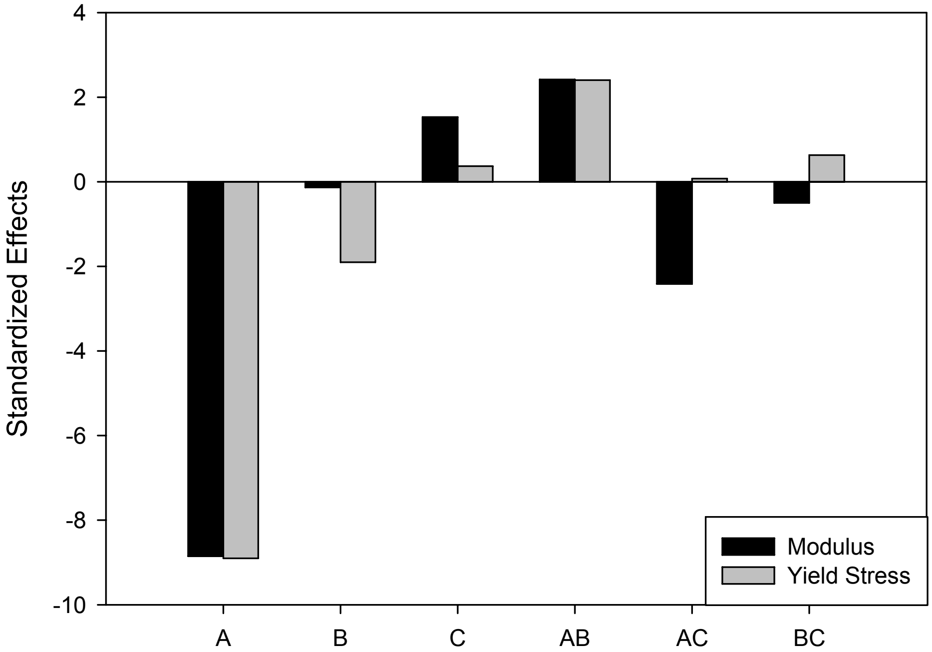

Figure 6-72: Standardized effects on modulus and yield stress of POM specimens

6.5.3 HDPE

The HDPE specimens exhibited necking exactly at the position of the aforementioned interface. The interface at the intersection of lowered mechanical properties and stress concentration might have acted as a notch, thus causing crack growth at a critical position. This unexpectedly produced a favourable experimental condition. The uniform necking position contributed to the stability of measured mechanical properties for HDPE experiments. Figure 6-73 shows that the modulus and yield stress for HDPE experiments, followed a similar pattern of variability with process conditions.

As shown in Figure 6-73, the mechanical behaviour of the micro injection molded HDPE (Sclair 2714), both tensile modulus and yield stress, followed a similar pattern with the skin layer thickness as displayed in Figure 6-66. The stable mechanical behaviour of the samples may be attributed to the low dispersion of the skin layer thickness in spite of the irregular flow reflected by the resulting morphology. The modulus ranged from 323 MPa to 394 MPa, which indicates that the modulus of the micro part was around 56% to 65% lower than the modulus values reported for macro samples (ca. 911 MPa) [169]. The modulus could be manipulated in a range up to approximately 20% by varying the processing parameters. The yield stress ranged from 19.7 MPa to 24.0 MPa, which fell within the data range reported for macro parts [87, 170]. Case 6, which yielded the maximum modulus and yield stress, was found to have the maximum skin layer thickness. The wider modulus and yield stress ranges indicates that HDPE is more sensitive to the process conditions than POM.

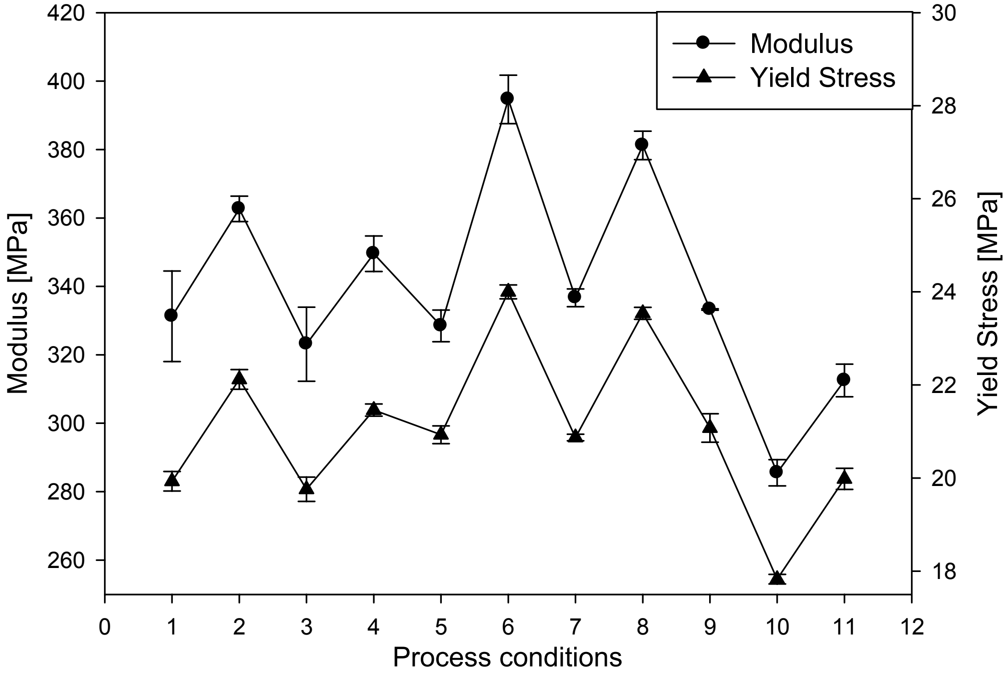

Figure 6-73: Modulus and yield stress of HDPE specimens

According to Figure 6-74, injection speed and melt temperature were the two most significant negative factors affecting both the modulus and yield stress for HDPE. Increasing them resulted in lower modulus and yield stress. This was probably because at higher injection speed and melt temperature, both the thickness of the skin layer and the molecular orientation in the skin layer become lower, as a result of higher material bulk temperature. Higher orientation would lead to higher stiffness in the orientation direction. The skin layer thickness and molecular orientation in the skin layer should make a larger contribution to mechanical behaviour of micro parts than in the case of macro parts, since the skin layer represents a larger fraction of the overall thickness in the case of micro parts.

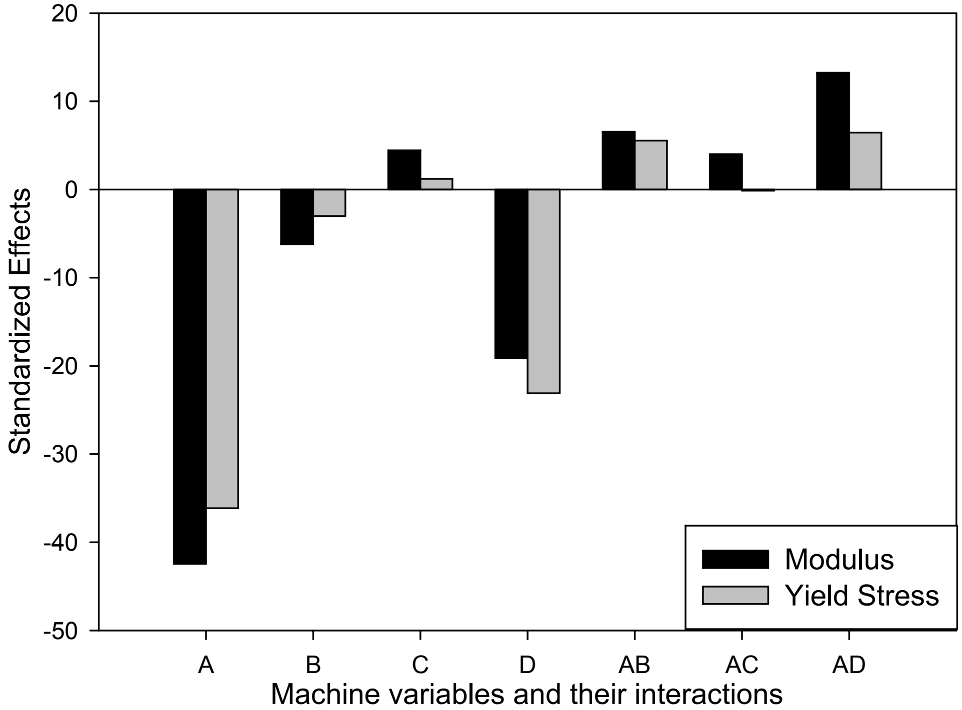

Figure 6-74: Standardized effects on modulus and yield stress of HDPE specimens

The injection speed/melt temperature interaction could have a minor positive effect on modulus. Since the DOE design of HDPE was a resolution IV design, the injection speed/melt temperature interaction was confounded with packing velocity/mold temperature interaction. Since both the injection speed and the melt temperature were more significant than packing velocity and mold temperature, the injection speed/melt temperature interaction should also tend to be significant [3, 136]. It can therefore, be concluded with a high confidence level that the injection speed/melt temperature has a significant positive effect on modulus. The effect of the injection speed/melt temperature interaction on yield stress is less significant and will not be discussed here, due to data variation.

The maximum modulus and yield stress were obtained in case 6, where injection speed, packing velocity, mold temperature, and melt temperature were all set at low levels. Thus, the materials may have experienced lower shear rate and fast solidification in this case. While lower mold temperature may result in lower crystallinity, the higher modulus and yield stress in this case might be attributed to the combined effects of increased thickness and orientation of the skin layer [4, 60, 171]. This argument is again supported by the observation that the minimum modulus and yield stress occurred for case 3, where both the melt temperature and injection speed were set at high levels. The low modulus and yield stress could result from low skin layer thickness and low molecular orientation that were formed at the high material bulk temperature.

The above analysis results were also confirmed with the additional experiments of cases 9 and 10, but large discrepancies appeared in case 11. The modulus and yield stress of Case 9, a center point case, were found to be approximately in the middle of the data range obtained for the HDPE samples, thus confirming the statistical analysis results.

Case 10 and case 11 were conducted at the same extreme high injection speed, but at different mold and melt temperature settings. It was found that the additional increase of injection speed in case 10 resulted in a further decrease in both modulus and yield stress. The modulus and yield stress of case 11, with high mold temperature and low melt temperature, were significantly higher than those of case 10, with low mold temperature and high melt temperature. However, the elongation at break in case 10 was as much as twice that of case 11, as displayed in Figure 6-75. The sample of case 10 has a large fraction of the self row nucleated structure as shown in Figure 6-64. The large strain in this case may be attributed to a cooperative deformation and slippage of lamellae between tie molecules in the row structure when strained [149]. Also, case 10 exhibited the more obvious strain hardening property in the stress-strain curve.

Figure 6-76 displays the images for the formation of neck, cold drawing, and fiber rupture of HDPE case 10, which were studied in an attempt to understand its extraordinary elongation or energy to break.

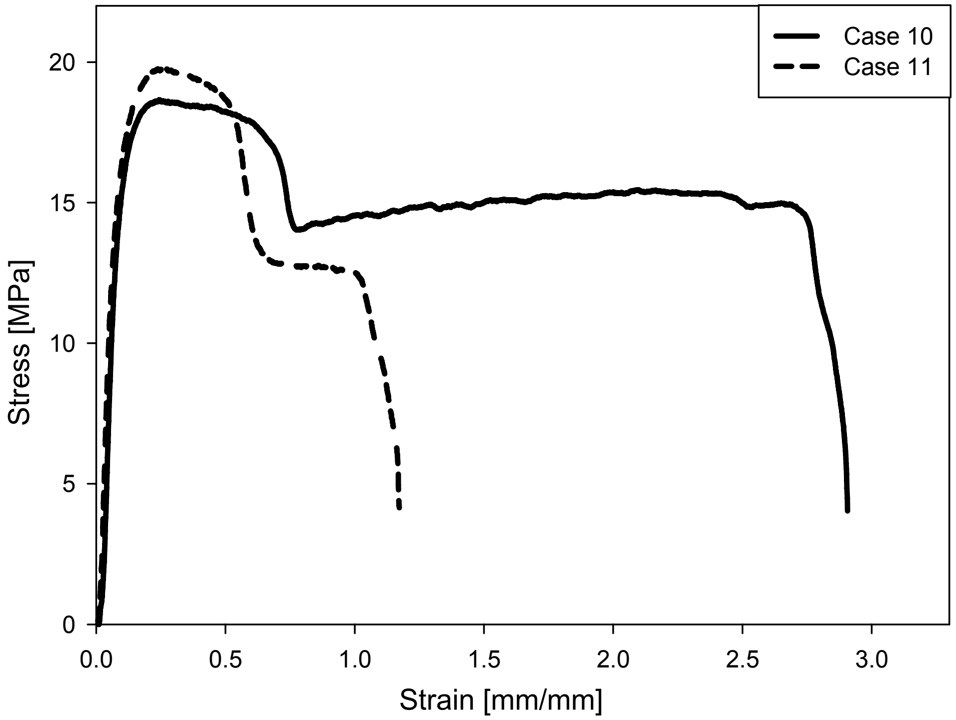

Figure 6-75: Typical stress-strain curves of HDPE case 10 and case 11

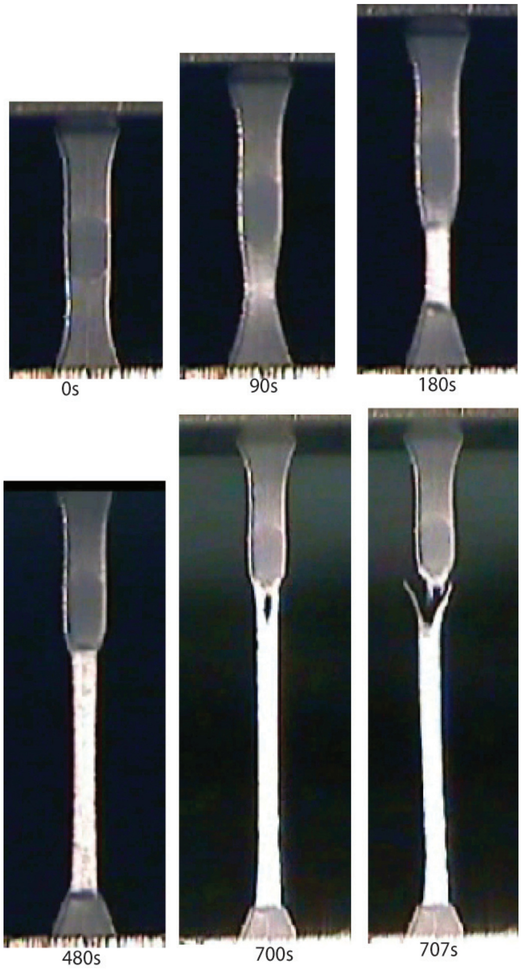

Figure 6-76: The formation of neck, cold drawing, and fiber rupture of HDPE case 10 at a test speed of 1 mm/s. (0s: original shape; 90s: initialization of neck at interface; 180s: formation of neck; 480s: development of neck; 700s: formation of voids; 707s: fibre ruptures)

6.5.4 PC

Figure 6-77 shows that the modulus of micro injection molded PC ranged from 1285 MPa to 1327 MPa. Thus, the modulus of the micro part was around 42% to 44% lower than the modulus reported for macro parts [169] (ca. 2280 MPa). The yield stress ranged from 58 MPa to 63 MPa, which was comparable to data reported by Haberstroh et al. [4].

According to the statistical analysis shown in Figure 6-78, the mold temperature was the major negative factor affecting Young's modulus, while injection speed was the minor positive factor affecting Young's modulus. Injection speed and mold temperature were the major and minor negative factors affecting yield stress. An increase in injection speed resulted in an increase in the modulus, but a decrease in the yield stress. It has to be emphasized that the analysis for the modulus of PC specimens might not be accurate, since the variation of modulus with processing conditions was within the scattering range.

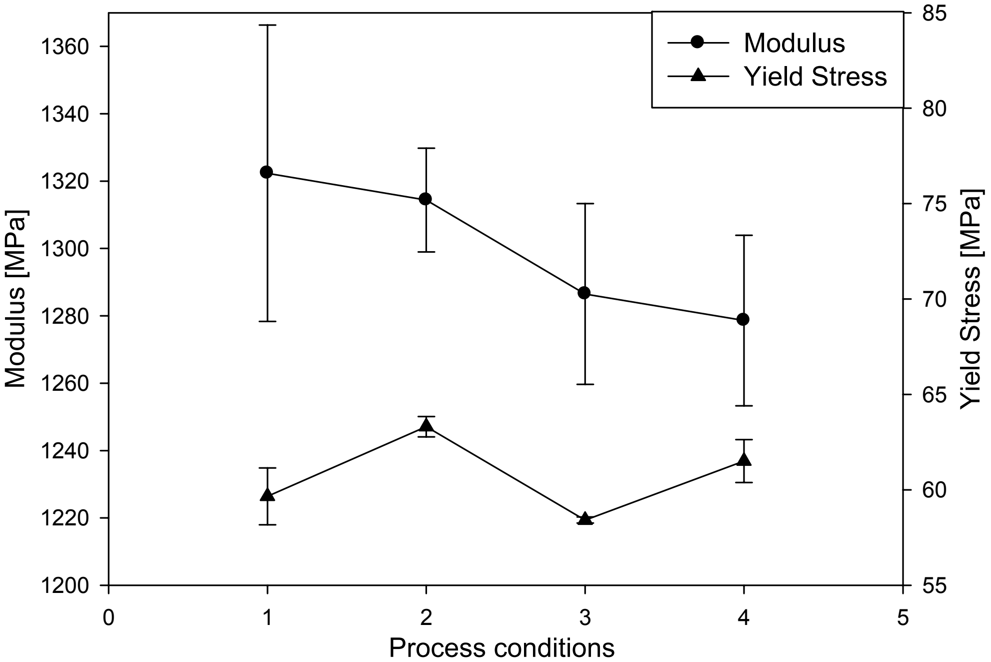

Figure 6-77: Modulus and yield stress of PC experiments

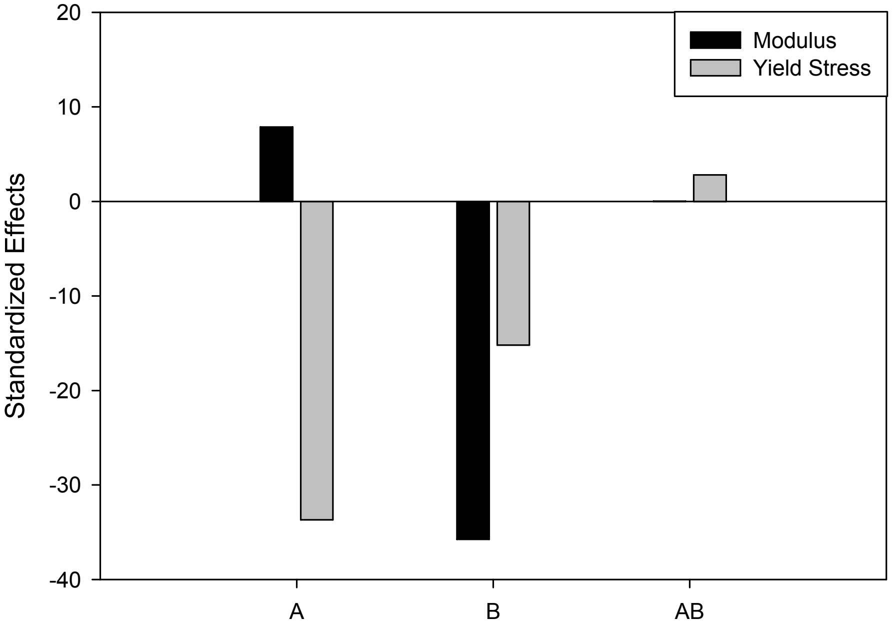

Figure 6-78: Standardized effects on modulus and yield stress

6.5.5 Effect of Injection Speed

Figure 6-79 shows that the modulus and yield stress of HDPE specimen exhibited a monotonic decreasing trend with increasing injection speed. This confirms the validity of the statistical analysis. The mechanical properties displayed are actually average values of modulus and yield stress of all cases of injection speed settings, 150 mm/s, 265/mm/s, 380mm/s, and 650 mm/s, respectively. This trend is in good agreement with the statistical analysis results, indicating that injection speed was the major factor affecting the mechanical properties.

6.5.6 Effect of test speed

Figure 6-80 displays the effect of test speed on the mechanical behaviour of the micro injection molded HDPE specimens. Samples of case 6 were selected for this test. The selected testing speeds were 0.5 mm/s, 1.0 mm/s, and 2.0 mm/s respectively. Both modulus and yield stress increased approximately linearly with increasing testing speed.

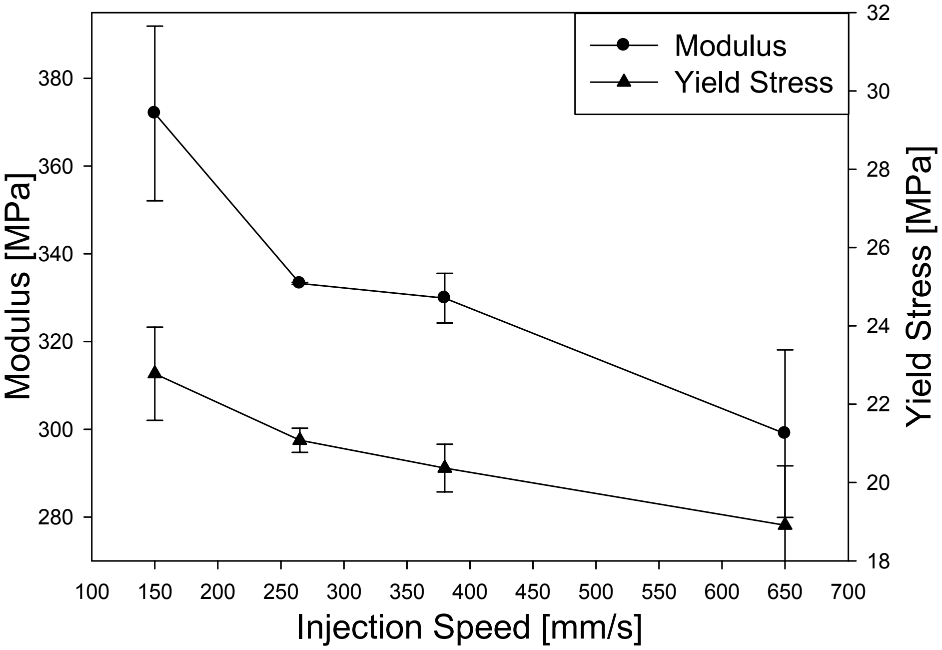

Figure 6-79: Modulus and yield stress vs. injection speed for HDPE specimens

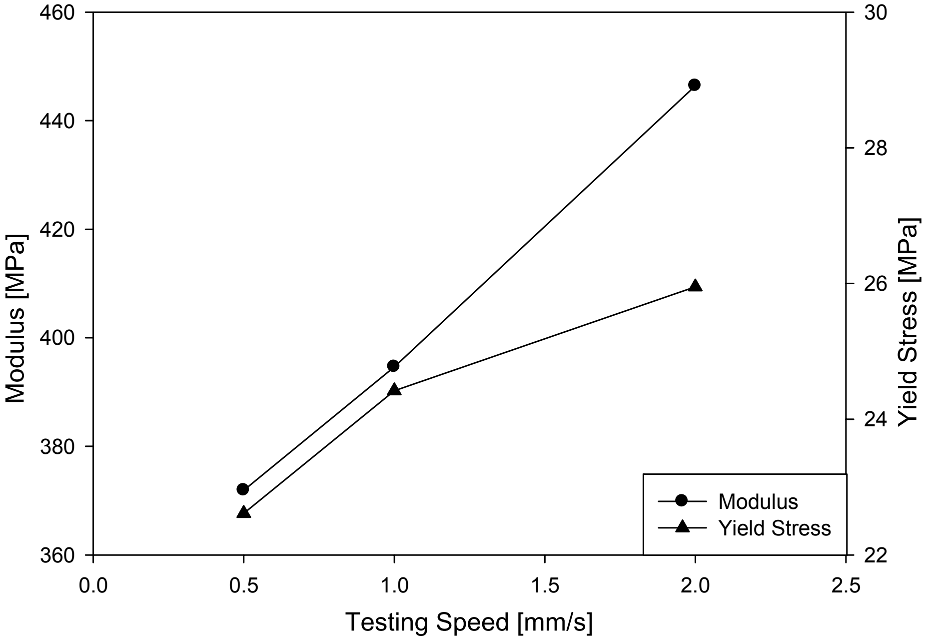

Figure 6-80: Effect of testing speed on mechanical behaviour

6.6 Nanoindentation

The local mechanical properties (modulus and hardness) were measured using a Hysitron TriboIndenter (Hysitron Incorporated), with a Berkovich tip (tip radius: 100 nm), in order to evaluate mechanical characteristics of different morphological layers in both the flow direction and the width direction. The area function was calibrated by performing a series of indentations on quartz, a standard material of known hardness.

In order to measure the modulus and hardness in the XY cross-section, the molding was firstly embedded in epoxy or acrylic resin using a specially designed embedding mold as illustrated in Figure 4-20. The embedding was followed by grinding and polishing to prepare the surface of the cross-section at a pre-selected position for nanoindentation measurements. Surface roughness should be minimized, in order to obtain satisfactory results.

6.6.1 HDPE (Escorene HD-6719)

The micro injection molded HDPE (Escorene HD-6719) samples were firstly embedded with epoxy resin and then ground and polished to prepare their surface for nanoindentation. The cross section normal to flow direction in the gate region as shown in Figure 4-10 was selected in the present study.

The indents were performed using a linear loading profile from 0 to 2000 μN over 10s, followed by a 5s hold time, and an unloading at the same rate of loading.

Figure 6-81 shows that the Young's modulus and hardness followed similar patterns across the thickness. The overall distributions of both modulus and hardness supported polarized light microscopy results regarding morphology and the skin-core structure. This microstructure is formed, as a result of the thermo-mechanical history experienced by the material. Modulus and hardness increased first from the surface of the skin layer toward the core of the specimen. The increases were followed by a downturn after the skin layer and before reaching the spherulitic core. The modulus and hardness in the core region were generally higher than for the skin layer and trans-crystalline layer. The low values of these mechanical properties in the spherulitic core region might be due to indentation positions in the amorphous region between the spherulites, which would be softer than its surrounding spherulitic region. The very high value at the left edge was probably caused by interference from the surrounding epoxy, which has higher modulus and hardness.

The asymmetry in mechanical properties with regard to the middle plane of the plate was probably caused by the unsymmetrical flow, which resulted in an unsymmetrical structure in the morphology near the gate region.

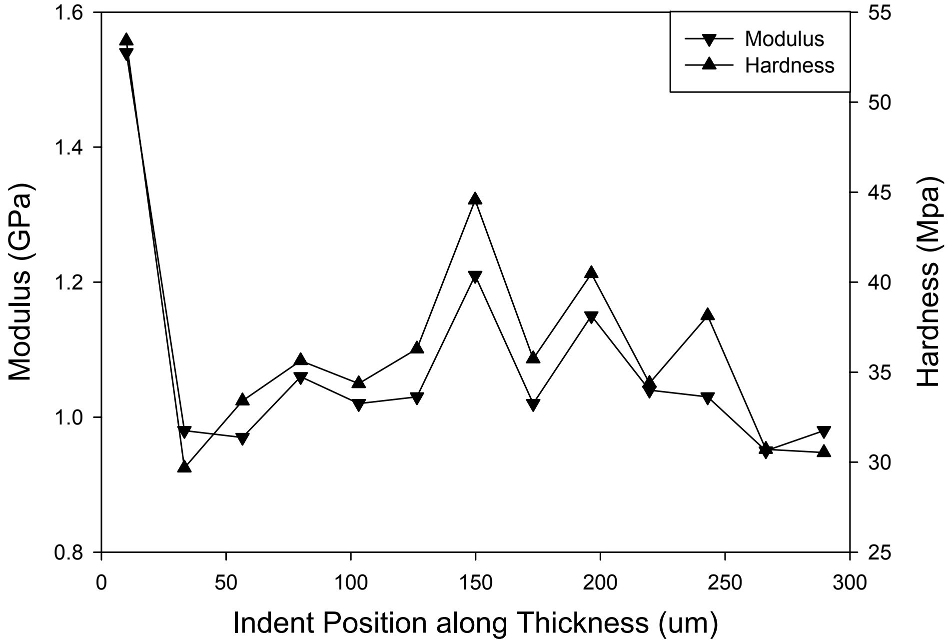

Figure 6-81: Distribution of modulus and hardness at a cross section normal to the flow direction near the gate region

6.6.2 POM

The micro injection molded POM samples were embedded with Acrylic cold mounting resin. The cross sections normal to the flow direction at position C, as shown in Figure 4-11, were selected in the present study.

The indents were performed using linear loading profile from 0 to 4000 µN over 15 s, followed by a 5 s hold time, and an unloading at the same rate of loading. Figure 6-82 displays the distribution of local mechanical properties in the micro injection molded POM specimen. The modulus and hardness followed approximately similar patterns, which were not symmetric across the thickness. In the left hand side of the figure, the mechanical properties decreased from the skin layer towards the next trans-crystalline layer, where minima were observed. In the right hand side, the mechanical properties firstly increased then dropped toward a minimum in the trans-crystalline layer. The unexpected low values obtained at the extreme right side were probably due to an undercut at the sample edge formed during polishing. The local modulus and hardness in the region of spherulitic core varied in a narrow range. They were higher than in the directly surrounding trans-crystalline layers. The variation in local mechanical properties may have been caused by differences in the orientation of lamellae [99].

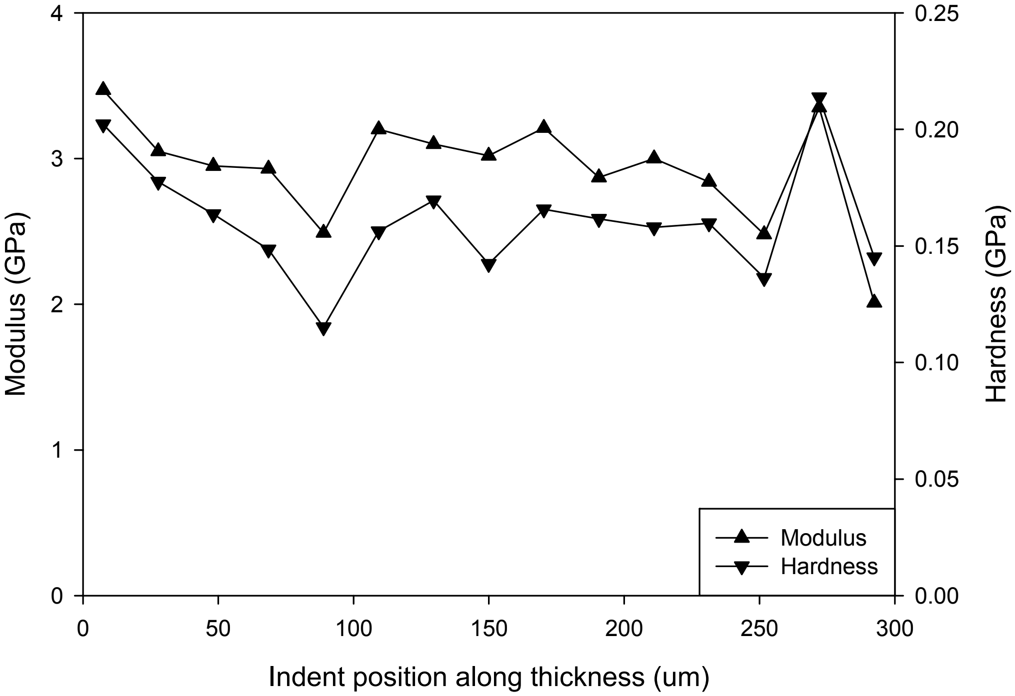

Figure 6-82: Distribution of mechanical behaviour across transversal cross section of position C normal to flow direction

6.6.3 HDPE (Sclair 2714)

The micro injection molded HDPE (Sclair 2714) samples were also embedded in Acrylic cold mounting resin. The indents were performed using a linear loading profile from 0 to 2000 μN over 10 s, followed by a 5 s hold time, and an unloading at the same rate of loading. Again, the measured mechanical properties can be associated with the different morphological features of the micro injection molded HDPE specimens. Two significant modulus and hardness dips were found between the spherulitic core and skin layers, as shown in Figure 6-83. Lower values at the two edges of the HDPE specimen were probably related to undercuts at the polishing surface.

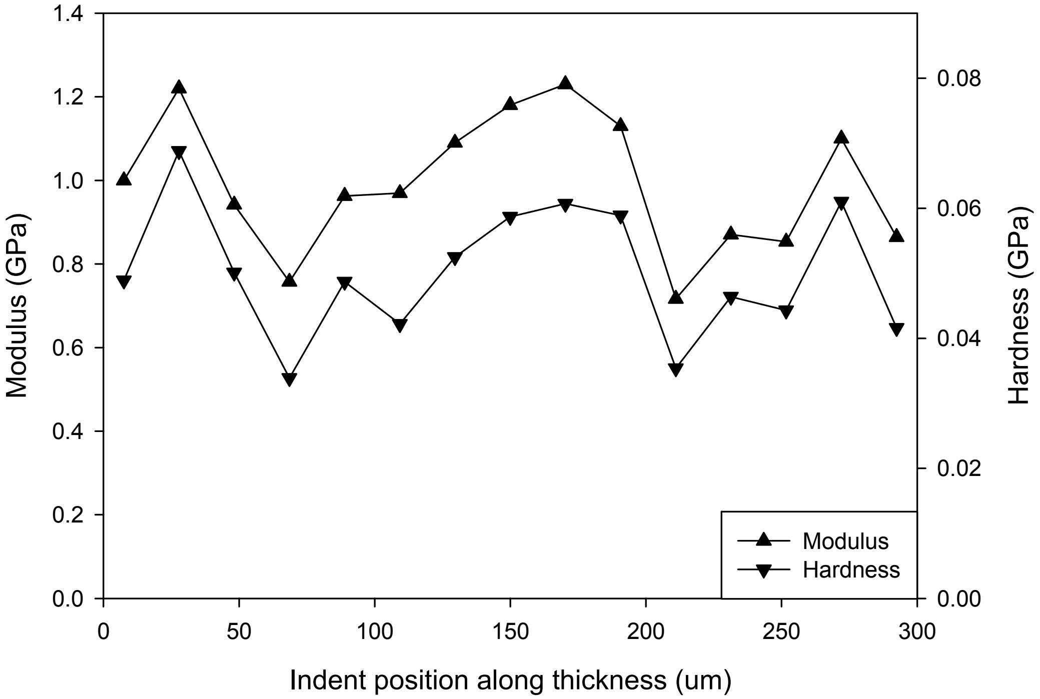

Figure 6-83: Distribution of mechanical behaviour across transversal cross section of position C

6.6.4 Relation between macro tensile properties and local mechanical properties by nanoindentation

The results indicate that the local moduli measured with the nanoindenter were much higher than the tensile moduli measured for the same micro moldings, and were close to the tensile moduli reported for macro samples, for all three materials studied. This observation might reinforce the conclusion that the lower values of the measured tensile modulus and strength of the micro tensile specimen were probably related to the specific geometry of the tensile specimens.

6.7 Shrinkage

6.7.1 POM (Delrin 900 P)

Figure 6-84 displays the measured longitudinal shrinkage between the two ribs, as shown in Figure 4-21. The shrinkage between the two ribs ranged from 0.1810 mm to 0.2454 mm, which accounted for 1.67% to 2.27% of the original dimension. During the molding cycle, stresses due to the adhesion between the polymer and the mold wall tend to prevent the material from experiencing shrinkage. Because the section between the two ribs is constrained tightly in the mold insert, the constrained shrinkage between the two ribs and the resulting residual stress will be determined by the temperature-time history experienced by the part, while it is in the mold. At high temperatures, most of this stress will be simply relaxed, while at lower temperatures a significant part will be stored as residual elastic stress. As the material leaves the mold, this stress is relieved, causing shrinkage of the material between the ribs.

According to Figure 6-85, injection speed is the most significant negative factor affecting the shrinkage of POM samples. An increase in injection speed results in lower shrinkage, or better dimensional stability. The higher material temperature, associated with high injection speed due to viscous dissipation, allows the polymer molecules to relax quickly and to conform to the dimensions of cavity, resulting in lower linear shrinkage. The mold temperature is a noticeable positive factor affecting the shrinkage, as shown in Figure 6-85. However, Figure 6-84 reveals that the increase in mold temperature resulted in higher shrinkage for low injection speed, and lower shrinkage for high injection speed. The effect of the mold temperature on shrinkage at low level of injection speed could be attributed to the variation of injection pressure with mold temperature. When the injection speed is set at the low level, both the peak injection pressure and the average injection pressure during filling at low mold temperature for case 1 and case 2 tend to be higher than those at high mold temperature for cases 7 and 8, as shown in Figure 6-2. The higher injection pressure may result in higher initial flow during the packing stage to compensate for the shrinkage, especially when the gate freezes very fast in the micro injection molding process.

When the injection speed is set at the high level, the shrinkage at lower mold temperature for case 3 and case 4 is larger than that at higher mold temperature for case 5 and case 6, although both the peak injection pressure and average injection pressure during filling are still higher in the cases of lower mold temperature, as shown in Figure 6-2. This is probably because the average plunger velocity at high mold temperature for case 5 and case 6 is significantly higher than that at low mold temperature for case 3 and case 4, thus resulting in more significant viscous dissipation, which in turn leads to lower shrinkage.

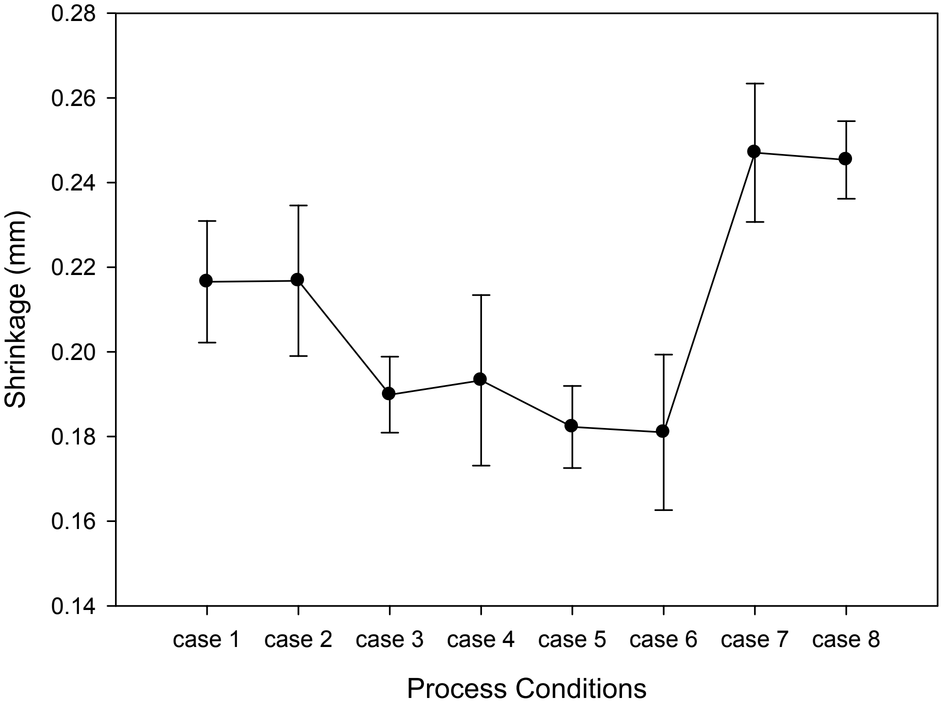

Figure 6-84: Shrinkage of Polyoxymethylene at different process conditions

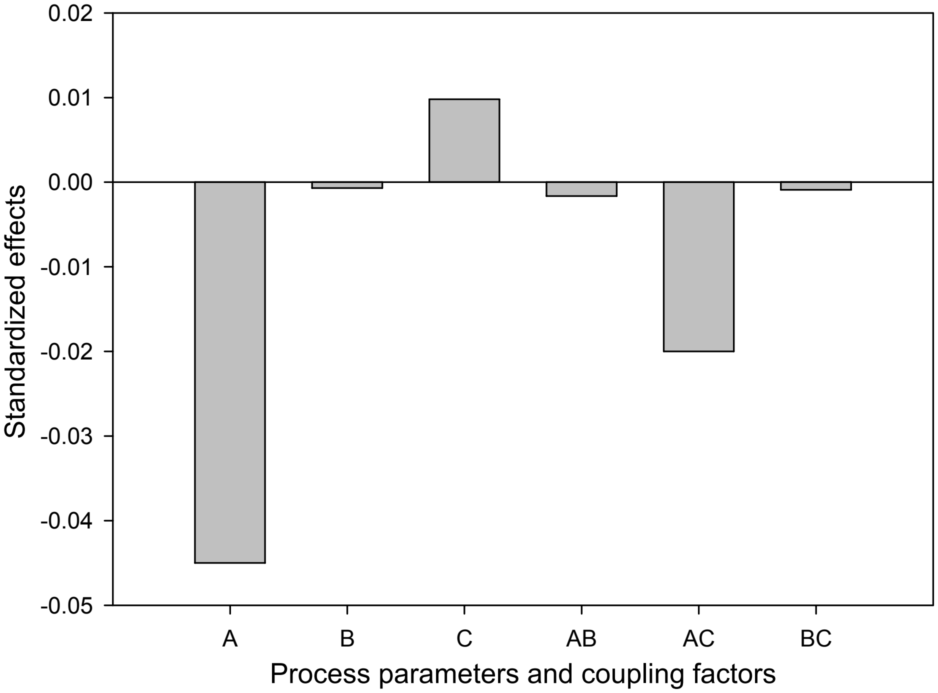

Figure 6-85: Standardized effects on shrinkage of POM samples

6.7.2 HDPE (Escorene HD-6719)

Figure 6-86 shows that the shrinkage of HDPE (Escorene HD-6719) in the X-direction of the 10 samples lies mostly between 0.2756 and 0.3874 mm except for sample 5, which was an obvious short shot. The X-direction shrinkage accounts for 1.8375% to 2.5825% of the original dimension.

Figure 6-87 shows that shrinkage in the Y-direction increased from position A to position B and then dropped to a minimum value at position C. The maximum shrinkage was found at point F, where, the cross sectional area increases suddenly as at position B, thus resulting in a corresponding large linear shrinkage in the Y-direction. The significant increase in shrinkage at positions E, F, and G may be due to the existence of the hole, which may have diminished the effect of packing pressure on the part behind the hole, due to both the pressure drop and early solidification of the hole region.

Figure 6-88 shows that the minimum shrinkage in the Z-direction is at position I and the maximum shrinkage is at position K. In the real measurement, the thickness at position I is always greater than the design thickness, due to flash. The flash is probably caused by the high pressure in that region due to the sudden decrease in cross section area.

The total measured volumetric shrinkage for the 3 mm x 15 mm x 0.3 mm plate with the circular hole, based on the average measured values of the linear shrinkage in the three dimensions, was around 12%. This is in reasonable agreement with the calculated shrinkage distribution values as shown in Figure 6-32.

The shrinkage in the Z-direction is significantly higher than those in the Y and X directions, which are lower than one third of the volumetric shrinkage. This is because the material is constrained in the plane of the molding, especially in this case by two ribs, while it is free to shrink in the thickness direction.

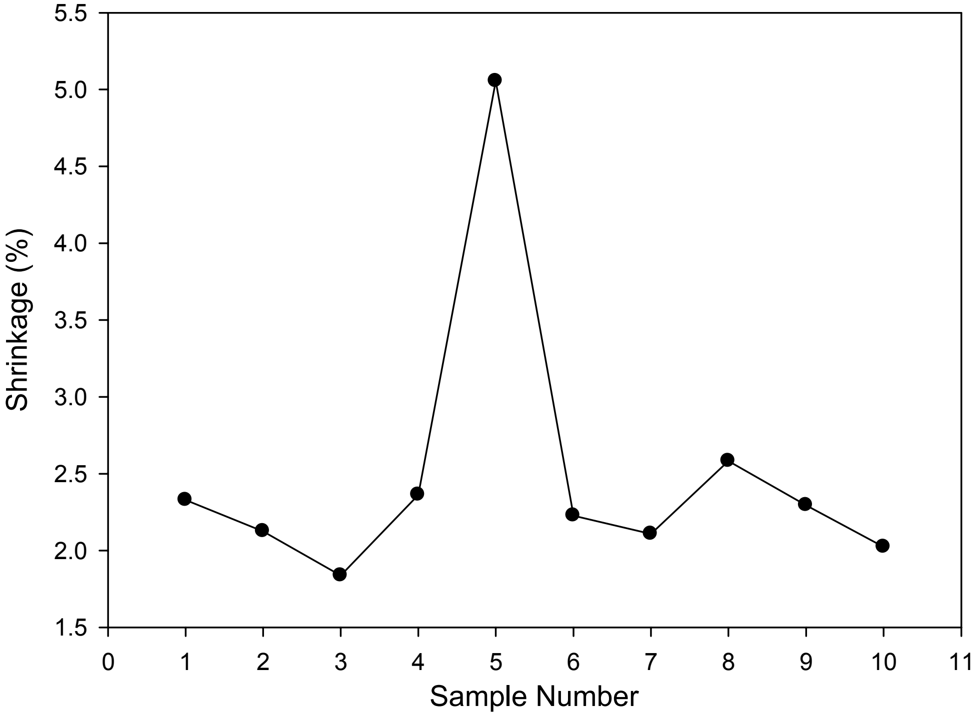

Figure 6-86: Shrinkage in the X-direction of 10 samples

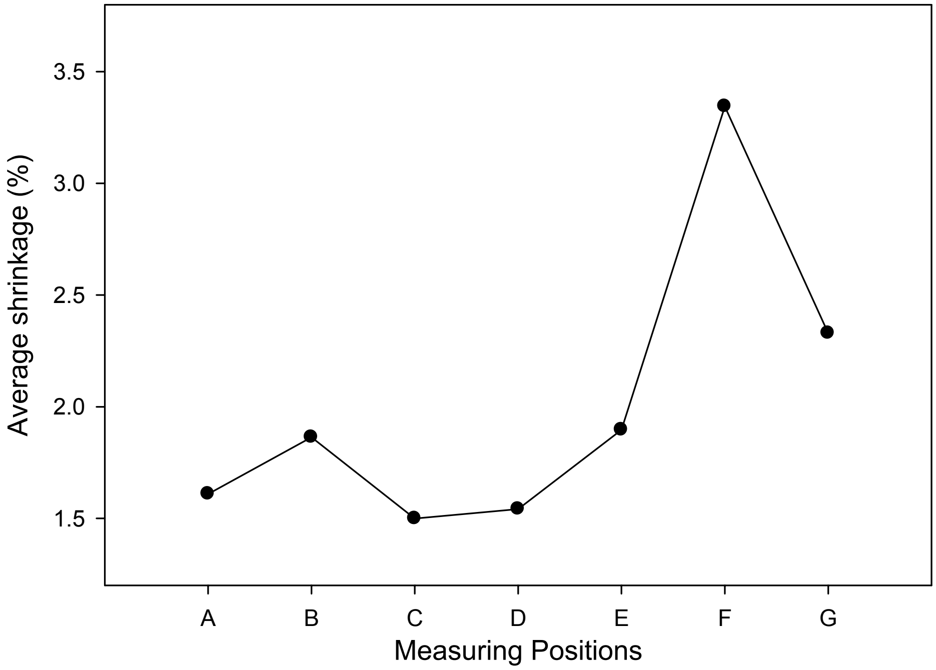

Figure 6-87: Shrinkage of Y-direction along flow at measuring positions

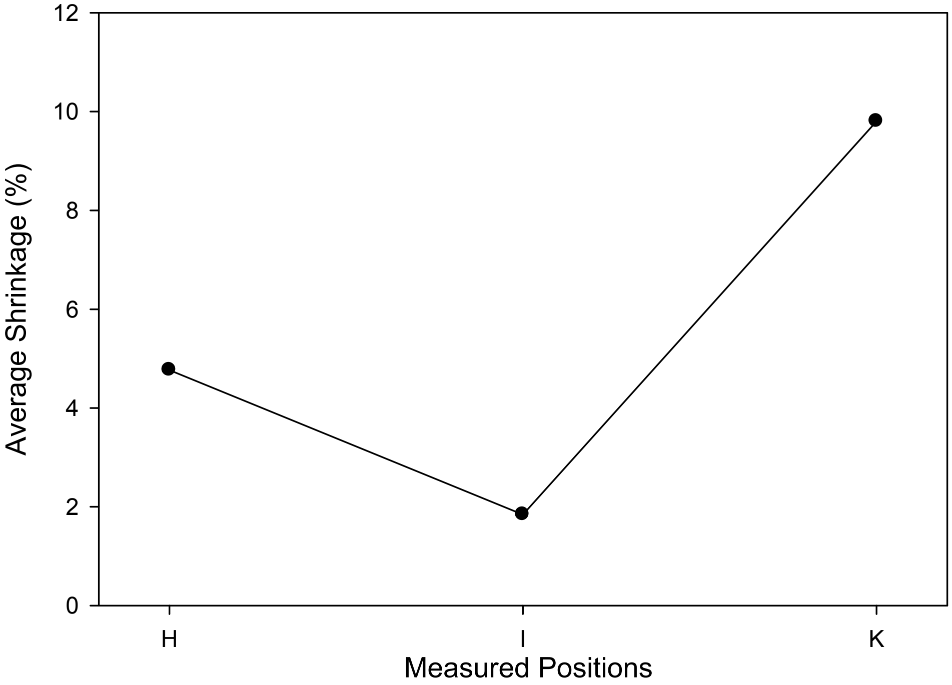

Figure 6-88: shrinkage in Z-direction along flow at measuring positions

6.8 Correlations of Experimental Results

In this section, the correlations among various measurements are presented. Considering the flow irregularity of HDPE (Sclair 2704), the discussion will be limited to results of POM experiments only.

6.8.1 Process – Structure

Figure 6-89 displays some correlations between selected characteristic process parameters (CPPs), average plunger velocity and metering size, and the skin layer thickness. The changes of skin layer thickness appear to follow a pattern similar to the corresponding changes in metering size. The patterns of skin layer thickness and metering size are effectively the opposite of the corresponding patterns of changes in average plunger velocity during the filling stage. Thus, when thicker skin layer is desirable for performance considerations, the machine parameters should be set, so as to obtain lower average plunger velocity. Metering size becomes higher, as a result of lower average plunger velocity. It is worth noting that process repeatability was lower at low injection speed for POM experiments.

The direct relations between skin layer thickness, average plunger velocity, and metering size are shown in Figure 6-90 and Figure 6-91 respectively. Overall, the skin layer thickness decreases with increasing average plunger velocity, but increases with increasing with increasing metering size. However, when average plunger velocity and metering size vary in a narrow range, the corresponding variation of skin layer thickness may follow an opposite trend. This is probably due to the data scattering of both average plunger velocity and skin layer thickness.

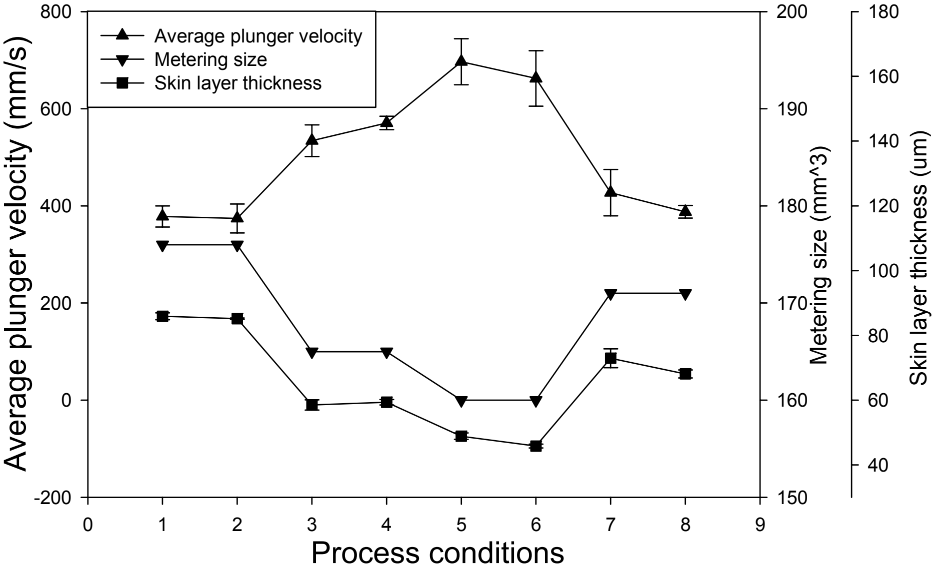

Figure 6-89: Process (average plunger velocity and metering size) - structure relation for POM

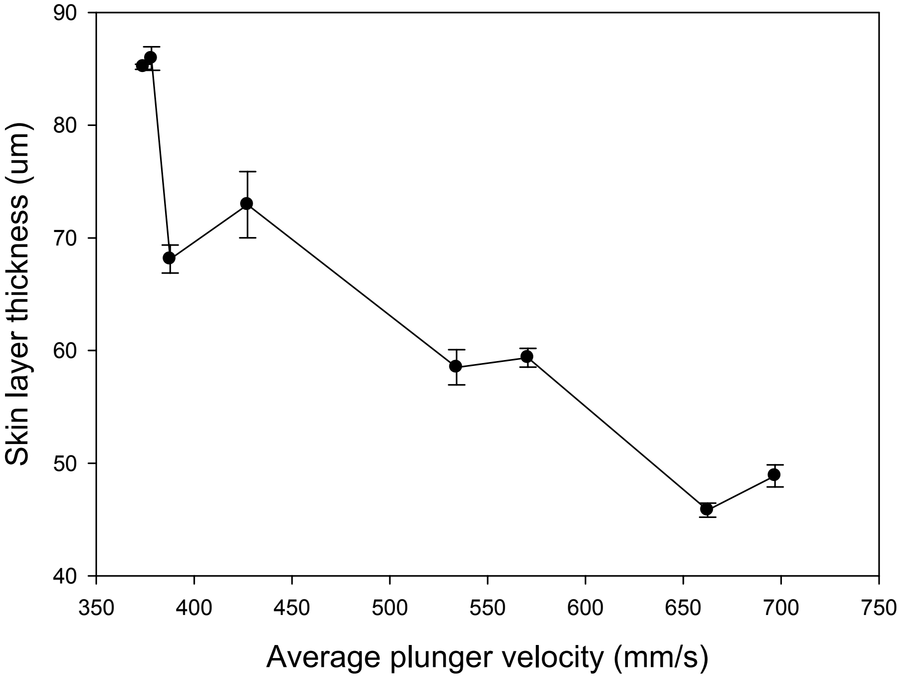

Figure 6-90: Direct relation between skin layer thickness and average plunger velocity during filling

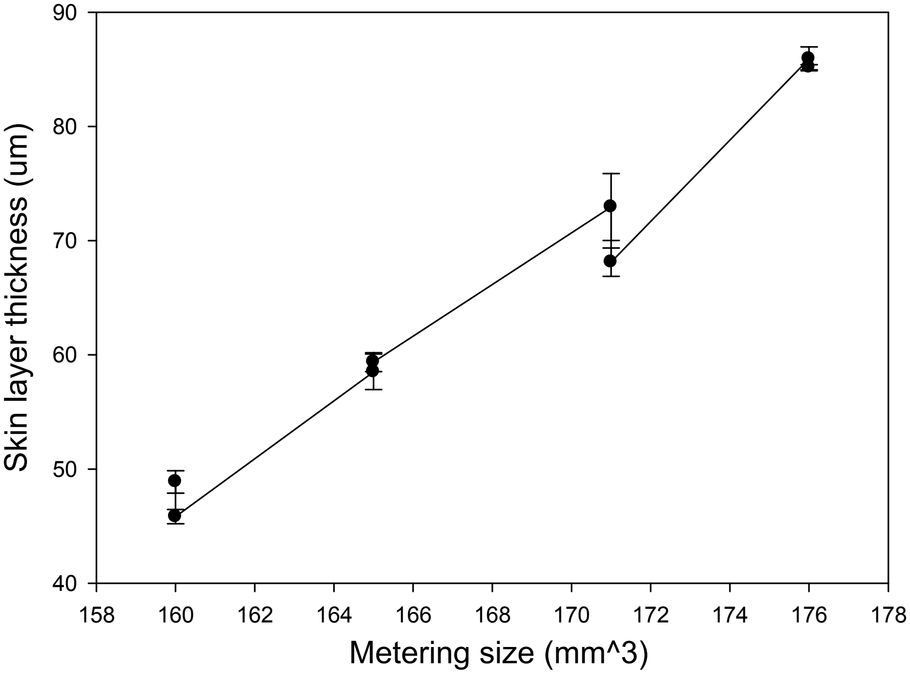

Figure 6-91: Direct relation between skin layer thickness and metering size

6.8.2 Process – Property

Figure 6-92 displays the relationships between selected CPPs, average plunger velocity and metering size, on one hand, and, modulus and shrinkage of the micro injection moldings, on the other hand.

It is interesting to note that the changes of modulus and shrinkage roughly follow a pattern similar to the corresponding changes in the metering size, while their patterns are opposite to that of average plunger velocity. When higher modulus is desirable, lower average plunger velocity will be required, but this will result in an increase in the linear shrinkage in the longitudinal direction, which is an important factor for dimensional stability. So, it should be considered in the design stage that high mechanical properties are probably obtained at the cost of lower dimensional stability.

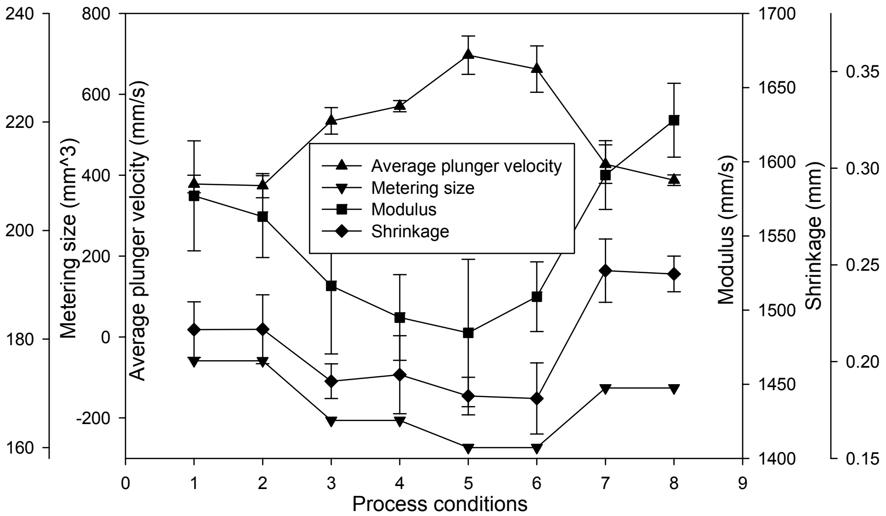

Figure 6-92: Process - property relationships for POM experiments

The direct relations between modulus, shrinkage and average plunger velocity are shown in Figure 6-93. The variations of modulus and shrinkage with average plunger velocity follow a similar pattern. This pattern is relatively complicated probably due to the effects of other process variables and coupling factors. According to Figure 6-94, both modulus and shrinkage approximately increase with increasing metering size from 160 mm^3 to 171 mm^3, then they decrease slightly with metering size upon further increasing to 176 mm^3.

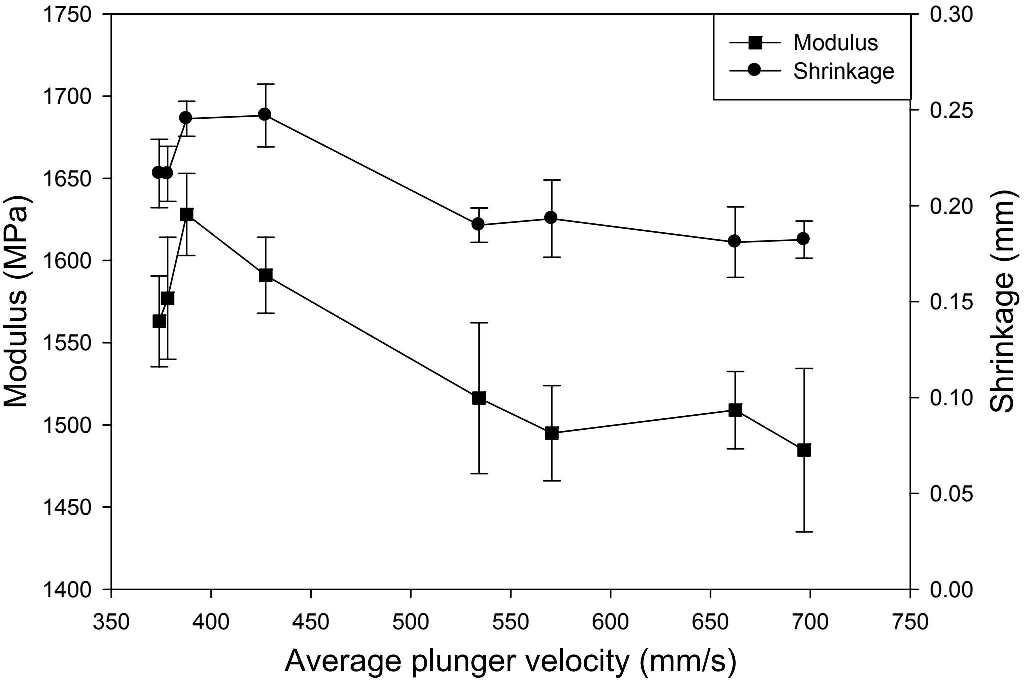

Figure 6-93: Direct relations between modulus, shrinkage and average plunger velocity

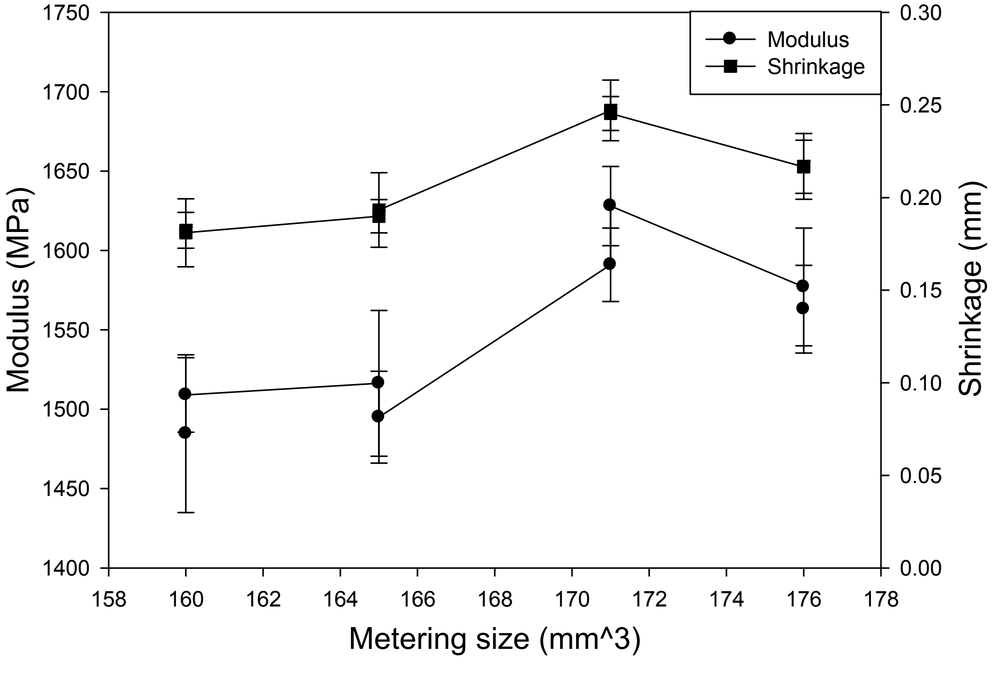

Figure 6-94: Direct relations between modulus, shrinkage, and metering size

6.8.3 Structure – Property

Figure 6-95 displays the relationships between structural characteristics, such as the skin layer thickness, and the selected macro properties of the micro injection moldings, modulus and shrinkage. Both modulus and shrinkage are closely related to the skin layer thickness.

The variation of shrinkage of the micro injection moldings with the skin layer thickness is in good agreement with results reported by Kantz et al [12, 105] for conventional injection molded polypropylene. The increase in the modulus with increase in skin layer thickness may be related to the greater number of fibril nuclei in the skin layer with orientation in the direction of stress.

The structure–property relationship does not only explain the variation of mechanical properties with different process conditions, but could also explain the variation of mechanical properties with cross section area reported in the literature, as reported by Tom et al. [9]. At a cross section area of 0.08 mm^2, the moduli of micro injection molded polyoxymethylene and cycloolefin copolymer were around 1/3 and 1/2 of the magnitudes of the moduli of the corresponding conventional injection moldings, respectively. When the cross section of the samples was reduced from 0.08 mm^2 to 0.02 mm^2, the moduli were increased again to become approximately identical with the moduli of conventional injection moldings. Similar results are also reported in the literature [4, 8, 102]. The increase of mechanical properties with further decrease of cross section could be explained by the increase of the relative size of the skin layer. These variations of mechanical properties with product size are very important for the design and dimensioning of micro products.

Figure 6-96 displays the direct relations between modulus, shrinkage, and skin layer thickness. Both modulus and shrinkage increase slightly as skin layer thickness increases from 45 µm to 59 µm, then they increase sharply as it increases to around 72 μm. This is followed by a slight decrease as skin layer thickness further increases to around 85 μm.

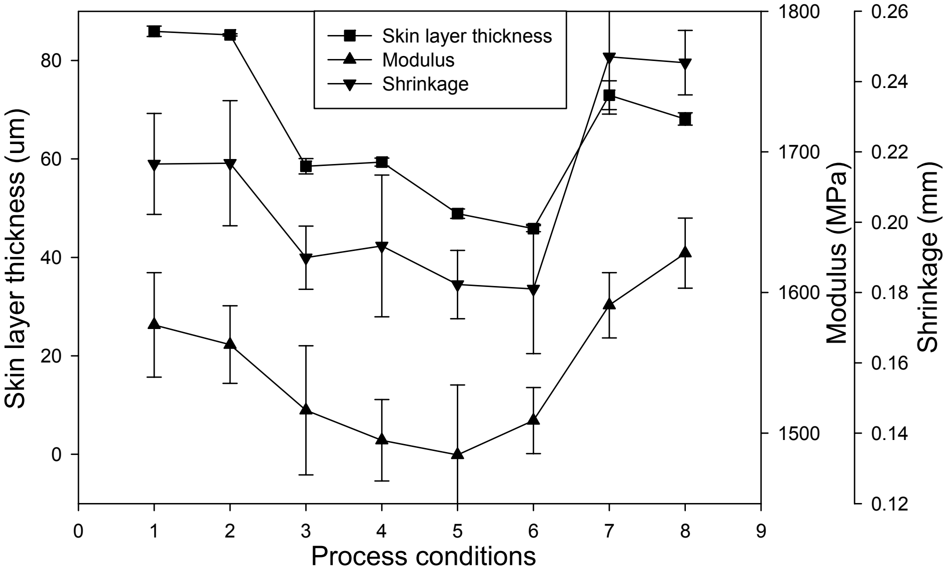

Figure 6-95: Structure-property relations for POM samples

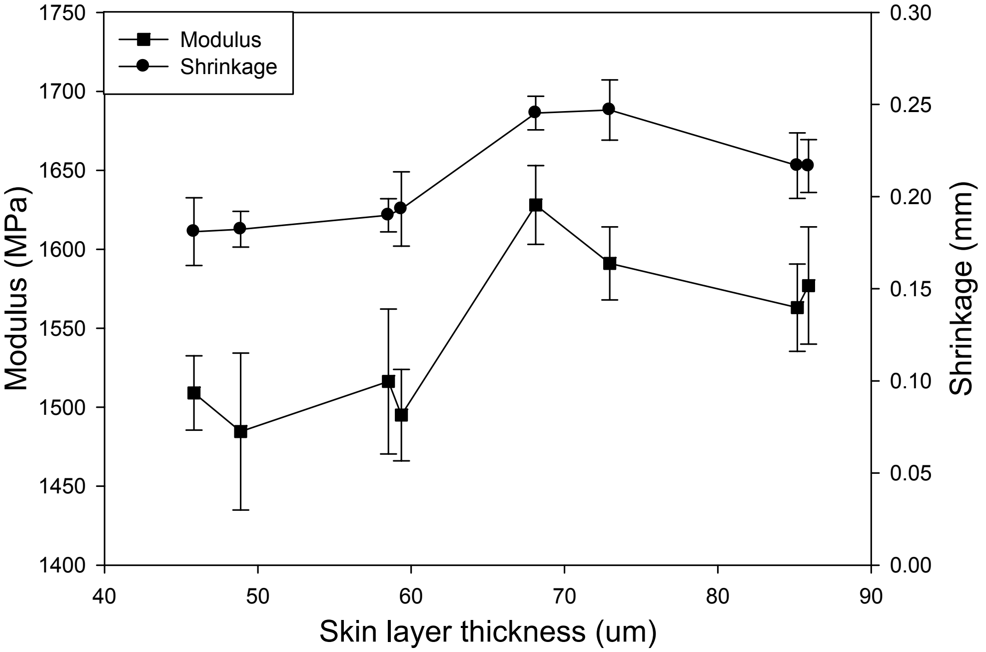

Figure 6-96: Direct relations between modulus, shrinkage, and skin layer thickness

6.8.4 Modulus – Crystallinity – Shrinkage

Generally, neither modulus nor shrinkage could be correlated with the crystallinity or other thermal properties, as determined in DSC measurements. Both mechanical properties and shrinkage of micro injection molded parts are probably more related to morphological structural features than to crystallinity itself.

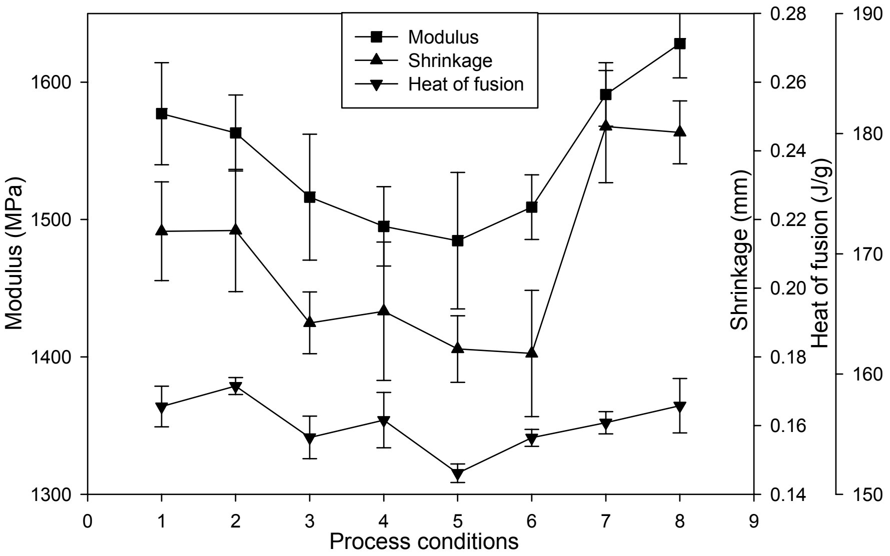

Figure 6-97: Modulus, shrinkage, and crystallinity relations

7. GENERAL CONCLUSIONS, ORIGINAL CONTRIBUTIONS, AND FUTURE WORK

7.1 Summary and General Conclusions

1. The cavity filling stage, in a plunger micro injection molding system, was monitored by using short-shot trials and analysis of data traces of the temporal evolution of injection pressure, runner pressure, and plunger position, at the millisecond time scale. Six characteristic process parameters (CPPs) were defined and derived from experimental data to identify critical process conditions. In addition, metering size was an optimized process parameter. This methodology provides a realistic approach the opportunity to achieve viable process and product quality control and optimization, consistent with the actual operating characteristics of the machine.
2. According to statistical analysis, injection speed is the most significant factor in affecting the process conditions for all three materials, while the roles of mold and melt temperature depend on the material and the specific CPPs of interest. The metering size was mainly determined by the average material temperature, which is determined by the balance between shear heating and heat transfer between mold surfaces and melt. The metering size influenced the microstructural characteristics and properties of the products.
3. Molding conditions at higher injection speed tended to exhibit better repeatability than at lower injection speed for POM, while the opposite was found for HDPE. The peak injection pressure and average injection pressure at 0.2s packing have better repeatability than other CPPs for all three materials studied, while

the plunger stroke at 0.2s packing and the average plunger velocity exhibited the highest coefficients of variation (COVs).

4. Moldflow commercial software was used to simulate the micro injection molding process. The estimated % flow rate vs. % shot volume was employed as the filling control profile. The calculated highest pressure at the injection location was around twice as high as the measured highest injection pressure during the filling stage. The large discrepancy was attributed to incomplete and inaccurate definition of boundary conditions and to the inadequacy of the rheological model, which was developed for the conventional injection molding process. The predicted extension rate, velocity, shear rate, temperature, viscosity, shrinkage, and flow pattern provided a qualitative basis for understanding the micro injection molding process and/or explaining some of the process characteristics and microstructure observations. The computed flow pattern for HDPE (Escorene HD-6719), in one of the experimental molds, indicated early solidification and explained the co-incidence of the weld line and crystalline profile behind the circular insert.
5. The thermal properties of micro injection molded HDPE and POM were evaluated using differential scanning calorimetry (DSC). The injection speed and mold temperature were found to be the major negative factors affecting the crystallinity of POM, while mold temperature was the major positive factor affecting the crystallinity of HDPE. The melting curves for micro molded POM revealed varying crystallinity and crystalline types along the flow direction.
6. Five morphological zones were identified across the thickness of micro-injection molded POM. These zones are different from those reported for conventional injection moldings of a similar material. The thicknesses of the morphological layers of micro-

injection moldings varied significantly with process conditions. Injection speed was found to be the most significant factor in affecting morphology, while mold temperature had a similar but less pronounced effect. The variation of morphological layer thickness along the flow direction followed a similar pattern to that observed in conventional injection molding. The results suggest that it is advisable to position the part required for high modulus and strength near the gate, where the skin layer thickness is high.

7. Morphological observations suggested three characteristic microscale flow features in the gate region for POM moldings. A repetitive V-shape pattern was observed, which was probably caused by the remelt and flow of the interior face of the skin layer. Other manifestation of the flow effects included the highly oriented polymer molecules next to the skin layer, which were formed at the very high shear rate, and high molecular orientation at the junction of gate and part.
8. Morphological observations provided evidence of flow irregularities all HDPE (Sclair 2714) samples. Each process condition exhibited multiple morphological patterns. Relatively stable skin-core structure was only obtained in case 4 and case 6, where the injection speed, melt and mold temperatures were all set to low levels. However, the skin layer thickness of the HDPE samples exhibited significantly lower data dispersion than that of polyoxymethylene. It exhibited the same variation pattern with process conditions as modulus and yield stress. Injection speed was the dominant negative factor affecting the skin layer thickness. The most common morphological feature is the row nucleated structure, where a string of spherulites have their origin in the same region of sheared material. The inflection point on the graph for the variation of morphological layer thickness along

the flow direction indicated the position where the viscous dissipation and heat loss to the cold mold wall were in balance.

9. A punch die was designed and fabricated to cut the micro molded samples precisely into tensile testing specimen. The tensile properties were measured accurately with a conventional INSTRON testing machine combined with specially designed sample holders to prevent slippage between the specimen and parts of sample holder and/or the conventional grips and to ensure specimen alignment with the pulling force. The Young's modulus of micro specimens with cross section area of 0.477 mm^2 was significantly lower than for conventional macro injection moldings of HDPE, POM, and PC, whereas the yield stress remained within the range of values reported for macro parts. The Modulus could be manipulated in a range of up to 20% for HDPE by varying the processing parameters, but in narrower ranges for POM and PC. Injection speed was found to be the most significant factor affecting the modulus and yield stress of the semi-crystalline materials, HDPE and POM, while mold temperature and injection speed were the major factors, affecting the modulus and yield stress of PC, respectively.
10. The local mechanical properties, modulus and hardness, were measured with a Hysitron TriboIndenter for both POM and HDPE. The local mechanical properties were comparable to those reported for macroscopic parts. The overall distributions of both modulus and hardness supported polarized light microscopy results regarding the skin-core morphology.
11. The shrinkage between two ribs was measured with a Nikon Measurescope for micro injection molded POM specimens. The longitudinal shrinkage varied in a pattern similar to that of the skin layer thickness. Injection speed was found to be the most significant negative factor affecting the magnitude of shrinkage,

while mold temperature and injection speed/mold temperature interaction also had significant positive and negative effects, respectively. For HDPE (Escorene HD-6719), shrinkage in the Y-direction revealed the importance of the effect of packing pressure. Shrinkage in the Z-direction (thickness) was larger than in the other two directions, due to the lack of constraint in this dimension.

12. Process – structure – property relationships were considered for POM experimental results. It was found that CPPs, such as average plunger velocity and metering size, are important for the development of microstructure within the product. In turn, microstructural features, such as skin layer thickness, determine the ultimate properties of the micro injection molded products, such as modulus, yield stress, shrinkage, and thermal properties. The skin layer/modulus relationship appears to explain the variation of mechanical properties with processing conditions. Moreover, it explains the variation of mechanical properties with specimen cross section area, as reported in the literature. The dispersion of the data was probably caused by some types of flaw or defects in microstructure, including voids at the edges of large spherulites, whose size increased along the flow direction. To avoid the negative effects of these defects, heterogeneous nucleants may be used in order to achieve smaller spherulitic structure in manufactured micro products. Also, it should be noted that desirable mechanical properties are probably obtained at the cost of lower dimensional stability.

7.2 Claims to Original Contribution

The overall efforts reported in this work represent significant contributions to the understanding of process dynamics of the micro injection molding process, of the microstructure development in micro injection molded parts, of some properties of micro-molded products, and of process-structure-property relationships.

The specific original contributions made in this work, may be summarized as follows:

1. Six CPPs, in addition to metering size, were defined to characterize the filling and packing behaviour of the micro injection molding process. The proposed process characterization provides the opportunity to achieve viable process and product control and optimization, consistent with the actual operating characteristics of the machine. It also provides more realistic and accurate inputs for modeling and computer simulation of the process.
2. Moldflow commercial software was used for the modeling and simulation of the micro injection molding process. The large discrepancy between experimental and simulation results was attributed to incomplete and inadequate description, in the software, of both boundary conditions and the rheological behaviour.
3. The thermal properties of semi-crystalline moldings were investigated systematically. This study revealed the evolution of crystallinity and crystalline types along the flow direction.
4. The influence of extreme high shear rates and thermal gradients on the multilayer microstructure arising in the semi-crystalline micro injection moldings was evaluated.
5. Three special flow-related microstructural features were found in the gate region, including repetitive V-shape pattern and high molecular orientation.

6. The mechanical properties of micro injection molded samples were measured for both semi-crystalline and amorphous materials using specially designed punch die and sample holders for various process conditions.
7. The three dimensional shrinkage distribution was described for micro injection molded POM and HDPE.
8. Process–structure-property correlations for micro injection moldings were explored, based on POM experiments.

7.3 Recommendations for Future Work

The following issues may be considered in the future to extend our understanding in the micro injection molding process and products

1. Process characterization:
    - Install sensors for measuring in-mold pressure and temperature distributions and gate freezing time;
    - Modify the LabVIEW program for reducing its execution time;
    - Visualize the flow structure and monitor the process with high speed camera or other techniques.
2. Apply similar methodology for the study of other polymer systems of interest, including nanocomposites.
3. The annealing effects on microstructure development and mechanical properties may be studied for design of micro parts.
4. Study the effects of nucleating agents on the structure development and mechanical properties in the micro injection molding process. The development of uniform and grainy morphology may be helpful for improving the mechanical properties of micro injection moldings.
5. Conduct a systematic study of the tensile mechanical properties of micro molded tensile specimens with various thicknesses, from 1mm down to 50 μm. Compare the measured results with die cut samples.

6. Study in more detail the control of skin layer development in the gate region, since it could be critical for the behaviour of the process and products.
7. Characterization of material properties at extreme high injection, shear, and cooling rate.
8. Employ more realistic modeling and simulation of the micro injection molding process.

8. REFERNCES

1 Osswald, T.A., Turng, L.-S.T. and Gramann, P.J. Injection Molding Handbook. (Hanser Gardner Publications Inc., 2002).

2 Whiteside, B.R., Martyn, M.T., Coates, P.D., Greenway, G., Allen, P. and Hornsby, P. Micromoulding: Process measurements, product morphology and properties. Plastics, Rubber and Composites, 2004, 33(1), 11.

3 Zhao, J., Mayes, R.H., Chen, G., Xie, H. and Chan, P.S. Effects of Process Parameters on the Micro Molding Process. Polymer Engineering and Science, 2003, 43(9), 1542.

4 Haberstroh, E. and Brandt, M. Determination of mechanical properties of thermoplastics suitable for micro systems. Macromolecular Materials and Engineering, 2002, 287(12), 881.

5 Tom, A.M., Angelov, A.K. and Coulter, J.P. An Experimental Investigation of A Micro Injection Molded Mechanical Device. ASME International Mechanical Engineering Congress and ExpositionNovember 5-11, Orlando, Florida USA, 2005).

6 Sha, B., Dimov, S., Griffiths, C. and Packianather, M.S. Investigation of micro-injection moulding: Factors affecting the replication quality. Journal of Materials Processing Technology, 2007, 183(2-3), 284-296.

7 Giboz, J., Copponnex, T. and Mele, P. Microinjection molding of thermoplastic polymers: a review. Journal of Micromechanics and Microengineering, 2007(17), 14.

8 Haberstroh, E. and Schulz, J. Determination of Mechanical Properties Suitable for Micro Systems. Journal of Polymer Engineering, 2001, 21.

9 Tom, A.M., Layser, G.S. and Coulter, J.P. Mechanical Property Determination of Micro Injection Molded Tensile Test Specimens. ANTEC 2006).

10 Kamal, M.R., Kalyon, D.M. and Dealy, J.M. An Integrated Experimental Study of the Injection Molding Behavior of Some Polyethylene Resins. Polymer Engineering and Science, 1980, 20(17).

11 Tan, V. and Kamal, M.R. Distribution and Development of Morphological and Strain States in Injection-Molded Thermoplastics. ANTEC 1976, 343.

12 Kantz, M.R., Newman, J. and Stigale, F.H. The Skin-Core Morphology and Structure-Property Relationships in Injection Molded Polypropylene. Journal of Applied Polymer Science, 1972, 16.

13 Piotter, V., Mueller, K., Plewa, K., Ruprecht, R. and Hausselt, J. Performance and simulation of thermoplastic micro injection molding. Microsystem Technologies, 2002, 8(6), 387.

14 Su, Y.-C., Shah, J. and Lin, L. Implementation and analysis of polymeric microstructure replication by micro injection molding. Journal of Micromechanics and Microengineering, 2004, 14(3), 415.

15 Yuan, S., Hung, N.P., Ngoi, B.K.A. and Ali, M.Y. Development of Microreplication Process-Micromolding. Materials and Manufacturing Processes, 2003, 18(5).

16 Bibber, D.M. Micro molding challenges. p. 3703 (Society of Plastics Engineers, Chicago, IL., United States, 2004).

17 Michaeli, W., Spennemann, A. and Gartner, R. New plastification concepts for micro injection moulding. Microsystem Technologies, 2002, 8(1), 55-57.

18 Noerholm, M., Bruus, H., Jakobsen, M.H., Telleman, P. and Ramsing, N.B. Polymer microfluidic chip for online monitoring of microarray hybridizations. Lab on a Chip, 2004, 4(1), 28-37.

19 Close, B.W. and Hall, T.A. Disposable needle assembly having sensors formed therein permitting the simultaneous drawing and

administering of fluids and method of forming the same. In Publ., U.S.P.A., ed 2003.

20 Carlson, K., Chidley, M., Sung, K.-B., Descour, M., Gillenwater, A., Follen, M. and Richards-Kortum, R. In vivo fiber-optic confocal reflectance microscope with an injection-molded plastic miniature objective lens. Applied Optics, 2005, 44(10).

21 Matthew, D., Chidley, Liang, C., Michael, R., Descour, Sung, K.-B. and Richards-Kortum, R. Miniature injection molded optics for fiber-optic, in vivo confocal microscopy. international optical design conference 2002.

22 Ahn, C.H.C., Jin-Woo; Puntambekar, Aniruddha; Hong, Chien-Chong; Zhu, Xiaoshan; Gao, Chuan; Trichur, Ramachandran; Chilukuru, Srikanth; Dutta, Madhulika; Murugesan, Suresh; Kim, Sanghyo; Sohn, Young-Soo; Nevin, Joseph H.; Beaucage, Gregory; Lee, Jeong-Bong; Lee, Jae Y.; Bissell, Michael G, . Disposable biochip cartridge for clinical diagnostics toward point-of-care systems. Micro Total Analysis Systems 2002, Proceedings of the TAS 2002 Symposium, 6th, Nov. 3-7, Nara, Japan, 2002).

23 Tolinski, M. Macro challenges in micromolding. Plastics Engineering, 2005, 61(9), 14.

24 Martyn, M.T., Whiteside, B., Coates, P.D., Allan, P.S. and Hornsby, P. Studies of the Process-property Interaction of the Micromoulding Process. ANTEC 2002.

25 Pirskanen, J., Immonen, J., Kalima, V., Pietarinen, J., Siitonen, S., Kuittinen, M., Monkkonen, K., Pakkanen, T., Suvanto, M. and Paakkonen, E.J. Replication of sub-micrometre features using microsystems technology. Plastics, Rubber and Composites, 2005, 34(5/6), 222-226.

26 Chu, J., Kamal, M.R. and Hrymak, A.N. Microstructural Characteristics of Micro-Injection Molded Thermoplastics. ANTEC 2007 Cincinnati.

27 Griffiths, C.A., Dimov, S.S., Brousseau, E.B. and Hoyle, R.T. The Effects of Tool Surface Quality in Micro-injection Moulding. Journal of Materials Processing Technology, 2007, 189(1-3), 418-427.

28 Whiteside, B.R., Spares, R., Howell, K., Martyn, M.T. and Coates, P.D. Micromoulding: Extreme process monitoring and inline product assessment. Plastics, Rubber and Composites, 2005, 34(9), 380-386.

29 Whiteside, B., Spares, R., Brown, E., Norris, K., Coates, P.D., Ono, Y., Kobayashi, M., Cheng, C.-C. and Jen, C.K. Combined Flow Visualization and Ultrasonic Techniques for Characterisation of The Micromoulding Process. Polymer Processing Society 24th Annual Meeting Salerno, Italy, 2008.

30 Whiteside, B., Martyn, M.T. and Coates, P.D. Micromoulding: Process evaluation. p. 757 (Society of Plastics Engineers, Chicago, IL., United States, 2004).

31 Whiteside, B.R., Brown, E.C., Ono, Y., Jen, C.K. and Coates, P.D. Real-time ultrasonic diagnosis of polymer degradation and filling incompleteness in micromoulding. Plastics, Rubber and Composites, 2005, 34(9), 387-392.

32 Whiteside, B.R., Martyn, M.T. and Coates, P.D. In-process Monitoring of Micromoulding - Assessment of Process Variation. International Polymer Processing, 2005 (2), P162-169.

33 Whiteside, B.R., Martyn, M.T., Coates, P.D., Greenway, G., Allen, P. and Hornsby, P. Micromoulding: Process characteristics and product properties. p. 592 (Society of Plastics Engineers, Nashville, TN, United States, 2003).

34 Whiteside, B.R., Spares, R., Howell, K., Martyn, M.T. and Coates, P.D. In-process monitoring and 3d dimensional assessment of micromouldings. pp. 83-87 (Society of Plastics Engineers, Brookfield, CT 06804-0403, United States, Boston, MA, United States, 2005).

35 Whiteside, B.R., Brown, E.C., Ono, Y., Jen, C.K. and Coates, P.D. Polymer degradation and filling incompletion monitoring for micromolding using ultrasound. pp. 200-204 (Society of Plastics Engineers, Brookfield, CT 06804-0403, United States, Boston, MA, United States, 2005).

36 Shen, Y.K. and Wu, W.Y. An analysis of the three-dimensional micro-injection molding. International Communications in Heat and Mass Transfer, 2002, 29(3), 423.

37 Shen, Y.K., Chien, H.W. and Lin, Y. Optimization of the micro-injection molding process using grey relational analysis and MoldFlow analysis. Journal of Reinforced Plastics and Composites, 2004, 23(17), 1799.

38 Mehta, N.M., Barry, C.M.F., Bibber, D.T. and Tully, D. Validation of flow simulation for micromolded parts. p. 3550 (Society of Plastics Engineers, Nashville, TN, United States, 2003).

39 Yu, L., Lee, L.J. and Koelling, K.W. Flow and heat transfer simulation of injection molding with microstructures. Polymer Engineering and Science, 2004, 44(10), 1866.

40 Yu, L., Lee, L.J. and Koelling, K.W. Flow and Heat Transfer Simulation of Thin-Wall Injection Molding with Microstructures. p. 602 (Society of Plastics Engineers, Nashville, TN, United States, 2003).

41 Yu, L., Koh, C.G., Lee, L.J., Koelling, K.W. and Madou, M.J. Experimental investigation and numerical simulation of injection molding with micro-features. Polymer Engineering and Science, 2002, 42(5), 871.

42 Kemmann, O. and Weber, L. Simulation of the Micro Injection Molding Process. ANTEC (58th Annual Technical Conference - Society of Plastics Engineers), P577, 2000.

43 Yao, D. and Kim, B. Simulation of the filling process in micro channels for polymeric materials. Journal of Micromechanics and Microengineering, 2002, 12(5), 604.

44 Ilinca, F., Hetu, J.-F. and Derdouri, A. Numerical simulation of the filling stage in the micro-injection molding process. p. 636 (Society of Plastics Engineers, Chicago, IL., United States, 2004).

45 Hieber, C.A. and Shen, S.F. Flow Analysis of The Non-isothermal Two-Dimensional Filling Process in Injection Moulding. Isr Conf on Mech Eng, pp. 248-254 Haifa, Isr, 1978).

46 Rosenbaum, E.E. and Hatzikiriakos, S.G. Wall slip in the capillary flow of moleten polymers subject to viscous heating. AIChE Journal, 1997, 43.

47 Kamal, M.R. and Moy, F.H. Detailed Microstructure Characterization in Injection Molded Polyethylene. Society of Plastics Engineers (Technical Papers), 1980, 316-320.

48 Kamal, M.R. and Moy, F.H. Microstructural Characterization of Injection-Molded Articles. Journal of Applied Polymer Science, 1983, 28(5), 1787-1804.

49 Kamal, M.R. and Moy, F.H. Microstructure in Polymer Processing. A Case Study - Injection Molding. Polymer Engineering Reviews, 1983, 2(4), 381-416.

50 Kamal, M.R. and Tan, V. Orientation in Injection Molded Polystyrene. Polymer Engineering and Science, 1979, 19(8).

51 Tan, V. and Kamal, M.R. Morphological Zones and Orientation in Injection-Molded Polyethylene. Journal of Applied Polymer Science, 1978, 22(8), 2341.

52 Moy, F.H. and Musa, R.K. Crystalline and Amorphous Orientation in Injection Molded Polyethylene. Polymer Engineering and Science, 1980, 20(14).

53 Kamal, M.R. and Tan, V. Orientation in injection Molded Polystyrene. 1978, 126.

54 Kamal, M.R., Lai-Fook, R.A. and Hernandez-Aguilar, J.R. Residual thermal stresses in injection moldings of thermoplastics: A theoretical and experimental study. Polymer Engineering and Science, 2002, 42(5), 1098.

55 Capt, L. and Kamal, M.R. Effect of pressure on crystallization of polyethylene, Annual Technical Conference - Society of Plastics Engineers, 1999, 57th (Vol. 2), 1969-1973.

56 Geil, P.H. Polymer Single Crystals. (Interscience, New York, 1963).

57 Schultz, J.M. Polymer Materials Science. (Prentice-Hall, New York, 1974).

58 Mandelkern, L. Crystallization of Polymers. (McGraw-Hill, New York, 1964).

59 Moy, F.H. Microstructure and Kamal, M. The Distribution of Tensile Properties in Injection Molded Polyethylene. Chemical Engineering (McGill University, Montreal, 1980).

60 Osswald, T.A. and Menges, G. Materials Science of Polymers for Engineers. (Hanser, 2003).

61 Keller, A. Note on single crystals in polymers: evidence for folded chain configuration. Philosophical Magazine, 1957, 2, 8th Series(21), 1171-1175.

62 Fischer, E.W. Step-wise and spiral crystal growth in high polymers. Zeitschrift fur Naturforschung A (Astrophysik, Physik und Physikalische Chemie), 1957, 12a (9), 753-754.

63 Hemsley, D.A., Curson, D.A., Saville, B.P., Hoffman, R., Calvert, P. and Billingham, N.C. Applied Polymer Light Microscopy. (Elsevier Applied Science, London and New York, 1989).

64 Avrami, M. Kinetics of phase change. I. General theory. Journal of Chemical Physics, 1939, 7, 1103-1122.

65 Avrami, M. Kinetics of phase change. II. Transformation-time relations for random distribution of nuclei. Journal of Chemical Physics, 1940, 8, 212-224.

66 Tadmor, Z. and Gogos, C.G. Principles of polymer processing. (Wiley-Interscience, 1979).

67 Hatakeyama, T., Hashimoto, T. and Kanetsuna, H. Compressiblity of Polyethylene Under Pressure Up to 5000 Kg/cm^2. Colloid and Polymer Science, 1974, 252(1), 15-19.

68 Geil, P.H., Anderson, F.R., Wunderlich, B. and Arakawa, T. Morphology of polyethylene crystallized from the melt under pressure. Journal of Polymer Science, Part A: General Papers, 1964, 2(8), 3707-3720.

69 Matsuoka, S. and Maxwell, B. Pressure-induced crystallization in polyethylene. United States Department of Commerce, Office of Technical Services, PB Report, 1959, 161,455, 73 pp.

70 Smith, F.S. and Steward, R.D. Crystallization of Oriented Poly(Ethylene Terephthalate). Polymer, 1974, 15(5), 283-286.

71 Alfonso, G.C., Verdona, M.P. and Wasiak, A. Crystallization Kinetics of Oriented Poly (Ethylene Terephthalate) from the Glassy State. Polymer, 1978, 19(6), 711-716.

72 Pennings, A.J., Schouteten, C.J.H. and Kiel, A.M. Hydrodynamically Induced Crystallization of Polymers From Solution. V. Tensile Properties of Fibrillar Polyethylene Crystals. pp. 167-193 Prague, Czechoslovakia, 1972.

73 Tadmor, Z. and Gogos, C.G. Principles of polymer processing. (Wiley-Interscience, Hoboken, N.J., 2006).

74 Mackley, M.R. and Keller, A. Flow induced crystallization of polyethylene melts. Polymer, 1973, 14(1), 16-20.

75 Peterlin, A. Molecular Aspects of Oriented Polymers Structure and Properties of Oriented Polymers. (Wiley, New York, 1975).

76 Katti, S.S. and Schultz, J.M. Microstructure of Injection-molded Semicrystalline Polymers - A Review. Polymer Engineering and Science, 1982, 22(16), 1001-1017.

77 Aoba, T. and Odaira, H. Flow of polymer melt in injection mold. 1970, 124-126.

78 Kamal, M.R. and Kenig, S. Injection molding of thermoplastics. II. Experimental test of the model. Polym. Eng. Sci. FIELD Full Journal Title: Polymer Engineering and Science, 1972, 12(4), 302-308.

79 White, J.L. and Dee, H.B. Flow Visualization for Injection Molding of Polyethylene and Polystyrene Melts. Polymer Engineering and Science, 1974, 14(3), 212-222.

80 Schmidt, L.R. Special mold and tracer technique for studying shear and extensional flows in a mold cavity during injection molding. Polym. Eng. Sci. FIELD Full Journal Title: Polymer Engineering and Science, 1974, 14(11), 797-800.

81 Kamal, M.R., Kuo, Y. and Doan, P.H. Injection Molding Behaviour of Thermoplastics in Rectangular Cavities. Transport & Road Research Laboratory (Great Britain), TRRL Report, 1974, 20, 539-544.

82 Kamal, M.R. and Kenig, S. Injection molding of thermoplastics. I. Theoretical model. Polym. Eng. Sci. FIELD Full Journal Title: Polymer Engineering and Science, 1972, 12(4), 294-301.

83 Farhoudi, Y. and Kamal, M.R. Theoretical and experimental study of thermal residual stresses in injection molded amorphous polymers. p. 521 (Soc of Plastics Engineers, Brookfield, CT, USA, Toronto, Can, 1997).

84 Tao, H. and Kamal, M.R. Morphological modeling of polymer solidification. Polymer Engineering and Science, 2000, 40(8), 1796-1808.

85 Wu, P.C., Huang, C.F. and Gogos, C.G. Simulation of the Mold-Filling Process. Polymer Engineering and Science, 1974, 14(3), 223-230.

86 Barrie, I.T. Understanding how an injection mold fills. 1971, 27(8), 64-69.

87 Osswald, T.A., Baur, Brinkmann, Oberbach and Schmachtenberg. International Plastics Handbook. (Hanser, 2006).

88 Tadmor, Z. Molecular Orientation in Injection Molding. Journal of Applied Polymer Science, 1974, 18(6), 1753-1772.

89 Mavridis, H., Hrymak, A.N. and Vlachopoulos, J. Finite Element Simulation of Fountain Flow in Injection Molding. Polymer Engineering and Science, 1986, 26(7), 449-454.

90 Mavridis, H., Hrymak, A.N. and Vlachopoulos, J. The Effect of Fountain Flow on Molecular Orientation in Injection Molding. Journal of Rheology, 1988.

91 Mavridis, H., Hrymak, A.N. and Vlachopoulos, J. Deformation and Orientation of Fluid Elements Behind an Advancing Flow Front. Journal of Rheology, 1986(30 (3)), 555-563.

92 Isayev, A.I. and Hieber, C.A. Toward a Viscoelastic Modeling of the Injection Molding of Polymers. Rheologica Acta, 1980, 19.

93 Guo, X., Isayev, A.I. and Guo, L. Crystallinity and microstructure in injection moldings of isotactic polypropylenes. Part 1: a new approach to modeling and model parameters. Polymer Engineering and Science, 1999, 39(10), P2096-2114.

94 Hsiung, C.M. and Cakmak, M. Computer simulations of crystallinity gradients developed in injection molding of slowly crystallizing polymers. Polymer Engineering and Science, 1991, 31(19), 1372-1385.

95 Nakamura, K., Watanabe, T., Katayama, K. and Amano, T. Some Aspects of Nonisothermal Crystallization of Polymers. I. Relationship between Crystallization Temperature, Crystallinity, and Cooling Conditions. Journal of Applied Polymer Science, 2003, 16, 15.

96 Vleeshouwers, S. and Meijer, H.E.H. A rheological study of shear induced crystallization. Rheologica Acta, 1996, 35(5), 391-399.

97 Heckmann, W. and Johnsen, U. Shear-induced Crystallization in Injection Moldings Made of HDPE. Colloid and Polymer Science, 1974, 252(10), 826-835.

98 Clark, E.S. Structure development in injection molding acetal homopolymer. Appl. Polym. Symp. FIELD Full Journal Title: Applied Polymer Symposia, 1973, No. 20, 325-332.

99 Clark, E.S. Morphology and properties of injection molded crystalline polymers. Appl. Polym. Symp. FIELD Full Journal Title: Applied Polymer Symposia, 1974, 24, 45-53.

100 Ehrenstein, G.W., Riedel, G. and Trawiel, P. Thermal Analysis of Plastics - Theory and Practice (HANSER, Munich, 2004).

101 Ito, H., Yagisawa, Y., Saito, T., Yasuhara, T., Kikutani, T. and Yamagiwa, Y. Fundamental study on structure development of thin-wall injection molded products. Theoretical and Applied Mechanics Japan, 2005, 54, 263-268.

102 Evrard, M., Derdouri, A., Hétu, J.F. and Nardini, N. Mechanical Properties of Micro-Molded Tensile Bars as Related to Processing Parameters. PPS 2005 Americas Regional Meeting Proceedings.

103 McCullough, R.L. Properties of Solid Polymeric Materials. (Academic Press, New York, 1972).

104 Beaumont, J. Successful Injection Molding: process, design, and simulation. (Hanser, Cincinnati, 2002).

105 Kantz, M.R. Effects of melt processing variables on the morphology and properties of injection molded polypropylene. International Journal of Polymeric Materials, 1974, 3(3), 245-258.

106 Kantz, M.R. Effects of melt processing variables on the morphology and properties of injection molded polypropylene. Predicting Plast. Performance, Div. Tech. Conf., Soc. Plast. Eng., 1973, 86-97.

107 Bowman, J., Harris, N. and Bevis, M. Investigation of the Relationships Between Processing Conditions, Microstructure and

Mechanical Properties of an Injection Moulded Semi-Crystalline Thermoplastic. Journal of Materials Science, 1975, 10(1), 63-76.

108 Jansen, K.M.B., Pantani, R. and Titomanlio, G. As-molded shrinkage measurements on polystyrene injection molded products. Polymer Engineering and Science, 1998, 38(2), 254-264.

109 Jansen, K.M.B., Van Dijk, D.J. and Husselman, M.H. Effect of processing conditions on shrinkage in injection molding. Polymer Engineering and Science, 1998, 38(5), 838-846.

110 Saini, T.S. Prediction of Shrinkage and the Effect of Heat Treatment for Injection Molded Plates. Chemical Engineering (McGill University, Montreal, 2005).

111 Jansen, K.M.B. and Titomanlio, G. Effect of pressure history on shrinkage and residual stresses - injection molding with constrained shrinkage. Polymer Engineering and Science, 1996, 36(15), 2029-2040.

112 Harrell Jr, E.R., Elleithy, R.H., McFarland, C.A. and Summers, J.W. Contribution of flow deformation to the shrinkage of injection molded PVC. Journal of Vinyl and Additive Technology, 1999, 5(3), 116-124.

113 Chu, J., Kamal, M.R., Derdouri, A. and Hrymak, A.N. Effects of Processing Conditions on Mechanical Properties and Crystallinity of Micro Injection Molded Thermoplastics. ANTEC 2008 Milwaukee).

114 Piotter, V., Merz, L., Ruprecht, R. and Hausselt, J. Current status of micro powder injection molding. p. 4233 (Trans Tech Publications Ltd, Madrid, Spain, 2003).

115 Evrard, M. Systeme de conversion du signal 'injection stroke piston'. (IMI, CNRC-NRC, Canada, Montreal, 2005).

116 Kuek, S.-C. and Angstadt, D.C. In-Situ Cavity Pressure Monitoring in Micro-Injection Molding. ANTEC (Society of Plastics Engineers, Cincinnati, OH, 2007).

117 ASTM. Standard Test Method for Tensile Properties of Plastics - ASTM D 638 - 03. pp. 50-63 West Conshohocken, 2003).

118 Shen, L., Liu, T. and Lv, P. Polishing effect on nanoindentation behaviour of nylon 66 and its nanocomposites. Polymer Testing, 2005, 24(6), 746-749.

119 Shen, L., Phang, I.Y., Chen, L., Liu, T. and Zeng, K. Nanoindentation and morphological studies on nylon 66 nanocomposites. I. Effect of clay loading. Polymer, 2004, 45(10), 3341-3349.

120 Shen, L., Phang, I.Y., Liu, T. and Zeng, K. Nanoindentation and morphological studies on nylon 66/organoclay nanocomposites. II. Effect of strain rate. Polymer, 2004, 45(24), 8221-8229.

121 Shen, L., Tjiu, W.C. and Liu, T. Nanoindentation and morphological studies on injection-molded nylon-6 nanocomposites. Polymer, 2005, 46(25), 11969-11977.

122 Fang, T.-H., Chang, W.-J. and Tsai, S.-L. Nanomechanical characterization of polymer using atomic force microscopy and nanoindentation. Microelectronics Journal, 2005, 36(1), 55-59.

123 Wright-Charlesworth, D.D., Miller, D.M., Miskioglu, I. and King, J.A. Nanoindentation of injection molded PLA and self-reinforced composite PLA after in vitro conditioning for three months. Journal of Biomedical Materials Research - Part A, 2005, 74(3), 388-396.

124 Briscoe, B.J., Fiori, L. and Pelillo, E. Nano-indentation of polymeric surfaces. Journal of Physics D: Applied Physics, 1998, 31(19), 2395-2405.

125 VanLandingham, M.R., Villarrubia, J.S., Guthrie, W.F. and Meyers, G.F. Nanoindentation of Polymers: An Overview. In Macromolecular Symposia, W.-V.V.G., Tsukruk, V. V. and Spencer, N. D., Recent Advances in Scanning Probe Microscopy. Proceedings. 220th American Chemical Society National Meeting, pp. 15-43 Washington, DC., 2001.

126 Klapperich, C., Komvopoulos, K. and Pruitt, L. Nanomechanical properties of polymers determined from nanoindentation experiments. Journal of Tribology, 2001, 123(3), 624-631.

127 Kang, H.J., Kim, J., Kim, O., Wang, J. and Talke, F. Nanomechanical properties of viscoelastic polymers. pp. 184-188 (Society of Plastics Engineers, Brookfield, CT 06804-0403, United States, Boston, MA, United States, 2005).

128 Oliver, W.C. and Pharr, G.M. Measurement of hardness and elastic modulus by instrumented indentation: Advances in understanding and refinements to methodology. Journal of Materials Research, 2004, 19(1), 3-20.

129 Pharr, G.M. and Oliver, W.C. Measurement of thin film mechanical properties using nanoindentation. MRS Bulletin, 1992, 17(7), 28.

130 Pharr, G.M., Oliver, W.C. and Brotzen, F.R. On the generality of the relationship among contact stiffness, contact area, and elastic modulus during indentation. Journal of Materials Research, 1992, 7(3), 613-617.

131 Pharr, G.M., Tsui, T.Y., Bolshakov, A. and Oliver, W.C. Effects of residual stress on the measurement of hardness and elastic modulus using nanoindentation. pp. 127-134 (Materials Research Society, Pittsburgh, PA, USA, 1994).

132 Crocker, J. Measurement of the Young's Modulus of Hexoloy Silicon Carbide Thin Films Using Nanoindentation. Department of Mechanical Engineering, p. 66 (McGill University, Montreal, 2008).

133 Fischer-Cripps, A. Nanoindentation. (Spinger, 2002).

134 Fischer-Cripps, A. Nanoindentation (Spinger, 2004).

135 TriboIndenter, H. The external Hysitron TriboIndenter image and its translation stage. (www.hysitron.com, 2008).

136 Montgomery, D.C. Design and Analysis of Experiments. (John Wiley & Sons, Inc. , Arizona State University, 2005).

137 Moldflow. Moldflow Plastics Insight Help File. 2008, Extension rate (3D) results.

138 Philippoff, W. and Gaskins, F. The Capillary Experiment in Rheology. Transactions of the Society of Rheology, 1958, 2.

139 Cogswell, F.N. MEASURING THE EXTENSIONAL RHEOLOGY OF POLYMER MELTS. Transactions of the Society of Rheology, 1972, 16(3), 383-403.

140 Cogswell, F.N. Converging flow of polymer melts in extrusion dies. Polymer Engineering and Science, 1972, 12(1).

141 Dealy, J.M. and Wissbrun, K.F. Melt rheology and its role in plastics processing: theory and applications. (Van Nostrand Reinhold, New York, 1990).

142 Kennedy, P. Flow Analysis of Injection Molds. (Hanser Publishers, 1995).

143 Huilier, D. and Patterson, W.I. Modeling of Polymer Processing. (Hanser, 1991).

144 Shoemaker, J. Moldflow Design Guide. (Hanser, 2006).

145 Cimmino, S., Di Pace, E., Silvestre, C., Mendes, L.C. and Bonfanti, G. High density polyethylene/hydrogenated Oligo(Cyclopentadiene) blends. Tensile stress-strain behavior. Journal of Polymer Science, Part B: Polymer Physics, 1995, 33(12), 1723.

146 Somani, R.H., Yang, L. and Hsiao, B.S. Precursors of primary nucleation induced by flow in isotactic polypropylene. pp. 145-157 (Elsevier Science B.V., 2002).

147 Somani, R.H., Yang, L., Hsiao, B.S., Agarwal, P.K., Fruitwala, H.A. and Tsou, A.H. Shear-induced precursor structures in isotactic polypropylene melt by in-situ rheo-SAXS and rheo-WAXD studies. Macromolecules, 2002, 35(24), 9096-9104.

148 Clark, E.S. Fine structure in moldings of `Delrin'. pp. 115-118 (Society of Plastics Engineers (SPE), 1967).

149 Clark, E.S. Structure and properties of polymer films. In Lenz, R.W. and Stein, R.S., eds. Borden Award Symposium in Honor of Richard S. Stein (New York: Plenum Press, 1973).

150 Zheng, G.-Q., Yang, W., Yang, M.-B., Chen, J.-B., Li, Q. and Shen, C.-Y. Gas-assisted injection molded polypropylene: The skin-core structure. Polymer Engineering and Science, 2008, 48(5), 976-986.

151 Wang, Y., Na, B., Fu, Q. and Men, Y. Shear induced shish-kebab structure in PP and its blends with LLDPE. Polymer, 2004, 45(1), 207-215.

152 Wang, Y.D. and Cakmak, M. Structural characterization of injection molded PVDF and PVDF/PMMA blends. pp. 1776-1782 (Soc of Plastics Engineers, Brookfield, CT, USA, Boston, MA, USA, 1995).

153 Henke, S.J., Smith, C.E. and Abbott, R.F. Effect of Mold Temperature on the Morphology and Properties of Polypropylene: 1. A Propylene-Ethylene Copolymer. Polymer Engineering and Science, 1975, 15(2), 4.

154 Hobbs, S.Y. and Pratt, C.F. The Effect of Skin-Core Morphology on the Impact Fracture of Poly(butylene Terephthalate). Journal of Applied Polymer Science, 1975, 19, 22.

155 Barish, L. Study of cracking and fracturing of spherulitic isotactic polypropylene. Journal of Applied Polymer Science, 1962, 6(24), 617-623.

156 Hammer, C.F., Koch, T.A. and Whitney, J.F. Fine structure of acetal resins and its effect on mechanical properties. Journal of Applied Polymer Science, 1959, 1(2), 169-178.

157 Mohajer, Y. and Wilkes, G.L. Structure-Property Behaviour of Films Containing Disk Spherulites: A Model Study. Journal of Polymer Science, Polymer Physics Edition, 1982, 20(3), 457-472.

158 Gargani, L. and Bruzzone, M. Fatigue Resistance of Polybutadienes and Effect of Microstructure. pp. 27-28 (ACS, Div of Polymer Chemistry, Washington, DC, USA, 1985).

159 Nielsen, L.E. and Landel, R.F. Mechanical Properties of Polymers and Composites. (Marcel Dekker, Inc., 1994).

160 Dao, T.T. and Archer, L.A. Stick-slip dynamics of entangled polymer liquids. Langmuir, 2002, 18(7), 2616-2624.

161 Lin, Y.H. Explanation for Slip-stick Melt Fracture in Terms of Molecular Dynamics in Polymer Melts. Journal of Rheology, 1985, 29(6), 605-637.

162 Prez-Gonzalez, J. Study of the stick-slip phenomenon of linear low-density polyethylene in a brass die by using electrical measurements. Journal of Rheology, 2005, 49(3), 571-583.

163 Toivola, Y., Somerday, B.P., Shediac, R. and Ivill, M.P. Stick-slip fracture of polymer/metal interfaces. pp. 87-92 (Materials Research Society, Boston, MA, United states, 2002).

164 Ram, A. Fundamentals of Polymer Engineering. (Springer - Verlag Haifa Isarel, 1997).

165 Gauthier, C. Non elastic deformation during a mechanical test. In Swallowe, G.M., ed. Mechanical Properties and Testing of Polymers (Kluwer Academic, 1999).

166 Peterlin, A. Crystalline character in polymers. Journal of Polymer Science -- Polymer Symposia, 1965(9, Part C), 61-89.

167 Sperling, L.H. Introduction to Physical Polymer Science. (Wiley Interscience, Lehigh University Bethlehem, Pennsylvania, 2006).

168 Beer, F.P. and Johnston, R. Mechanics of Materials. (McGraw-Hill, Inc., 1992).

169 Moldflow. Moldflow Database. 2006.

170 Swallowe, G.M., ed. Mechanical Properties and Testing of Polymers. (Kluwer Academic, 1999).

171 Guo, X., Isayev, A.I. and Guo, L. Crystallinity and microstructure in injection moldings of isotactic polypropylenes. Part II: Simulation and Experiment. Polymer Engineering and Science, 1999, 39(10).

Appendix A: Viscosity and P-V-T properties of the selected materials

The viscosity and P-V-T properties of the selected materials used in the Moldflow commercial software [169] are shown as below:

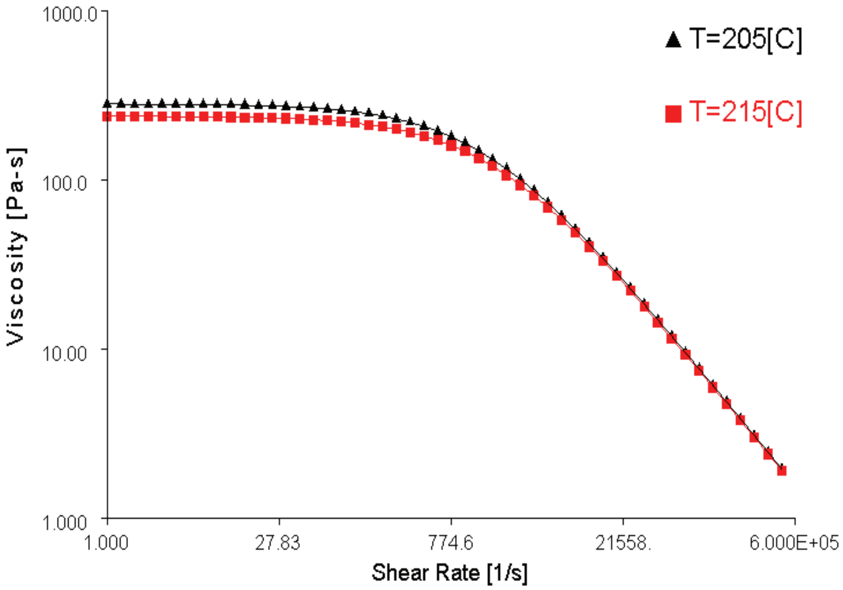

(a)

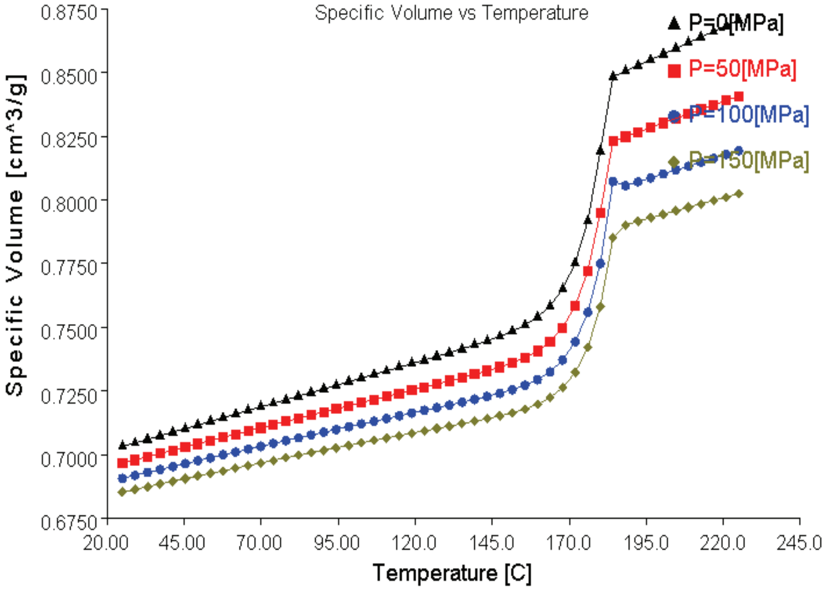

(b)

Figure A1: a) Viscosity of POM (Delrin 900P, Cross-WLF); b) P-V-T of POM (Two-domain Modified Tait) [169]

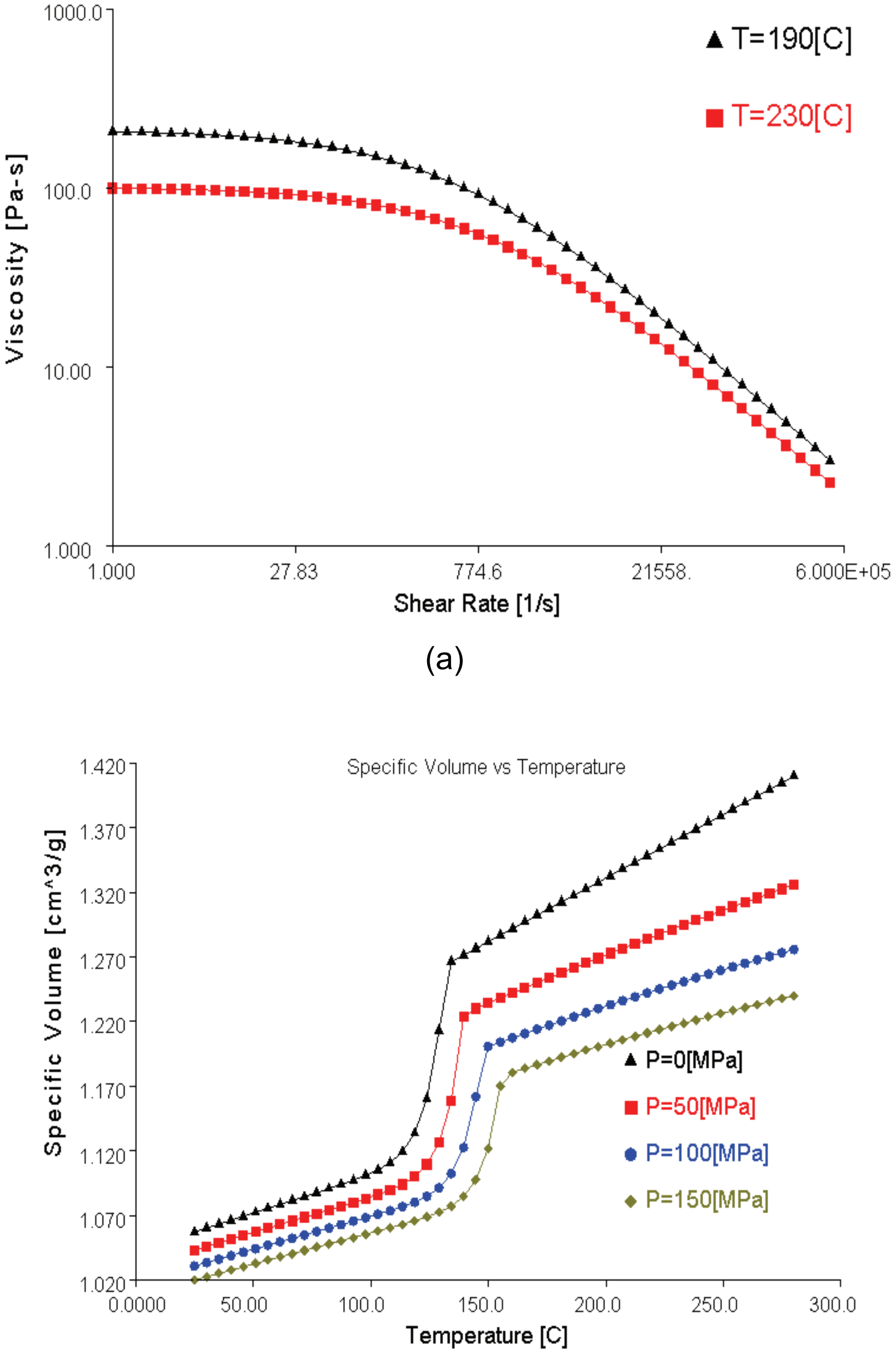

(a)

(b)

Figure A2: a) Viscosity of HDPE (Sclair 2714, Cross-WLF); b) P-V-T of HDPE (Two-domain Modified Tait) [169]

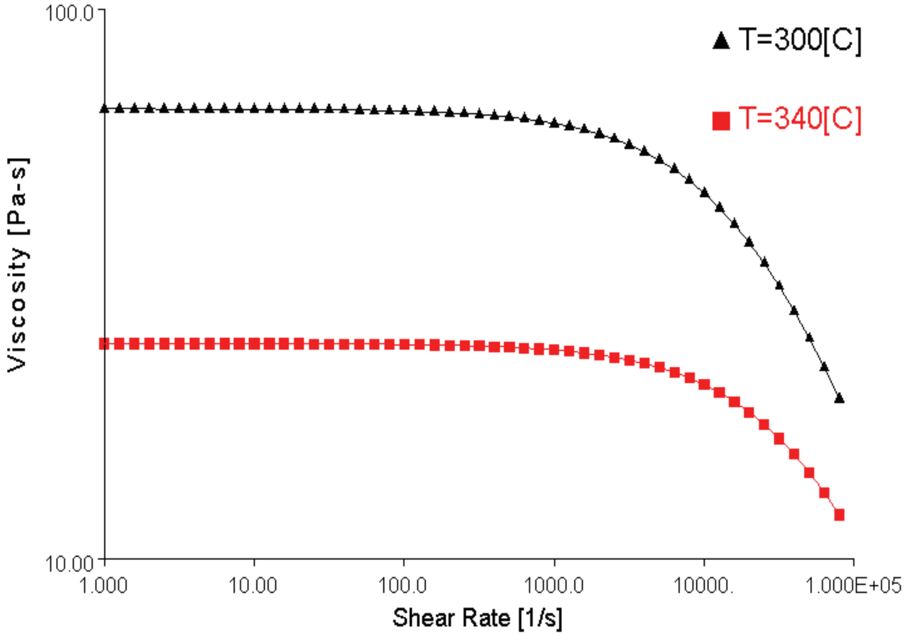

(a)

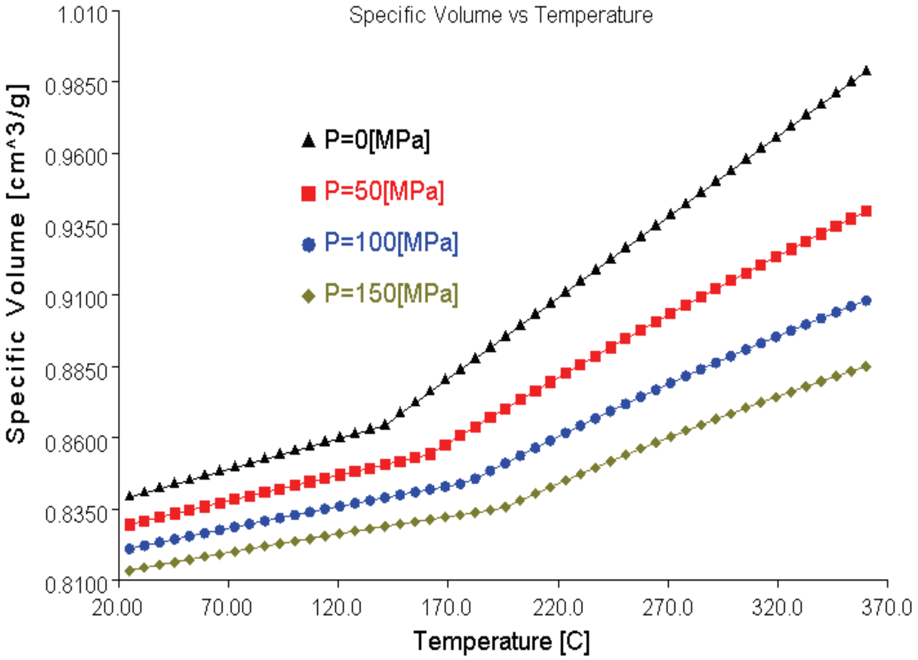

(b)

Figure A3: a) Viscosity of PC (Calibre 1080 DVD, Cross-WLF); b) P-V-T of PC (Two-domain Modified Tait) [169]

Appendix B: Governing equations for the filling phase

The equations governing the behaviours of a fluid motion include conservation of mass, conservation of momentum, and conservation of energy are shown in from Equation B1 to Equation B3 [142].

$$\frac{\partial \rho}{\partial t} + \left(\nabla . \rho \vec{\upsilon}\right) = 0 \qquad \text{Equation B1}$$

$$\frac{\partial}{\partial t}\left(\rho \vec{\upsilon}\right) = \rho \vec{g} + \left[\nabla . \underline{\sigma}\right] - \left[\nabla . \rho \vec{\upsilon} \vec{\upsilon}\right] \qquad \text{Equation B2}$$

$$\rho c_p \left(\frac{\partial T}{\partial t} + \vec{\upsilon} . \nabla T\right) = \beta T \left(\frac{\partial p}{\partial t} + \vec{\upsilon} . \nabla p\right) + p \nabla . \vec{\upsilon} + \left(\underline{\sigma} : \left\{\nabla \vec{\upsilon}\right\}\right) - \nabla . \left(\kappa \nabla T\right) \qquad \text{Equation B3}$$

These equations are quite general and hold for all common fluids. It is not feasible to solve them in complicated domains like injection mold cavities because of the limitations in computer hardware and material testing technology. A number of assumptions are made in order to make solution times and material data requirements more reasonable. The material properties, used in the software, are assumed as following:

1. During the filling phase, the melt is assumed to be incompressible. This assumption means that the density is constant.
2. The melt can be represented as a Generalized Newtonian Fluid. This assumption implies that visco-elastic effects will be ignored.
3. The thermal conductivity of the material is assumed to be constant.

Enforcing the assumptions above gives the following three equations:

$$\nabla . \vec{\upsilon} = 0 \qquad \text{Equation B4}$$

$$\rho \frac{\partial \vec{\upsilon}}{\partial t} = \rho \vec{g} - \nabla p + + \left[\nabla . \eta \dot{\gamma}\right] - \rho \left[\vec{\upsilon} . \nabla \vec{\upsilon}\right] \qquad \text{Equation B5}$$

$$\rho c_p \left(\frac{\partial T}{\partial t} + \vec{\upsilon} . \nabla T\right) = \beta T \left(\frac{\partial p}{\partial t} + \vec{\upsilon} . \nabla p\right) + \eta \dot{\gamma}^2 + \kappa \nabla^2 T \qquad \text{Equation B6}$$

These equations were used in the early versions of the Moldflow commercial software and may have been updated in the current version.

However, the updated equations are not available in the help file of Moldflow.